Realtime detection of high-energy neutrinos and search for correlations with candidate source classes

Dissertation
zur Erlangung des akademischen Grades
doctor rerum naturalium
(Dr. rer. nat.)

im Fach: Physik
Spezialisierung: Experimentalphysik

eingereicht an der
Mathematisch-Naturwissenschaftlichen Fakultät
der Humboldt-Universität zu Berlin

von
Cristina Lagunas Gualda, M. Sc

Präsidentin der Humboldt-Universität zu Berlin
Prof. Dr. Julia von Blumenthal

Dekanin der Mathematisch-Naturwissenschaftlichen Fakultät
Prof. Dr. Caren Tischendorf

Gutachterinnen:
Prof. Dr. Anna Franckowiak, Ruhr-Universität Bochum
Prof. Dr. Anna Nelles, Friedrich-Alexander-Universität Erlangen
Prof. Dr. Dorothea Samtleben, Leiden University

Tag der mündlichen Prüfung: 19. Januar 2024

Colophon
This document was typeset with the help of KOMA-Script and LaTeX using the open-source kaobook template class.

The source code of this thesis is available at:
https://github.com/clagunas/thesis

Publisher
First printed in 2024 by Humboldt Universität zu Berlin

Abstract

The IceCube Neutrino Observatory is the largest neutrino telescope in the world, located at the South Pole. IceCube discovered an all-sky isotropic flux of astrophysical neutrinos in 2013, but their origin remains mostly unknown. The goal of this thesis is to identify the sources of the most energetic neutrino events detected by IceCube. These so-called neutrino alert events are very likely to be of astrophysical origin. This work is the first analysis performed in IceCube that searches for correlations between a catalog of neutrino alert events and potential sources.

Two source classes are considered, gamma-ray blazars from the *Fermi*-LAT 4LAC-DR2 catalog and radio-bright Active Galactic Nuclei from the RFC 2022a catalog. Both classes have been suggested as neutrino emitters in many theoretical models due to the extreme acceleration that happens inside and the high density of their surrounding matter. To quantify the contribution of each source in the catalog to the final result, a weight is applied. This weight depends on the model of the neutrino production mechanism. For the *Fermi*-LAT 4LAC-DR2 catalog, two weighting schemes are considered: the normalized 10-year average energy flux in gamma rays, and the normalized energy flux in the 1-month time bin that coincides with the neutrino arrival time. For the RFC 2022a catalog, the sources are weighted by the flux density integrated over VLBI images at 8.6 GHz. There is no significant neutrino emission in any of the three searches. This result is compatible with a small fraction of sources ($< 1\%$) emitting neutrino alert events.

As part of this thesis, the impact of systematic uncertainties on the angular reconstruction of neutrino alert events is studied. Two datasets of simulated events were created using a method that ensures the similarity of all events within each defined category. These events are then reconstructed with the algorithm that is applied to neutrino alert events. The results from these studies prove that a more robust treatment of the systematic uncertainties is needed, since the uncertainty contours calculated with the current method do not correspond to the expected confidence levels for individual events. Furthermore, this work enables a direct comparison to other reconstruction algorithms for the first time, revealing that these alternative methods achieve better angular resolution at a fraction of the computational cost.

Zusammenfassung

Das IceCube Neutrino Observatory ist das größte Neutrinoteleskop der Welt und befindet sich am Südpol. IceCube hat im Jahr 2013 einen isotropen Fluss astrophysikalischer Neutrinos entdeckt, aber ihre Herkunft bleibt größtenteils unbekannt. Das Ziel dieser Doktorarbeit ist es, nach den Quellen der energiereichsten Neutrinoereignisse zu suchen, die von IceCube detektiert wurden. Diese sogenannten 'Neutrino Alert'-Ereignisse sind höchstwahrscheinlich astrophysikalischen Ursprungs. Diese Arbeit präsentiert die Ergebnisse der ersten IceCube Analyse, die nach Korrelationen zwischen einem Katalog von 'Neutrino Alert'-Ereignisse und potenziellen Quellen sucht.

Zwei Quellenklassen werden untersucht: Gammastrahlen-Blazare aus dem *Fermi*-LAT 4LAC-DR2-Katalog und radiohelle Aktive Galaktische Kerne aus dem RFC 2022a-Katalog. Beide Klassen wurden in vielen theoretischen Modellen als Neutrinoquellen vorgeschlagen. Sowohl aufgrund der extremen Beschleunigung, die in ihnen stattfindet, als auch der hohen Dichte ihrer umgebenden Materie. Um den Beitrag jeder Quelle im Katalog zum gesamten Ergebnis zu quantifizieren, wird ein Gewicht angewendet. Dieses Gewicht hängt vom Modell des Neutrinoproduktionsmechanismus ab. Für den *Fermi*-LAT 4LAC-DR2-Katalog werden zwei Gewichtungsschemata betrachtet: der normalisierte 10-Jahres-Durchschnittsenergiefluss in Gammastrahlen und der normalisierte Energiefluss im 1-Monats-Zeitintervall, das mit der Ankunftszeit des Neutrinos zusammenfällt. Für den RFC 2022a-Katalog werden die Quellen nach der Flussdichte gewichtet, die über VLBI-Bilder bei 8,6 GHz integriert ist. Es wurde keine signifikante Neutrinoemission in einer der drei Katalogsuchen festgestellt. Dieses Ergebnis ist mit einem kleinen Anteil von Quellen ($< 1\%$), die Neutrinos hoher Energie emittieren, vereinbar.

Als Teil dieser Doktorarbeit wird die Auswirkung von systematischen Unsicherheiten auf die Winkelrekonstruktion von 'Neutrino Alert'-Ereignissen untersucht. Zwei Datensätze simulierter Ereignisse wurden erstellt, die eine Methode verwenden, die sicherstellt, dass alle Ereignisse innerhalb jeder definierten Kategorie ähnlich sind. Diese Ereignisse werden dann mit dem Algorithmus rekonstruiert, der für 'Neutrino Alert'-Ereignisse angewendet wird. Die Ergebnisse dieser Studien zeigen, dass eine robusterer Umgang mit den systematischen Unsicherheiten erforderlich ist, da die Unsicherheitskonturen, die mit der aktuellen Methode berechnet werden, nicht den erwarteten Vertrauensniveaus für einzelne Ereignisse entsprechen. Darüber hinaus ermöglicht diese Arbeit zum ersten Mal einen direkten Vergleich mit anderen Rekonstruktionsalgorithmen, die eine bessere Winkelauslösung bei einem Bruchteil der Rechenkosten erreichen.

Contents

Abstract i

Zusammenfassung iii

Contents v

1 Introduction 1

Theoretical and experimental introduction 5

2 Multimessenger Astronomy 7
2.1 Cosmic Rays . . . 8
2.2 Photons . . . 11
2.3 Neutrinos . . . 15
2.4 Gravitational Waves . . . 17

3 IceCube Neutrino Observatory 19
3.1 The IceCube Neutrino Observatory . . . 19
3.2 Neutrino detection . . . 22
3.3 Data taking and processing . . . 28
3.4 Calibration and the Antarctic ice . . . 30

The IceCube Realtime Program and reconstruction improvements 33

4 The IceCube Realtime Program 35
4.1 Introduction to the IceCube Realtime Program . . . 35
4.2 Reconstruction methods . . . 38
4.3 Improvements to the angular reconstruction . . . 44
4.4 Relevant alerts . . . 45
4.5 The IceCube Event Catalog of Alert Tracks (IceCat-1) . . . 50

5 Golden Muons 53
5.1 Simulation . . . 53
5.2 Reconstruction . . . 56
5.3 First round of Golden Muons . . . 56
5.4 Second round of Golden Muons . . . 62
5.5 Comparison to other reconstruction methods . . . 65

6 Resimulation of realtime alerts 69
6.1 Method . . . 69
6.2 Study cases . . . 70
6.3 Comparison to other reconstruction methods . . . 76

7 Path forward 81
7.1 *Finding (track) reco* project . . . 81
7.2 New resimulation scheme . . . 82
7.3 New candidates to the realtime reconstruction method . . . 83
7.4 Outlook . . . 85

SEARCH FOR CORRELATIONS OF NEUTRINO ALERT EVENTS AND CANDIDATE SOURCES 87

8 Active Galactic Nuclei as neutrino sources 89
8.1 Structure of an AGN . . . 89
8.2 Classification of AGNs . . . 90
8.3 Gamma-bright blazars as neutrino sources . . . 91
8.4 Other radio-loud AGNs as neutrino sources . . . 94
8.5 Radio-quiet AGNs as neutrino sources . . . 96

9 Statistical analysis 99
9.1 Hypothesis testing . . . 99
9.2 Stacking analysis . . . 100
9.3 Analysis procedure . . . 101

10 Results of the stacking analyses 105
10.1 Samples . . . 105
10.2 Sensitivities and discovery potentials . . . 110
10.3 Results . . . 111
10.4 Discussion . . . 113
10.5 Cross-checks to previous analyses . . . 115

CONCLUSION 119

11 Summary and outlook 121

APPENDIX 123

A GCN Notice and Circular for an example event 125
A.1 GCN Notice . . . 126
A.2 GCN Circular . . . 127

B Golden Muons 129

C Resimulation of realtime alerts 133

D Additional information to the stacking analyses 137

Acknowledgements 149

Bibliography 151

List of Figures

1.1 A celestial map from the 17th century . . . 1
1.2 High-energy particles produced in an active galactic nucleus . . . 2
1.3 A window to multimessenger studies. . . . 3

2.1 Measured energy spectrum of gamma rays, neutrinos and cosmic rays . . . 7
2.2 Measurements of the increase of radiation with altitude by Hess . . . 8
2.3 Cosmic-ray energy spectrum . . . 9
2.4 Hillas diagram . . . 10
2.5 The electromagnetic spectrum . . . 11
2.6 Measured and expected fluxes of neutrinos . . . 16

3.1 The IceCube Neutrino Observatory . . . 20
3.2 Components of a Digital Optical Module . . . 20
3.3 IceCube geometry . . . 21
3.4 Neutrino Deep Inelastic Scattering cross-sections . . . 23
3.5 Cherenkov radiation . . . 24
3.6 Event morphologies in IceCube . . . 25
3.7 Energy losses of muons in ice . . . 26
3.8 Muon neutrino events detected in 9.5 years of data . . . 27
3.9 Diagram of the Data Acquisition System. . . . 29
3.10 Scattering and absorption lengths of photons . . . 30

4.1 Realtime Program pipeline . . . 37
4.2 IceCube's coordinate system . . . 38
4.3 Example of a skymap scan with Millipede . . . 41
4.4 Difference in LLH for resimulations of IC160427A . . . 42
4.5 Error contours derived with Wilks' theorem and with IC160427A resimulations. . . . 43
4.6 Error contours derived with IC170922A and with IC160427A resimulations. . . . 44
4.7 Comparison of the 90% circularized error between SplineMPE and Millipede for the realtime alerts 44
4.8 Containment regions for IC160427A . . . 45
4.9 Containment regions for IC170922A . . . 46
4.10 Containment regions for IC191001A . . . 47
4.11 Containment regions for IC191119A . . . 48
4.12 Containment regions for IC200530A . . . 49
4.13 The IceCat-1 catalog . . . 50

5.1 SnowStorm Monte Carlo illustration . . . 55
5.2 Simulation chain for resimulation of events . . . 56
5.3 Example of the zoomed-in scan . . . 56
5.4 Event views of 4 out of the 10 categories of resimulations . . . 58
5.5 Cumulative distribution of -2ΔLLH for the *Far from DOMs* and *Close to DOMs* Golden Muons . 60
5.6 Cumulative distribution of -2ΔLLH for the *Horizontal* Golden Muons . . . 60
5.7 Cumulative distribution of -2ΔLLH for four selected categories of Golden Muons . . . 60
5.8 Coverage of Golden Muons . . . 61
5.9 Examples of scans of the Golden Muons . . . 62
5.10 Idea for the calculation of correction values for each realtime alert . . . 63
5.11 Energy distribution of the events in the IceCat-1 catalog . . . 64

5.12 Cumulative distribution of −2ΔLLH for the *Horizontal* muons in the second round of Golden Muons 64
5.13 Distribution of the 50% and 90% correction values for the *Horizontal* muons in the second round of Golden Muons . . . 65
5.14 Results using SplineMPE with the "max" configuration . . . 66
5.15 Results using SplineMPE with the full-sky scan implementation . . . 67

6.1 IC170922A: Event view of the TXS neutrino event. . . . 70
6.2 IC170922A: Cumulative distribution of −2ΔLLH values, with old and new resimulations . . . 71
6.3 IC170922A: Cumulative distribution of −2ΔLLH values, compared with Golden Muons . . . 72
6.4 IC170922A: New contours and shift of resimulations . . . 72
6.5 IC191001A: Event views of the Bran Stark neutrino event . . . 73
6.6 IC191001A: New contour and shift of resimulations . . . 73
6.8 IC200530A: New contour and shift of resimulations . . . 74
6.7 IC200530A: Event views of the Tywin neutrino event . . . 74
6.10 IC200530A: Event views of 5 randomly selected Tywin resimulations . . . 75
6.9 IC200530A: Likelihood scan of a randomly selected Tywin neutrino resimulation . . . 75
6.11 IC200530A: Attenuation coefficient for a subset of Tywin resimulations . . . 76
6.12 IC191119A: Event views of the Lancel neutrino event . . . 76
6.13 IC170922A: Shift of resimulations for different methods . . . 77
6.14 IC191001A: Shift of resimulations for different methods (1) . . . 78
6.15 IC191001A: Shift of resimulations for different methods (2) . . . 79
6.16 IC200530A: Shift of resimulations for different methods . . . 79

7.1 Energy depositions in segments with the new resimulation scheme . . . 83
7.2 Results from the likelihood scan implementation of SplineMPE applied to the realtime benchmark simulations . . . 84
7.3 Results from the updated Millipede applied to the realtime benchmark simulations . . . 85

8.1 AGN Unification Model . . . 91
8.2 Spectral Energy Distribution of PKS 1502+106 . . . 92
8.3 Neutrino energy spectrum from AGN cores . . . 95
8.4 Neutrino fluxes for NGC 1068, TXS 0506+056 and diffuse neutrino background . . . 97

9.1 Conversion of −2ΔLLH map to probability map . . . 101
9.2 Sketch showing the sensitivity and discovery potential . . . 102
9.3 Sketch showing the steps for the signal injection . . . 102
10.1 Cross-section of *Fermi*-LAT . . . 105

10.2 Isotropy study of the *Fermi* 4LAC-DR2 catalog for the longitude coordinate . . . 107
10.3 Isotropy study of the *Fermi* 4LAC-DR2 catalog for the latitude coordinate . . . 107
10.4 Energy flux in gamma rays of TXS 0506+056 as function of time . . . 108
10.5 Values of the gamma-ray energy flux and the radio flux density $S_{8.6\,\mathrm{GHz}}$ for the sources that appear in both *Fermi* 4LAC-DR2 and RFC 2022a catalogs. . . . 109
10.6 Isotropy study of the RFC 2022a catalog . . . 109
10.7 Sensitivities and discovery potentials of the three stacking analyses . . . 110
10.8 Results of the three stacking analyses performed . . . 112
10.9 Number of correlations with TS_i greater than threshold with *Fermi* 4LAC-DR2 . . . 114
10.10 TS distributions of x% selected and injected blazars, from the *Fermi* 4LAC-DR2 catalog . . . 114
10.11 TS distributions of x% selected and injected blazars, from the RFC 2022a catalog . . . 115
10.12 Simplification and scaling of error contours in a previous study . . . 116
11.1 Geometry of IceCube-Gen2 . . . 121

11.2 Expected sensitivity for IceCube-Gen2 . . . 122

A.1 Millipede reconstruction scan of the neutrino alert IC230401A . . . 125

B.1 Event views of Golden Muons (1) . . . 129
B.2 Event views of Golden Muons (2) . . . 130
B.3 Event views of Golden Muons (3) . . . 131
B.4 Event views of Golden Muons (4) . . . 132

C.1 IC191001A: Cumulative distribution of the -2ΔLLH values for the Bran Stark resimulations . . . 133
C.2 IC200530A: Cumulative distribution of the -2ΔLLH values for the Tywin resimulations . . . 133
C.3 IC170922A: Zoomed-in likelihood scans of resimulated events . . . 134
C.4 IC191001A: Zoomed-in likelihood scans of resimulated events . . . 135
C.5 IC200530A: Zoomed-in likelihood scans of resimulated events . . . 136

D.1 Error contours for the top 10 contributors to the TS_{data} of the *Fermi*-LAT 4LAC-DR2 catalog with average energy flux weights . . . 138
D.2 Error contours for the top 10 contributors to the TS_{data} of the *Fermi*-LAT 4LAC-DR2 catalog with monthly energy flux weights . . . 142
D.3 Error contours for the top 10 contributors to the TS_{data} of the RFC 2022a catalog with average energy flux weights . . . 145
D.4 Most significant neutrino events in previous study using neutrino alert events and RFC 2019c catalog. . . . 148

List of Tables

4.1 Summary of relevant alerts . . . 49
4.2 Observed alert events in 10 years . . . 50
4.3 Expected alert events in 10 years . . . 50

5.1 SnowStorm parametrizations . . . 55
5.2 Results from the KS test comparing the *Far from DOMs* (*Far*) and the *Close to DOMs* (*Close*) categories. 59
5.3 Correction values for the four selected categories of Golden Muons . . . 59
5.4 Correction values for the *Horizontal* muons of the second round of Golden Muons . . . 65

6.1 Surviving events for the resimulation of realtime events after each applied cut . . . 70
6.2 Correction values for the three datasets of IC170922A resimulations . . . 71

10.1 Number of sources of each AGN type in the 4LAC-DR2 catalog. . . . 106
10.2 Isotropy studies of *Fermi* 4LAC-DR2 catalog . . . 106
10.3 Results from the *Fermi* 4LAC-DR2 catalog with average flux weights . . . 111
10.4 Results from the *Fermi* 4LAC-DR2 catalog with monthly flux weights . . . 113
10.5 Results from the RFC 2022a catalog . . . 113
10.6 Results from the cross-checks to a previous study . . . 117

D.1 Results for RFC 2022a + IceCat-1 catalogs, without scaling . . . 141
D.2 Results for RFC 2022a + IceCat-1 catalogs, with scaling . . . 141
D.3 Results for RFC 2019c + Alert-like events, without scaling . . . 141

D.4 Results for RFC 2019c + Alert-like events, with scaling 141

1 Introduction

Since the beginning of history, humans have been interested in the night sky. *Astronomy*, which in ancient Greek means "law of the stars" or "culture of the stars", was born thousands of years ago as an effort to understand stars and celestial objects, and to use them for navigation, timekeeping and agricultural planning. The early astronomers meticulously recorded the positions and movements of celestial objects, laying the groundwork for the development of more advanced astronomical theories.

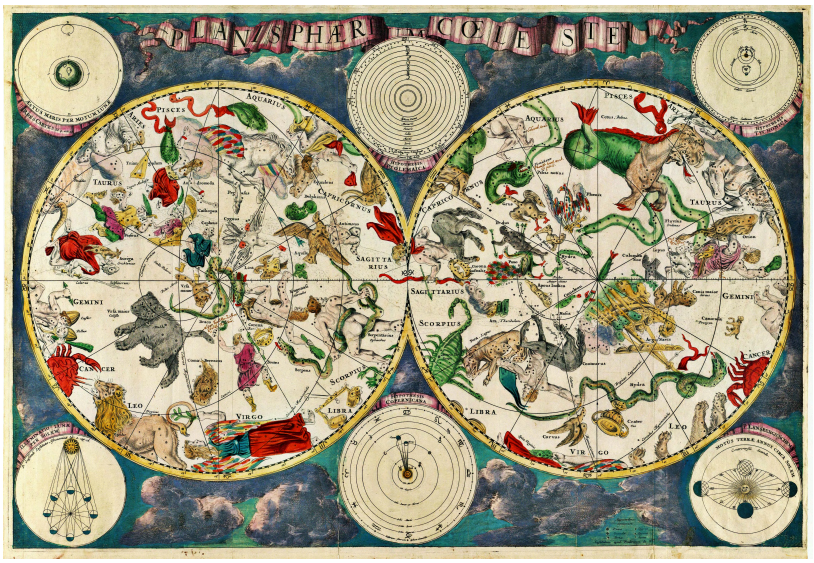

Figure 1.1: A celestial map from the 17th century, by the Dutch cartographer Frederik de Wit.

Multimessenger astronomy is the most recent branch of astronomy, and combines the information from various cosmic messengers (cosmic rays, photons, neutrinos and gravitational waves) to create a comprehensive picture of astrophysical phenomena. Learning about the production and propagation of these different messengers allows us to better understand our universe and the physical processes that occur there.

The most elusive astrophysical messenger particles are neutrinos, which interact only weakly with matter. They provide a unique perspective on the energetic processes happening inside their sources, since they can travel through the intergalactic space undisturbed. They are produced in the same sites as cosmic rays, so they offer an insight into the extreme environments in which the cosmic rays are accelerated. Huge detector volumes and long exposure times are needed to capture the rare interactions between neutrinos and matter. IceCube is a cubic-kilometer neutrino detector buried in the Antarctic ice, that discovered an all-sky isotropic flux of astrophysical high-energy neutrinos in 2013 [1], starting the field of *neutrino astronomy*.

[1]: Aartsen et al. (2013), 'Evidence for High-Energy Extraterrestrial Neutrinos at the IceCube Detector'

The core objective of this thesis is to find the sources of astrophysical neutrinos. The focus is set on the most energetic neutrinos detected by IceCube, which are likely to be of astrophysical origin. A good pointing

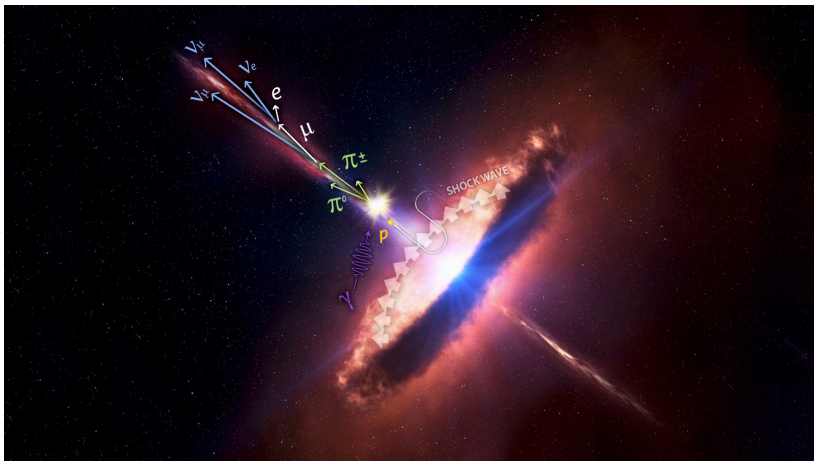

Figure 1.2: Astrophysical particles produced in an active galactic nucleus. Credit: IceCube Collaboration.

accuracy is key, and half of this thesis is devoted to study and improve the impact of systematic uncertainties on the angular reconstruction of the detected neutrinos. The second half focuses on how to use multimessenger information to select classes of objects that are candidate neutrino emitters, and develop an analysis method to search for coincidences between those sources and high-energy neutrinos. In particular, we apply this method to several catalogs of radio-loud Active Galactic Nuclei (AGNs).

The thesis is structured in three main parts, each of which contains several chapters. All chapters are described below.

Theoretical and experimental introduction

Chapter 2 Introduction to multimessenger astronomy. A description of the properties of cosmic rays, their sources and interactions is given. Then, astronomy with photons is briefly introduced, with special focus on the observations at different wavelengths. After that, the history of neutrino physics is presented. Lastly, a brief summary of gravitational wave astronomy is included.

Chapter 3 Description of the IceCube Neutrino Telescope. The different elements that compose IceCube are shown and the physical principles of neutrino detection in the ice are explained. The recording and processing of the data is presented, and a brief introduction to the detector calibration and the modeling of the antarctic ice is given.

The IceCube Realtime Program and reconstruction improvements

Chapter 4 Description of the IceCube Realtime Program. Alert events, the processing pipeline and the realtime program are introduced. The different reconstruction methods that are applied to alert events are discussed, as well as the improvements that are studied in this thesis. Lastly, some note-worthy alerts are presented, and a catalog of neutrino alert events is introduced.

Chapter 5 Study of the treatment of systematic uncertainties on the angular reconstruction of neutrino alert events. The simulation of a sample of events is explained, which are later used for a verification of the angular reconstruction method employed in the realtime program.

Chapter 6 Dedicated study of the angular uncertainty contours of neutrino alerts of interest. Here, alert events are simulated with slight variations in their direction, energy and light deposition, and reconstructed to calculate the 90% confidence level error contour. These events are also used to study the reconstruction method itself.

Chapter 7 Future plans for the angular reconstruction of the Realtime System are introduced, based on the work from the previous two chapters.

Search for correlations of neutrino alert events and candidate sources

Chapter 8 Theoretical introduction to AGNs. Neutrino emission predictions and the state-of-the-art analyses looking for neutrinos from AGNs are discussed.

Chapter 9 The statistical method developed for this thesis. The method is explained, which calculates the overall correlation between neutrino alert events and a catalog of candidate sources.

Chapter 10 Description of the three analyses performed with this method, two using the *Fermi*-LAT 4LAC-DR2 catalog, and one using the Radio Fundamental Catalog. The results are discussed and compared to previous studies.

Chapter 11 states the main conclusions of the thesis and discusses the future outlook of the work presented.

Appendices Supplementary information is given. Appendix A contains examples of a GCN Notice and a Circular. Appendix B shows representative event views for each category of simulated muons in the Golden Muons dataset. Appendix C includes additional figures from the resimulation of neutrino alert events. Appendix D shows error contours of the most significant correlations found in this work and the results of a cross-check on a previously published study.

Figure 1.3: A window to multimessenger studies. Credit: IceCube Collaboration.

Theoretical and experimental introduction

Multimessenger Astronomy 2

2.1 Cosmic Rays 8
2.2 Photons 11
2.3 Neutrinos 15
2.4 Gravitational Waves 17

Astronomy is one of the oldest and most traditional of sciences. Since the beginning of history, humans have looked up at the sky and tried to understand what they could observe by eye. There have been many technological advancements with time, from the first astronomical instrument, the telescope, to satellites that orbit the Earth, allowing us to see fainter objects and deeper in space.

During centuries, astronomy consisted only of electromagnetic observations in multiple wavelengths. We were already able to start talking about *Multimessenger Astronomy* with the cosmic ray measurements that began in the 20th century, but it wasn't until very recently that the other two messengers, neutrinos and gravitational waves, were detected.

It is only through the combined information from all the different messengers that we can hope to create a complete picture of our Universe. The production, acceleration and propagation mechanisms of cosmic rays, photons and neutrinos are intertwined. This is reflected in Figure 2.1, which shows that the flux densities of the three messengers follow a power-law distribution proportional to $E^2\phi$, where ϕ is the isotropic neutrino flux [2]. Photons and neutrinos are neutral particles and are not deflected by magnetic fields, pointing back to their sources, where cosmic rays are also expected to be produced. Therefore, each messenger provides a different insight into the same underlying physical processes.

[2]: Ackermann et al. (2019), 'Astrophysics Uniquely Enabled by Observations of High-Energy Cosmic Neutrinos'

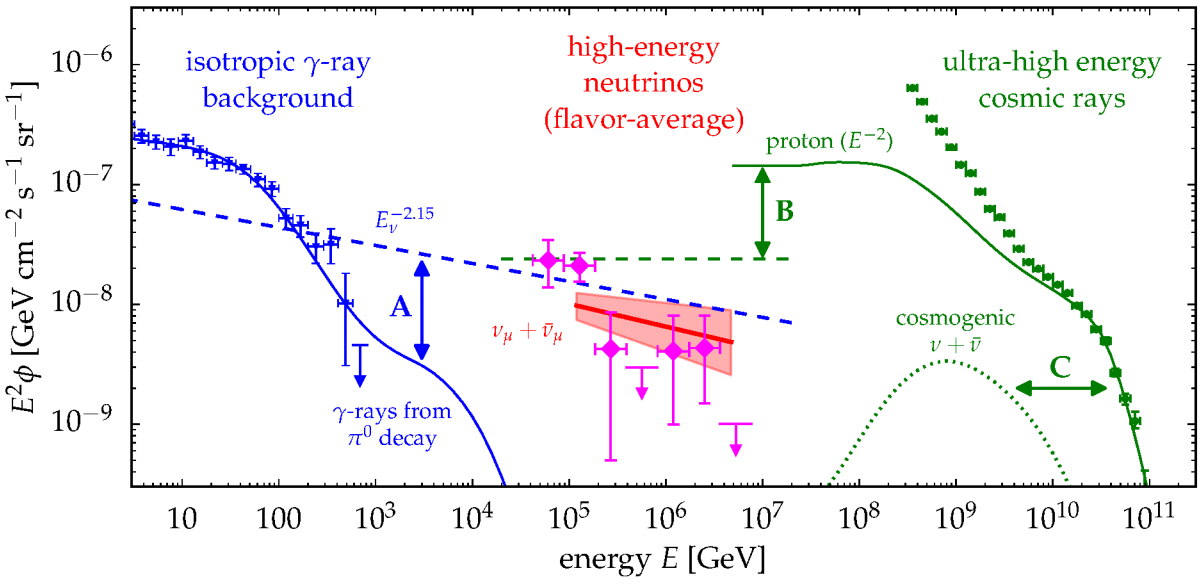

Figure 2.1: Measured energy spectrum of gamma rays, neutrinos and cosmic rays, from left to right. The three messengers follow approximately the same power-law spectrum at different energy ranges. From [2].

2.1 Cosmic Rays

Cosmic rays are high-energy charged particles, mostly protons, that originate and are accelerated in different sources, and that produce cascades of secondary particles when they interact with the Earth's atmosphere [3]. They were detected for the first time by Victor Hess in 1912 with balloon experiments [4]. He observed that the radiation increased with the altitude, concluding that it came from outside of the Earth, as opposed to what it was believed at the time. In Figure 2.2 the results from these experiments are shown.

Since then, several instruments in space and on Earth have been developed to measure and study the composition, energy spectrum and possible origin of these cosmic rays.

[3]: Gaisser et al. (2016), *Cosmic Rays and Particle Physics*

[4]: Hess (1912), 'Über Beobachtungen der durchdringenden Strahlung bei sieben Freiballonfahrten'

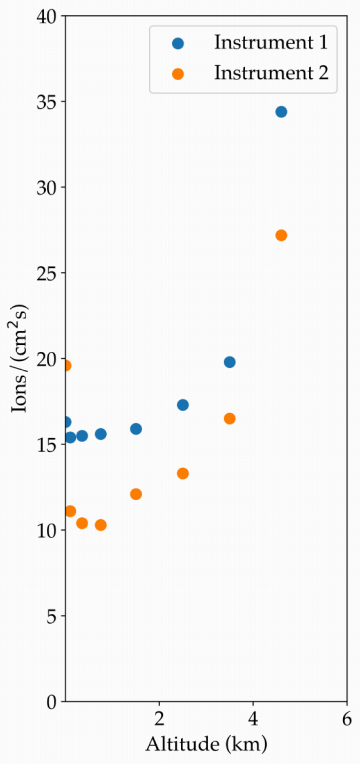

Figure 2.2: Measurements of the increase of radiation with altitude by Hess. Instrument 1 had an ionization volume of 2039 cm^3 and instrument 2 had a volume of 2970 cm^3. Adapted from [4].

[5]: Workman et al. (2022), 'Review of Particle Physics'

[6]: (2015), 'The Pierre Auger Cosmic Ray Observatory'

[7]: Abu-Zayyad et al. (2012), 'The surface detector array of the Telescope Array experiment'

[8]: Souza (2017), 'Testing the agreement between the X_{max} distributions measured by the Pierre Auger and Telescope Array Observatories'

[9]: Hörandel (2007), 'Cosmic Rays from the Knee to the Second Knee: 10^{14} to 10^{18} eV'

[10]: Hörandel (2003), 'On the knee in the energy spectrum of cosmic rays'

[11]: Stanev (2010), *High Energy Cosmic Rays*

Composition

Cosmic rays can be *primary*, when they are produced at the source, or *secondary*, after the propagation through space. Primary cosmic rays are composed of 74% free protons, ~ 18% helium nuclei and the rest are heavier elements [5]. Secondary cosmic rays interact with the Earth's atmosphere and are measured at the Earth's surface, underground, or in atmosphere short after the interaction.

The events at energies higher than 10^{18} eV are called Ultra-High-Energy Cosmic Rays (UHECRs) and their composition is studied by the ground-based detectors Pierre Auger Observatory (PAO) [6] and the Telescope Array (TA) [7]. A joint analysis states that both detectors observe data compatible with a light composition (mostly protons) below 10^{19} eV and with a mixed and heavier composition above 10^{19} eV [8].

Energy spectrum

The differential energy spectrum of proton and heavier nuclei cosmic rays can be seen in Figure 2.3. It covers several orders of magnitude in energy, from a few MeV up to hundreds of EeV per particle, and has three distinct features. First, between 10^{15} eV and 10^{16} eV there is a steepening in the spectrum called the *knee*. The second steepening, the *second knee*, happens at 10^{17} eV. Lastly, the *ankle* of the spectrum is found at $10^{18.5}$ eV. The overall shape can be approximated by different power-law spectra $dN/dE \propto E^{-\gamma}$, where $\gamma = 2.7$ before the knee, softens to $\gamma \approx 3.1$ after the first knee, $\gamma \approx 3.3$ after the second knee and flattens back to $\gamma \approx 2.7$ after the ankle [9].

The first part of the spectrum up to the knee at ~ 3 PeV can be explained by particle acceleration in Galactic sources, mostly supernova remnants. The steepening at the knee could indicate that the accelerators have reached the maximum energy to which they can accelerate protons, which depends on the strength of magnetic fields in the acceleration region [10]. It could also point to leakage of cosmic rays from the Galaxy due to interactions with the protons in the interstellar medium during their propagation [11]. The second knee can be also explained with

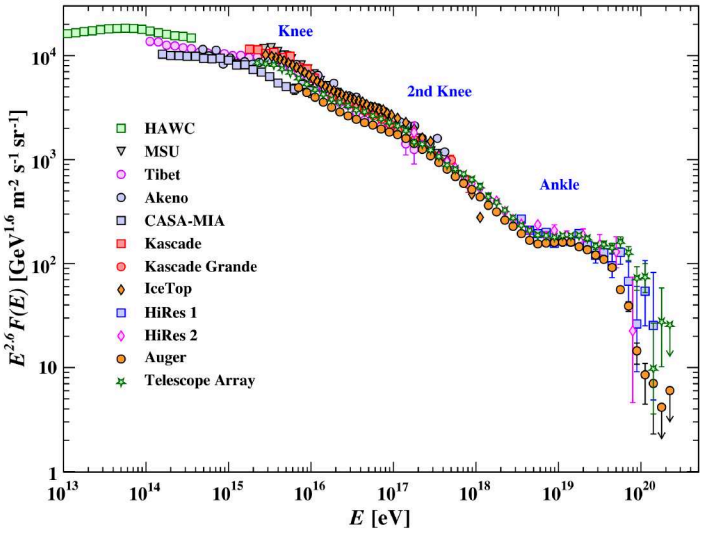

Figure 2.3: The all-particle cosmic ray energy spectrum from air shower experiments. From [5].

the same models applied to heavy elements, which cannot be further accelerated, or escape the Galaxy.

At energies of $\sim$ 6 EeV, the spectrum hardens and the spectral index becomes $\gamma \approx -2.7$ again, creating the *ankle* region. Some of the models proposed to explain this feature suggest a change in the dominant component, from galactic to extragalactic [12–14].

At the highest energies, $E > 10^{18}$ eV, an attenuation of the cosmic ray flux is expected. This is due to the *Greisen–Zatsepin–Kuzmin (GZK) mechanism* [15, 16], in which pions are produced via photohadronic interactions of protons with ambient cosmic microwave background (CMB) photons. In order to explain this spectral cutoff with the GZK effect, a proton-only composition is necessary, which is disfavored by the PAO and TA measurements [8, 17]. Alternatively, the observed suppression could also be related to the maximum cosmic-ray acceleration energy at the source [18].

Candidate sources

Cosmic rays are charged particles and are deflected by the many magnetic fields in the Universe on their way to Earth, making it challenging to determine their sources. However, there are theoretical limits to what kind of astrophysical objects could accelerate particles to such extreme energies. This requirement is called the *Hillas criterion* and establishes that the particles must be contained on site during the acceleration [19]. This is possible as long as their Larmor radius is smaller than the radius R of the accelerator. Using this, one can obtain the maximum energy E_{max} to which particles can be accelerated:

$$\frac{E_{\text{max}}}{\text{PeV}} \approx 1600 \times \frac{B}{\text{gauss}} \times \frac{R}{10^{16}\text{cm}} \times \beta Z, \tag{2.1}$$

where B is magnetic field strength, β is the velocity of the shock front and Z is the cosmic-ray charge number. Equation 2.1 constrains the minimum magnetic field and source size needed to accelerate cosmic rays, and is

[12]: Unger et al. (2015), 'Origin of the ankle in the ultrahigh energy cosmic ray spectrum, and of the extragalactic protons below it'
[13]: Aloisio et al. (2012), 'Transition from galactic to extragalactic cosmic rays'
[14]: Mollerach et al. (2019), 'Ultrahigh energy cosmic rays from a nearby extragalactic source in the diffusive regime'
[15]: Greisen (1966), 'End to the Cosmic-Ray Spectrum?'
[16]: Zatsepin et al. (1966), 'Upper limit of the spectrum of cosmic rays'
[8]: Souza (2017), 'Testing the agreement between the X_{max} distributions measured by the Pierre Auger and Telescope Array Observatories'
[17]: Aab et al. (2016), 'Evidence for a mixed mass composition at the 'ankle' in the cosmic-ray spectrum'
[18]: Das et al. (2021), 'Modeling the spectrum and composition of ultrahigh-energy cosmic rays with two populations of extragalactic sources'
[19]: Hillas (1984), 'The Origin of Ultra-High-Energy Cosmic Rays'

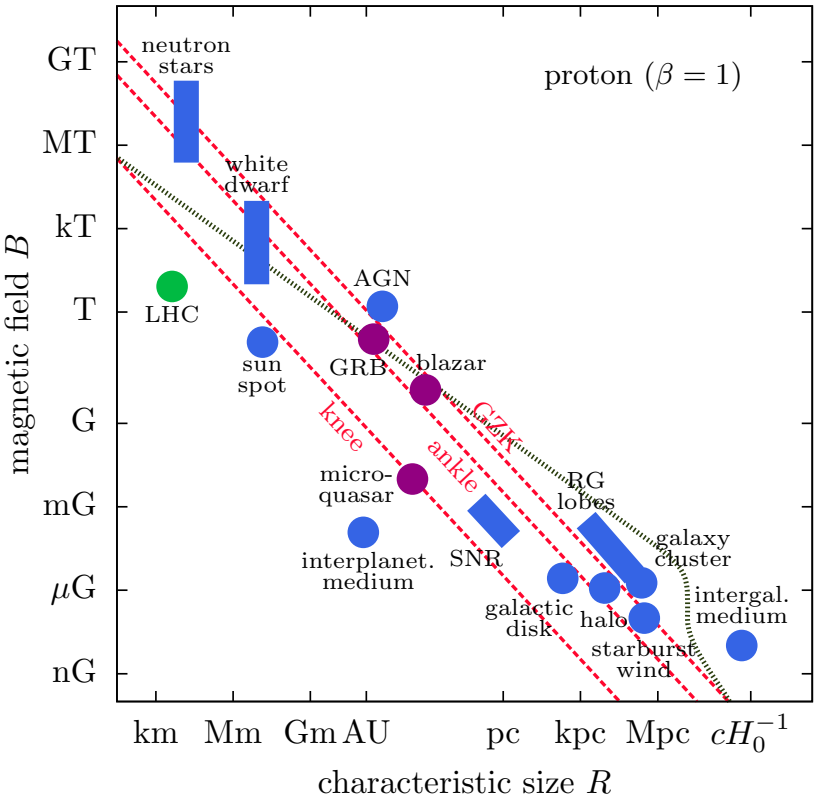

Figure 2.4: Hillas diagram illustrating different candidate source classes of cosmic rays. From [20].

illustrated by a *Hillas diagram* such as the one in Figure 2.4. The diagonal lines represent the threshold below which the Hillas condition is not satisfied and sources are not capable of accelerating particles with charge Z up to an energy E_{max}.

Acceleration mechanism

An astrophysical object not only has to satisfy the Hillas condition, but also has to accelerate the particles in a timescale shorter than the particle cooling timescale in order to produce cosmic rays. The main acceleration mechanism is *Fermi acceleration* [21], in which charged particles are reflected by magnetic fields in collisionless shocks. Direct particle collisions would cause energy losses, making the acceleration inefficient or even impossible to happen.

[21]: Fermi (1949), 'On the Origin of the Cosmic Radiation'

Depending on the exact process, there are two types of Fermi acceleration. In the *first-order Fermi acceleration*, also called *diffuse shock acceleration*, the charged particles scatter off of the irregularities that precede and follow the shock wave. The energy gain per shock is proportional to the velocity of the shock. Multiple reflections lead to an increase in energy of the charged particle, which follows a power-law spectrum $dN/dE \propto E^{-\gamma}$, with the index γ independent of the shock's velocity. This acceleration mechanism is widely used for modeling particle acceleration, with $\gamma = 2$ in most typical models.

The other mechanism is called *second-order Fermi acceleration*, and consists of collisions with a moving magnetic field. If the charged particle gets reflected from a magnetic field moving towards it, it will gain energy. If the field is moving in the opposite direction, the energy will decrease. In

a random motion environment, the particles are on average accelerated. The energy gained per shock in this case depends on the shock velocity squared, which makes this mechanism not as efficient as the first-order mechanism for particle acceleration. The energy flux of the charged particle follows a power-law spectrum $dN/dE \propto E^{-\gamma}$ in this case as well.

2.2 Photons

The detection of electromagnetic radiation is the oldest area of astronomy. Only through the combination of measurements of photons of various energies (see Figure 2.5) can we hope to completely understand the mechanisms of particle production and acceleration that take place in some astrophysical objects.

2.2.1 Types of emission

There are two classes of photon radiation, thermal and non-thermal emission, depending on the physical processes that they originate in. Thermal emission is generated by the thermal motion of particles in an object with a temperature greater than absolute zero, while non-thermal emission comes from particle acceleration [22]. Many astrophysical objects have both types of emission, contributing at different wavelengths.

Thermal emission

Thermal photons are generated by all matter with a temperature greater than zero due to the thermal motion of the particles in the matter.

A black body is a radiating object whose surface is in thermodynamic equilibrium and absorbs all incident electromagnetic radiation. It also emits electromagnetic black-body radiation according to Planck's law, with the spectrum determined by the temperature. Moreover, Wien's displacement law states what is the most likely frequency range of the radiation, which peaks at the corresponding wavelength $\lambda_{\text{peak}} = b/T$, where b is a proportionality constant. When the temperature increases, the frequency range moves to higher frequencies.

The spectral radiance (thermal radiation power) B of a body as a function of the frequency ν at absolute temperature T is given by

$$B(\nu, T) = \frac{2\pi\nu^3}{c^2} \frac{1}{e^{h\nu/k_b T} - 1} \tag{2.2}$$

where h is the Planck constant and k_b is the Boltzmann constant.

All astrophysical objects emit thermal radiation, which typically happens in infrared, optical or UV wavelengths.

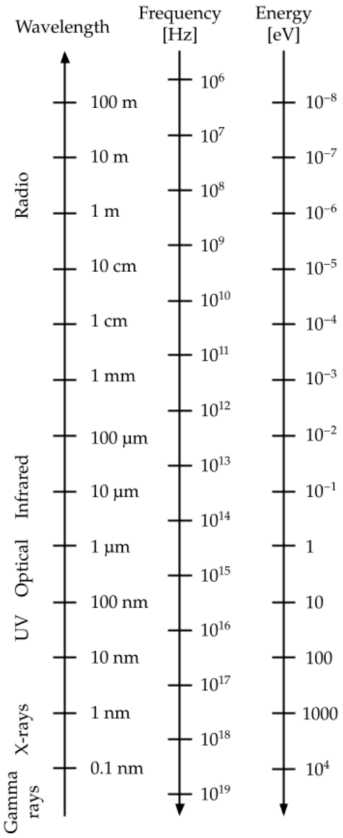

Figure 2.5: The electromagnetic spectrum. The photon wavelength is inversely proportional to the frequency and the energy.

[22]: Rybicki et al. (1986), *Radiative Processes in Astrophysics*

Non-thermal emission

Non-thermal emission is produced by the accelerated particles and typically follows a power-law spectrum. The detection of non-thermal photons is a key element for the identification of sources of cosmic rays and neutrinos, since it implies the presence of charged particles being accelerated.

One of the main processes that produce non-thermal emission is **synchrotron radiation**. It is emitted by a charged particle, usually an electron, moving in a magnetic field at relativistic speeds. It follows the power-law spectral shape from the Fermi acceleration of cosmic rays. Some synchrotron radiation emitters are pulsars, supernova remnants or radio galaxies.

At low energies, the synchrotron radiation is suppressed due to the scattering of synchrotron photons off electrons. This is known as **Synchrotron Self-Absorption**. That reduces the total synchrotron flux detected at Earth, where we only see emitted photons from a thin layer near the surface of the source. This spectral break usually happens at radio frequencies for electrons. At the higher energies of the spectrum we find a hard upper limit, since the electrons cannot get accelerated to energies that would make the gyro-radius larger than the accelerating region, thus limiting their synchrotron emission up to IR, optical, UV or X-ray wavelengths.

Two different scenarios can explain the production of the very-high-energy photons called gamma rays: **leptonic** and **hadronic models**. The most popular leptonic model is the **Synchrotron Self-Compton** mechanism. Low energy photons (radio to X-rays) produced by synchrotron emission from relativistic electrons at the source are further scattered off that same population of electrons via Inverse Compton (IC) scattering. The energy of the outgoing photon is larger than the incoming one, ending up in the gamma-ray regime.

In hadronic models, the cosmic rays interact with surrounding matter or radiation and the resulting neutral pions decay into two photons with energies in the gamma-ray range. In these models, the gamma rays are accompanied by pions and thus neutrinos are also produced in the same interactions. More commonly, one can find **leptohadronic models**, in which the cosmic rays interact with the synchrotron photons from the relativistic electrons or with thermal photons. At high energies it is difficult to distinguish between leptonic, hadronic or leptohadronic scenarios, which means that the detection of gamma rays does not assure the production of neutrinos from the same source.

2.2.2 Wavelengths

The variation in wavelength means that we need different instruments and methods to measure the full electromagnetic spectrum of astrophysical objects. Here an overview of the main telescopes and observations in every wavelength is presented.

Radio

Radio astronomy focuses on the longest wavelengths of the electromagnetic spectrum, between approximately 20 meters and 0.3 millimeters, or, equivalently, frequencies of 0.1 to 10 GHz. Since the radio window covers 4 orders of magnitude, radio telescopes have to be built in different sizes, or even have their signals combined in a process called Very Long Baseline Interferometry (VLBI) to simulate a larger antenna. Some primary examples are the Very Large Array (VLA) in New Mexico [23], or the Low-Frequency Array (LOFAR) which is located in Europe [24].

Radio observations allowed us to observe for the first time objects or processes that do not emit at visible wavelengths, like the Cosmic Microwave Background [25] or pulsars [26]*, the latter being magnetized rotating neutron stars that emit electromagnetic radiation. Radio galaxies, in which the central supermassive black hole ejects particles at relativistic speeds, can be detected by radio telescopes since the electrons in the plasma produce synchrotron radiation. Sources that are surrounded by clouds of dust and gas are also interesting for radio astronomers, because radiation emitted in shorter wavelengths is often obscured by the dust, whereas radio emission is not. The origin of many astrophysical objects happens inside of such clouds, so radio observations are particularly helpful in this field [27].

[23]: Napier et al. (1983), 'The very large array: Design and performance of a modern synthesis radio telescope'

[24]: Haarlem et al. (2013), 'LOFAR: The LOw-Frequency ARray'

[25]: Penzias et al. (1965), 'A Measurement of Excess Antenna Temperature at 4080 Mc/s.'

[26]: Hewish et al. (1968), 'Observation of a Rapidly Pulsating Radio Source'

[27]: Rodríguez (2007), 'Radio Astronomy: The Achievements and the Challenges'

Infrared

Infrared radiation comprises wavelengths from 0.75 μm to 1000 μm. Using infrared radiation we can observe distant galaxies, exoplanets, probe dust clouds and study molecules [28]. The infrared photons are less scattered by the dust than visible light, allowing us to see objects that are obscured in the optical range.

The first observations in the infrared started in the 19th century, when Professor Langley invented an instrument called "bolometer" to study solar radiation†. Nowadays, most telescopes that observe in the infrared cover also the optical and UV range.

[28]: Walker (2000), 'A brief history of infrared astronomy'

Optical and UV

The optical photons have a typical energy of $E_\gamma \sim 1$ eV and are mostly produced by the black body radiation from objects with thermal emission. Most objects emit some amount of IR/optical/UV radiation, like stars or supernovae. One of the most famous optical telescopes (also detecting infrared emission) is the James Webb Space Telescope [29], located in space. In the coming years the Vera C. Rubin Observatory will also be ready to start the Legacy Survey of Space and Time (LSST) [30], imaging

[29]: Gardner et al. (2006), 'The James Webb Space Telescope'

[30]: LSST Science Collaboration et al. (2009), 'LSST Science Book, Version 2.0'

* The discovery of the pulsar led to one of the most controversial Nobel Prizes in Physics, since it was awarded to A. Hewish instead of to J. Bell, the postgraduate student that discovered the signal.

† His student wrote the following poem:
Prof. Langley devised a bolometer,
it's really a sort of thermometer,
it'll detect the heat
of a polar bear's feet
at a distance of half a kilometre!

the entire available sky every few nights.

The Zwicky Transient Facility (ZTF) [31], of relevance to this thesis, is an optical time-domain survey that uses the Palomar 48 inch Schmidt telescope, with a 47 deg^2 field of view. Some specific follow-up observations of IceCube's neutrino events performed by ZTF motivate part of the technical studies of this thesis and will be discussed in Chapter 6.

[31]: Bellm et al. (2018), 'The Zwicky Transient Facility: System Overview, Performance, and First Results'

X-rays

The abundance of X-ray production mechanisms makes them a valuable messenger to study the physical properties and structure of astrophysical objects. Since X-rays are absorbed in the Earth's atmosphere, the only way to detect them is in space: ROSAT [32], the Neil Gehrels Swift Observatory [33], the Chandra X-Ray Observatory [34], and the Nuclear Spectroscopic Telescope Array (NuSTAR) [35] are some of the X-ray space telescopes.

Several types of objects emit radiation in X-rays, such as galaxy clusters, black holes, stars or supernova remnants. Some Solar System bodies, like the moon, reflect X-rays from the Sun. X-rays can be produced by both thermal and non-thermal emission: from bremsstrahlung, blackbody radiation, synchrotron radiation, or inverse Compton scattering of lower-energy photons by relativistic electrons.

[32]: Truemper (1982), 'The ROSAT mission'

[33]: Gehrels et al. (2004), 'The Swift Gamma-Ray Burst Mission'

[34]: Weisskopf et al. (2000), 'Chandra X-ray Observatory (CXO): overview'

[35]: Harrison et al. (2013), 'The Nuclear Spectroscopic Telescope Array (NuSTAR) High-Energy X-Ray Mission'

Gamma rays

Photons with energies above $\sim$ 100 keV are called gamma rays. They form the most energetic part of the spectrum, with the highest-energy photon detected so far at 1.4 PeV by the Large High Altitude Air Shower Observatory (LHAASO) [36]. As explained before, gamma rays are non-thermal emission, meaning that they can probe acceleration sites where cosmic rays can also be produced. Gamma-ray astronomy can give answers to the origin of cosmic rays, since photons are not deflected as they travel and point back to their sources. At TeV energies and above, gamma rays can interact with CMB photons or with Extragalactic Background Light (EBL) creating electron-positron pairs, so the very-high-energy extragalactic Universe is only completely transparent to neutrinos.

[36]: Cao et al. (2021), 'Ultrahigh-energy photons up to 1.4 petaelectronvolts from 12 γ-ray Galactic sources'

The Earth's atmosphere absorbs gamma rays, so satellite observatories are needed to detect them directly. Some space-based gamma-ray observatories are INTEGRAL (International Gamma-Ray Astrophysics Laboratory) [37], AGILE (Astro-rivelatore Gamma a Immagini Leggero) [38] and *Fermi*, which includes LAT, the Large Area Telescope [39], and GBM, the Gamma-Ray Burst Monitor [40]. *Fermi*-LAT will be discussed in more detail in Chapter 10, since its data is used in this thesis.

[37]: C, Winkler et al. (2003), 'The INTEGRAL mission'

[38]: Tavani et al. (2009), 'The AGILE Mission'

[39]: Atwood et al. (2009), 'The Large Area Telescope on the Fermi Gamma-ray Space Telescope mission'

[40]: Meegan et al. (2009), 'The Fermi Gamma-Ray Burst Monitor'

Going to space is not the only option: gamma rays produce electromagnetic air showers when they interact with matter at the top of the atmosphere that can be observed with ground-based telescopes at photon energies above $\sim$ 30 GeV. Imaging Atmospheric Cherenkov Telescopes (IACTs) detect the Cherenkov light emitted in the atmosphere by the charged shower particles, whereas with the Extensive Air Shower (EAS)

technique the shower particles themselves are detected by surface detectors. IACTs include H.E.S.S [41], VERITAS [42], MAGIC [43] and, as the planned next-generation, the Cherenkov Telescope Array (CTA) [44]; as EAS arrays we can find HAWC [45] and LHAASO [46].

[41]: Balzer et al. (2014), 'The H.E.S.S. central data acquisition system'

[42]: Weekes et al. (2002), 'VERITAS: the Very Energetic Radiation Imaging Telescope Array System'

[43]: Bigongiari (2005), 'The MAGIC Telescope'

[44]: Acharya et al. (2013), 'Introducing the CTA concept'

[45]: Springer (2016), 'The High Altitude water Cherenkov (HAWC) Observatory'

[46]: Cao et al. (2019), 'The Large High Altitude Air Shower Observatory (LHAASO) Science Book (2021 Edition)'

2.3 Neutrinos

Neutrinos are neutral, weakly-interacting elementary particles. They are fermions, particles with spin 1/2, and exist in three leptonic flavors: electron neutrinos (ν_e), muon neutrinos (ν_μ) and tau neutrinos (ν_τ). For each neutrino, there is also a corresponding antiparticle, called an antineutrino. Their origin varies from terrestrial to extragalactic, extending over 20 orders of magnitude in energy, as can be seen in Figure 2.6.

Neutrinos were postulated as a solution to the so-called *beta decay problem*. In a beta minus decay, a neutron in the nucleus decays into a proton and an electron is emitted. The energy spectrum of such a process was measured by J. Chadwick for the first time in 1914 [48], and he observed that it was continuous, meaning that a third particle was involved. W. Pauli proposed a chargeless particle with a very small mass to explain the missing energy from the beta decay: **the neutrino**‡ [50].

[48]: Chadwick (1914), 'Intensitätsverteilung im magnetischen Spectrum der β-Strahlen von radium B + C'

[50]: Pauli (1933), 'Structure et propriétés des noyaux atomiques'

Neutrinos were not detected until 20 years later, when F. Reines and C. Cowan measured a neutrino flux coming from a power plant which was produced via beta capture [51]. The next problem appeared soon after, when the Homestake experiment measured the flux of **solar neutrinos** (electron anti-neutrinos) [52], which was one third of what the solar models predicted [53]. After some theories proposed the mixing or oscillation between flavors of neutrinos [54, 55], an excess of muon neutrinos from the sun was finally observed by the Sudbury Neutrino Observatory [56]. This explained the deficit of electron neutrinos, since they would oscillate via $\nu_e \rightarrow \nu_\mu$. In parallel, the SuperKamiokande detector showed that muon neutrinos produced in the interactions of cosmic rays with the Earth's atmosphere oscillate into tau neutrinos [57].

[51]: Reines et al. (1956), 'The neutrino'

[52]: Davis et al. (1968), 'Search for Neutrinos from the Sun'

[53]: Bethe (1939), 'Energy Production in Stars'

[54]: Maki et al. (1962), 'Remarks on the Unified Model of Elementary Particles'

[55]: Pontecorvo (1967), 'Neutrino Experiments and the Problem of Conservation of Leptonic Charge'

[56]: Ahmad et al. (2001), 'Measurement of the Rate $\nu_e + d \rightarrow p + p + e^-$ Solar Neutrinos at the Sudbury Neutrino Observatory'

[57]: Fukuda et al. (1998), 'Evidence for Oscillation of Atmospheric Neutrinos'

Neutrino oscillations imply that neutrinos have mass, as opposed to what is considered in the Standard Model. Multiple experiments have tried to measure the oscillation parameters with different approaches. Most of them are sensitive to the difference in squared masses of the mass states (neutrino flavor states are a combination of the mass states), and the current measurements are $\Delta m^2_{21} = (0.753 \pm 0.018) \times 10^{-4}\,\text{eV}^2$ and $\Delta m^2_{32} = (24.4 \pm 0.6) \times 10^{-4}\,\text{eV}^2$ [5]. The absolute value of the mass is more challenging, and only recently the electron antineutrino mass was measured to be $m_\nu < 0.8\,\text{eV}$ by KATRIN [58]. Constraints on the sum of the three neutrinos masses come from cosmological observations, and are currently set to $\sum m_\nu < 0.12\,\text{eV}$ [59].

[5]: Workman et al. (2022), 'Review of Particle Physics'

[58]: Aker et al. (2022), 'Direct neutrino-mass measurement with sub-electronvolt sensitivity'

[59]: Aghanim et al. (2020), 'Planck 2018 results'

Neutrino astronomy became a reality in 1987, when 25 neutrinos from the **supernova SN 1987A** in the Large Magellanic Cloud were detected [60]. Neutrinos and anti-neutrinos are produced simultaneously when the

[60]: Arnett et al. (1989), 'Supernova 1987A'

‡ In the famous "Dear radioactive ladies and gentlemen" letter directed to the Tübingen conference on radioactivity [49], Pauli calls this new particle "neutron". It is later renamed to "neutrino" by Fermi after the discovery of the neutron by Chadwick.

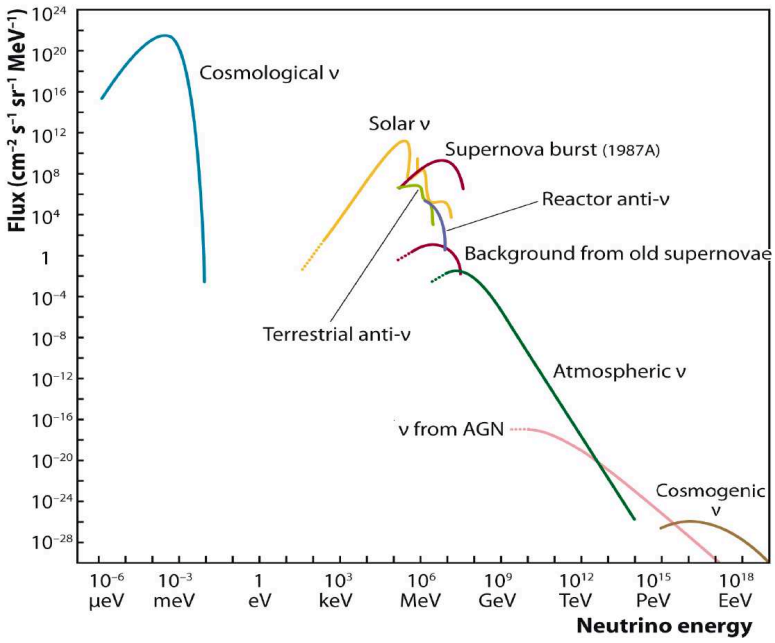

Figure 2.6: Measured and expected fluxes of neutrinos from natural and reactor sources, from [47]. The fluxes at the lowest and highest energy ranges (cosmological neutrinos, neutrinos from AGNs and cosmogenic neutrinos) are predicted values, while the other curves show measured fluxes.

core of a massive star collapses, and arrive at the Earth well before the visible light, carrying 99% of the explosion energy. Supernovae are still a promising candidate to produce astrophysical neutrinos in the MeV range [61], but only those that are nearby could produce a detectable flux.

[61]: Kharusi et al. (2021), 'SNEWS 2.0: a next-generation supernova early warning system for multi-messenger astronomy'

This discovery was also the beginning of multimessenger astronomy, which is one of the main science cases for experiments like IceCube. An all-sky isotropic flux of **astrophysical neutrinos** was discovered in 2013 [1], although the sources are still largely unknown. The first hint of a neutrino source, at the 3σ level, came from the spatial and temporal correlation of a high-energy neutrino and the blazar TXS 0506+056 [62], and the subsequent search for neutrino emission from the direction of said blazar [63]. More recently, strong evidence that the active galaxy NGC 1068 is a neutrino source was found, at the 4.2σ level [64]. However, these individual candidates are not enough to explain the isotropic flux of neutrinos, and a search for a general class of neutrino sources is the main objective of this thesis.

[1]: Aartsen et al. (2013), 'Evidence for High-Energy Extraterrestrial Neutrinos at the IceCube Detector'

[62]: Aartsen et al. (2018), 'Multimessenger observations of a flaring blazar coincident with high-energy neutrino IceCube-170922A'

[63]: Aartsen et al. (2018), 'Neutrino emission from the direction of the blazar TXS 0506+056 prior to the IceCube-170922A alert'

[64]: Abbasi et al. (2022), 'Evidence for neutrino emission from the nearby active galaxy NGC 1068'

Neutrinos are produced along-side photons in hadronic interactions of cosmic rays. The cosmic rays interact with surrounding matter or radiation at the source in hadronuclear (pp) or photohadronic ($p\gamma$) interactions:

$$p + p \rightarrow \begin{cases} \pi^{\pm} + X \\ \quad \hookrightarrow \mu^{\pm} + \overset{(-)}{\nu}_{\mu} \\ \quad\quad \hookrightarrow e^{\pm} + \overset{(-)}{\nu}_{e} + \overset{(-)}{\nu}_{\mu} \\ \pi^{0} + X \\ \quad \hookrightarrow \gamma + \gamma \end{cases} \tag{2.3}$$

$$p + \gamma \rightarrow \Delta^+ \rightarrow \begin{cases} \pi^+ + n \\ \quad \hookrightarrow \mu^+ + \nu_\mu \\ \qquad \hookrightarrow e^+ + \nu_e + \bar{\nu}_\mu \\ \pi^0 + p \\ \quad \hookrightarrow \gamma + \gamma \end{cases} \tag{2.4}$$

In both interaction channels, charged pions are produced that ultimately decay to muon neutrinos and muons, which will further decay to electrons and two other neutrinos. In the same processes, neutral pions are produced which decay to two gamma rays. On average, there are six neutrinos (three from each type of pion) for every two gamma rays. However, it is possible that the sources of neutrinos are obscured to gamma rays, i.e. gamma rays are absorbed in the surrounding material while neutrinos can escape.

More prominent than the astrophysical neutrino flux measured at Earth is the **atmospheric neutrino flux**, which is the main background for neutrino astronomy in IceCube. Cosmic rays can also interact with the atmosphere in the same way as in astrophysical sources, thus producing atmospheric neutrinos and muons. The atmospheric muons are relatively easy to discard by applying various cuts to select astrophysical neutrino events, while the atmospheric neutrinos remain an irreducible background. Only at high energies it is possible to distinguish an astrophysical signal.

From the interaction of cosmic-ray protons with atmospheric nuclei one would also expect a flux of charm or **prompt atmospheric neutrinos**. These are produced at higher energies, where the interaction creates heavier, charm mesons that decay to neutrinos of the three flavors. So far, this has not been measured, since it depends not only on the modelling of the charm contribution but also on the astrophysical neutrino flux, which contains relatively large uncertainties.

At very high energies of the order of PeV-EeV, we find **cosmogenic neutrinos**. These are theorised to be produced when cosmic rays at the GZK limit, i.e. with energies of the order of $\sim 10^{19}$ eV, interact with the cosmic microwave background radiation. These cosmogenic neutrinos are still out of reach for the existing neutrino observatories, but future experiments aim to extend the range of neutrino energies to EeV, potentially allowing us to detect them for the first time [65].

[65]: Aartsen et al. (2021), 'IceCube-Gen2: the window to the extreme Universe'

2.4 Gravitational Waves

Gravitational wave (GW) astronomy is the newest addition to the multi-messenger family. GWs are propagating disturbances in the space-time which are produced by the deformation of a local gravitational field as a result of the change in the structure of very massive, rapidly accelerating compact objects. The first gravitational wave signal was detected by LIGO in 2015, and it was the product of the merger of two black holes [66]. During the merger of compact objects, particles are accelerated and gamma rays and neutrinos are expected to be produced. This was partially confirmed by the multimessenger observation of the gravitational

[66]: Abbott et al. (2016), 'Observation of Gravitational Waves from a Binary Black Hole Merger'

wave event GW170817 (a binary neutron star merger), which was also detected in gamma rays [67]. This has motivated multiple searches of neutrinos coming from the direction of GWs, with no significant detection so far [68].

[67]: Abbott et al. (2017), 'Multi-messenger Observations of a Binary Neutron Star Merger*'

[68]: Abbasi et al. (2023), 'IceCube Search for Neutrinos Coincident with Gravitational Wave Events from LIGO/Virgo Run O3'

IceCube Neutrino Observatory | 3

3.1 The IceCube Neutrino Observatory 19
3.2 Neutrino detection 22
3.3 Data taking and processing 28
3.4 Calibration and the Antarctic ice 30

Neutrinos are key to understand the origin of cosmic rays, since they are the smoking-gun signature of particle acceleration and hadronic interactions. However, astrophysical neutrinos are incredibly difficult to detect due to the small interaction cross-sections and the low fluxes from astrophysical objects expected at Earth. Therefore, a big detection volume is needed. Neutrinos are detected via the induced Cherenkov photons from the daughter particles of their interactions, so the telescopes have to be located in a transparent medium. The relatively inexpensive option to have such a large volume of detection medium is to use natural resources: water, either in lakes or seas; or ice.

The main advantage of using water as the medium is the low scattering coefficient, which permits a good angular resolution. The best-known neutrino water-telescopes up to this day are located in the Mediterranean Sea: ANTARES [69], and its successor KM3NeT [70], which comprises ORCA (optimized for neutrino oscillation measurements) and ARCA (optimized for the search for point sources). In an early development stage we also find Pacific Ocean Neutrino Experiment (P-ONE) [71] which will be deployed off the coast of Canada. With the goal of combining the advantage of water as the detection medium with the ease of deployment in a frozen environment, the Baikal-GVD [72] neutrino telescope is located in the Lake Baikal in Russia.

The focus of this thesis is the IceCube Neutrino Observatory (successor of AMANDA [73]), located at the South Pole. Neutrino telescopes in ice have technical advantages for construction and deployment, and the ice has better absorption properties than the water, leading to a more precise energy resolution.

A next-generation detector called IceCube Gen-2* is planned to be fully operational by 2033 surrounding IceCube, adding $\mathcal{O}(10^4)$ new detector units and a radio array at the surface to measure PeV neutrinos. A prototype radio neutrino detector is currently operated as RNO-G in Greenland [74].

[69]: Ageron et al. (2011), 'ANTARES: The first undersea neutrino telescope'

[70]: Margiotta (2014), 'The KM3NeT deep-sea neutrino telescope'

[71]: Agostini et al. (2020), 'The Pacific Ocean Neutrino Experiment'

[72]: Shoibonov et al. (2019), 'Baikal-GVD - the Next Generation Neutrino Telescope in Lake Baikal'

[73]: Andres (2000), 'The AMANDA neutrino telescope: principle of operation and first results'

[74]: Aguilar Sánchez et al. (2021), 'The Radio Neutrino Observatory Greenland (RNO-G)'

3.1 The IceCube Neutrino Observatory

IceCube is a cubic-kilometer scale neutrino detector built at the South Pole [75]. The construction of the full detector configuration was finished in 2011, but it has been collecting data since the first strings were deployed. It consists of 5160 Digital Optical Modules (DOMs) located on 86 strings at depths between 1450 m and 2450 m. In the center of the array of strings there is a denser instrumented region, DeepCore, deployed at a depth of 1750 m to 2450 m. The in-ice array is complemented by a cosmic air-shower array on the surface of the ice called IceTop, comprised of 81 stations with ice-filled tanks. Lastly, the IceCube Laboratory (ICL), the

[75]: Aartsen et al. (2017), 'The IceCube Neutrino Observatory: instrumentation and online systems'

* The name is inspired by the gentoo penguin, a penguin species that lives at the South Pole.

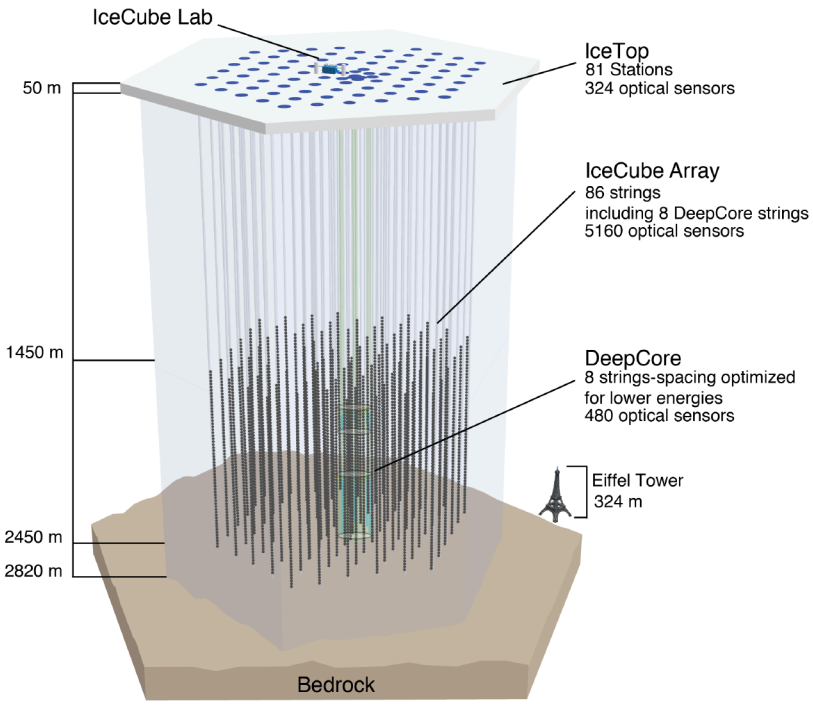

Figure 3.1: The IceCube Neutrino Observatory. From top to bottom, the central operations building IceCube Lab, the cosmic-ray air shower array IceTop, the in-ice IceCube array and the DeepCore sub-array. From [75].

operations building, sits on the surface in the center of the array. All these elements can be seen in Figure 3.1.

3.1.1 Digital Optical Module

The main detection unit in IceCube is the Digital Optical Module (DOM), which detects the Cherenkov light and acquires data based on different triggers. It consists of a pressure glass sphere containing a downward-facing Hamamatsu R7081-02 Photomultiplier Tube (PMT), an LED flasher board for calibration and the main board with all the required electronics to process the signal. These components can be seen in Figure 3.2. A mu-metal grid made of a wire mesh covers the PMT to minimize the effects of the 550 mG South Pole magnetic field, which would reduce the collection efficiency and the resolution of single photoelectrons of the PMTs [75]. A 1 cm Silicon gel coat fills the DOM to provide good optical coupling and reduce photon loss. The glass sphere protects the electronics and PMT against the constantly applied ice pressure of 250 bar and the temporary pressure of up to 690 bar during the refreezing of the drill hole from the deployment. Each DOM is connected by wires to the ICL and to the neighbouring DOMs above and below, to allow for time-correlated signals.

[75]: Aartsen et al. (2017), 'The IceCube Neutrino Observatory: instrumentation and online systems'

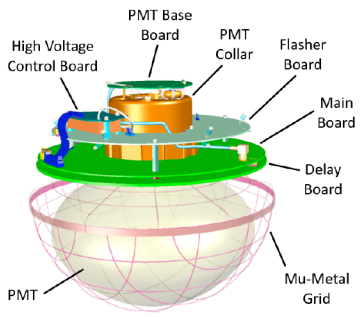

Figure 3.2: Components of a Digital Optical Module (DOM), from [75].

[76]: Abbasi et al. (2010), 'Calibration and characterization of the IceCube photomultiplier tube'

3.1.2 PhotoMultiplier Tube

The Photomultiplier Tube (PMT) [76] is the 10" diameter R7081-02 made by Hamamatsu Photonics. The photocathode in the PMT is made of bialkali material (Sb-Rb-Cs, Sb-K-Cs) and is sensitive to the wavelength range of 300 nm to 650 nm, with peak quantum efficiency of 25% (one in four photoelectrons arriving at the PMT is detected) achieved at 390 nm. The dark count rate in the −40 °C to −20 °C range is approximately 300 Hz,

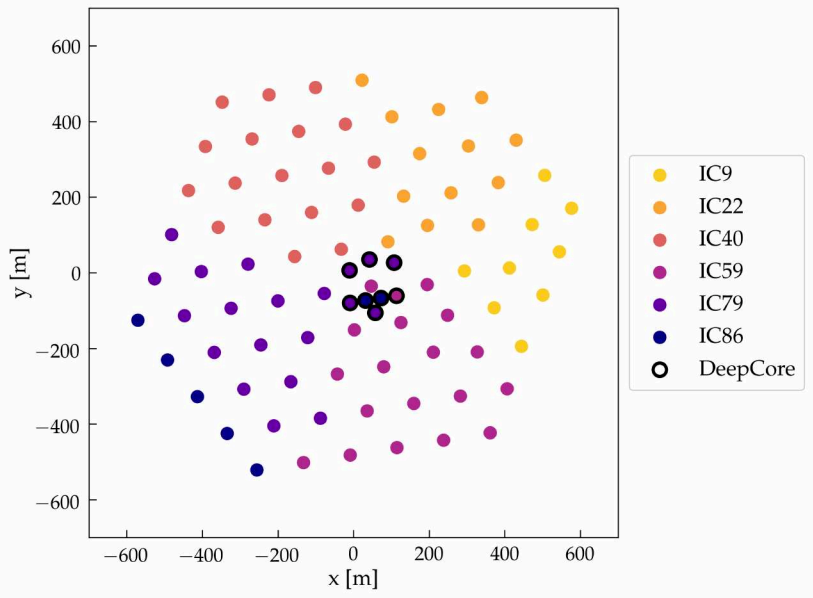

Figure 3.3: Location of the strings in the (x, y) plane in the IceCube coordinate system. The colors represent the strings that were deployed in each season, with the label names *ICXX* encoding the cumulative number of strings XX.

which allows to detect the Cherenkov signal induced by neutrinos with low energy such as those coming from a supernova event, above an energy threshold of 100 GeV.

3.1.3 Deployment and geometry of the in-ice array

The deployment started in 2004 with the first string, and continued in the field seasons in the consecutive summers until 2011, when the final configuration was reached. To create the holes where the strings are set, hot water drills were used. The holes were drilled with a larger diameter of approximately 60 cm (instead of the 35 cm diameter of the DOMs) to allow enough time to deploy also the instrumentation in the water-filled holes before they refroze.

During drilling, measures of the ice properties and the location of the holes were taken. The (x, y)-positions of the strings are determined by the position of the drill tower. The strings are assumed to be completely vertical, so all the DOMs on each string have the same (x, y) coordinates. In reality, the water drill suffered some deviation of an average maximum of 2 m in (x, y), but an accurate measurement location is not possible for all the DOMs due to lack of instrumentation.

The depth (z-coordinate) was calculated in two steps. Firstly, the measurements taken by the pressure sensor of the drill were converted to depth, while the vertical spacing between DOMs was measured with a laser pointing downwards from the top of the hole after each DOM deployment. Secondly, these values were corrected using the LED flashers on the DOMs. The final uncertainty on the depth is on the order of 1 m.

The final layout is 86 strings in a hexagonal footprint on a grid with 125 m horizontal spacing, with a total instrumented volume of 1 km^3. Each string contains 60 DOMs connected by a single cable. For the main in-ice array, which consists of 78 of the strings, the DOMs are vertically separated by 17 m. Figure 3.3 shows the position of the strings in the (x, y) plane, color-coded by the strings added in each deployment season.

Coordinate system

The origin of the coordinate system in IceCube is close to the geometrical center of the in-ice array. The y axis is aligned with the Prime Meridian and points towards Greenwich, UK. The x axis points 90 degrees clock-wise from the y axis, and the z axis is normal to the Earth's surface, pointing "up".

3.1.4 DeepCore and IceTop

DeepCore [77] is an inner sub-array that is more densely instrumented and has a lower energy threshold than the main in-ice array. It is comprised of 8 strings located at a depth of 1750 m to 2450 m, with 60 DOMs on each string (Figure 3.1). The bottom 50 DOMs have a vertical spacing of 7 m, while the top 10 have a spacing of 10 m and are used as veto. The DeepCore volume has an un-instrumented region between 1850 m and 2100 m due to the increased optical scattering and absorption there (the so-called dust layer, explained in Section 3.4). The PMTs in the DeepCore DOMs have a higher quantum efficiency than the other modules, which, along with the closer spacing, allows for a lower energy threshold of 10 GeV. DeepCore is optimized and mainly used for Beyond the Standard Model searches, such as neutrino oscillations [78] or Dark Matter searches [79], and detection of neutrinos from Supernovae.

[77]: Abbasi et al. (2012), 'The design and performance of IceCube DeepCore'

[78]: Aartsen et al. (2019), 'Measurement of atmospheric tau neutrino appearance with IceCube DeepCore'

[79]: Abbasi et al. (2022), 'Search for GeV-scale dark matter annihilation in the Sun with IceCube DeepCore'

On the surface there is an array of 162 tanks filled with clear ice to detect cosmic-ray air showers, called IceTop [80]. These tanks are grouped in 81 stations following the same grid as the IceCube strings and each of them is instrumented with two PMTs that detect the Cherenkov radiation produced by particles from the shower. The deposited light in the tanks and the spread of the air shower (usually over several stations) are used to measure the properties of cosmic rays, such as the energy spectrum and the mass composition [81].

[80]: Abbasi et al. (2013), 'IceTop: The surface component of IceCube'

[81]: Aartsen et al. (2019), 'Cosmic ray spectrum and composition from PeV to EeV using 3 years of data from IceTop and IceCube'

In the work presented here, data from DeepCore and IceTop are not utilized.

3.2 Neutrino detection

Neutrinos are detected in IceCube via the charged secondary particles that are produced in the interactions in the ice or the bedrock, with a very small interaction cross-section. The secondary particles emit Cherenkov radiation, which is then recorded by the PMTs and transformed into a digital signal. The cumulative charge, position and timing information is used to reconstruct the direction and energy of the incoming neutrino.

3.2.1 Neutrino interactions at high energies

Cross-section

At high energies of $E_\nu \sim 20 - 500\,\text{GeV}$, the Deep Inelastic Scattering (DIS) is the most common interaction for neutrinos [82]. In this process, the neutrino scatters off an individual quark in a nucleon N via the exchange of a virtual W or a Z boson. The final state is a lepton ($l^\pm$ or ν_l, with $l = e, \nu, \tau$) and a hadronic system X, both in Charged Current (CC) or Neutral Current (NC) interactions, see Equations 3.1 and 3.2. In a CC interaction a charged lepton is produced with the same flavor as the parent neutrino, while in the NC interaction there is only a transfer of momentum. At these energies, the cross-section grows linearly with the neutrino energy and is larger for neutrinos than for anti-neutrinos, see Figure 3.4.

[82]: Formaggio et al. (2012), 'From eV to EeV: Neutrino cross sections across energy scales'

Neutrino interactions

Charged Current (CC) interaction:

$$(\nu_\ell, \bar{\nu}_\ell)\, N \rightarrow (\ell^-, \ell^+)\, X \quad (3.1)$$

Neutral Current (NC) interaction:

$$(\nu_\ell, \bar{\nu}_\ell)\, N \rightarrow (\nu_\ell, \bar{\nu}_\ell)\, X \quad (3.2)$$

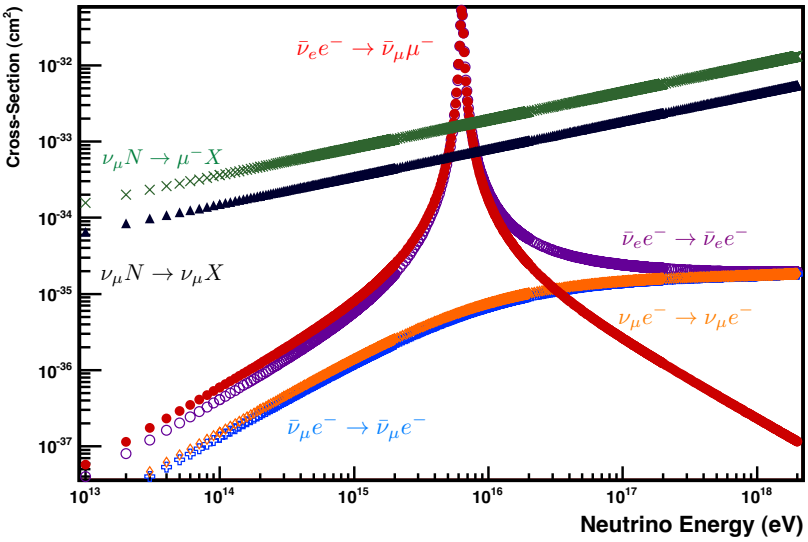

Figure 3.4: Neutrino cross-sections for Deep Inelastic Scattering interactions with a nucleus. CC and NC interactions of electron and muon neutrinos are shown, as well as the Glashow resonance at an energy of 6.3 PeV. From [82].

At higher energies of $E_\nu \sim 0.5\,\text{TeV} - 1\,\text{EeV}$, relevant for neutrino astronomy in IceCube, the cross-section does not depend linearly on the neutrino energy, and in fact it is suppressed by the propagator of the boson for energies $E_\nu > 10\,\text{TeV}$. The cross-sections for neutrino and anti-neutrino interactions become almost identical [83]. However, at an energy of $E^{\text{res}}_{\bar{\nu}_e} = m_W^2/(2m_e) \approx 6.3\,\text{PeV}$, the Glashow resonance takes place [84]. In this case, an electron antineutrino $\bar{\nu}_e$ interacts with an electron, forming an intermediate W boson via a resonant enhancement. This mechanism has a higher cross-section than the other interactions at these energies, as one can see in Figure 3.4. The Glashow resonance was recently measured by IceCube [85], and is the first confirmation of the detection of an astrophysical antineutrino.

[83]: Gandhi et al. (1998), 'Neutrino interactions at ultrahigh energies'

[84]: Glashow (1960), 'Resonant Scattering of Antineutrinos'

[85]: Aartsen et al. (2021), 'Detection of a particle shower at the Glashow resonance with IceCube'

Interaction length

While the neutrino interaction cross-sections $\sigma_{\nu N}$ grow with the neutrino energy E_ν, the (water-equivalent) interaction length decreases as

$$L_{\text{int}} = \frac{1}{\sigma_{\nu N}(E_\nu) N_{\text{A}}}, \tag{3.3}$$

where $N_{\text{A}} = 6.022 \cdot 10^{23}\text{cm}^{-3}$ is Avogadro's number. At energies greater than 40 TeV, the Earth's diameter is larger than the CC interaction length of neutrinos, becoming opaque to them. The effective area of IceCube is impacted by this, and at the highest energies a large fraction of the detected neutrinos originate from directions close to the horizon as seen from the South Pole.

3.2.2 Cherenkov radiation

When the neutrino interacts in the ice or the bedrock surrounding the instrumented volume of IceCube, the secondary charged particle travels faster than the phase velocity of light in ice and polarizes the medium. The

molecules that were excited re-emit the received energy as photons to go back to their ground state. The overlapping electromagnetic waveforms form a coherent superposition and create a light signal cone-shaped around the moving particle. This effect is called *Cherenkov radiation*. The angle θ_C of the Cherenkov light cone for a particle moving with velocity βc in a medium with refraction index n, shown in Figure 3.5, is

$$\cos\theta_C = \frac{1}{n\beta}. \tag{3.4}$$

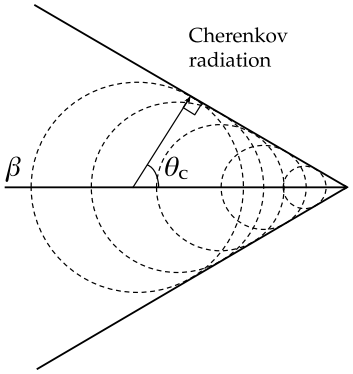

Figure 3.5: Scheme of the Cherenkov radiation induced by a charged particle with a relativistic speed $v = \beta c$.

The number of photons produced per unit path length x of a particle with charge ze and per unit wavelength λ is given by the Frank-Tamm formula [86],

$$\frac{d^2N}{dxd\lambda} = \frac{2\pi\alpha z^2}{\lambda^2}\left(1 - \frac{1}{\beta^2 n^2(\lambda)}\right), \tag{3.5}$$

where $\alpha \approx 1/137$ is the fine-structure constant. A relativistic particle ($\beta = 1$) in ice, where the refraction index is typically $n \approx 1.33$ [5], produces $N \approx 250\,\mathrm{cm}^{-1}$ optical photons in wavelengths between 300 nm and 500 nm, which is where IceCube's PMTs are most sensitive. This corresponds to an angle of $\theta_C \approx 41°$. For particles with $\beta < 1$ the Cherenkov angle and the number of photons decrease. The Cherenkov threshold is given by $\beta \leq 1/n$, which is equivalent to $\theta_C = 0°$. All the secondary particles from the interaction of the outgoing lepton with the medium also emit Cherenkov light and contribute to the overall brightness of the event [87].

[86]: Tamm (1991), 'Radiation Emitted by Uniformly Moving Electrons'

[5]: Workman et al. (2022), 'Review of Particle Physics'

[87]: Rädel et al. (2012), 'Calculation of the Cherenkov light yield from low energetic secondary particles accompanying high-energy muons in ice and water with Geant4 simulations'

3.2.3 Event morphologies

We call the different patterns that the light from the secondary particles form in the instrumented volume of IceCube *morphologies*. There are three morphologies depending on the type of interaction and neutrino flavor: tracks, cascades and double-bangs. An example of each can be seen in Figure 3.6 as *event views*.

Tracks are the signature of the charged-current interaction of a muon neutrino, where a muon is produced. The light is deposited along an elongated path, which results in a good angular resolution on the directional reconstruction of the neutrino due to the long lever arm. There can be *through-going* tracks, if the muon is produced outside of the detector and then reaches it, or *starting* tracks, if the CC ν_μ interaction vertex is contained within the instrumented volume. In the latter case, a small hadronic cascade is also present at the beginning of the track.

Cascades are roughly spherical light depositions and are produced after a CC interaction of electron and tau neutrinos, or a NC interaction of any neutrino flavor. For CC ν_e interactions, the outgoing electron immediately produces an electromagnetic cascade without an outgoing track. At energies lower than $\sim$ 1 PeV, ν_τ CC interactions also produce a point-like light deposition, since the outgoing tau only travels in the ice less than 50 m before decaying and the second cascade cannot be distinguished from the first one. In

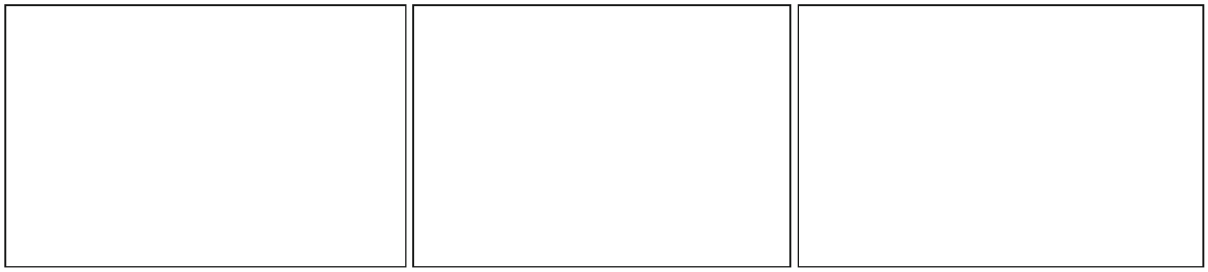

Figure 3.6: Examples of the three event morphologies observed by IceCube: a track event (left), a cascade event (middle) and a simulated double-bang event (right). Each sphere represents a DOM, the coloured ones are those that detected photons from the event. The radius of the sphere is proportional to the deposited charge and the colours show the temporal evolution from early photons (red) to late photons (blue). From [65].

NC interactions, the nucleus receives energy from the incoming neutrino and produces a hadronic shower of charged and neutral particles and an outgoing neutrino that carries a fraction of the energy. The uncertainty on the reconstructed energy is thus larger than for electromagnetic cascades [88].

Double-bangs are expected from the CC interaction of a tau neutrino. The tau that is produced is accompanied by a hadronic cascade and decays quickly due to the short lifetime. If it decays into $\mu + \nu_\mu$ ($\sim$ 17% of the cases), a track comes out, forming a so-called *lollipop* event. If the decay products are $e + \nu_e$ ($\sim$ 17% of the cases) or hadrons (remaining 65%), a second cascade is formed. The double-bang signature is only possible for high-energy tau neutrinos, since the traveled length depends on the energy as $50\,\mathrm{m} \cdot (E_{\nu_\tau}/\mathrm{PeV})$. The first candidates of tau neutrinos were identified recently by IceCube based on their double-bang signature [89, 90].

[88]: Aartsen et al. (2014), 'Energy Reconstruction Methods in the IceCube Neutrino Telescope'

[89]: Abbasi et al. (2022), 'Detection of astrophysical tau neutrino candidates in IceCube'

[90]: Abbasi et al. (2023), 'Summary of IceCube tau neutrino searches and flavor composition measurements of the diffuse astrophysical neutrino flux'

The tracks have better angular resolution on the order of < 1 deg due to their elongated, directional signature, compared to the angular resolution of cascades which is on the order of $\sim$ 10 deg. The interaction angle between the muon neutrino and the child muon is $0.7° \cdot (E_{\nu_\mu}/\mathrm{TeV})^{-0.7}$ [91], which is negligible compared to the angular resolution for tracks in the full neutrino energy (E_{ν_μ}) range.

[91]: Learned et al. (2000), 'High-Energy Neutrino Astrophysics'

On the other hand, the energy resolution is better for cascades, since most of the light emitted is contained in the instrumented volume, that can act as a calorimeter. The average energy resolution is 10% at TeV energies. For tracks, the energy resolution is a factor of $\sim 0.25 \log_{10} E_\mu$ of the energy of the secondary muon E_μ [88], since at energies above $\sim$ 300 GeV the typical length of the track is larger than the scale of the detector and an unknown fraction of the energy is deposited outside. The analyses presented in this thesis are focused on track-like events.

[88]: Aartsen et al. (2014), 'Energy Reconstruction Methods in the IceCube Neutrino Telescope'

3.2.4 Energy losses

The charged secondary particles from the interacion of the neutrino suffer other energy losses apart from Cherenkov radiation, which in fact only corresponds to a very small fraction of the total energy loss for muons [92]. At energies of the order of hundreds of GeV, muons lose energy mostly via ionization: the charged particle transfers some energy to an atom in the medium, which loses an electron in consequence.

[92]: Abbasi et al. (2013), 'An improved method for measuring muon energy using the truncated mean of dE/dx'

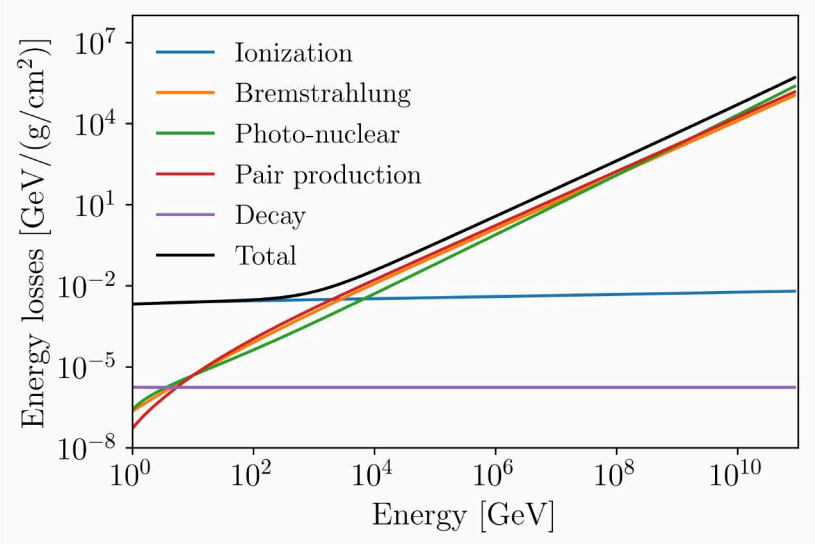

Figure 3.7: Energy losses of muons in ice. Adapted from [93].

Ionization is independent of the muon's energy and constant per unit length, so it is considered a *continuous energy loss*.

[92]: Abbasi et al. (2013), 'An improved method for measuring muon energy using the truncated mean of dE/dx'

At higher energies, at 10 TeV and above, ionization only accounts for 9% of the total muon energy loss [92], and the rest is due to *stochastic energy losses*. The main processes are bremsstrahlung, pair production and photonuclear interactions.

Bremstrahlung is electromagnetic radiation that occurs when a charged particle is deflected by the Coulomb field of another charged particle; in this case, a muon with a nucleus in the ice. The muon is decelerated, and the kinetic energy is converted into photons. In *pair production*, the muon interacts with an atom and creates an electron-positron pair. Lastly, the *photonuclear interaction* is the inelastic scatttering of the muon with a nucleon or nucleus through a virtual photon exchange. The total energy loss for a muon is then expressed by

$$-\left\langle \frac{\mathrm{d}E_\mu}{\mathrm{d}x} \right\rangle = A + BE_\mu, \tag{3.6}$$

[5]: Workman et al. (2022), 'Review of Particle Physics'

where $A \approx 0.0024$ GeV $(\mathrm{g/cm^2})^{-1}$ accounts for the energy loss due to ionization and $B \approx 0.000032$ $(\mathrm{g/cm^2})^{-1}$ is the sum of the contributions from the stochastic energy losses [5]. Figure 3.7 shows the energy lost due to the individual processes as a function of the muon energy. A 300 GeV muon will travel $\sim$ 1 km in ice before losing all its energy, while the path length for 1 TeV is $\sim$ 2 km. At an energy of 1 PeV, a muon can travel 20 km before stopping.

3.2.5 Atmospheric background or astrophysical signal?

The track events that are detected in IceCube can have three different origins: they could be muons produced in interactions of cosmic rays in the Earth's atmosphere (*atmospheric muons*), neutrinos produced in the same atmospheric interactions (*atmospheric neutrinos*) or neutrinos from astrophysical sources (*astrophysical neutrinos*). The objective of neutrino astronomy is to detect these astrophysical neutrinos and identify their

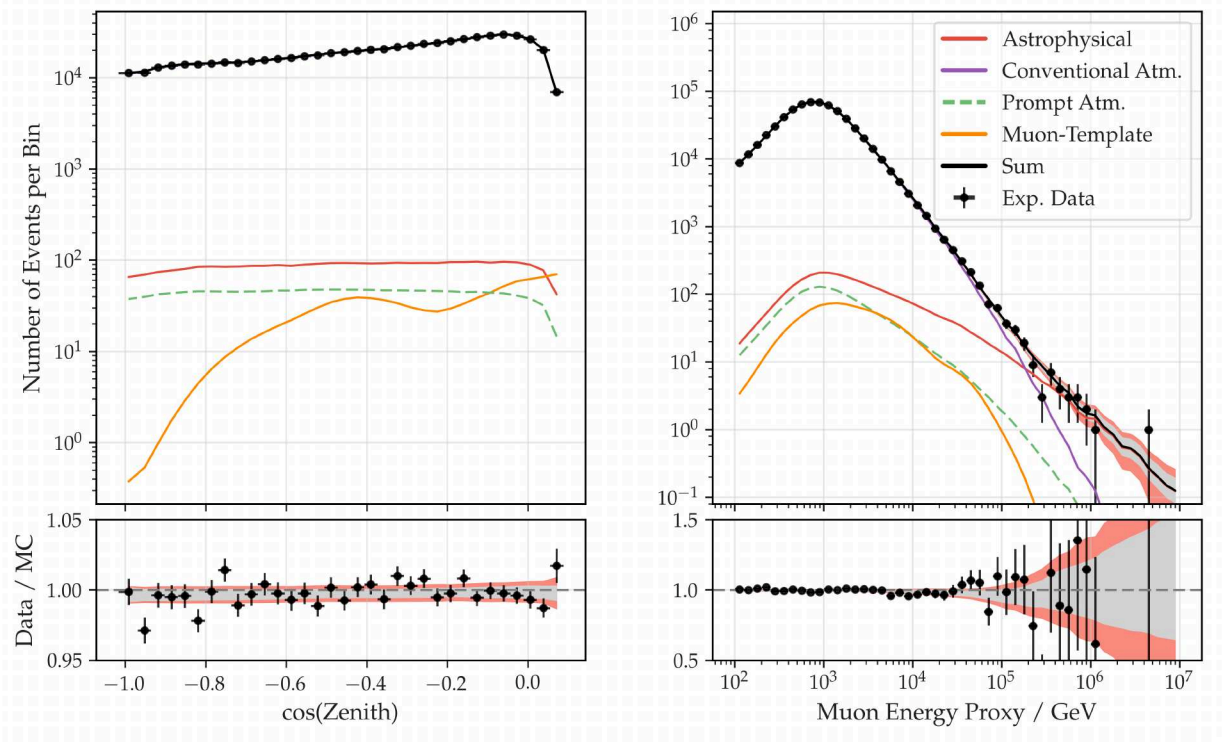

Figure 3.8: Muon neutrino events detected in 9.5 years of data on reconstructed zenith angle and muon energy. Experimental data is shown as black dots, and the colored lines are the best-fit expectations from simulation. From [94].

sources. In order to achieve that, a good discrimination of the atmospheric background is needed.

The majority of events detected by IceCube are atmospheric muons, which are energetic enough to traverse the kilometer of ice and reach the detector. These can be relatively easily rejected in the Northern Hemisphere, since they only produce downgoing tracks as the Earth acts as a shield and suppresses the muons travelling in an upward direction (in IceCube's coordinates). Sometimes, however, multiple atmospheric muons can produce simultaneous tracks that are misreconstructed as a single upgoing event, or a downgoing event with higher energy than expected for an atmospheric muon, making it pass the selection criteria. Therefore, even with strict cuts on the energy and direction of the event, a contamination from atmospheric muons is expected.

The atmospheric neutrino background, on the other hand, is irreducible and can only be discriminated with a large data sample. The flux of atmospheric neutrinos is expected to follow an $E^{-3.7}$ energy spectrum, while the astrophysical neutrino flux reflects the spectrum of the parent particles at the source, typically a powerlaw distribution with E^{-2} (see Figure 3.8). At very high energies the expected number of atmospheric events is dramatically reduced, and the astrophysical flux starts dominating.

Other sophisticated methods to reject background are the so-called *self-veto*, using IceTop data to veto events with an accompanying air shower or selecting starting events exclusively. With the self-veto, multiple events that are detected simulaneously are rejected, because at high energies the air shower from the cosmic-ray interaction produces several muons

that accompany the atmospheric neutrino. A starting-track selection has historically been the preferred way of achieving a high purity sample. The outermost layer of strings in IceCube is used as a veto, so the atmospheric muon background is almost negligible, but the effective volume is reduced as a downside.

3.3 Data taking and processing

The IceCube Data Acquisition System (DAQ) is an automated set of data collection and filtering systems. It collects the data from the DOMs, calibrates and processes it on a computing cluster at the South Pole, and applies pre-defined event selections. It is decentralized, meaning that the optical signals captured by each DOM are digitized in that same DOM individually, and runs continuously. Lastly, it also generates alert messages (relevant for this thesis) and transmits the information from the South Pole to the IceCube data center, located at the University of Wisconsin, Madison.

3.3.1 Data taking

IceCube ultimately detects photons produced in the interaction of a neutrino in the surrounding ice and the propagation of the secondary charged particles. These photons hit the photocathode material of the PMT, ejecting electrons (called photoelectrons, or PE) from the surface due to the *photoelectric effect*. These photoelectrons are accelerated and sent to the electron multiplier, which consists of 10 dynodes that produce secondary electrons when they are impacted. The signal is therefore amplified, with a typical PMT gain of 10^7. Each single photon is detected as a charge distribution over time. If the signal passes the discriminator threshold of ~ 0.25 PEs, it is digitized as voltage over time and called *waveform* [95].

[95]: Abbasi et al. (2009), 'The IceCube data acquisition system: Signal capture, digitization, and timestamping'

To convert the analog signal from the PMT to the digital output, the data is split into two paths at the input to the DOM main board. One is for the trigger and the timestamp capture, while the other is the main signal path which goes through a 75 ns high-quality delay line. There, the signal is split to three separate (×16, ×2, and ×0.25) band-width amplifiers to cover the full PMT dynamic range while preserving the waveform shape. The signal is limited to a 0 V to 3 V range. The data is then presented to one of the two *Analog Transient Waveform Digitizers* (ATWDs).

The channel with the ×16 amplification is converted first. If this channel is saturated, the ×2 gain channel is digitized to recover more information. In the same way, if this channel saturates, the ×0.25 channel is digitized. The ATWD takes a total of 29 μs to digitize a waveform, and records data during 427 ns. A longer digitization of 6.4 μs occurs simulaneously through a fourth PMT signal path called *fast Analogue Digital Converter* (fADC), which is long enough to record all the light from even the most energetic events.

If the waveform passes the discriminator threshold of ~ 0.25 PEs in the trigger path, the digitization happens and the waveforms are recorded in the basic, fundamental datum in IceCube, called *hit*. The hit contains a

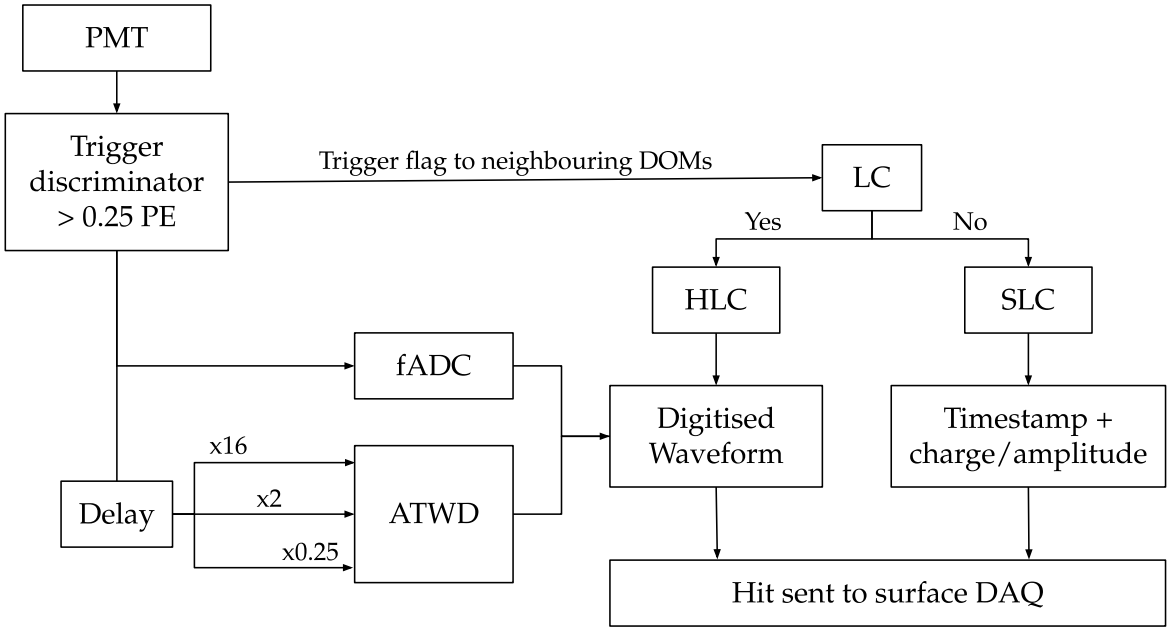

Figure 3.9: Diagram of the data acquisition procedure in IceCube. Adapted from [95].

timestamp and the waveform information. Once a hit is recorded and during a time window of not more than 1 μs, the DOM can receive a tag signal, meaning the neighbouring DOM also detected a hit, and the local coincidence (LC) requirement is satisfied. In the same way, if a DOM that has not detected a hit receives a tag signal, it will expect a hit in a similar time window. The information of the hit includes the tag signals from neighbouring DOMs, reducing the PMT noise and rate.

The *Hard Local Coincidence* (HLC) mode records the full waveform data for hits with a LC tag, while all isolated non-LC hits are flagged as *Soft Local Coincidence* (SLC) and only contain the timestamp and amplitude and charge information. This reduces the amount of dark noise, which is more likely to produce untagged hits.

3.3.2 Data processing

The IceCube DAQ system receives the hit signal and applies different filters and algorithms on a computing cluster located at the detector site. The first condition for neutrino alert searches is that at least 8 DOMs must receive hit signals within 5 μs. All the hits in a $+6/-4$ μs window around the trigger time are unified into a single event by the DAQ.

The DAQ system then converts the calibrated waveforms into photon arrival and amplitude information, with an accuracy of 1.2 ns in time [88]. The direction, position and energy of the events are reconstructed, and a selection called *OnlineL2* uses those values to select 1% of the events as potential neutrinos to be further analyzed at the South Pole.

[88]: Aartsen et al. (2014), 'Energy Reconstruction Methods in the IceCube Neutrino Telescope'

The next relevant step for this thesis in the filtering process is the dedicated online *alert system* (see Chapter 4), which applies strict criteria [96] to select events from the OnlineL2 selection based on the quality of the reconstruction, the energy and the morphology. These are then

[96]: Blaufuss et al. (2019), 'The Next Generation of IceCube Real-time Neutrino Alerts'

reconstructed with a more sophisticated reconstruction method than the one used in the OnlineL2 selection, still at the South Pole. After that, the *IceCube Live*[1] control system sends the data to the primary data center, located in the Northern Hemisphere at the University of Wisconsin, Madison.

This is done in two different steps. First, a JSON[2] message is sent with the basic information (time, direction and energy of the event) needed for the instruments which perform follow-up observations, with a median latency of ~ 33 seconds. Second, a larger message is transmitted containing the light arrival information from the DOMs for further reconstruction and quality verification checks. This processing scheme for the neutrino events utilized in this thesis reduces the data rate from ~ 1 Tb/day to ~ 1 event every two weeks.

3.4 Calibration and the Antarctic ice

Before the deployment of the DOMs and the associated electronics, they were tested and calibrated in the laboratory. The most important systematic uncertainty in the reconstruction of events comes from our relatively limited knowledge of the glacial ice where IceCube is located, which can only be studied in-situ. The propagation of the light in a medium is impacted by two processes: *scattering* and *absorption*. The scattering length is the average distance that a photon would travel before scattering, i.e. before changing its direction. The absorption length is the path length after which the probability of the photon to have survived is $1/e$. This determines from how far the DOMs will see light of an event.

Figure 3.10 shows the absorption and scattering coefficients for different ice models as a function of depth in the detector. The corresponding scattering and absorption lengths are simply the inverse of the coefficients. One can see that the lower part of the detector has clearer ice and larger scattering and absorption lengths, so an event crossing the detector there would yield more light than that same event in the upper half. This improvement in the optical properties is due to the high pressure that compresses the air bubbles present in the ice. Just above the clear ice, between 2000 m and 2100 m, dust that was deposited during volcanic eruptions is trapped there, worsening the absorption and scattering. These layer is called the *dust layer* and divides the detector horizontally.

These and other properties are considered in the South Pole Ice (SPICE) models that are used for calibration in the simulation and reconstruction of data. There are three models of relevance for this thesis. The first one is *SPICE MIE* [97], which uses the Mie scattering theory [98] to model the scattering. *SPICE 3.2.1* includes a one dimensional description of the *ice tilt* in the ice sheet layers, which is caused by the non-uniform surface of the bedrock, affecting the layers of ice that are deposited on top. This description is a depth-dependent function of the distance along the tilt gradient, and the scattering and absorption coefficients are dependent on the three-dimensional position in the ice instead of on the depth exclusively. Lastly, *SPICE BFR-v2* [99] accounts for an observed azimuthal *anisotropy* in charge aligned with the flow of the ice, which could be caused by birefringent ice crystals. The correction of the

1: https://live.icecube.wisc.edu

2: https://www.json.org/

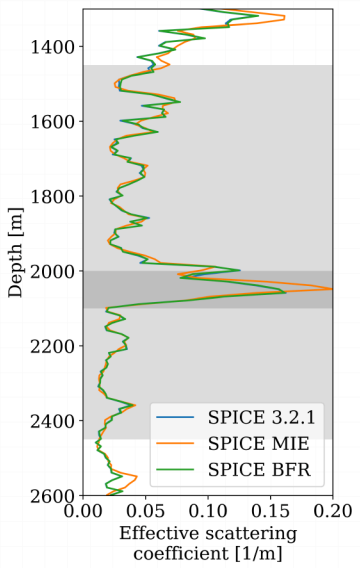

(a)

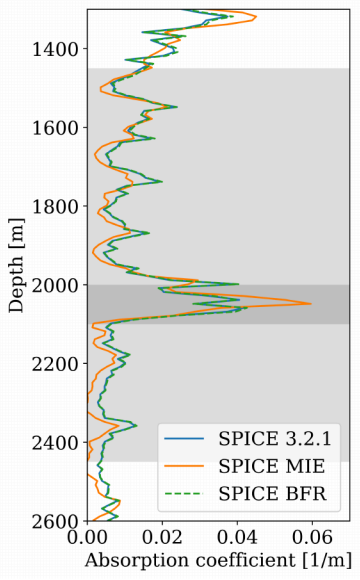

(b)

Figure 3.10: Values of the effective scattering (panel a) and absorption (panel b) coefficients at 400 nm in IceCube, comparing the three ice models relevant to this thesis. Light grey area represents the main in-ice array, while the dark grey area is the dust layer.

[97]: Aartsen et al. (2013), 'Measurement of South Pole ice transparency with the IceCube LED calibration system'

[98]: Hahn (2004), 'Light Scattering Theory'

[99]: Chirkin et al. (2019), 'Light diffusion in birefringent polycrystals and the IceCube ice anisotropy'

scattering coefficient was calculated to −8% in the direction of the glacial flow, meaning that the photons effectively fly a curve towards the flow axis.

The ice models are based on data taken by *dust loggers* [100], which are vertical measuring devices with a 404 nm laser that emits light horizontally at one end and have a PMT at the other end, which detects the photons that have been scattered back to the device. The measurements were taken during the deployment of the in-ice array. They yield high resolution stratigraphy in bins of 10 m, but the absolute absorption and scattering length values cannot be derived. The dust logger data has to be normalized with the flasher LED calibration system from the DOMs.

[100]: Aartsen et al. (2013), 'South Pole glacial climate reconstruction from multi-borehole laser particulate stratigraphy'

The IceCube Realtime Program and reconstruction improvements

The IceCube Realtime Program 4

4.1 Introduction to the IceCube Realtime Program

4.1 Introduction to the IceCube Realtime Program 35
4.2 Reconstruction methods . . 38
4.3 Improvements to the angular reconstruction 44
4.4 Relevant alerts 45
4.5 The IceCube Event Catalog of Alert Tracks (IceCat-1) . . 50

The origin of the astrophysical neutrinos that IceCube detects is still largely unknown, although there have been multiple associations with electromagnetic counterparts throughout the years. The first potential extragalactic neutrino source was the blazar TXS 0506+056, which was flaring in gamma rays when IceCube detected a high-energy neutrino event coming from the same direction [62].

[62]: Aartsen et al. (2018), 'Multimessenger observations of a flaring blazar coincident with high-energy neutrino IceCube-170922A'

This detection was possible thanks to the IceCube Realtime Program. The goal of the program is to help uncover the sources of neutrinos by sending out messages to other observatories on the most promising high-energy neutrino events, called *neutrino alerts events*, which have a high probability of being astrophysical in origin. As part of the Realtime Program, IceCube also follows up on external alerts [101] (mostly transient object detected by electromagnetic observations), looking for spatially and temporally coincident neutrino events.

[101]: Abbasi et al. (2021), 'Follow-up of Astrophysical Transients in Real Time with the IceCube Neutrino Observatory'

Since July 2020, IceCube has started issuing alerts for cascade-like events as well[1]. However, this Chapter and the work done in this thesis focuses exclusively on track-like alerts.

1: `https://gcn.gsfc.nasa.gov/amon_icecube_cascade_events.html`

4.1.1 Event selections

The IceCube Realtime Program started in 2016 [102] and it was updated in 2019 [96]. Originally it contained two classes of alerts: *High-Energy Starting Events* (HESE) [103] and *Extremely High-Energy* (EHE) events [104]. A third alert selection was included after the revision of the program: the *Gamma-ray Follow-Up* (GFU) alerts.

[102]: Aartsen et al. (2017), 'The IceCube Realtime Alert System'

[96]: Blaufuss et al. (2019), 'The Next Generation of IceCube Real-time Neutrino Alerts'

[103]: Abbasi et al. (2021), 'IceCube high-energy starting event sample: Description and flux characterization with 7.5 years of data'

[104]: Aartsen et al. (2016), 'Constraints on Ultrahigh-Energy Cosmic-Ray Sources from a Search for Neutrinos above 10 PeV with IceCube'

HESE alerts are track-like events whose interaction vertex is inside the fiducial volume of IceCube. The background of atmospheric neutrinos is reduced by this criterion, since these events would mostly appear as through-going tracks. Another condition of minimum deposited light of 6000 photoelectrons per event is required to further remove any possible background. Historically, HESE has been used as a very high purity sample to discover an all-sky astrophysical neutrino flux, using a slightly different selection criteria [103].

[103]: Abbasi et al. (2021), 'IceCube high-energy starting event sample: Description and flux characterization with 7.5 years of data'

EHE stream selects track-like events with energies between 500 TeV and 10 PeV. If the cosine of the event reconstructed zenith angle is small or equal to 0.1 (see Figure 4.2), a minimum deposited charge of $10^{3.6}$ photoelectrons detected in DOMs is required. For a larger cosine of the zenith angle, the minimum required number of photoelectrons increases with the angle. With these cuts, the average purity of the stream is 50%, meaning that half of the events are expected to be astrophysical.

GFU are through-going tracks with energies of $\mathcal{O}(100)$ TeV. Events from the Northern or Southern Hemisphere are selected using separate boosted decision trees. The majority of IceCube alerts are selected by this stream.

In 2019, two refined categories were introduced: *Gold* and *Bronze* alerts*. These were defined so that the average astrophysical purity of the samples is 50% and 30%, respectively. The purity is represented by a quantity called *signalness*, which is the probability of a neutrino to be of astrophysical origin, and is calculated after the event is selected as an alert based on its properties. The signalness is defined as

$$\text{Signalness}(E,\delta) = \frac{N_{\text{signal}}(E \geq E_{\text{reco}},\delta)}{N_{\text{signal}}(E \geq E_{\text{reco}},\delta) + N_{\text{background}}(E \geq E_{\text{reco}},\delta)}, \tag{4.1}$$

where E_{reco} is the reconstructed energy of the neutrino, δ is its declination, and N_{signal} and $N_{\text{background}}$ are the expected number of signal and background events at a given declination and above the energy E_{reco}. In the Gold alert stream, the average signalness of the alerts is 50%, and for Bronze it is 30%. The expected numbers and, thus, the average signalness in each channel, were calculated with simulations assuming an astrophysical neutrino spectrum of $E^{-2.19}$ [105]. The latest diffuse astrophysical muon neutrino flux measured by IceCube [94] has a spectral index of 2.37 ± 0.09. The impact of a different spectral index on the signalness depends on the energy of the neutrino, and for the most energetic ones, the current signalness would be overestimated. However, there are currently no plans of updating the simulations to reflect this new spectral index.

[105]: Haack et al. (2017), 'A measurement of the diffuse astrophysical muon neutrino flux using eight years of IceCube data.'

[94]: Abbasi et al. (2022), 'Improved Characterization of the Astrophysical Muon–neutrino Flux with 9.5 Years of IceCube Data'

The previous alert streams were redirectioned into these two new ones with a hierarchical scheme. A neutrino can pass various alert criteria, but only one alert will be sent out. The Gold stream contains GFU Gold, EHE Gold, and HESE Gold in that order; while the Bronze stream is GFU Bronze and then HESE Bronze. Similarly, an event classified as Gold and Bronze will be labelled as Gold. Expected number of Gold and Bronze alerts and of the different subsets can be seen in Table 4.3 in Section 4.5.

4.1.2 Pipeline

To start the realtime pipeline, a neutrino event must pass the alert criteria in the online filtering system that happens at the South Pole. Then a machine-readable GCN[2] Notice[3] is issued automatically including the angular direction reconstructed with an algorithm called SplineMPE (explained in Section 4.2.2). All the members in the Realtime Oversight Committee (ROC) as well as the realtime shifter receive an email and a SMS with this basic information.

2: General Coordinates Network, https://gcn.nasa.gov

3: https://gcn.gsfc.nasa.gov/amon_icecube_gold_bronze_events.html

The event data is sent to the IceCube computing center in the Northern Hemisphere, where a more sophisticated and computing-expensive method called Millipede automatically starts to reconstruct the direction

* A *Silver* alert stream was planned to select cascade events of likely astrophysical origin, but ultimately they were named *Cascade* alerts, more information can be found here: https://gcn.gsfc.nasa.gov/doc/High_Energy_Neutrino_Cascade_Alerts.pdf.

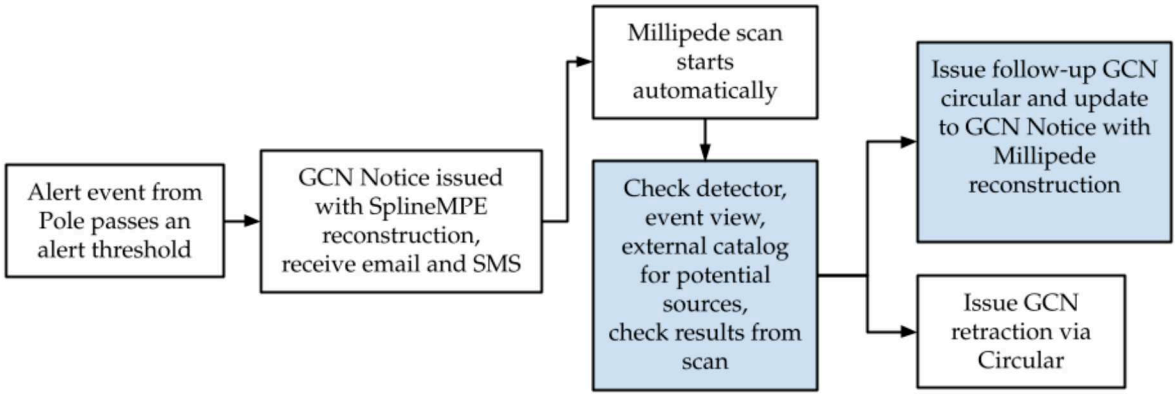

Figure 4.1: Realtime program pipeline, with all the main steps from the detection of the neutrino to the publication of the GCN Circular with the final information on the alert. Blue squares represent active participation and responsibilities of the realtime shifter. The rest are done automatically, do not require human intervention or must be done by one of the Realtime Oversight Committee members.

in a likelihood grid scan. The job of the shifter is to visually inspect the event view of the neutrino, check the operating state of the detector, ensure that the scan is running correctly, and update the ROC with the status of the reconstruction. At the same time, the shifter or one of the ROC members writes up a GCN Circular[4] that will be sent out with the final localization. From the almost-elliptical 90% C.L. uncertainty contour obtained with the reconstruction method, only the right ascension and declination values that define the minimal rectangle that encapsulates it are published. An example of a GCN Notice, a Circular and the corresponding scan of that alert are shown in Appendix A.

4: https://gcn.nasa.gov/circulars

A prompt reaction to issues that might arise is also needed. The solutions vary from simply restarting the scan to manually adjusting the parameters that are used for the minimization. In some occasions, a background event might be misclassified as a neutrino alert, and a GCN Circular is issued informing the community of the retraction after a proper inspection confirms that the event is likely not astrophysical.

Publication of the GCN Circulars always requires the review approval from at least two ROC members. In Figure 4.1 a diagram of the steps taken can be seen. One day after the alert has been detected, the Fast Response Analysis [106] is run to search for lower-energy neutrino events from the alert direction in two time windows of ±500 seconds and ±1 day around the alert event time. However, the author of this thesis was not involved in this analysis and therefore will not be covered in detail here.

[106]: Abbasi et al. (2023), 'Constraints on Populations of Neutrino Sources from Searches in the Directions of IceCube Neutrino Alerts'

4.1.3 The bot

A *realtime bot* is implemented, which is ultimately a listener to IceCube Live (the experiment control system for the IceCube Detector explained in Section 3.3), that receives events from the South Pole, checks if they pass the alert criteria, and if they do, starts the reconstruction scan. Part of the duties of the author as the main realtime shifter included maintaining and further automating the bot.

One of the main changes that was implemented was an update from Python 2 to Python 3, since Python 2 was no longer supported. A

dedicated user account on IceCube's computing cluster, along with an environment including all necessary dependences was set up to maintain and develop the realtime bot. Now work is being continued by other IceCube members to structure the bot so that it has a "server" and a "client" component. The server takes care of reading the event to scan and "splitting" the work into a sequence of pixels to reconstruct, the client loads the data package ("message") sent by the server. It also applies the required reconstruction algorithm, sending back the result to the server. Moreover, the bot is being made independent of the chosen reconstruction method, as a consequence of the studies that are presented in this thesis.

4.2 Reconstruction methods

As introduced in Chapter 3, the signal that a neutrino leaves in the detector is the optical light from the Cherenkov emission of charged secondary particles. The number of photons and their arrival time at the DOMs allows us to infer the direction and energy of the incoming neutrino. In general, the trajectory can be described by a position (x, y, z) at a time t, and the direction that the neutrino is moving towards, usually given in zenith θ and azimuth ϕ coordinates. The energy E can only be estimated as a lower bound on the initial energy of the neutrino in case of track events, since it depends on the light yield which is typically not fully contained in the detector.

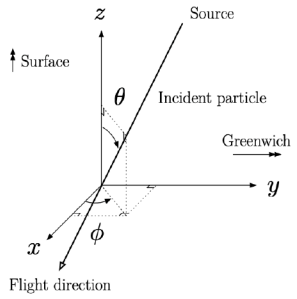

Figure 4.2: IceCube's coordinate system, from https://docs.icecube.aq/icetray/main/projects/dataclasses/coordinates.html

4.2.1 Energy reconstruction

Energy reconstruction algorithms rely on the assumption that the light yield is proportional to the energy deposited in the detector, and that the initial energy of the event can be estimated from that. For high energy tracks, such as the realtime events, the calculation is complicated since the muon is long-lived enough to exit the detector if it was created inside the instrumented volume (starting track) and to reach the detector from outside if the interaction point was located outside (through-going track). In both cases, the track is not fully contained: part of the deposited energy is not recorded by the PMTs, so the reconstructed energy is just a lower bound on the true energy.

A good approximation comes from the energy loss of the muon as it travels through the detector, dE_μ/dx, which above 1 TeV depends linearly on the total muon energy and is proportional to the number of photons detected. This number is assumed to follow a Poisson distribution with mean $\lambda = \Lambda E$, where Λ is the expected number of photons arriving at a PMT based on a template track. The likelihood of detecting k photons given an energy E is

$$\mathcal{L} = \frac{\lambda^k}{k!} \cdot e^{-\lambda} = \frac{(\Lambda E)^k}{k!} e^{-\Lambda E}. \tag{4.2}$$

To generalize this equation so that it includes the expected number of noise photons ρ (e.g., from PMT noise), one simply replaces $\lambda \rightarrow \Lambda E + \rho$ in the previous equation, which after taking the logarithm becomes

$$\ln \mathscr{L} = k \ln(\Lambda E + \rho) - (\Lambda E + \rho) - \ln(k!). \tag{4.3}$$

There are two energy reconstruction methods relevant to realtime events, both of which take into account the stochastic energy losses that dominate for muons above 1 TeV: *Truncated Energy* and *Millipede*.

Truncated Energy

This method aims to estimate the muon energy from the differential energy loss rate $\mathrm{d}E/\mathrm{d}x$ in the detector. The track is divided into segments j of 120 m length and $\mathrm{d}E_j/\mathrm{d}x$ is calculated in each segment to account for stochastic energy losses. The highest 40% of the values are discarded before calculating the truncated mean $\mathrm{d}E/\mathrm{d}x$ to minimize the effect of large stochastic energy losses [92]. The differential energy loss rate per segment is calculated as the ratio between the observed number of photoelectrons to the expected number for a fixed energy loss.

[92]: Abbasi et al. (2013), 'An improved method for measuring muon energy using the truncated mean of dE/dx'

Millipede

The variation of the energy losses happens at scales shorter than the 120 m assumed for Truncated Energy. To correct for that, the *Millipede* reconstruction algorithm assumes that the light emission from a high-energy muon can be described by a series of cascades whose energies (E_i) can be estimated [88]. The light that reaches the PMTs is a combination of photons emitted from everywhere along the track. To introduce the possibility of multiple sources of energy losses with variable energies we substitute the mean λ by

[88]: Aartsen et al. (2014), 'Energy Reconstruction Methods in the IceCube Neutrino Telescope'

$$\lambda = \sum_{\text{sources } i} E_i \Lambda_i + \rho, \tag{4.4}$$

where Λ_i is the expected light yield in a particular DOM and time bin from cascade i, and ρ is the expected number of noise photons. Substituting in Equation 4.3, the resulting likelihood that has to be minimized to find the best-fit $\overrightarrow{E}$ is

$$\ln \mathscr{L} = k \ln(E_i \Lambda^i + \rho) - E_i \Lambda^i - \rho - \ln(k!), \tag{4.5}$$

where $E_i \Lambda^i = \overrightarrow{E} \cdot \overrightarrow{\Lambda}$. Summing then over the time bins j, we get

$$\begin{aligned} -\sum_j \ln \mathscr{L} = -\sum_j k_j \ln\left(\overrightarrow{E} \cdot \overrightarrow{\Lambda}_j + \rho_j\right) + \sum_j \left(\overrightarrow{E} \cdot \overrightarrow{\Lambda}_j - \rho_j\right) \\ + \sum_j \left(\ln k_j!\right). \end{aligned} \tag{4.6}$$

The reconstructed energy $\overrightarrow{E}$ is then the one that minimizes $-\sum_j \ln \mathcal{L}$ (or maximizes the logarithm of the likelihood).

4.2.2 Angular reconstruction: SplineMPE

[107]: Abbasi et al. (2021), 'A muon-track reconstruction exploiting stochastic losses for large-scale Cherenkov detectors'

SplineMPE [107] is a likelihood based reconstruction that uses the arrival time of the photons to infer the direction of the incoming neutrino. The likelihood is defined as

$$\mathcal{L}_{1\text{st}} = \prod_{j=1}^{N_{\text{DOM}}} p_{j,1\text{st}}(t_1), \tag{4.7}$$

where N_{DOM} is the total number of DOMs that receive light from the event, and $p_j(t)$ is the photon arrival Probability Density Function (PDF) at the DOM j. SplineMPE uses only the PDF of the first photon to compensate for the assumption of a minimum ionizing muon in homogeneous ice that goes into the description of the likelihood. In reality, the ice properties are not uniform throughout the detector, and high-energy muons suffer from stochastic energy losses. The first photons to arrive at DOMs are less likely to be affected by these unphysical assumptions. The photon arrival PDF of the first photon $p_{j,1\text{st}}(t)$ can be calculated exactly, and the likelihood becomes

$$\mathcal{L}_{1\text{st}} \propto \prod_{j=1}^{N_{\text{DOM}}} [p_j(t_1)]^{q_1} \times (1 - P_j(t_1))^{Q_j - q_1}, \tag{4.8}$$

where $P(t)$ is the cumulative distribution function of $p(t)$, evaluated at the time of the first hit t_1. The data is weighted by the observed charge of the first hit, q_1, and the total observed charge per DOM, $Q = \sum_i q_i$. A track hypothesis is assumed, with x, y, z, and t as the track position parameters and zenith θ and azimuth ϕ as the track direction. The optimization is done on these 6 parameters, and the track hypothesis that leads to the minimum likelihood value is the best-fit reconstruction.

[97]: Aartsen et al. (2013), 'Measurement of South Pole ice transparency with the IceCube LED calibration system'

To incorporate a more realistic description of the ice, the data from LED flashers in the DOMs is used to model the optical properties [97]. Then, high dimensional histograms are created by simulating muons in various parts of the instrumented volume of IceCube and recording the photons that reach the DOMs. The photon arrival time PDF is obtained from fitting these histograms with B-Splines, so that it depends on the orientation and position of the track.

A **B-Spline** is a function defined piecewise by polynomials that has minimal support with respect to a given degree, smoothness, and domain partition.

Lastly, other modifications are implemented to correct the assumption of a minimum ionizing particle. A hit-cleaning algorithm based on a Kolmogorov-Smirnov test [108, 109] and an energy-dependent blend between the likelihood described above and another likelihood that considers each single photoelectron individually constitute the "fast" configuration. The "max" configuration also includes accurate noise modeling, and convolving the likelihood with an energy-dependent Gaussian function.

[108]: Kolmogorov (1933), 'Sulla determinazione empirica di una legge di distribuzione.'
[109]: Smirnov (1948), 'Table for Estimating the Goodness of Fit of Empirical Distributions'

"Max" configuration is slower and has better resolution and is typically preferred for searches of neutrino sources in IceCube analyses, while

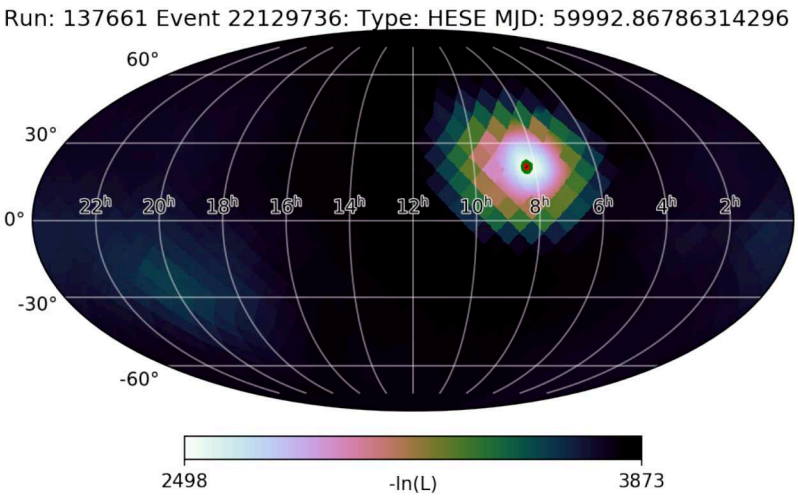

Figure 4.3: Example of a skymap scan with Millipede. The colored circles represent the 5σ (green), 3σ (red) and 90% (black) uncertainty contours assuming Wilks' theorem. The event is the Bronze alert IC230217A.

the "fast" configuration is run for the online angular reconstruction of realtime events and the outcome is distributed in the initial GCN Notice.

4.2.3 Angular reconstruction: Millipede

The energy reconstruction algorithm Millipede can also be used to reconstruct the direction of high-energy muons. First, the best-fit energy losses and the likelihood are calculated for a fixed direction. Second, the direction and the reference location are varied and the energy losses and likelihood are re-calculated. These two steps can be repeated until the global maximum likelihood is found.

In practice, this is done on a pixel grid using *Hierarchical Equal Area isoLatitude Pixelation of a sphere* (*HEALPix*) [110]. In a typical scan, the full sky is divided into pixels of equal area, with iteratively finer binning near the maximum. The first binning is done with $n_{\text{side}} = 8$, which divides the sky into 768 pixels of 53.83 deg^2. Then the pixel with the current best fit is further divided into pixels with $n_{\text{side}} = 64$, corresponding to 0.84 deg^2 per pixel. The final step is done with $n_{\text{side}} = 512$, or 0.013 deg^2 pixels. An example of such a skymap scan can be seen in Figure 4.3.

[110]: Gorski et al. (2005), 'HEALPix: A Framework for High-Resolution Discretization and Fast Analysis of Data Distributed on the Sphere'

4.2.4 Error contour calibration and the IC160427A case

Millipede creates a likelihood landscape which can be used to derive error contours that correspond to a given containment. This is performed by finding the locations in the sky for which the difference in likelihood to the best-fit position is a certain value. These values can be calculated using Wilks' theorem [111] or Monte Carlo resimulations, if systematic uncertainties have a critical impact on the localization.

[111]: Wilks (1938), 'The Large-Sample Distribution of the Likelihood Ratio for Testing Composite Hypotheses'

Wilks' theorem

Wilks' theorem states that, with a sufficiently large sample, the log-likelihood ratio statistic follows an asymptotic distribution which can be used to produce confidence intervals. This distribution is typically a χ^2 distribution [111].

Resimulations were done for the first time for the high-energy track IC160427A, for which a possible counterpart supernova was found by Pan-STARRS1 [112]. They consist of simulating muons that are "similar" to one specific event, varying the parameters of the ice model used to propagate the particles. For this study, similarity was defined as difference

[112]: Kankare et al. (2019), 'Search for transient optical counterparts to high-energy IceCube neutrinos with Pan-STARRS1'

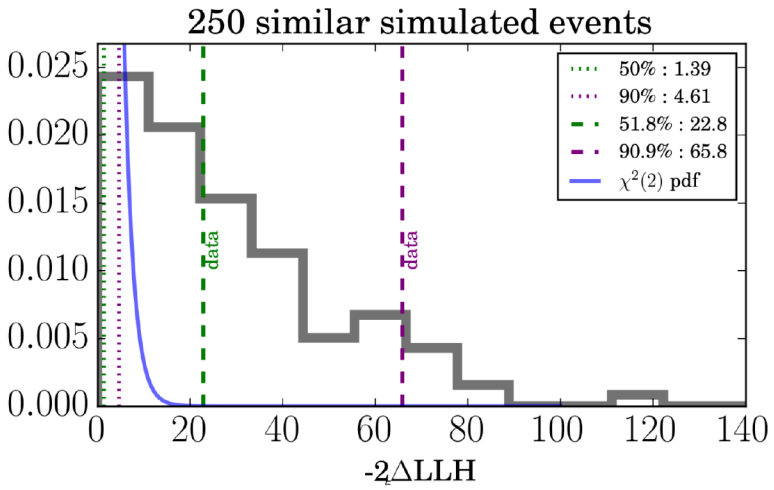

Figure 4.4: Distribution of the difference in log-likelihood between the best-fit position reconstructed with Millipede and the simulated direction for each of the resimulated events similar to the neutrino alert IC160427A. The green and magenta dashed lines represent the 50% and 90% containment for the data, while the dotted lines represent the same values if the Wilks' theorem could be applied and the data followed a χ^2 distribution.

in the true direction of ±2 degrees, distance from the simulated track to the original reconstructed track below 30 m, and ±20% of the charge deposited in the detector by the photons. This choice ensured that every simulated event closely resembled the original neutrino.

The systematic uncertainties were included by modifying the ice model used in the photon propagation in each resimulation. To create each modified ice model, parameters are sampled from a predefined ice model. The scattering and absorption coefficients are then varied with the appropriate cross-correlations, assuming a Gaussian distribution centered in the nominal values.

Subsequently, the muons were reconstructed using the Millipede reconstruction method. For each event, the likelihood of the pixel containing the best fit ($\mathscr{L}_0$) and the pixel with the Monte Carlo truth, which is the simulated direction, ($\mathscr{L}_{\text{sim}}$), are calculated. A histogram with the distribution of $-2\Delta\text{LLH} = -2\left(\log\mathscr{L} - \log\mathscr{L}_0\right)$ can be then constructed. Figure 4.4 shows the normalized distribution of -2ΔLLH for the $\mathscr{L}_{\text{sim}}$ value of 250 events similar to IC160427A.

If Wilks' theorem is valid, the -2ΔLLH distribution should follow a χ^2 distribution, represented in Figure 4.4 by the blue curve. In that ideal case, the -2ΔLLH values that correspond to a 50% and 90% containment (median and 0.9 quantile of the distribution) are 1.4 and 4.6, respectively. However, one clearly sees that the simulated data does not resemble the χ^2 distribution, and the values that are used to calibrate the contours (or *correction values*) are represented by the green and magenta dashed lines. For IC160427A, 50% of events are reconstructed with an offset in -2ΔLLH of less than 22.2, and 90% of events had an offset of less than 64.2.

The information from the resimulations is used to convert the likelihood landscape of the Millipede scans to 50% (90%) error contours for every alert by searching for the pixels whose likelihood differs from the likelihood of the best-fit pixel by $-2\Delta\text{LLH} = 22.2$ (64.2). The difference between the uncertainty contours calculated with Wilks' theorem and with the IC160427A correction values are shown in Figure 4.5.

The resimulation process is expensive both in time and computing resources, taking several thousand CPU hours, and is not feasible for

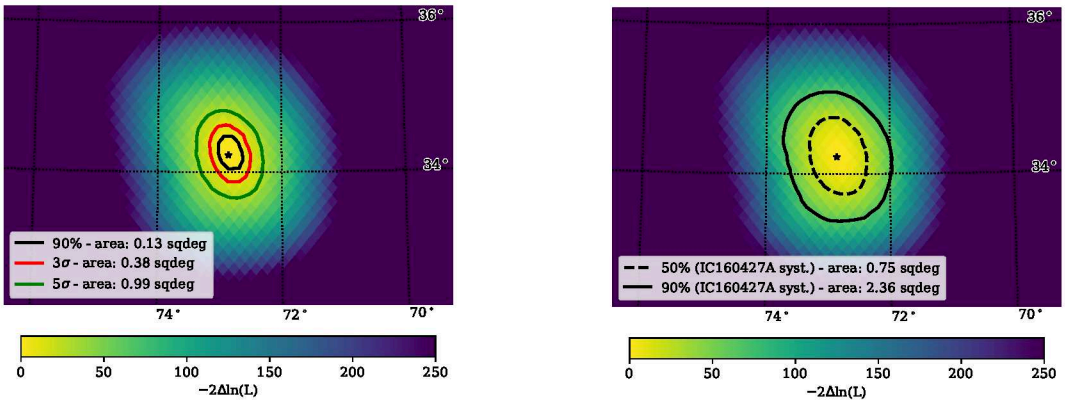

(a) Contours calculated assuming Wilks' theorem is valid.

(b) Contours calculated with IC160427A correction values.

Figure 4.5: Comparison of the error contours derived with Wilks' theorem and with the correction values from the IC160427A resimulations, for the same example event. In both cases the likelihood landscape is identical. The black solid line represents in both figures the 90% error contour. The axes are in equatorial coordinates.

every realtime alert. Therefore, alert events are all calibrated using the IC160427A correction values. Only for one additional event, IC170922A, dedicated resimulations were performed in the past before the work done in this thesis. In that case, the correction values agree roughly with those from IC160422A, at 9.74 and 41.55 for the 50% and 90% containment, respectively. The impact of applying different correction values depends greatly on the steepness of the likelihood landscape. For well-reconstructed events, the change in the error region area is minimal, while for events with a softer landscape and wider uncertainties, it can be many tens of square degrees. This can be seen in Figure 4.6, where these two sets of correction values are used. The new method developed in this thesis for resimulating events is cross-checked with the correction values from the IC170922A resimulations, and discussed in Chapter 6.

4.2.5 Problems with the current methods

The current reconstruction procedure is constantly being improved to be as efficient and accurate as possible, but still suffers from computing limitations and the impact of known and unknown systematic uncertainties. The first issue is the apparent mismatch in the angular errors between the online and offline reconstructions (i.e., SplineMPE and Millipede). The online reconstruction gives error regions with an area that is almost always smaller than the more sophisticated, offline one. In some occasions, the best fit from either reconstruction is not contained within the 90% error contour of the other. This effect seems to be independent of the neutrino energy, as one can see in Figure 4.7.

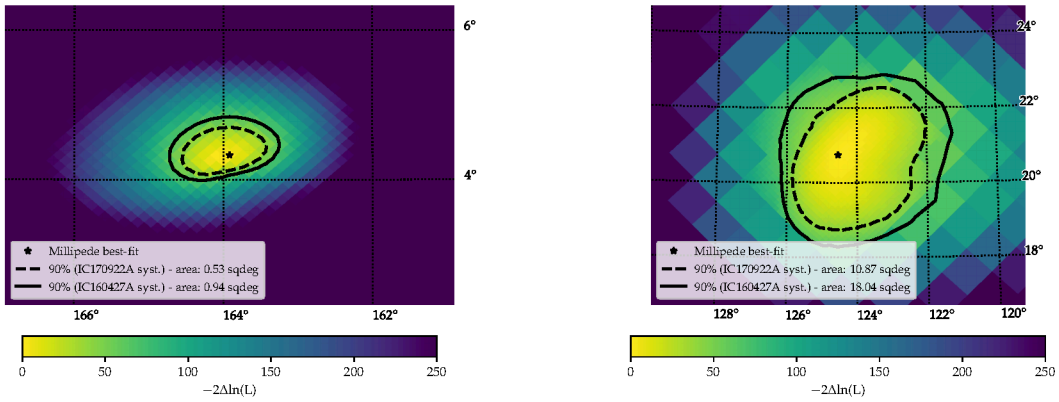

(a) Example of a well-localized event (IC220630A).

(b) Example of an event with poor localization (IC230217A).

Figure 4.6: Comparison for two different events of the 90% confidence level contours using the correction values from IC170922A and IC160422A resimulations, in dashed and solid black lines, respectively. The axes are in equatorial coordinates.

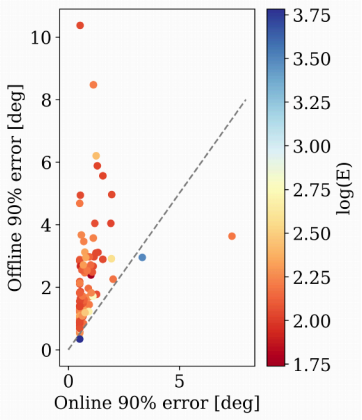

Figure 4.7: Comparison of the 90% circularized error between SplineMPE (online) and Millipede (offline) for the realtime alerts. Only the alerts that were published in realtime as Bronze/Gold are shown. The colors represent the logarithm of the most probable neutrino energy. The gray line represents an equal error value for both reconstructions. One can also see the floor of ~ 0.5 deg established for the online reconstruction.

The second potential issue is that using the correction values is only valid under the assumption that the alert that they are applied to is **similar** to the event that was resimulated and from which the correction values were obtained. In general, this is intuitively not correct, since another position of the track in the detector already means that the ice properties and their uncertainties are completely different, and therefore the light deposition changes.

The event IC160427A is a HESE alert, i.e. a starting track, and has a very different geometry to the majority of alerts, which are through-going tracks, as one can see in Table 4.2. However, resimulations of the TXS neutrino led to broadly consistent correction values to those of IC160427A, hinting that the specific light pattern of the event was not critical. Part of this thesis was developed to check the validity of this statement, which turned out to be incorrect. Simulations were reconstructed and the error contours obtained using IC160427A correction values did not have the expected coverage. The procedure and results will be explained and discussed in the following Chapters.

4.3 Improvements to the angular reconstruction

To study and fix the issues that the Millipede reconstruction method suffers from, particularly those related to how the error contours are calculated, two similar methods to the one described in Section 4.2.4 were developed. One was created to answer the question of how to treat every neutrino alert in the realtime program in a robust and systematic way, while the other was designed to obtain dedicated error contours for the most interesting alerts, i.e. those with promising electromagnetic counterparts that point to potential sources. Moreover, both new methods are used to quantify whether Millipede is currently the optimal reconstruction method for the realtime program. Here a summary of the two options is presented, and the details can be found in Chapter 5 and Chapter 6.

4.3.1 Categories of muons

This method aims to be the default way of calculating error contours for every realtime alert. The result would be sets of 50% and 90% correction values for different categories of muons that would cover the vast majority of events. When the neutrino is detected, it is classified into one of the categories and the corresponding correction values are used.

The procedure is also based on resimulations, but is different to the one explained in Section 4.2.4 and it is explained in detail in Chapter 5. The resimulations within each category have the same true values (direction, initial neutrino energy, and muon energy losses), with slight variations in the ice model parameters that affect the photon propagation and therefore the light yield in the detector. This sample of simulated events was called the *Golden Muons*.

This method comes with its difficulties, which will be discussed in depth in Chapter 5. The definition of categories, which parameters to base them on, and how broad they should be, are major questions to be answered.

4.3.2 Resimulation of alerts

On the contrary, the *resimulation of alerts* method is a dedicated study of the impact of systematic uncertainties on the angular reconstruction of individual alerts. In this case, the resimulated events are "similar" to the original alert, following the IC160427A procedure explained in Section 4.2.4. On top of that, the systematic uncertainties on the ice are varied as well.

The definition of "similarity" between events is up for debate. Even with a conservative definition, simulations may vary greatly, leading to different Millipede likelihood landscapes. Moreover, resimulations are not feasible for every alert, since they need a lot of computing time and resources. This method is discussed in detail in Chapter 6.

4.4 Relevant alerts

Some alerts have been of special interest due to potential electromagnetic counterparts. Here all of the alerts that will be relevant for this thesis (many of them of high scientific impact) are presented in chronological order.

The convention is that the alerts are named after the UTC date of detection, with an IceCube prefix and a letter to indicate the order of alerts on a given day. In this Section, the events are accompanied by the internal nickname that they were given in IceCube to make it easier to distinguish between them in the following chapters.

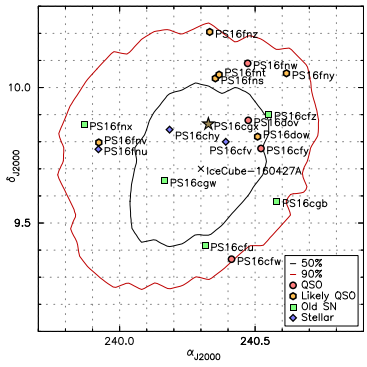

Figure 4.8: The 50% and 90% containment regions for the neutrino IC160427A (black and red contours, respectively). The black cross represents the best-fit position, while the star shows the position of PS16cgx. From [112].

[113]: Blaufuss (2016), 'ICECUBE-160427A neutrino candidate event: updated direction information.'

4.4.1 IC160427A: The Pan-STARRS neutrino

The IC160427A event was the first HESE alert ever detected in realtime [113]. The Pan-STARRS1 telescope followed up all realtime events from 2016 to 2017 and found an optical transient, the supernova PS16cgx, that could be temporally coincident with IC160427A [112]. This motivated a detailed study of the localization of the event, in which 250 resimulations were produced and reconstructed with Millipede to calculate dedicated error contours as explained in Section 4.2.4. The best estimate of the event direction was RA = 240.3, dec = 9.7, with a 90% error ellipse contour with semi major (minor) axis of 0.54 (0.45) deg, shown in Figure 4.8.

[112]: Kankare et al. (2019), 'Search for transient optical counterparts to high-energy IceCube neutrinos with Pan-STARRS1'

The transient PS16cgx was initially classified as a Type Ic supernova, an astrophysical class of potential cosmic-ray sources and emitters of neutrinos, based on its spectra and rising light curve in a timescale of days. However, further measurements showed that the light curve evolution of PS16cgx is compatible to that of a Type Ia supernova, which is the thermonuclear explosion of a white dwarf star. Type Ia supernovae are not expected to produce high-energy neutrinos, so the association most likely happened by chance.

4.4.2 IC170922A: The TXS neutrino

The neutrino alert IC170922A was originally selected by the EHE alert stream [114] and later classified as a Gold alert. With an energy of 263 TeV and a signalness of 63%, this is arguably the best known individual neutrino alert event ever detected by IceCube. At a distance of 0.1 degrees from the best-fit position (RA, dec) = ($77.43^{+1.3}_{-0.8}$, $5.72^{+0.7}_{-0.4}$) deg (Figure 4.9), the blazar TXS 0506+056 was flaring in gamma rays at the time of the neutrino detection.

[114]: Kopper et al. (2017), 'IceCube-170922A - IceCube observation of a high-energy neutrino candidate event.'

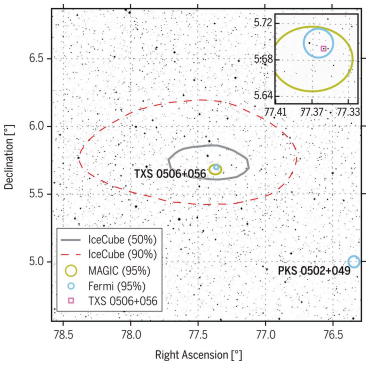

Figure 4.9: The 50% and 90% containment regions for the neutrino IC170922A (dashed red and solid gray contours, respectively). From [62].

This spatial and temporal correlation launched a wide follow-up campaign in multiple wavelengths. A subsequent archival search was performed with 9.5 years of data, looking for neutrino events coincident with the TXS 0506+056 direction [63]. An excess of neutrinos was found in a time window of 158 days, independent of the 2017 detection, with a significance of 3.5σ. More details on this blazar are given in Chapter 8.

Given the relevance of the alert, this neutrino was also resimulated in the same manner as IC160427A, the results of which are discussed in Section 4.2.4. In this thesis, this event is also resimulated as a verification of the method that was developed, and will be shown in Chapter 6.

[63]: Aartsen et al. (2018), 'Neutrino emission from the direction of the blazar TXS 0506+056 prior to the IceCube-170922A alert'

4.4.3 IC190730A: The PKS neutrino

The neutrino event IC190730A was a Gold alert with a signalness of 67%, and a reconstructed energy of 289 TeV [115]. It was a well-localized event, with the best-fit position being (RA, dec) = ($225.79^{+1.28}_{-1.43}$, $10.47^{+1.14}_{-0.89}$) deg, leading to a 90% error region of only 5.61 deg^2. The blazar PKS 1502+106, the 15th brightest blazar in terms of gamma-ray energy flux, was contained within the error region.

[115]: Stein (2019), 'IceCube-190730A - IceCube observation of a high-energy neutrino candidate event'

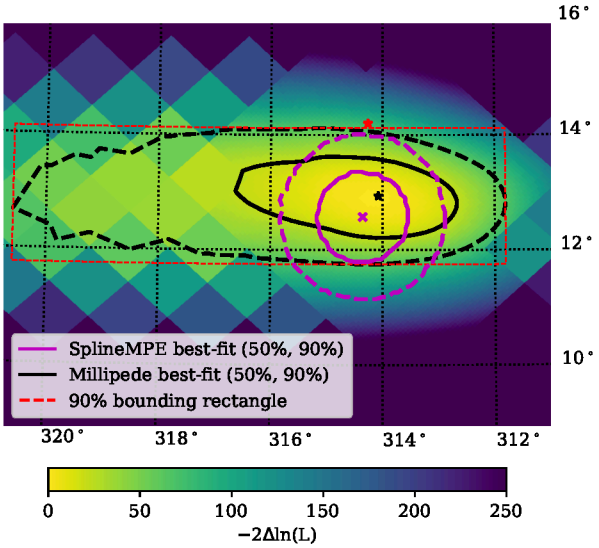

Figure 4.10: The 50% and 90% containment regions for the neutrino IC191001A reconstructed with Millipede (black and red contours, respectively). In purple, the online reconstruction with SplineMPE. The red star marks the location of the TDE AT2019dsg.

Due to the brightness of the blazar, this coincidence also triggered a wide follow-up campaign. The blazar was not flaring in gamma rays at the neutrino arrival time. A multi-wavelength and multi-messenger modeling of this source predicts a neutrino flux correlated with the gamma-ray and X-ray fluxes, but finds that the detection of the neutrino during the quiescent state is still compatible with the model [116].

The radio flux shows a long-term flare that started 2014 and peaked at the highest flux density ever detected during the arrival of IC190730A [117, 118]. Some studies attribute this behavior to a suppression of gamma rays during efficient neutrino production [119].

[116]: Rodrigues et al. (2021), 'Multi-wavelength and Neutrino Emission from Blazar PKS 1502 + 106'

[117]: Kiehlmann et al. (2019), 'Neutrino candidate source FSRQ PKS 1502+106 at highest flux density at 15 GHz'

[118]: Franckowiak et al. (2020), 'Patterns in the Multiwavelength Behavior of Candidate Neutrino Blazars'

[119]: Kun et al. (2021), 'Cosmic Neutrinos from Temporarily Gamma-suppressed Blazars'

4.4.4 IC191001A: The Bran Stark neutrino

This neutrino alert was detected in 2019 as a Gold alert, selected by the GFU stream. A Tidal Disruption Event (TDE) called AT2019dsg was found by the Zwicky Transient Facility (ZTF) in coincidence with the alert [120], with a chance probability of 0.5%. The ZTF internally assigned nicknames for TDEs are based on the HBO series *Game of Thrones*, this one being the Bran Stark TDE.

[120]: Stein et al. (2021), 'A tidal disruption event coincident with a high-energy neutrino'

TDEs are transients that occur when a star passes close to a Supermassive Black Hole (SMBH) and gets disrupted by the tidal force due to the strong gravity. This creates a very bright electromagnetic flare that lasts for months. TDEs have been proposed as high-energy neutrino and ultra-high-energy cosmic ray sources [121].

[121]: Hayasaki (2021), 'Neutrinos from tidal disruption events'

The neutrino event has a signalness of 59% and reconstructed energy of 218 TeV, and its best-fit position is (RA, dec) = $(314.08^{+6.56}_{-2.26}, 12.94^{+1.5}_{-1.47})$ deg, see Figure 4.10. The 90% localization region of 15.84 deg^2 is larger than the median 90% contour area of all alerts, which is 5.96 deg^2. AT2019dsg is located almost at the border of the error contours, at a distance of 1.3 degrees to the best-fit position. This raised some concerns within IceCube. As part of this thesis, the author resimulated this alert (and

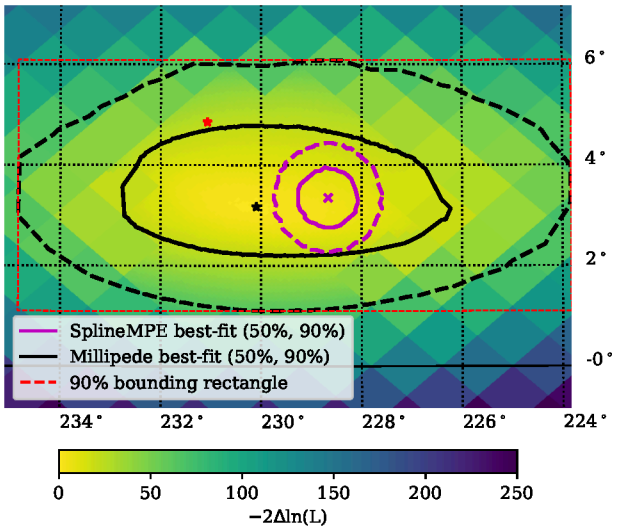

Figure 4.11: The 50% and 90% containment regions for the neutrino IC191119A reconstructed with Millipede (black and red contours, respectively). In purple, the online reconstruction with SplineMPE. The red star marks the location of the TDE AT2019aalc.

started the process with the two following ones) to obtain dedicated correction values for the contour calibration and verify the correlation.

4.4.5 IC191119A: The Lancel neutrino

This potential correlation was found during an archival search instead of being a follow-up observation of a realtime alert event. After the detection of the Bran Stark neutrino and the Tywin neutrino (explained below), a systematic study was performed looking for neutrino alert events coincident with TDEs that show a flare in infrared emission after the optical peak. The increase in infrared brightness is produced by the reprocessing of the light from the flare by the surrounding dust [122].

[122]: Velzen et al. (2021), 'Establishing accretion flares from massive black holes as a major source of high-energy neutrinos'

The statistical significance of the analysis is 3.7σ, corresponding to a p-value of $1.9 \cdot 10^{-4}$. From the analysed sample of 36 neutrinos and 63 accretion flares, only three neutrino-TDE associations contribute to the result: IC191001A, IC200530A (already known), and one additional neutrino event, IC191119A. Its coincident TDE candidate with a strong dust echo was AT2019aalc (nicknamed Lancel). IC191119A was a Gold alert, with a reconstructed energy of 177 TeV and signalness of 45%. The best-fit position is (RA, dec) = $(230.1^{+4.76}_{-6.48}, 3.17^{+3.36}_{-2.09})$ deg, shown in Figure 4.11. In this case, the 90% localization region is even larger than for the Bran Stark neutrino, at 42.5 deg^2.

4.4.6 IC200530A: The Tywin neutrino

The second potential coincidence between neutrino alerts and TDEs or TDE candidates (in chronological order of detection) was the Gold alert IC200530A and the TDE candidate AT2019fdr (named Tywin following the ZTF custom) [123]. The neutrino has a signalness of 59%, reconstructed energy of 82.2 TeV, best-fit direction of (RA, dec) = $(255.37^{+2.48}_{-2.56}, 26.61^{+2.33}_{-3.28})$ deg and a 90% localization region of 23.68 deg^2 (Figure 4.12).

[123]: Reusch et al. (2022), 'Candidate Tidal Disruption Event AT2019fdr Coincident with a High-Energy Neutrino'

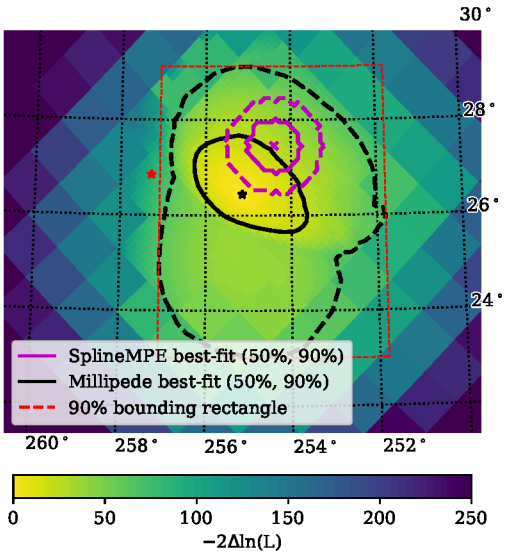

Figure 4.12: The 50% and 90% containment regions for the neutrino IC200530A reconstructed with Millipede (black and red contours, respectively). In purple, the online reconstruction with SplineMPE. The red star marks the location of the TDE AT2019fdr.

Table 4.1: Summary of relevant alerts for later reference. The values of the reconstructed direction and associated uncertainties are taken from the IceCat-1 and can differ slightly from the ones calculated and published in realtime and mentioned in the text. The distance quoted in the Table is between the Millipede best-fit position and the location of the associated source.

Neutrino alert	Nickname	RA (deg)	dec (deg)	Type of counterpart	Counterpart	Distance (deg)
IC160427A	Pan-STARRS	$240.29^{+0.44}_{-0.48}$	$9.71^{+0.57}_{-0.42}$	Supernova	PS16cgx	0.17
IC170922A	TXS	$77.43^{+1.3}_{-0.8}$	$5.72^{+0.7}_{-0.4}$	Blazar	TXS 0506+056	0.1
IC190730A	PKS	$225.79^{+1.28}_{-1.43}$	$10.47^{+1.14}_{-0.89}$	Blazar	PKS 1502+106	0.3
IC191001A	Bran Stark	$314.08^{+6.56}_{-2.26}$	$12.94^{+1.5}_{-1.47}$	TDE	AT2019dsg	1.3
IC191119A	Lancel	$230.1^{+4.76}_{-6.48}$	$3.17^{+3.36}_{-2.09}$	TDE candidate	AT2019aalc	1.9
IC200530A	Tywin	$255.37^{+2.48}_{-2.56}$	$26.61^{+2.33}_{-3.28}$	TDE candidate	AT2019fdr	1.7

The probability of finding two neutrino-TDE associations by chance was calculated to be $3.4 \cdot 10^{-4} (3.4\sigma)$ and it was done by selecting TDE candidates that are at least as bright as AT2019fdr and neutrinos that were followed up by ZTF.

The light curve of AT2019fdr was modeled as a mix of two blackbodies, since two distinct peaks in luminosity could be observed. The infrared emission was delayed in time and interpreted as a dust echo, meaning that the first blackbody heats up the surrounding dust, making it glow. This is an indication of large amounts of matter, a promising signature of neutrino production. The neutrino arrival time also coincides with this second peak in the light curve, motivating the archival search for dust echos in accreation flares coincident with neutrino alert events explained before [122].

[122]: Velzen et al. (2021), 'Establishing accretion flares from massive black holes as a major source of high-energy neutrinos'

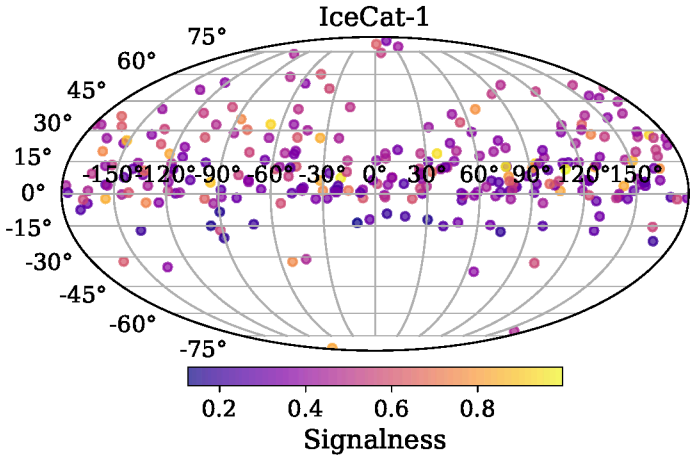

Figure 4.13: Neutrino events which have passed the alert criteria in the period between 2011 and 2020. The colours represent the probability that the neutrino is of astrophysical origin (signalness).

4.5 The IceCube Event Catalog of Alert Tracks (IceCat-1)

IceCube has only been sending out neutrino alerts since 2016, but it has been detecting high-energy neutrinos already several years before. An archival search for neutrino alerts was conducted, and the selected events were classified and reconstructed according to the up-to-date (as of 2020) criteria. In total, 275 neutrino alerts were found in the period from May 2011 to December 2020[†]. Table 4.2 contains the number of observed events for each alert stream, while Table 4.3 shows the expected number of signal and background events in 10 years of data, calculated for a spectral index of 2.37 [94]. The expected number of events for the Bronze alert stream exclude the events labeled also as Gold.

The IceCube Event Catalog of Alert Tracks (IceCat-1) [124] contains said alert events. An accompanying online version of the catalog was also released[5]. In Figure 4.13 the spatial distribution of the alerts is shown, with the colours representing the signalness of each event. The varying density in the number of events reflects the dependence of IceCube's effective area on the declination of the neutrino direction.

The selected alerts were reconstructed with Millipede using the commercially available computing cluster Amazon Web Services (AWS)[6]. The author of this thesis contributed to the IceCat-1 by reconstructing some events for which the minimization of the likelihood failed in the AWS, and a forced scan around the expected minimum was needed. The tools that were developed for the resimulation studies presented in this thesis were crucial for this. Additional classification criteria were run on the alerts, to distinguish the morphology of the events and to flag those that were more likely to be caused by atmospheric background.

A data sample consisting of alerts has high purity, with a large proportion of neutrinos being of astrophysical origin. This has always motivated the scientific community to search for correlations between alerts and different candidate sources (see publications on individual coincidences

[94]: Abbasi et al. (2022), 'Improved Characterization of the Astrophysical Muon–neutrino Flux with 9.5 Years of IceCube Data'

[124]: Abbasi et al. (2023), 'IceCat-1: the IceCube Event Catalog of Alert Tracks'

5: https://dataverse.harvard.edu/dataset.xhtml?persistentId=doi:10.7910/DVN/SCRUCD

Table 4.2: Observed events during the 10 year time window, included in IceCat-1.

Event type	Observed
GFU Gold	72
EHE Gold	22
HESE Gold	9
GFU Bronze	164
HESE Bronze	8

Table 4.3: Expected number of signal and background (Bkg) events in 10 years based on an spectral index of 2.37 (signal).

Event type	Signal	Bkg
GFU Gold	28.9	47
EHE Gold	5.4	19
HESE Gold	5.3	4
GFU Bronze	26.9	138
HESE Bronze	0.9	9

6: https://aws.amazon.com

[†] During two of those years, the author of this thesis was the main realtime shifter, reacting and sending out approximately 40 alerts. By chance, 34% of these arrived on a weekend or a public holiday.

referenced above, or the analyses performed in [125–127]). In [124], there is a simple time-independent search for spatial correlations between a list of the most commonly-used candidate source catalogs and the neutrinos alerts from the IceCat-1 catalog, whose result is compatible with a chance coincidence.

The main scientific goal of this thesis is to develop a method to calculate the overall correlation between neutrino alerts and any catalog of sources using all the internally available information to be more sensitive to potential signal. Three stacking analyses were performed using this method and will be discussed in detail in Chapter 10.

[125]: Giommi et al. (2020), 'Dissecting the regions around IceCube high-energy neutrinos: growing evidence for the blazar connection'

[126]: Plavin et al. (2020), 'Observational Evidence for the Origin of High-energy Neutrinos in Parsec-scale Nuclei of Radio-bright Active Galaxies'

[127]: Plavin et al. (2022), 'Growing evidence for high-energy neutrinos originating in radio blazars'

[124]: Abbasi et al. (2023), 'IceCat-1: the IceCube Event Catalog of Alert Tracks'

5 Golden Muons

5.1 Simulation 53
5.2 Reconstruction 56
5.3 First round of Golden Muons 56
5.4 Second round of Golden Muons 62
5.5 Comparison to other reconstruction methods 65

The IceCube Realtime Program uses the Millipede reconstruction method to infer the direction of the incoming neutrino by optimizing the likelihood of the observed energy losses assuming a track hypothesis (Section 4.2.3). This is done in a grid of pixels over the entire sky, creating a likelihood landscape where the best-fit position of the event is given by the pixel with the maximum likelihood value.

If Wilks' theorem [111] applies, one can derive error contours directly from this landscape. However, as shown in Section 4.2.4, the impact of systematic uncertainties on the directional reconstruction and thus the likelihood landscape is not negligible, and a different treatment is needed. The values to scale the contours, called *correction values*, obtained for the IC160427A neutrino alert, are applied nowadays to every realtime event. Part of this work focused on testing the validity of this procedure. Afterwards, the goal was to develop a new, more robust method. With that objective in mind, the set of simulated events called *Golden Muons* was created, as introduced in Chapter 4.

In this Chapter the simulation of events in IceCube will be discussed, with a focus on the particular simulation method that is used in this thesis and the necessary modifications. Then, the configuration for the reconstruction method is briefly explained. Lastly, the development and findings of the Golden Muon approach is shown. Part of this Chapter was published in the *International Cosmic Ray Conference 2021* (ICRC2021) proceedings [128].

[111]: Wilks (1938), 'The Large-Sample Distribution of the Likelihood Ratio for Testing Composite Hypotheses'

[128]: Abbasi et al. (2021), 'Studies of systematic uncertainty effects on IceCube's real-time angular uncertainty'

5.1 Simulation

Simulation is one of the pillars of most analyses in IceCube. Searches for the sources of astrophysical neutrinos are conducted in a *blind* manner, so that the statistical method to test the significance of any result is designed and developed without looking at data to avoid biases. One possibility to realize the blindness criteria is to use simulations. Typically, an ensemble of neutrinos is simulated in equal numbers of flavors and neutrino-antineutrinos, $\nu : \bar{\nu} = 1 : 1$ and $\nu_e : \nu_\mu : \nu_\tau = 1 : 1 : 1$. For a full analysis, the individual events are then weighted according to the astrophysical or atmospheric flux to match the expected event rate, since the Monte Carlo simulation is usually generated with an unphysical spectrum to optimize computing resources. Weighting also allows to test different flux hypotheses without re-running expensive computations. The studies presented here only consider individual events, so a weighting scheme is not needed.

Simulation also allows us to know the underlying true properties of every event, which permits the study of the performance and the calibration of energy and angular reconstruction methods. This is really important in neutrino astronomy, since there is not any object in the sky that can act as

a standard candle with which we can test the algorithms*. In this Section, the steps that are taken in a typical simulation chain are explained, with special emphasis on a novel method for photon propagation in ice. The modifications needed for resimulating the Golden Muons are also clarified here.

5.1.1 Typical simulation chain

Event generation: The first step is typically the simulation of the primary particle, which can be an astrophysical neutrino or a cosmic-ray particle that induces an air shower, producing atmospheric neutrinos and muons. In simulation production, atmospheric and astrophysical neutrinos are indistinguishable and thus treated in the same way. The software used for the simulations of this work is `LeptonInjector` [130]. The point of the neutrino interaction is in a region close enough to the detector so that the charged secondary particles can reach the instrumented volume.

The muons from the atmospheric air showers are propagated into the instrumented volume of IceCube with the `MuonGun` software [131], which is a parametrized version of `CORSIKA` (*Cosmic-Ray Simulations for Kascade*) [132]. The atmospheric muon flux inside the ice expected from air showers is parametrized as function of depth, zenith angle, multiplicity, and energy, and individual muons or muon bundles are drawn from the distribution.

Lepton propagation: If the secondary lepton from the interaction is a muon, either atmospheric or from an astrophysical neutrino, it is propagated through the ice in the second step. This is done with the software `PROPOSAL` (*Propagator with Optimal Precision and Optimized Speed for All Leptons*) [133], which also creates new secondary particles along the way. Therefore, the energy losses that the muon suffers are fixed at this step. It assumes a negligible interaction angle between the incoming neutrino and the outgoing muon, and that the particle travels at the speed of light, which is expected at the energies relevant for IceCube.

Photon propagation: Once the energy losses and the secondary particles are established, the Cherenkov photons from the charged particles are propagated through the ice. If the secondary lepton is an electron or a tau, i.e. the morphology is a cascade, the previous step is skipped. The energy losses produce a point-like light deposition and the path traversed by the lepton is negligible. The software used in this thesis for the photon propagation is *SnowStorm* [134], which is explained in detail in Section 5.1.2. This program also simulates the photoelectron production in the DOMs.

Detector response: Whether the light emitted from all the charged particles is detected in IceCube depends on the response of the PMTs, which is also included in the simulation chain. The sensitivity of the PMTs depends on their quantum efficiency, and the wavelength and incident angle of the photon. The hardware is calibrated in the

[130]: Abbasi et al. (2021), 'LeptonInjector and LeptonWeighter: A neutrino event generator and weighter for neutrino observatories'

[131]: Santen (2014), 'Neutrino Interactions in IceCube above 1 TeV: Constraints on Atmospheric Charmed-Meson Production and Investigation of the Astrophysical Neutrino Flux with 2 Years of IceCube Data taken 2010–2012'

[132]: Heck et al. (1998), 'CORSIKA: A Monte Carlo code to simulate extensive air showers'

[133]: Koehne et al. (2013), 'PROPOSAL: A tool for propagation of charged leptons'

[134]: Aartsen et al. (2019), 'Efficient propagation of systematic uncertainties from calibration to analysis with the SnowStorm method in IceCube'

* The *moon shadow* can be used to test the pointing accuracy of angular reconstructions [129]. The moon absorbes cosmic rays that would induce muons in the atmosphere, producing a deficit in the muon flux. Several algorithms have been studied, all of which show a systematic shift of up to 0.2 deg. However, this was performed on a low-energy sample, with muon energies from 1 TeV to 10 TeV.

laboratory before deployment, and the thermal and non-thermal noise in the DOMs due to decays and scintillation is simulated. The possible saturation at the PMTs is modelled to reflect the impact on the pulses. The electronic noise is calculated as well at this step.

L1 and L2 processings: At this stage the simulation of an individual event is done, and this final step simply runs the online triggers that are applied to real data at the South Pole. Of relevance to this thesis are the L1 and L2 processings, which are run on all data to classify events, remove those that are more likely atmospheric background and reconstruct the energy and direction. More details on the triggers can be found in Section 3.3.

5.1.2 SnowStorm

The lepton and photon propagation simulation utilizes an ice model with fixed parameters (see Section 3.4). However, these are not fully known and carry some uncertainty with systematic effects. The uncertainties on the ice model parameters can be added as nuisance parameters, and be varied in an ensemble of events. This is typically done through Monte Carlo (MC) simulations, where each sample is created with a different set of nuisance parameters. This method is limited by the computing capabilities, since a high-statistics sample is needed for each realization. Moreover, we do not simulate discrete sets with various parameter values off-baseline due to this limitation, so the correlations between parameters could be neglected.

As a solution to this problem, the SnowStorm simulation method was developed [134]. In a SnowStorm MC ensemble, each event is generated with a unique set of nuisance parameters. The impact of the variations on the parameters can be studied by analyzing a single simulation set. A schematic comparison of this method to the "multiple simulation ensembles, each with a different set of nuisance parameters" approach can be seen in Figure 5.1. For this method to be valid, the effect of systematic uncertainties has to be sufficiently small so that they can be treated in perturbative manner, where second and higher order corrections can be dropped, which is an assumption that often goes into systematic uncertainty calculations. Moreover, the statistical uncertainty on the MC set has to be small compared to the one on data.

For each event, the perturbations that are applied to the parameters of the chosen ice model are selected from distributions whose shape and range are based on calibration data. Table 5.1 shows the range for the different ice systematics considered for this work. For all the parameters, the perturbations are sampled from a uniform distribution. The absorption and scattering parametrizations scale the global ice coefficient with reference to the baseline ice model. The ice anisotropy scale modifies the anisotropy strength (not the direction of the anisotropy axis) [99]. The DOM efficiency parametrization scales the efficiency of all DOMs with a factor. Lastly, the two Hole Ice parameters modify the model that describes the properties of the refrozen column of ice around the DOMs [135].

This novel method for the photon propagation differs from the procedure used in the IC160427A resimulations, where the parameter were simply

[134]: Aartsen et al. (2019), 'Efficient propagation of systematic uncertainties from calibration to analysis with the SnowStorm method in IceCube'

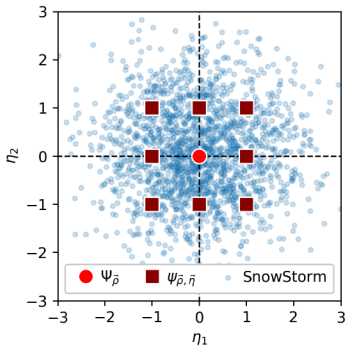

Figure 5.1: Illustration showing the different treatment of nuisance parameters. In red squares, discrete shifts of the nuisance parameters require an entire Monte Carlo set. In blue dots, a single ensemble of simulated events with SnowStorm. From [134].

[99]: Chirkin et al. (2019), 'Light diffusion in birefringent polycrystals and the IceCube ice anisotropy'

[135]: Abbasi et al. (2021), 'A calibration study of local ice and optical sensor properties in IceCube'

Table 5.1: SnowStorm parametrizations used in this thesis. The values for the ice model are taken from the range quoted in the table, assuming a uniform distribution.

Parameter	Range
Absorption	$[0.9, 1.1]$
Scattering	$[0.9, 1.1]$
Ice anisotropy scale	$[0, 2]$
DOM efficiency	$[0.9, 1.1]$
Hole Ice	$[-0.84, +0.3]$ $[-0.134, 0.05]$

varied assuming a Gaussian distribution centered around the baseline value, see Section 4.2.4. SnowStorm has a more robust treatment of systematic uncertainties, since the choices for the distributions and the ranges to vary the parameters are based on calibration data and have been intensively studied. The baseline ice model to which the perturbations are applied here, *SPICE 3.2.1*, is an updated and improved version of the model for the IC160427A resimulations, *SPICE MIE* (see Section 3.4 for details on the ice models).

5.1.3 Simulation chain for Golden Muons

With the goal of isolating the impact of systematic uncertainties on the angular reconstruction of muon events, the simulation chain was "simplified" to create the sample of Golden Muons. The categorization was done by visually selecting one event from a pool of simulations with fixed direction and energy that matched the desired energy loss pattern, or the *stochasticity*.

Then, within each category, the initial event was simulated hundreds of times by repeating the simulation chain only from the photon propagation onwards, using the SnowStorm method. The *resimulations* of each Golden Muon have the same true values (energy and incoming direction of the muon from the CC interaction, and differential energy losses along the track), so they can be considered to be *the same event* simulated with a slightly varied ice model each time. This differs to what was done for the resimulations of IC160427A, for which each simulation was started from the beginning of the chain, so the set consisted of *similar events* (Figure 5.2) with different incoming directions and energy depositions.

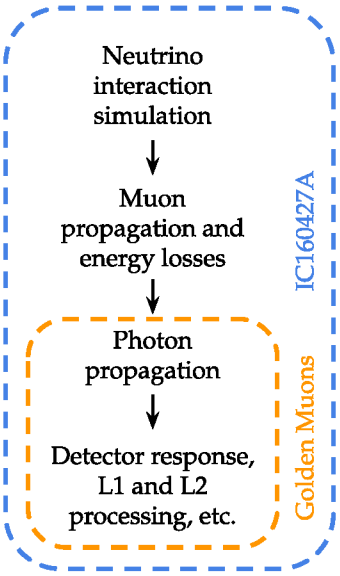

Figure 5.2: Simulation chain for a neutrino event. The steps that need to be taken for each resimulation of a Golden Muon category are circled in orange. In blue, the steps for the resimulation of realtime events, in the same way as for the IC160427A alert.

5.2 Reconstruction

The main difference to the likelihood scan for angular reconstruction explained in Section 4.2.3 is that here it is done in a smaller scale to save computing resources. The scan is centered around the simulated direction, or true direction, and is performed only within a circle of a predefined radius. Inside the circle, the sky is divided in pixels of $\sim 0.013\,\mathrm{deg}^2$, which corresponds to $n_{\mathrm{side}} = 512$ for the whole sky. Typically for the Golden Muons, a 3 deg radius was large enough to find the best-fit position with Millipede. One such example can be seen in Figure 5.3. For those events whose best fit was at the edge of the circle or close to (i.e., angular distance between the reconstructed direction and the true direction of 2.8 deg or larger), the scan was repeated with a radius of 5 deg. With this configuration, a simulated event is scanned in $\sim$ 1000 CPU hours.

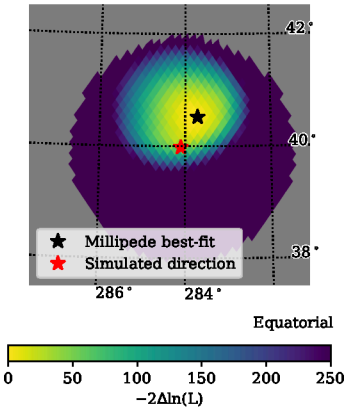

Figure 5.3: Example of the zoomed-in scan.

5.3 First round of Golden Muons

To check the validity of the values to scale up the error contours, i.e. *correction values*, from the IC160427A resimulations (see Section 4.2.4), the first step was to test the scaling with a sample of simulated neutrinos that resembled the majority of events in the detector. That mainly means

through-going tracks between 80 and 140 degrees in zenith angle (θ). The event IC160427A is a starting track, from which there are only a small fraction in the IceCat-1 catalog, see Table 4.2. All the simulated events have a neutrino energy of 150 TeV, which is close to the median neutrino energy of IceCube's alerts. This first set of events was simulated by E. Ganster and J. Stettner, and reconstructed by the author of this thesis.

5.3.1 Definition of the categories

As a first, simple approach two main classes were defined: *Horizontal* ($\theta = 90$ deg, see Figure 4.2) and *Upgoing* ($\theta = 130$ deg) muons. The main source of systematic uncertainties is the ice model, whose properties depend roughly on the depth z. Therefore, for the *Horizontal* class two more categories were selected, one in the upper half of the detector at $z = 200$ m (*Shallow*) and the other in the lower half at $z = -400$ m (*Deep*). With these values, the *Shallow* muons are above the dust layer and the *Deep* ones are below.

There are two subsets in each of the *Horizontal* classes: the *Far From DOMs* muons, which traverse the detector through a "corridor" between strings (see Figure 5.4), and the *Close to DOMs* muons, which cross the detector hitting at least one DOM.

Finally, both for the *Upgoing* and the *Horizontal* muons, the impact of stochasticity was also considered, and two more subdivisions were created. The *Smooth* muon is defined with continuous energy losses along the track. Similarly, the category *Stochastic* is represented by a muon with at least one big stochastic energy loss in the track. The stochasticity for these first simulations was approximated by visually inspecting the event views of the muons, but it can be calculated based on the maximum energy loss deposition along the track, and it was analyzed as a possible parameter to consider for the subsequent resimulation studies. The one event selected for each of the 10 categories was resimulated 100 times as explained in Section 5.1.3. In Figure 5.4 the event views of representative muons from some of the categories can be seen. Event views from the rest of the categories are shown in Appendix B.

5.3.2 Results

The events were reconstructed with the Millipede reconstruction method in the realtime fashion, with the zoomed-in version of the scan explained in Section 5.2. The path forward with this analysis was constantly being reshaped when new results were obtained, and the changes are presented here in chronological order.

Merging categories and final correction values

The first decision was to combine the *Far from DOMs* and *Close to DOMs* categories. This decision was taken to optimize the time and computing resources needed, since it was not expected that they would have a great impact on the correction values. That was checked for a low statistics sample, shown in Figure 5.5 as the cumulative distribution of the difference

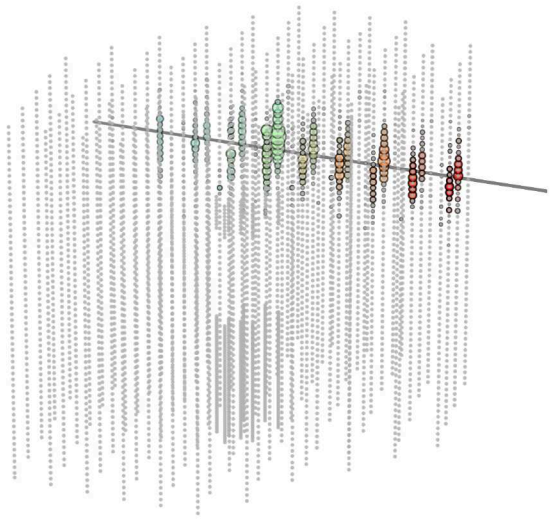

(a) *Horizontal Shallow Smooth Far from DOMs*

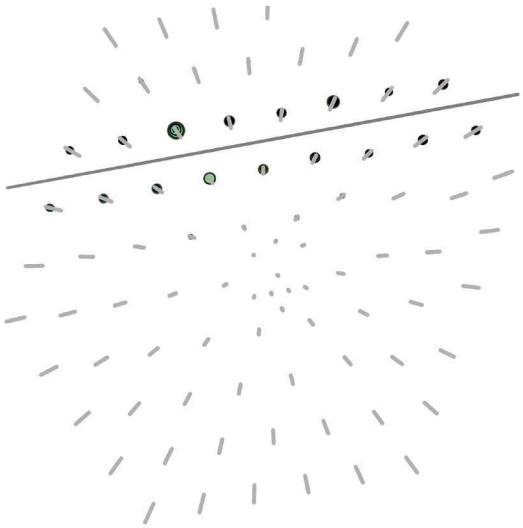

(b) *Horizontal Shallow Smooth Far from DOMs*, top view.

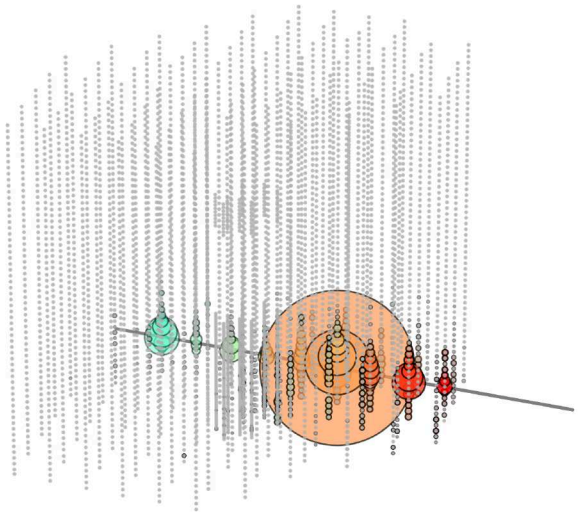

(c) *Horizontal Deep Stochastic Close to DOMs*

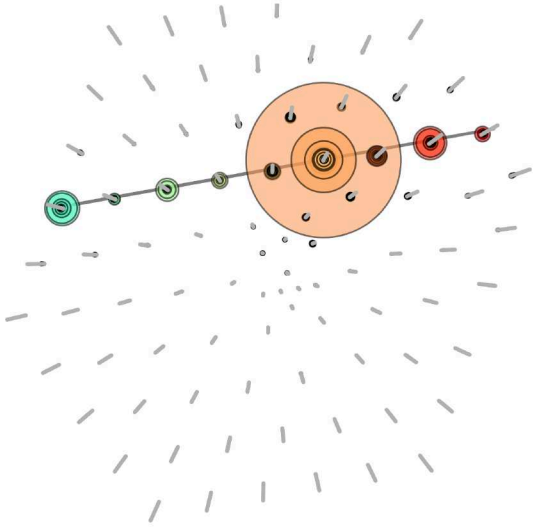

(d) *Horizontal Deep Stochastic Close to DOMs*, top view.

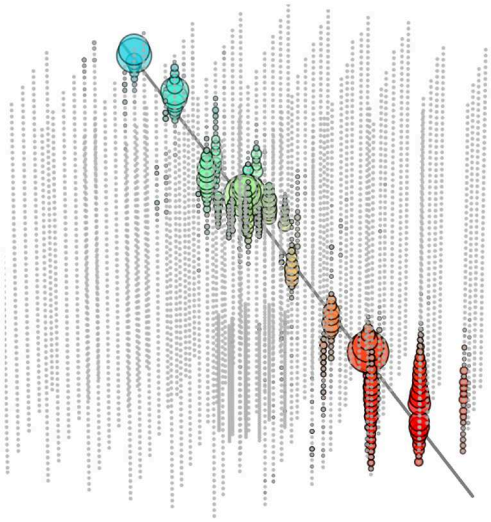

(e) *Upgoing Smooth*

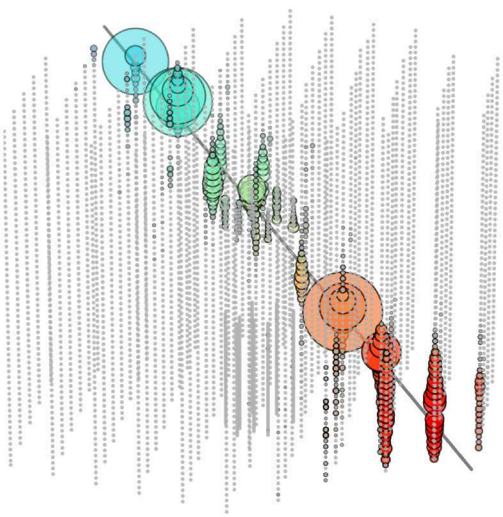

(f) *Upgoing Stochastic*

Figure 5.4: Event views of 4 out of the 10 categories of resimulations. The gray line shows the track of the muon. The color represents the arrival time of the photons, from early (red) to late (blue). The size of the hits is proportional to the deposited charge.

Category	N. of *Far*	N. of *Close*	p-value
Deep Smooth	20	20	0.012
Deep Stochastic	69	20	0.22
Shallow Smooth	30	20	0.26
Shallow Stochastic	78	30	0.08

Table 5.2: Results from the KS test comparing the *Far from DOMs* (*Far*) and the *Close to DOMs* (*Close*) categories.

Table 5.3: The correction values for the selected categories, along with the number of reconstructed events at the time of writing this proceeding. Not all simulated events are included as they have not been reconstructed. For comparison, the values from the IC160427A resimulations are also shown.

Category	50% containment	90% containment	Number of events
Horizontal Shallow	4.5	12.5	158
Horizontal Deep	31.9	83.2	129
Upgoing Smooth	51.8	193.8	80
Upgoing Stochastic	88.9	301.7	80
IC160427A	22.2	64.2	250

in likelihood between the best-fit positions and the simulated directions (-2ΔLLH). The two-sample Kolmogorov-Smirnov (KS) test [108] was performed to study the compatibility of the distributions, resulting in the p-values shown in Table 5.2. The only two distributions that are incompatible are the *Deep Smooth* muons, but the number of reconstructed resimulations is significantly lower than in the other cases. Considering the arguments presented, the *Far from DOMs* and *Close to DOMs* were merged for the Millipede studies. However, as it will be discussed later, the reconstruction method SplineMPE (used in the first GCN Notice that is issued for every alert, see Section 4.2.2) is negatively impacted by events going through a corridor.

[108]: Kolmogorov (1933), 'Sulla determinazione empirica di una legge di distribuzione.'

Then, once those categories were merged, the remaining *Horizontal* muons were studied, shown in Figure 5.6. One can visually see that stochasticity does not play an important role in the calibration of the reconstruction for these categories either. A KS test was again conducted to compare them, resulting in a p-value of 0.67 (0.65) for the *Smooth* (*Stochastic*) muons. Therefore, the categories are further merged into *Horizontal Shallow* and *Horizontal Deep*.

In Figure 5.7, the cumulative distribution of the difference in likelihood between the best-fit positions and the simulated directions for the four selected categories is shown. Table 5.3 shows the correction values that correspond to the 50% and 90% confidence levels and the number of reconstructed events. Despite a difference in the number of resimulations, one can clearly see that each class has a unique set of values; the impact of systematic uncertainties depends on the position and shape of the track in the detector. This strongly implies that the error contours calculated with the resimulations of IC160427A do not have the correct confidence levels when generalized to every neutrino alert.

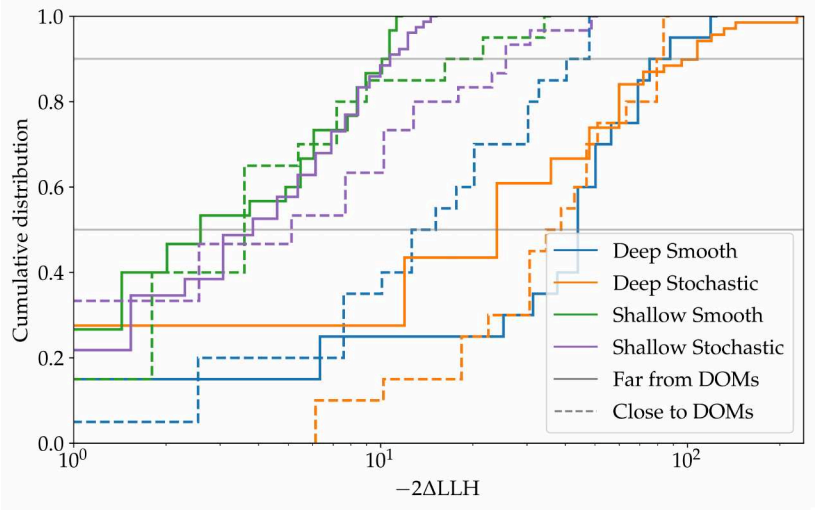

Figure 5.5: Cumulative distribution of −2ΔLLH for the *Horizontal* muons divided in the *Far from DOMs* and the *Close to DOMs* categories, represented by the solid and dashed lines, respectively.

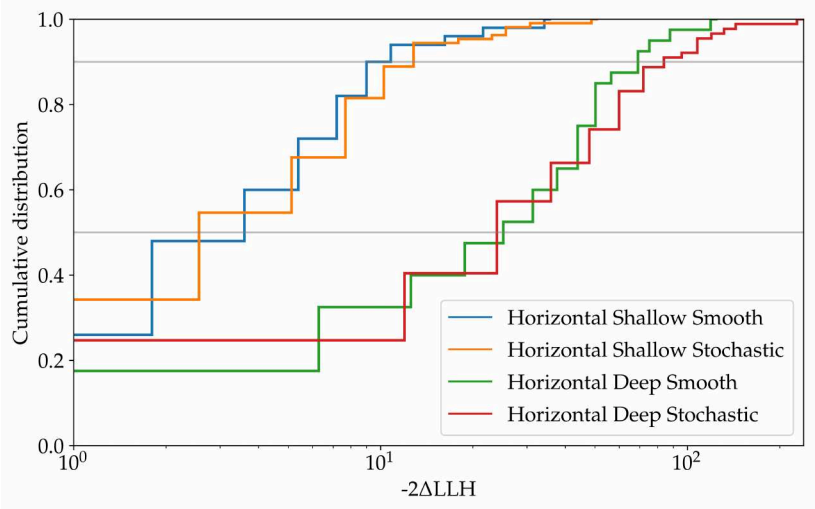

Figure 5.6: Cumulative distribution of −2ΔLLH for the *Horizontal* muons. The two *Smooth* and *Stochastic* classes are visually compatible, which is confirmed with a Kolmogorov-Smirnov test.

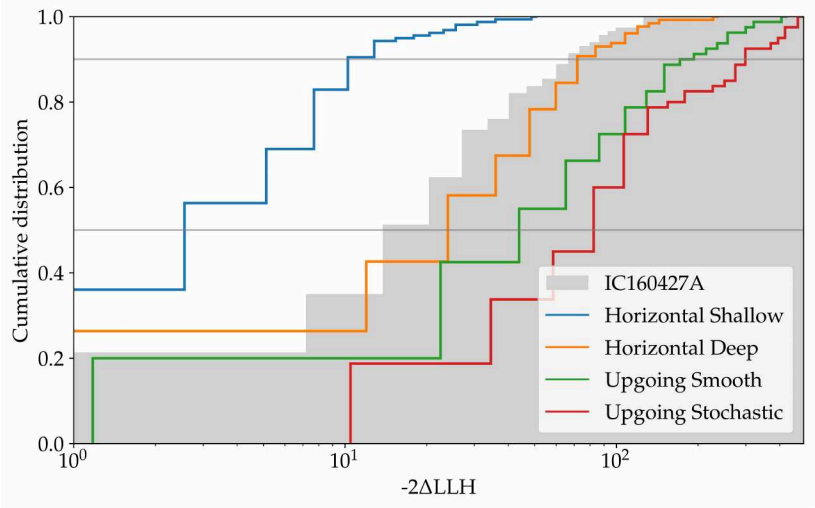

Figure 5.7: Cumulative distribution of −2ΔLLH for the four selected categories of simulated Golden Muons. For comparison, the cumulative distribution for IC160427A is included in gray.

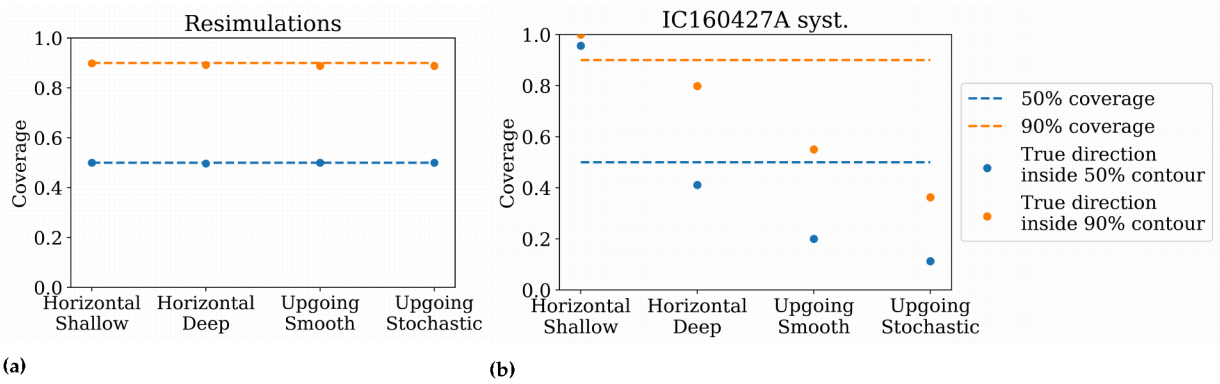

Figure 5.8: Study of the coverage of the contours calculated with the resimulations of each category (Figure 5.8a) and with the IC160427A correction values (Figure 5.8b). The dashed lines indicate that for 50% (90%) of the reconstructed events the simulated direction lies within the 50% (90%) error contour. The dots represent the actual percentage of events that satisfy this condition.

Coverage study

To measure the performance of this method, the *coverage* of the contours is studied. All the events within each category except one are used to calculate the correction values. For the remaining event, we check if the simulated direction is inside the error contours calculated with the values from the previous step. We repeat this procedure selecting each time a different event to evaluate the correction values. The coverage, i.e. fraction of times the evaluation events were contained within the 50% and 90% contours, is shown in Figure 5.8a. To compare the performance of the original correction values, the coverage is evaluated again using the contours calculated with the IC160427A resimulations (Figure 5.8b).

In both Figures, accurate contours would lead to blue (orange) dots located around the blue (orange) dashed line. The coverage values for the resimulations follow these lines very precisely, which is expected by construction. However, the coverage calculated with the IC160427A resimulations shows that only for the *Horizontal Deep* category the IC160427A correction values are a good approximation. For the other categories, we go to extreme values. The *Horizontal Shallow* muons have in more than 90% of the cases the true direction inside of the 50% error contour. On the opposite side of the spectrum, the true values of the *Upgoing Stochastic* category are outside the 90% error contours approximately in 60% of the resimulations.

It is not trivial to know what the overall impact of using the incorrect values for the contour determination on the IceCat-1 catalog would be. Approximately 60% of alerts, however, have a zenith angle between 75 deg and 105 deg, and are more similar to the muons from the *Horizontal* category than from the *Upgoing* category. This means that for those, the contours slightly overcover the localization of the event or have a similar area to what could be obtained with resimulations.

Change in the likelihood scans

Lastly, the error contours calculated using IC160427A (black line) and the new resimulations (red line) for a random event of each category are shown in Figure 5.9. This expresses that the area of the contour ultimately

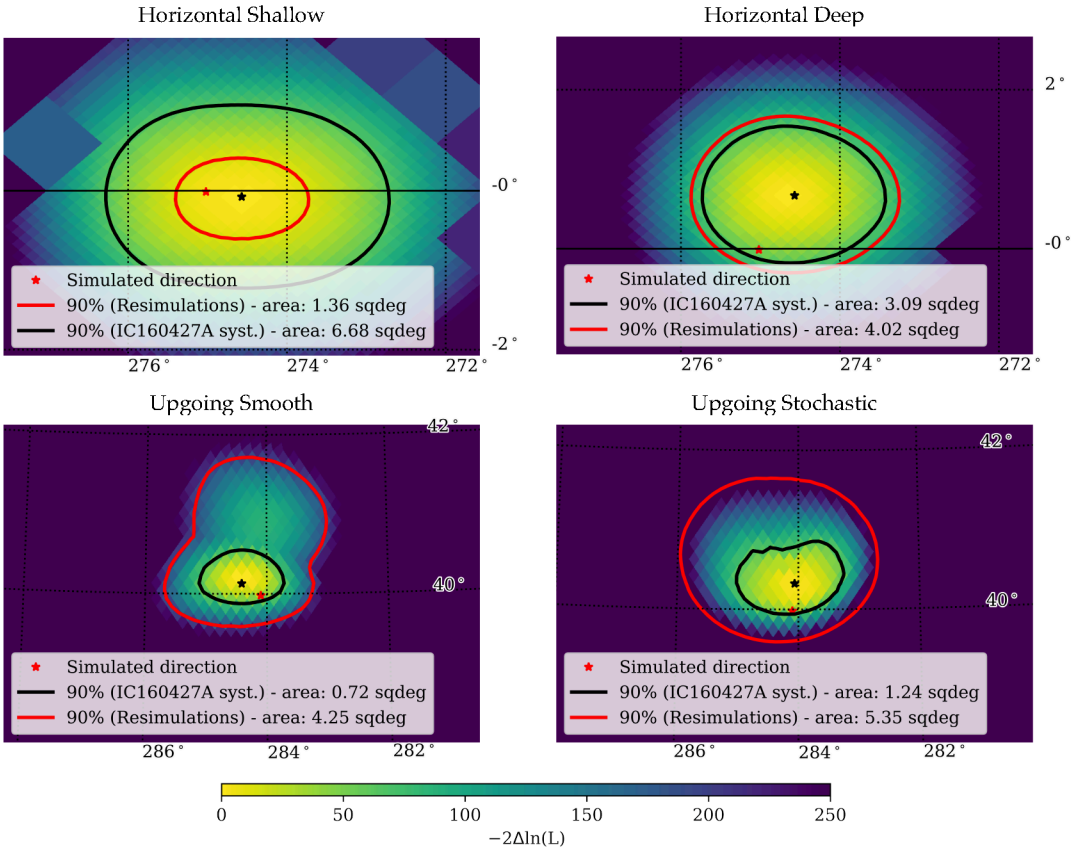

Figure 5.9: Results of the Millipede scan for one representative event of each category. The black star represents the scan best fit and the red star is the true direction. The black line is the 90% contour calculated with the IC160427A correction values (currently used for every realtime alert) and the red line is the 90% contour calculated with the correction values of the event's category. The figures are in equatorial coordinates.

depends on the steepness and shape of the likelihood landscape, so the scaling has a different impact for each alert. It also means that, while we now know that using the same parameters is not correct, on average it is a good approximation to our new, more reliable error contours. It must be noted that it is not possible to calculate "true" error contours that would account for all existing systematic uncertainties because some of them are known but not implemented in the simulation software whereas some are completely unknown.

5.4 Second round of Golden Muons

After the first results from the Golden Muons, it was clear that the impact of systematic uncertainties depends on the angle and position of the track in the detector. A new strategy was developed by the author to correct for the varying systematic uncertainties for the different event categories. However, based on the work of this thesis that was happening in parallel, a different strategy came up and was followed instead. In this Section, the initial plan is presented.

One possible option was to create a fixed amount of pre-defined categories, obtain the correction values for those and assign the realtime events to one of those categories. For example, with the current Golden Muons, a

track with a zenith angle of 100 degrees crossing the detector through the clear ice at the bottom of the instrumented volume would be classified as a *Horizontal Deep* event. Deciding and testing how many categories are needed would not be a trivial task, since there are infinite possibilities for the track position, length and direction, and light deposition pattern, which all affect the reconstruction of the event.

The alternative solution was to create a set of simulated muons at different angles and depths, and interpolate between the correction values based on the properties of the detected event. In practice, strictly horizontal muons would be simulated at 5 different depths (400 m, 200 m, 0 m, −200 m and −400 m). A function of the 50% and 90% correction values dependent of depth could be obtained by fitting the calculated values. Then, muons at other zenith angles would be simulated at some of the pre-selected depth values. Assuming that the distribution of correction values follows the same trend, one could scale the fitted curve from the horizontal muons to the values at other zenith angles. In Figure 5.10 a simple cartoon explains the process. The simulations were processed by H. Thomas, and reconstructed by the author of this thesis with Millipede.

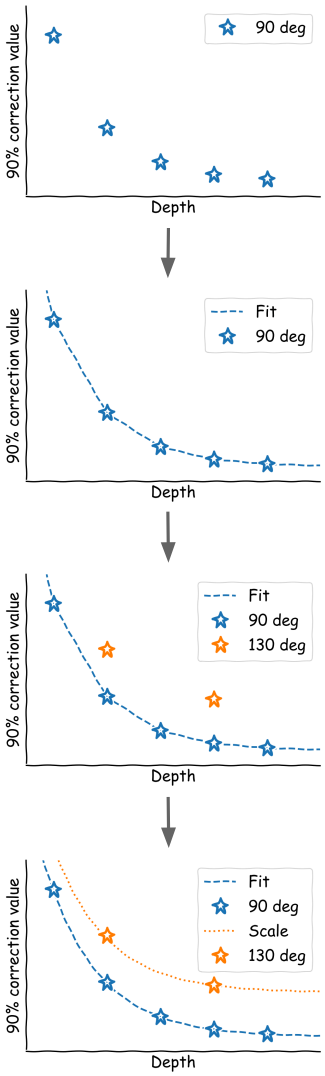

Figure 5.10: Sketch with the idea for the calculation of correction values for each realtime alert. The stars represent correction values calculated with resimulations. The blue dashed line is a curve fitted to the blue data points. The orange dotted line is the same curve scaled up to match the orange data points.

The events would be simulated at two energies: 150 TeV and 5 PeV. The median neutrino energy of the events in the IceCat-1 catalog is 154 TeV, close to 150 TeV, and the majority of them have an energy of < 300 TeV. That value is taken as the threshold for the classification, so that all events with a reconstructed energy smaller than 300 TeV would get the correction values from the simulated muons at 150 TeV. The very-high-energy events above 300 TeV would get the correction values from the 5 PeV resimulations, which is an approximation to the root mean square energy of events above the threshold, RMS($E > 300$ TeV) = 5.23 PeV. The energy distribution of alerts from the IceCat-1 catalog can be seen in Figure 5.11. As a future step, a finer binning in energy could be pursued.

Based on a study done by H. Thomas, the stochasticity was not considered for the second round of Golden Muons. There are four methods that can be used to calculate the stochasticity of an event: the maximum deviation from the median energy loss along the track, maximum deviation from the mean energy loss, a χ^2 test applied to a linear fit to the energy losses, and a combination of the peak over mean and the χ^2 test. The four measurements were applied to all the events in the IceCat-1, and it was found that each method leads incompatible stochasticity values, making them not reliable to properly define an event. The events were also visually inspected, with very inconsistent classifications. This, combined with the results from the first round of Golden Muons that indicated that the stochasticity does not play an important role for the majority of events, drove the decision of dropping stochasticity as a study parameter.

Lastly, as a relatively simple and fast solution for the realtime program, the alert events that are starting tracks or with a track length shorter than 200 m would get assigned the correction values of IC160427A. Including them would greatly increase the dimensionality of the problem, so it was decided that these classes of events would be studied in detail in the future. The rest of realtime alert events would enter this classification scheme after being reconstructed with Millipede. The zenith angle, depth of the center of gravity of the track, and energy of the neutrino would be

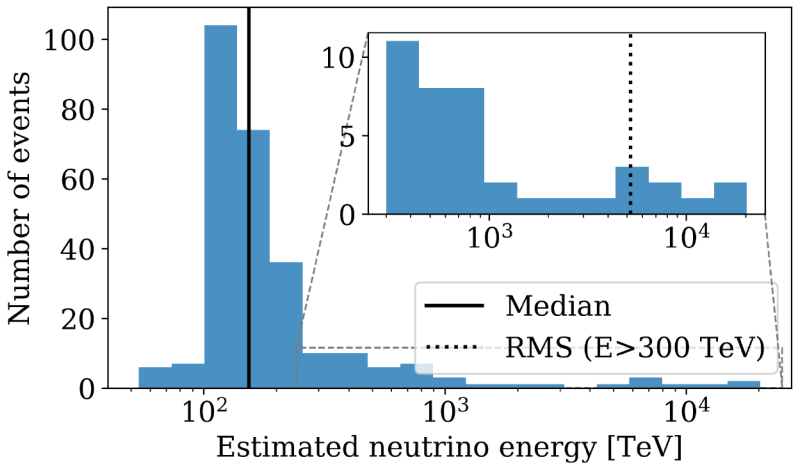

Figure 5.11: Energy distribution of events in the IceCat-1 catalog. The black solid line represents the median energy of all events, $E_{\text{median}} = 154\,\text{TeV}$. The upper Panel shows a zoom-in of the events with energy larger than 300 TeV. The root mean square of that selection is 5.23 PeV.

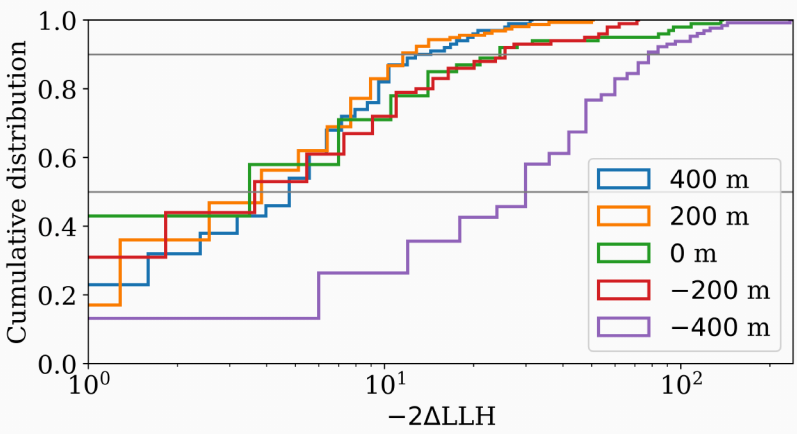

Figure 5.12: Cumulative distribution of the −2ΔLLH values for the *Horizontal* muons in the second round of simulated Golden Muons. Each category is simulated at a different depth in the detector.

used to calculate the uncertainty contours with the correct coverage by interpolation of the analyzed parameter space.

The results from the horizontal muons at 150 TeV can be seen in Figure 5.12 and Figure 5.13. The only category for which the values divert greatly is the muons at a depth of −400 m, where the original *Horizontal Deep* Golden Muons were located. The efforts to define depth for the non-horizontal muons as well as the reconstruction of those events started, but soon after the results from SplineMPE came for both the Golden Muons (Section 5.5) and for the resimulations of alerts (Section 6.3), and a different direction to solve the issue of systematic uncertainties was taken.

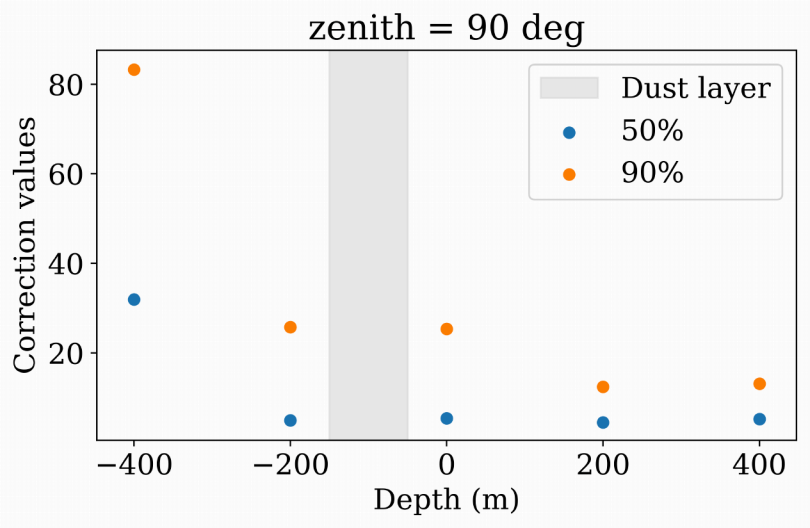

Figure 5.13: Distribution of the 50% and 90% correction values as a function of depth for the *Horizontal* muons in the second round of simulated Golden Muons. The dust layer is represented as the grey area.

Depth [m]	N. of events	50% containment	90% containment
400	100	5.23	13.12
200	158	4.49	12.46
0	100	5.39	25.33
−200	100	4.92	25.75
−400	129	31.91	83.24

Table 5.4: Correction values for the *Horizontal* muons (θ = 90 deg) of the second round of Golden Muons, along with the number of reconstructed simulations. The events at 200 m and −400 m are the same as shown in Table 5.3.

5.5 Comparison to other reconstruction methods

This work was continuously discussed with the IceCube Collaboration members, looking for volunteers to reconstruct the direction of the events with other methods. Millipede is slow and computationally expensive, therefore no direct comparison to other algorithms had ever been done before. Millipede is expected to perform better for individual tracks, since it uses more of the available information from the emitted Cherenkov photons, as opposed to SplineMPE, which only considers the arrival time of the first photon for the angular reconstruction.

At the same time that the Golden Muons were being studied, the resimulation of high-energy realtime events was started, which will be presented in Chapter 6. These created a lot of interest within the collaboration, and many people volunteered to help with other algorithms. Thanks to these resimulations, a systematic comparison was finally achievable.

The first round of Golden Muons was reconstructed using two implementations of SplineMPE. In one, the SplineMPE algorithm is run as explained in Section 4.2.2, with the "max" configuration. In the other, the likelihood of each track hypothesis that is assumed to find the minimum is used to create a likelihood landscape in a pixelated grid similar to the Millipede scan (Figure 5.15, left panel). The likelihood scan version has the advantage of scanning all locations in the sky, avoiding local minima. The studies with SplineMPE were performed by H. Niederhausen and G. Sommani. Thanks to the speed and simplicity of the reconstruction method, for the comparison studies the events were also resimulated and reconstructed using the *Nominal Ice* model, i.e. without varying the ice model properties at the photon propagation step. This allows us to

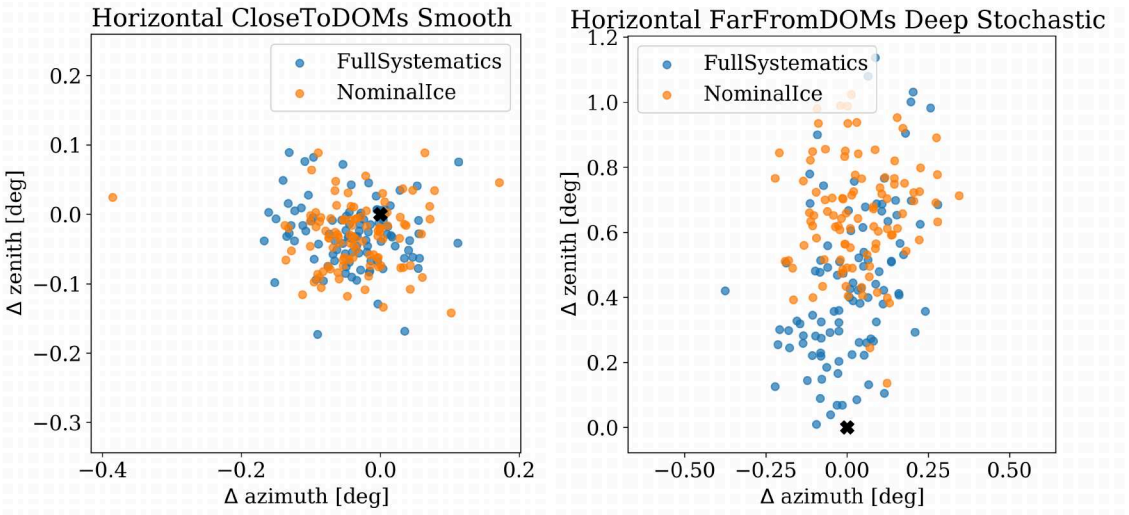

Figure 5.14: Results from two categories of Golden Muons, reconstructed using SplineMPE with the "max" configuration. Courtesy of H. Niederhausen.

measure the impact of the uncertainty of the ice model parameters on the reconstruction.

For both implementations the accuracy of SplineMPE seems to be better than of Millipede, at a fraction of the computation cost. With the standard SplineMPE version, the only categories that show a potential issue are the *Far from DOMs*, an example of which is shown in Figure 5.14. A bias seems to be present when the events go through a corridor in the detector, which is more pronounced for the *Nominal Ice* events than for the *Full Systematics* (with variations in the ice model parameters). In general, the impact of systematic uncertainties is negligible compared to the impact of geometric differences between events.

The same can be observed in the full-sky scan version of SplineMPE. The right panel on Figure 5.15 shows the p-values of the two-sample KS test comparing the -2ΔLLH distribution for SplineMPE to a χ^2 distribution for all categories of Golden Muons, with the *Full Systematics* configuration. In some cases, the distributions are compatible, which removes the need for a scaling factor to obtain the contours with the desired confidence levels. The *Deep Far From DOMs* muons are again the events with the worst localization. A high-statistic study of those categories that are not compatible, that was prohibitively expensive with Millipede, is possible with SplineMPE.

These results, and specially the ones from the comparison of the angular reconstruction algorithms using the resimulation of realtime alert events, shown in Chapter 6, shifted the efforts from calibrating Millipede to modifying the reconstruction method used in the IceCube's Realtime Program.

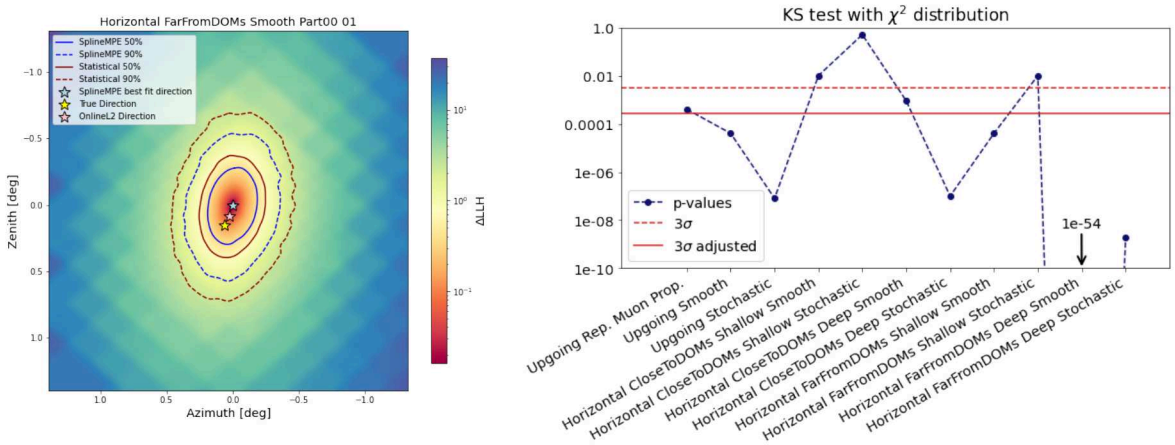

Figure 5.15: Results using SplineMPE with the full-sky scan implementation, courtesy of G. Sommani.

Resimulation of realtime alerts 6

6.1 Method 69
6.2 Study cases 70
6.3 Comparison to other reconstruction methods 76

The method explained in Chapter 5 aims to create a solution for the realtime program that is feasible to run in a timely manner. However, for alerts that are considered interesting, i.e. that lie in spatial or temporal coincidence with a potential source, a dedicated study of the error region could be beneficial to reject or strengthen the correlation. In this Chapter we explain the method of resimulating realtime alerts to calculate correction values specific to those events.

The final goal is to develop a method that can be run semi-automatically on those alerts that trigger a strong response from the multimessenger community, due to the detection of a potential counterpart. As a first step, we calculated correction values with Millipede for some already-known neutrino alerts. In the case of the IC170922A neutrino, the resimulations were compared to previous studies to validate the method. The other alert events were resimulated as a response to external papers where neutrinos were found in coincidence with Tidal Disruption Events (TDEs). The development of the method, the simulations and the Millipede reconstructions were performed by the author of this thesis. The events were also reconstructed with other algorithms by IceCube collaborators to compare the performances.

6.1 Method

The simulation chain for the realtime alerts uses the same steps and algorithms as explained in Section 5.1. As opposed to the Golden Muons simulation method, for each resimulation of an alert the first step is the event generation. Each resimulation is by definition different to all others, since during the muon propagation the energy losses are recalculated. The process is summarized in Figure 5.2 as the blue circle.

The resimulations are also created with variations in the initial incoming direction and energy, since the true values of the real event are unknown. The choice of the range for both parameters is such that the resimulations closely resemble the original track. For the work presented here, the same definition of *similarity* as for the IC160427A resimulations was used, introduced in Section 4.2.4. The steps are the following:

Neutrino simulation and sky position cut: The neutrino is simulated as coming from a position in the sky close to the reconstructed direction of the real event $(\mathrm{RA}, \mathrm{dec})_{\mathrm{event}}$. In practice, instead of using the more sophisticated `LeptonInjector` software, a simpler method was developed. In this, the information is read from the event data file, the interaction point is simulated with a random direction chosen from $\pm 2.2 \cdot (\mathrm{RA}, \mathrm{dec})_{\mathrm{event}}$ and the angular distance to $(\mathrm{RA}, \mathrm{dec})_{\mathrm{event}}$ is calculated. If the simulated direction lies within a radius of 2 deg, the criterium is met.

Table 6.1: Surviving events for the resimulation of realtime events after each applied cut. The numbers represent the percentage of events that survive each cut with respect to the previous step.

Event	Geometric cut	Charge cut	N. of events
TXS (*Full Systematics*)	0.87%	5.62%	106
TXS (*Nominal Ice*)	0.87%	5.56%	108
Bran Stark	0.36%	5.52%	100
Tywin	0.30%	4.27%	51

Muon propagation and geometric cut: The muon is propagated, and only if the simulated track is close to the reconstructed track of the real event, the simulation is selected. The maximum allowed distance between tracks at the closest approach point is 30 m. Another geometric cut is applied, that only allows tracks with entry and exit points (intersection points between the track and the detection volume of IceCube) at a distance of < 30 m from the entry and exit points of the original reconstructed track.

Photon propagation and charge cut: The photons are propagated, and the detector response is simulated. A cut on the deposited charge measured by the PMTs is applied, and only if the simulated event has ±20% of the deposited charge of the real event, it is finally accepted.

In Table 6.1, the surviving events after the geometric cut (second step) and the charge cut (third step) are shown as the percentage of events that pass each criterium. For the TXS neutrino resimulations, two ice model configurations were tested and will be discussed in the following. In either case, the starting number of simulations (after the sky position cut) was $\sim 2 \times 10^5$, and only ~ 100 events were selected. For the Bran Stark neutrino resimulations, the geometric cut was more restrictive, and double the number of initial neutrinos ($\sim 5 \times 10^5$) was needed to arrive at a total of 100 resimulations. The same trend was observed with the Tywin neutrino resimulations, but the study was brought to a stop as will be explained in Section 6.2.

Lastly, the reconstruction method and configuration were the same as in Section 5.2. Since the TDE events have a shorter track length or a more stochastic deposition of light than the Golden Muons, many simulated events needed a radius of 5 deg for the zoomed-in scan, which increased the computing time considerably.

6.2 Study cases

Here the results of the Millipede reconstruction applied to resimulations of the 4 selected neutrinos are presented.

6.2.1 IC170922A: The TXS neutrino

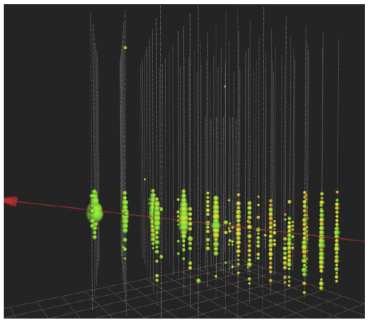

Figure 6.1: Event view of the IC170922A (TXS) neutrino event.

The resimulations of IC170922A (the event view of which can be seen in Figure 6.1) were used as a validation set to cross-check the current method. Newer and more sophisticated algorithms were used in the simulation, and the reconstruction algorithm had been already improved since then. The results can be directly compared with the correction values calculated for the angular uncertainties that went into the publication of the multimessenger observations of TXS 0506+056 [62], mentioned in

[62]: Aartsen et al. (2018), 'Multimessenger observations of a flaring blazar coincident with high-energy neutrino IceCube-170922A'

Dataset	N. of events	50% C.L.	90% C.L.
Nominal Ice	108	7.73	20.69
Full Systematics	103	16.95	101.87
Previous study	160	9.74	41.55

Table 6.2: Correction values for the three datasets of IC170922A resimulations.

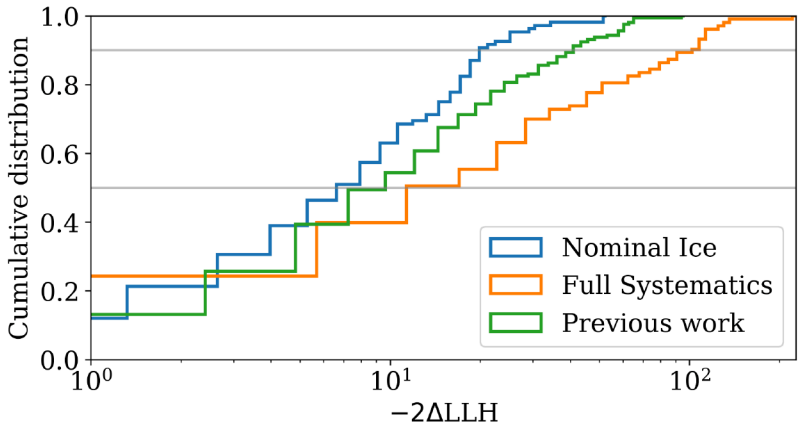

Figure 6.2: Cumulative distribution of the −2ΔLLH values of the IC170922A (TXS) neutrino event, for several samples. *Nominal Ice* and *Full systematics* are the result of the work of this thesis, while the *Previous work* values were calculated in a previous study [62].

Section 4.2.4.

To isolate the impact of variations in the direction and energy of the resimulations, the *Nominal Ice* and the *Full Systematics* SnowStorm configurations were considered. The first one is simply the baseline configuration from SPICE 3.2.1 (see Section 3.4 for more details on the ice model), while in the second one the ice model parameters are varied within the ranges shown in Table 5.1 on top of the SPICE 3.2.1 baseline. The −2ΔLLH distributions can be seen in Figure 6.2, and the corresponding correction values and number of events are shown in Table 6.2.

The TXS neutrino has an almost horizontal muon path, with a reconstructed zenith angle of 5.72 deg. This event can be categorized as a *Horizontal Deep* muon, which allows for another cross-check with the Golden Muons resimulations. The difference in the correction values can tell us if this event would have had the proper coverage if the Golden Muons method for scaling the uncertainty contours had been in place. The result can be seen in Figure 6.3. Both distributions look compatible, and the containment values lead to almost identical error regions, as can be seen in the right panel in Figure 6.4.

Figure 6.4 also shows the angular distance between the reconstructed and the true (simulated) direction of the resimulations with the *Full Systematics* configuration as blue dots. Overlaid are the 90% error contours from the Millipede likelihood landscape of the real event, calculated with the correction values from the different data sets.

6.2.2 The TDE neutrinos

The three neutrino events that will be discussed here were found in coincidence with TDEs and TDE candidates, and were introduced in Chapter 4. The potential sources were all detected with the Zwicky Transient Facility (ZTF) [31], an optical telescope at the Palomar Observatory, located in California. The camera of ZTF is mounted on a 48-inch robotic telescope, and has a wide field of view of 47 deg^2. ZTF scans the Northern

[31]: Bellm et al. (2018), 'The Zwicky Transient Facility: System Overview, Performance, and First Results'

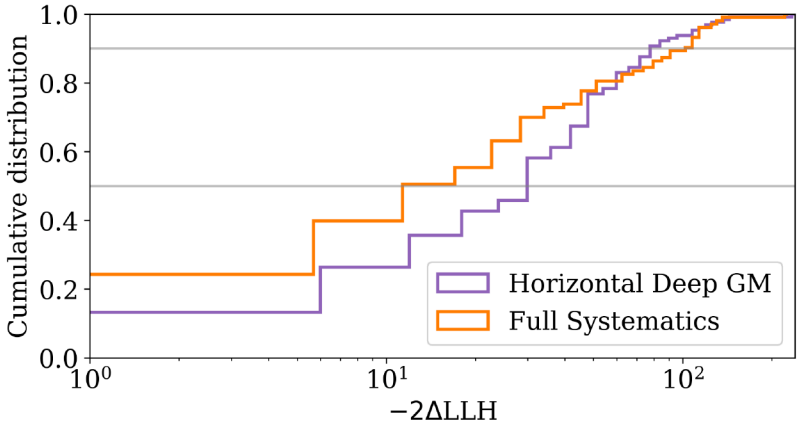

Figure 6.3: Cumulative distribution of the −2ΔLLH values of the *Full systematics* sample of the TXS neutrino resimulations and of the *Horizontal Deep* category of Golden Muons.

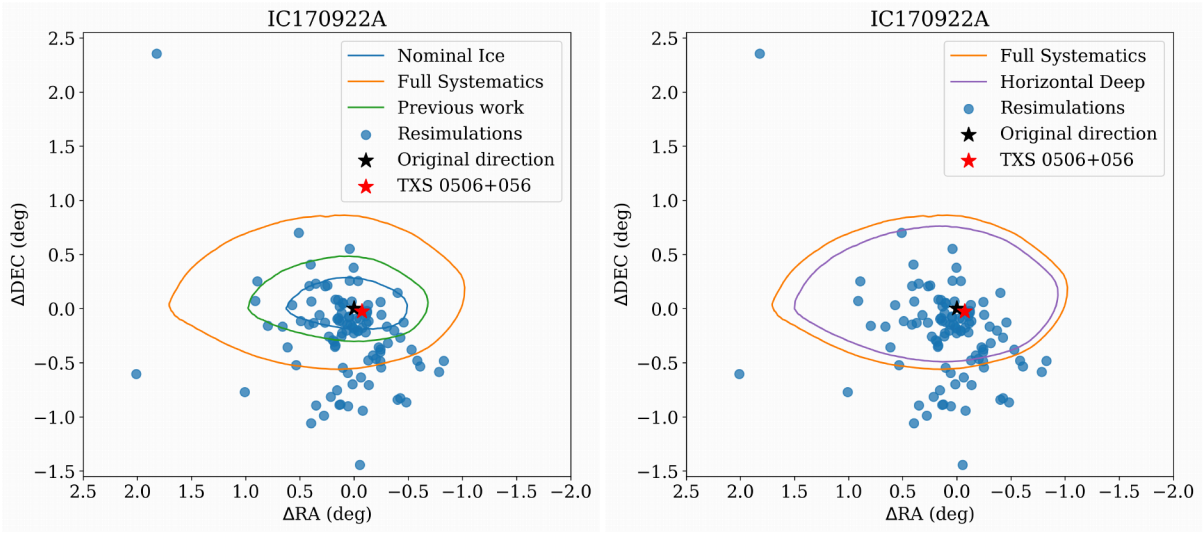

Figure 6.4: Error contours at 90% C.L. for the IC170922A (TXS) neutrino, calculated with the scaling factors from the data sets shown in Figure 6.2 (left panel) and Figure 6.3 (right panel). The blue dots show the shift between the true (simulated) directions and the reconstructed directions of the resimulations. The black star represents the reconstructed direction of the real event. The red star shows the location of TXS 0506+056.

sky with a high cadence of ~ 2 days in a systematic, multi-filter survey that allows for time-domain astronomy studies.

The relatively significant result of the stacking analysis between TDE and TDE candidates and neutrino alerts, as well as the individual studies of IC191001A and IC200530A, started a long discussion within the IceCube collaboration. This is partially due to the fact that it couples to the issues that the realtime reconstruction method suffers from. Since the three TDE neutrinos were located far from their candidate sources compared to the median angular resolution of offline analyses (< 1 deg), the veracity of such correlations was questioned. This served as a good test case for the resimulation of alerts, which happened simultaneously to the developments and findings of the Golden Muons simulations.

After a succesful resimulation of the TXS neutrino, the TDE neutrinos proved to be more challenging to simulate and calculate proper correction values of. The criteria for selecting a simulated event, although reasonable, made the process very inefficient and the vast majority of the events were dropped at different simulation stages. For the surviving ones, the slight differences between them still had a big impact on the reconstruction.

The comparison to other reconstruction methods also showed that those methods performed as well or even better than Millipede in terms of the angular resolution, at a fraction of the computational cost. In this Section, the results with Millipede are presented.

IC191001A: The Bran Stark neutrino

The first TDE neutrino event that was resimulated was the Bran Stark neutrino, whose event views are displayed in Figure 6.5. This event starts in the dust layer and exits the detector, so it was selected as a Gold alert by the GFU and HESE selections. This peculiar geometry made it inefficient to resimulate it, since the dust layer has a big impact on the propagation of the lepton and the photons, and thus on the direction of the track. This is reflected in Table 6.1, where one can see that the percentage of surviving events after the geometry cut is half of what was achieved with the TXS neutrino.

The 50% and 90% correction values calculated with 100 resimulations are 18.95 and 87.33, respectively. The cumulative distribution of the -2ΔLLH values is included in Appendix C (Figure C.1). The distribution of resimulated events around the true direction is shown in Figure 6.6, along with the 90% uncertainty contours obtained with the IC160427A resimulations and with the dedicated resimulations of the Bran Stark event. The distance from the simulated to the reconstructed directions seems to be shifted and does not match the shape of the likelihood landscape of the Bran Stark neutrino. However, the individual reconstructed skymaps also show an elongated shape, as can be seen in Figure C.4.

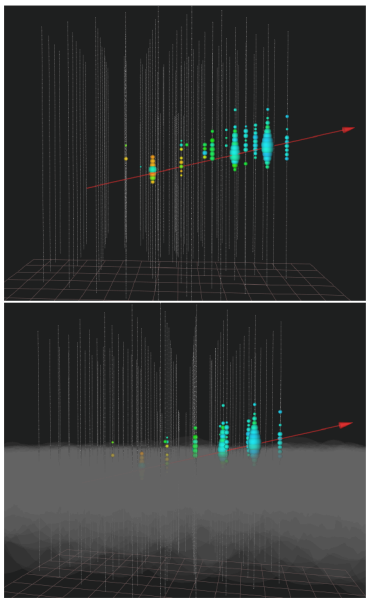

Figure 6.5: Event views of the IC191001A (Bran Stark) neutrino event, without showing the dust layer (top panel), and with the dust layer shown in grey (bottom panel).

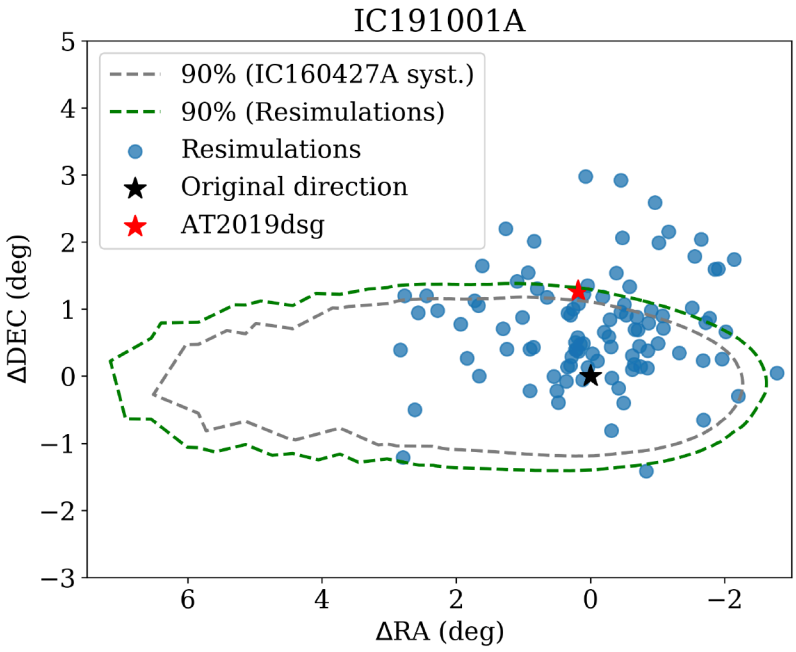

Figure 6.6: Error contours at 90% C.L. for the IC191001A (Bran Stark) neutrino, calculated with the scaling factor from the IC160427A resimulations (grey) and from the dedicated resimulations (green). The blue dots show the shift between the true (simulated) directions and the reconstructed directions of the resimulations. The black star represents the reconstructed direction of the real event. The red star shows the location of the candidate counterpart AT2019dsg.

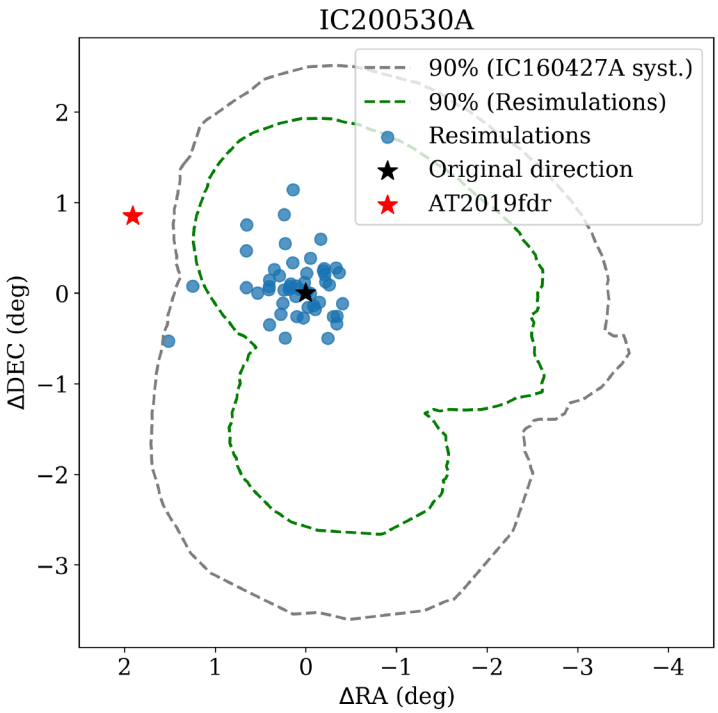

Figure 6.8: Error contours at 90% C.L. for the IC200530A (Tywin) neutrino, calculated with the scaling factor from the IC160427A resimulations (grey) and from the dedicated resimulations (green). The blue dots show the shift between the true (simulated) directions and the reconstructed directions of the resimulations. The black star represents the reconstructed direction of the real event. The red star shows the location of the candidate counterpart AT2019fdr.

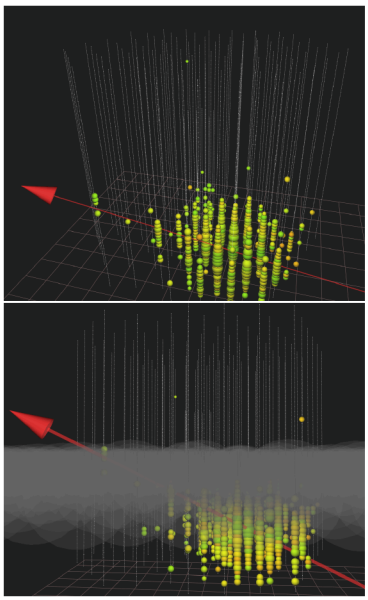

Figure 6.7: Event views of the IC200530A (Tywin) neutrino event, without showing the dust layer (top panel), and with the dust layer shown in grey (bottom panel).

IC200530A: The Tywin neutrino

As can be seen in Figure 6.7, this event also crosses the dust layer, at the end of the muon trajectory. Only a few hits were detected just before the muon exited the detector. Most of the simulations missed the required criteria, and a large number of resimulations was needed.

The studies stopped after the reconstruction of 51 resimulations (resulting in 50% and 90% correction values of 18.81 and 42.78, respectively, shown in Figure C.2), because their likelihood landscape was steeper than the one from the real event (see Figure 4.12). A randomly selected example of the likelihood scans can be seen in Figure 6.9, and 6 more in Figure C.5. The scans of the resimulations are better localized than the real event. This is reflected in Figure 6.8 as well, where the spread of angular distances for the resimulations does not follow the contours from the likelihood landscape of the real event. The use of correction values to scale the contours to account for systematic uncertainties is only valid under the assumption that the simulations are similar to the event itself, and thereby also the likelihood space of the reconstructions should be similar to the lanscape of the real event.

Visual inspection of the event views of the resimulations (examples can be seen in Figure 6.10, not corresponding to the scans in Figure 6.9 or Figure C.5) showed that, although the main deposition of energy occurred before the dust layer as in the real event, there is more light in the dust layer and in the last segment of the track than expected. This means that the resimulations can be better localized, since the lever arm is longer. Since the brightness of an event depends on the optical properties of the ice, the next step was to study the variations that were included in the ice model parameters during the lepton and photon propagation with SnowStorm.

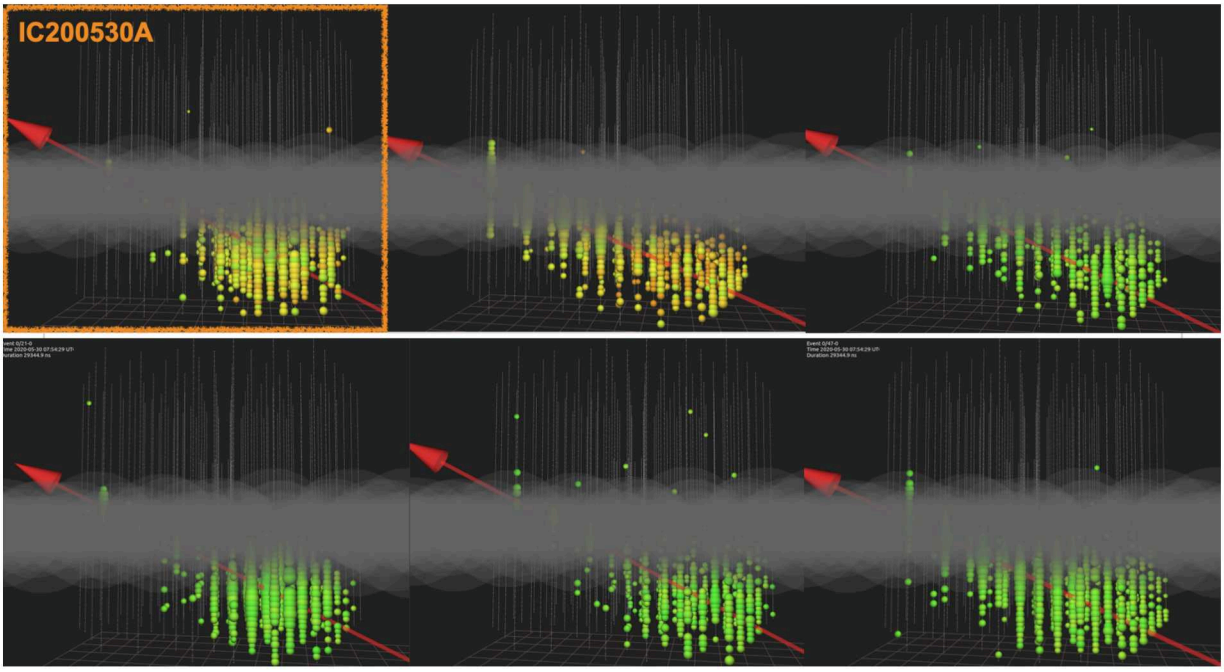

Figure 6.10: Event views of 5 randomly selected IC200530A (Tywin) resimulations, with the real event marked with an orange square. The event views show the dust layer as the grey cloudy area. In the resimulations, more light is deposited in the dust layer or at the end of the track than in the real event, which can be seen by the number of DOMs (colored spheres) that detected photons.

Figure 6.11 shows the attenuation coefficient as a function of depth for 10 randomly selected events with different ice model realizations (with the *Full Systematics* parametrizations from Table 5.1) as colored curves, compared to the baseline model *SPICE 3.2.1* in black. The attenuation coefficient is given by the square root of the absorption coefficient times the effective scattering, which is defined as the average stopping point of the center of the Cherenkov photon cloud as it propagates through a medium [97]. The attenuation coefficient combines the effects of the scattering and absorption processes. As already mentioned in Section 5.1.2, the range for the parametrizations was chosen to match the available calibration data, and is expected to cover only reasonable variations. However, the attenuation coefficient shows a trend in the dust layer in most of the resimulations. This could be producing more light in the simulations than would be emitted by a real event. To study this potential issue was beyond the scope of this work, and it was communicated to other IceCube collaborators.

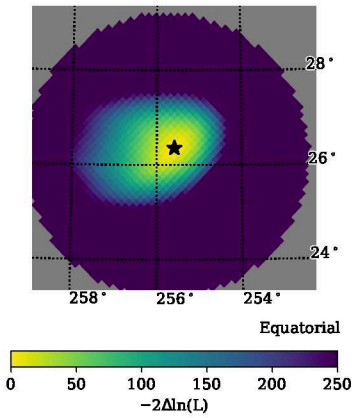

Figure 6.9: Likelihood scan of a randomly selected Tywin neutrino resimulation.

[97]: Aartsen et al. (2013), 'Measurement of South Pole ice transparency with the IceCube LED calibration system'

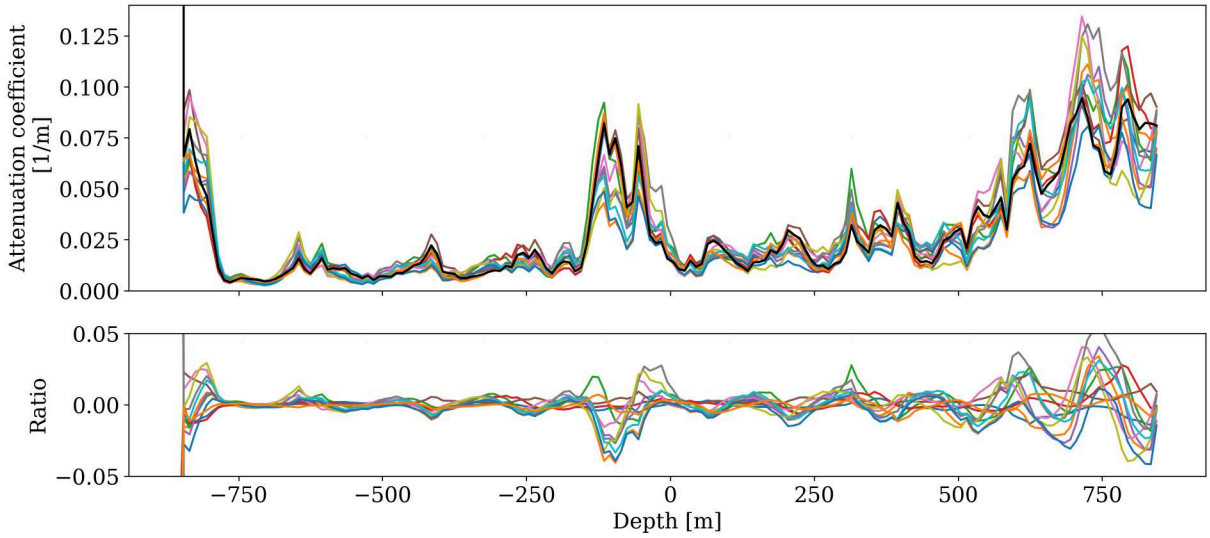

Figure 6.11: Attenuation coefficient as a function of depth for a randomly selected subset of IC200530A (Tywin) resimulations. In the top pannel, the colored curves show the variations introduced by the SnowStorm method, compared to the attenuation coefficient from the baseline ice model, *SPICE 3.2.1*, in black. The bottom panel shows the ratio between the ice model variations and the baseline model.

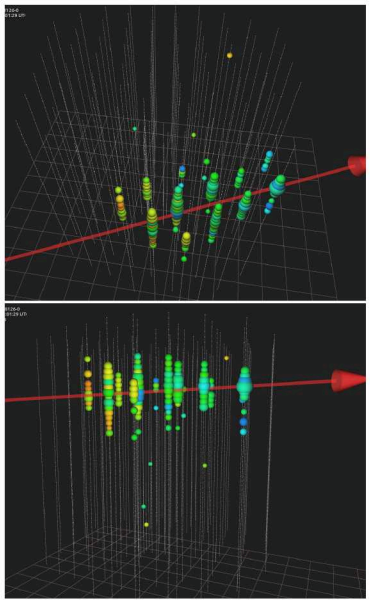

Figure 6.12: Event views of the IC191119A (Lancel) neutrino event. Top view of the event and side view are shown in the top and bottom panels, respectively. The dust layer is not shown.

[107]: Abbasi et al. (2021), 'A muon-track reconstruction exploiting stochastic losses for large-scale Cherenkov detectors'

IC191119A: The Lancel Neutrino

From the first 216522 resimulations, only 3 survived the cuts (0.02% survived the first one, 8% the second one). With a very short track length (see Figure 6.12), this event proved to be difficult to resimulate with the "similar events" method. Along with the other TDE neutrino resimulations, they sparked a discussion about the definition of similarity, which will be covered in Chapter 7. As with the Tywin neutrino resimulations, the study was brought to a stop due to the better results with the SplineMPE reconstruction method.

6.3 Comparison to other reconstruction methods

The resimulations presented here were reconstructed with other methods to compare the angular resolution of Millipede to less computationally expensive and simpler algorithms. The two implementations of SplineMPE introduced in Section 5.5 were applied to some of the samples by H. Niederhausen and G. Sommani. In addition, the Bran Stark neutrino resimulations were also reconstructed by S. Athanasiadou using another reconstruction algorithm called *SegmentedSpline* [107]. This method consists of a combination of the SplineMPE and Millipede methods, where the muon track reconstructed with SplineMPE is subdivided into segments, and in each segment a cascade-like light deposition is fitted with Millipede. This method aims to account for stochastic energy losses, and improves up to 20% the angular resolutions at high energies for through-going tracks when compared to SplineMPE.

As for the Golden Muons, the simulation of neutrinos and reconstruction work done with Millipede in this thesis allowed for the first time a direct comparison between the different methods with a relatively high

statistics sample. In every study case, the spread of reconstructions with SplineMPE was narrower than with Millipede, and clearly clustered around the reconstructed direction of the real event.

The TXS neutrino

The TXS event with the *Full Systematics* configuration was reconstructed with both implementations of SplineMPE. Figure 6.13 Panel (a) shows the spread of the shift in direction from the simulated to the reconstructed directions for Millipede, for SplineMPE in "max" configuration and for SplineMPE in the likelihood scan. The spread is narrower with both implementations of SplineMPE, with the likelihood scan version leading to a slightly better localization. This is visible in Figure 6.13 Panel (b), where the distribution of the angular distances (calculated as the angle between the two sightlines) for each resimulation between reconstructed and simulated directions is presented. The two SplineMPE methods result in almost the same angular resolution, since they only differ in the implementation. Both reconstruct 90% of the events within ~ 0.3 deg of their original direction, while the 0.9 percentile for Millipede is located at 0.94 deg.

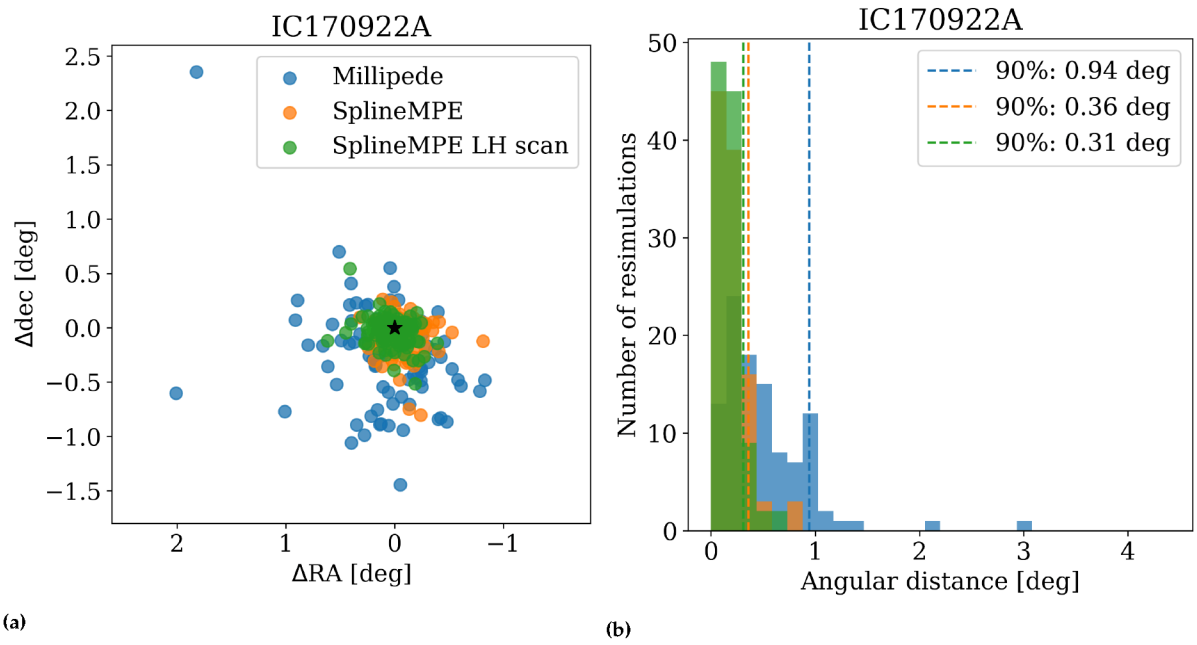

Figure 6.13: Comparison of reconstruction methods for the TXS event. Panel (a): the data points show the shift between the true direction of the resimulations and their reconstructed values, using Millipede (blue), SplineMPE with the "max" configuration (orange) and SplineMPE in a likelihood skyscan (green). Panel (b): angular distance between reconstructed and simulated directions, calculated as the angle between the two sightlines, for the same reconstruction methods as in Panel (a).

The Bran Stark neutrino

A similar trend is observed for the Bran Stark neutrino, see Figure 6.14. SplineMPE leads to a better angular resolution in both configurations, with the likelihood scan achieving again a slightly better result. The 90% percentile of SplineMPE is in both cases of the order of 1 deg, while for Millipede it is more than double that value.

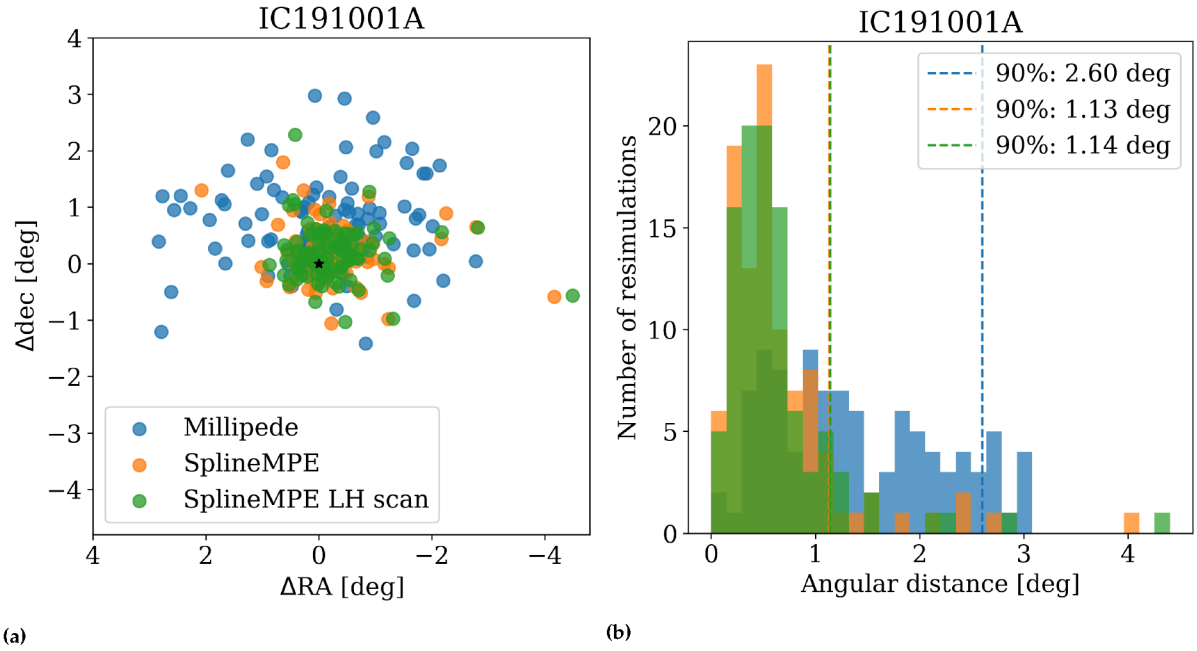

Figure 6.14: Comparison of reconstruction methods for the Bran Stark event. Panel (a): the data points show the shift between the true direction of the resimulations and their reconstructed values, using Millipede (blue), SplineMPE with the "max" configuration (orange) and SplineMPE in a likelihood skyscan (green). Panel (b): angular distance between reconstructed and simulated directions, calculated as the angle between the two sightlines, for the same reconstruction methods as in Panel (a).

The Bran Stark neutrino was also reconstructed with SegmentedSpline. Due to software incompabilities, only 50 out of the 100 resimulations could be studied. The results, shown in Figure 6.15, are very similar to the SplineMPE reconstruction, included in the figure for comparison. The 0.9 percentile is at 1.64 deg, and some events are poorly localized, with a shift of almost 8 deg, which is not observed with the other reconstruction methods. This served as a test for SegmentedSpline applied to a high-energy neutrino sample, but it was not considered an option for the next generation of the Realtime Program. This method is not as well established and maintained as the other algorithms, requires more computing resources than SplineMPE, and does not perform significantly better at this stage.

The Tywin neutrino

Lastly, the SplineMPE "max" configuration was applied to the 51 available Tywin resimulations. Even though the simulated events did not resemble the original event, they can be used as a benchmark sample. Again, SplineMPE delivers a good angular resolution, as can be seen in Figure 6.16. SplineMPE reconstructs 90% of the studied events within 0.33 deg of their original direction, while Millipede has a wider spread of angular distances, and its 0.9 percentile is at 0.77 deg.

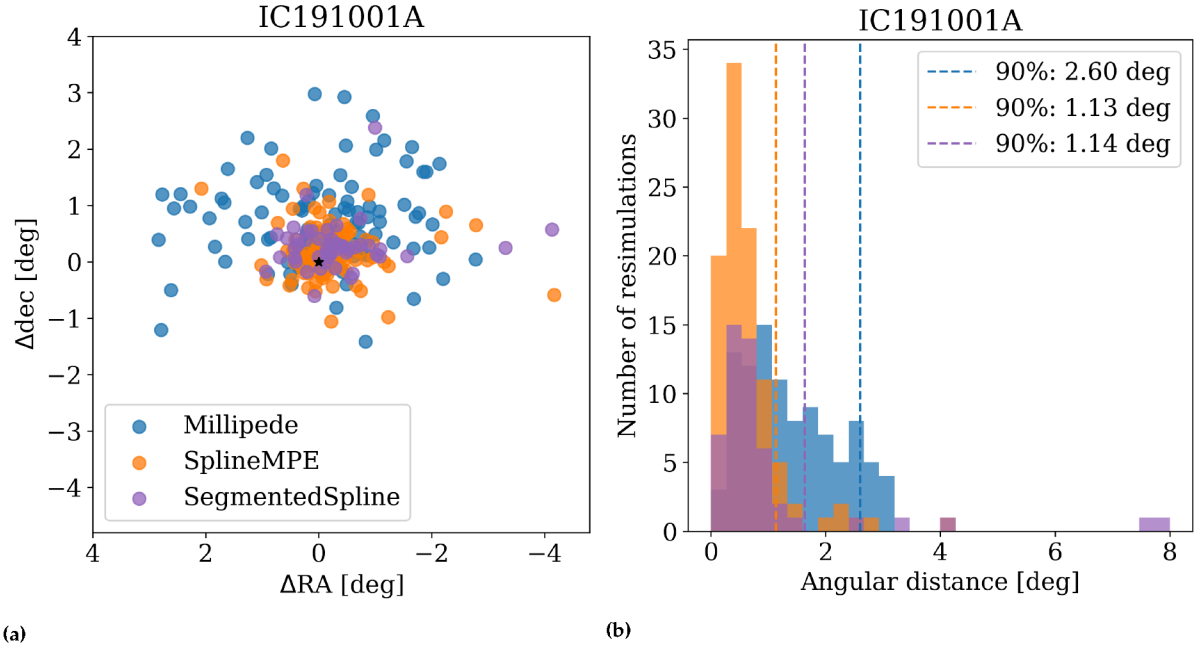

Figure 6.15: Comparison of reconstruction methods for the Bran Stark event. Panel (a): the data points show the shift between the true direction of the resimulations and their reconstructed values, using Millipede (blue), SplineMPE with the "max" configuration (orange) and SegmentedSpline (purple). Panel (b): angular distance between reconstructed and simulated directions, calculated as the angle between the two sightlines, for the same reconstruction methods as in Panel (a).

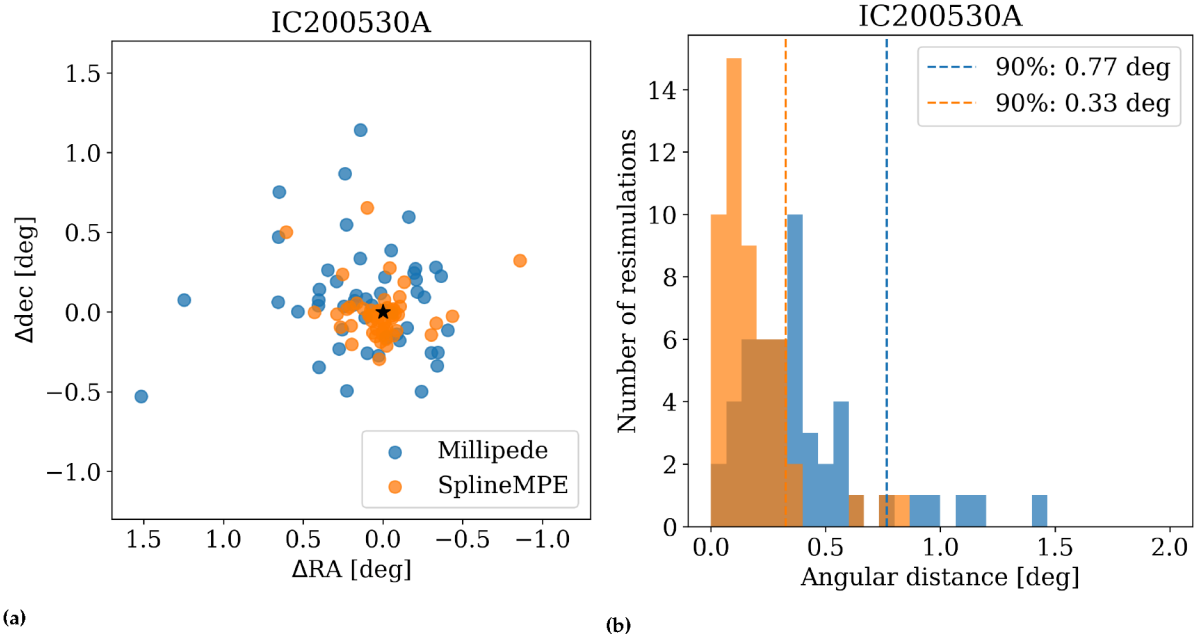

Figure 6.16: Comparison of reconstruction methods for the Tywin event. Panel (a): the data points show the shift between the true direction of the resimulations and their reconstructed values, using Millipede (blue) and SplineMPE with the "max" configuration (orange). Panel (b): angular distance between reconstructed and simulated directions, calculated as the angle between the two sightlines, for the same reconstruction methods as in Panel (a).

Path forward 7

7.1 *Finding (track) reco* project . 81
7.2 New resimulation scheme . 82
7.3 New candidates to the realtime reconstruction method 83
7.4 Outlook 85

The results from the Golden Muons study and the resimulation of alerts, presented in Chapter 5 and Chapter 6, have proven that the reconstruction method used in IceCube's Realtime Program does not provide the expected coverage of the uncertainty region of the events. Moreover, the performance is comparable to computationally less expensive, faster and simpler algorithms. A working solution for IceCube's Realtime Program is needed soon, while we work on fully understanding the track reconstruction. These are two separate goals, and we should not prioritize one over the other. The problem should not persist until we find the definite solution, since many studies rely on the reconstucted parameters that are constantly being released. We should find an intermediate fix and implement it while we work towards a reconstruction method that is well understood and robust against systematic uncertainties. In either case, any potential solution must prove that it works for individual, high-energy tracks, which are the object of interest for follow-up studies and multimessenger astronomy, and not just on average on an ensemble of low-to-high energy events.

Parts of this Chapter were presented at the *International Cosmic Ray Conference (ICRC) 2023* by the author of this thesis and collaborators [136–138].

[136]: Abbasi et al. (2023), 'Towards a more Robust Reconstruction Method for IceCube's Realtime Program'
[137]: Abbasi et al. (2023), 'Search for High-Energy Neutrinos from TDE-like Flares with IceCube'
[138]: Abbasi et al. (2023), 'Approximating New Ice Models with B-splines for Improved IceCube Event Reconstruction: Application to Cascades and Tracks'

7.1 *Finding (track) reco* project

The *Finding (track) reco* project was born in collaboration with other IceCube members to develop the criteria to benchmark any candidate algorithm for the angular reconstruction method of track-like events used in the realtime program. Beyond that, it can also be applied to methods used in offline searches, to ensure a common threshold for all.

The basic element of this project is a dataset of simulated events that realisticly represent the realtime track alerts. This dataset is based on a previously simulated sample that was created to obtain the expected number of signal events at given energy and declination for the calculation of signalness (Equation 4.1). To form the dataset for this project, called the *realtime benchmark simulations*, 100 events that would pass the GFU selection were randomly selected from that previously simulated sample.

Then, each event was resimulated in the Golden Muons manner, i.e. only varying the photon propagation, both with the nominal ice model and with the SnowStorm variations. Three different ice models were considered: *SPICE MIE*, *SPICE 3.2.1* and *SPICE BFR-v2* (more details on Section 3.4). This would allow us to see if the improvement on the knowledge of the ice model has a bigger impact than the remaining uncertainty on the parameters. An improved version of the resimulation based on similarity is also being developed for this project and will be discussed in the following Section.

7.2 New resimulation scheme

To test the methods on real events, uncertainties have to be added on top of the "true" values, since these are unknown for real data, for which we can only have a best estimate from reconstruction. A resimulation based on similarity is therefore needed. The same process can be applied to the realtime benchmark simulations to validate the similarity definition. Such a resimulation process would also allow us to keep benchmarking the methods in the future, and building up a sample of realistic simulations of neutrino alerts. Moreover, in case of a strong hint of correlation between an alert event and an electromagnetic counterpart, dedicated contours could be produced easily.

A new scheme was designed to ensure that the events are always similar to the original event and simulated in a more efficient way. Instead of simulating the neutrino interaction and then applying a cut on the angular distance, the muon is directly simulated to be created on the original event's track and outside of the detector, 300 m away from the outer layer of strings, so that the light from the hadronic cascade at the interaction point does not reach the detector.

Then, the muon is propagated with the usual procedure. At this step, the energy losses of the muon in the detector are fixed, and they are used as a proxy for the deposited charge as a function of the distance traveled. The simulated track is divided into segments, and the energy lost in each segment is obtained from the Monte Carlo truth. For the original event, the reconstructed track is also divided into segments, and the energy deposited in each segment is calculated with the method *TruncatedEnergy* [88] (introduced in Section 4.2.1).

[88]: Aartsen et al. (2014), 'Energy Reconstruction Methods in the IceCube Neutrino Telescope'

For each segment, the ratio of measured deposited energy to simulated energy is calculated. The metric to establish if two events are similar is the logarithm of the ratio for the segment i with the largest ratio, $M = \max(\log_{10}(E_{\text{meas},i}/E_{\text{sim},i}))$. If $M < 1.5$, we conclude that the two events are similar (in this case, the resimulated event resembles the original muon) and we procede with the photon propagation and subsequent steps.

Figure 7.1 shows the first results of this new simulation scheme, applied to the Tywin neutrino by J. Necker. The top panel shows the deposited energy in each segment, defined from 0 to 8 along the direction of the track. The blue curves represent the resimulated events, which very closely follow the energy deposition of the real event (in black). The bottom panel shows the ratio between the simulated and the real data. The other neutrino alert events from Chapter 6 were cross-checked or resimulated again with this scheme, and the results are presented in [137].

[137]: Abbasi et al. (2023), 'Search for High-Energy Neutrinos from TDE-like Flares with IceCube'

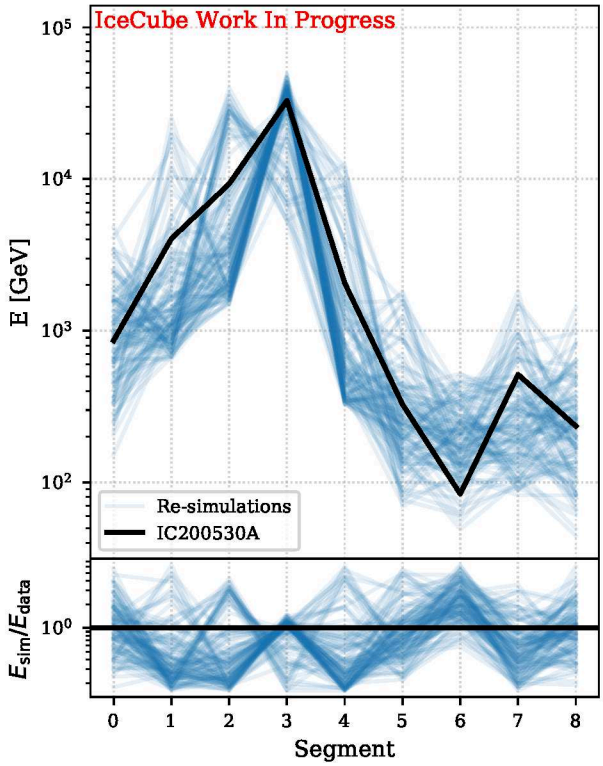

Figure 7.1: Energy depositions in segments along the muon track for the Tywin event (black line) and the resimulations (in blue) with the new scheme. From [137].

7.3 New candidates to the realtime reconstruction method

The task of solving the realtime reconstruction problem was handed over from the author of this thesis to other IceCube collaborators, and the two main options are summarized in this Section. At the time of writing this thesis, a decision about which one will be implemented has not yet been made.

7.3.1 Likelihood skyscan with SplineMPE

As already introduced in previous Chapters, SplineMPE with the likelihood scan implementation has proven to be reliable and has delivered good angular resolutions for the Golden Muons and the resimulations of alerts at a fraction of the cost of Millipede. This method was applied to the realtime benchmark simulations, and the distribution of the -2ΔLLH values between the best-fit positions and the simulated directions were compared to the χ^2 distribution that Wilks' theorem predicts [136]. The comparison was done with a two-sampled Kolmogorov-Smirnoff (KS) [108] test, and the p-values are shown in Figure 7.2. For 56% of the events, the -2ΔLLH and the χ^2 distributions are compatible, meaning that one could derive error contours directly from the likelihood landscape that the reconstruction method produces. For the rest, studies are on-going, which involve improving the algorithm or creating contours by following the procedure explained in Chapter 5.

[136]: Abbasi et al. (2023), 'Towards a more Robust Reconstruction Method for IceCube's Realtime Program'

[108]: Kolmogorov (1933), 'Sulla determinazione empirica di una legge di distribuzione.'

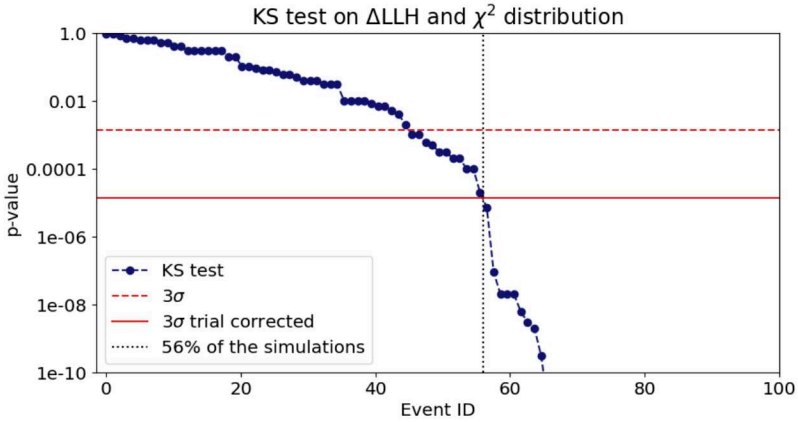

Figure 7.2: Results from the likelihood scan implementation of SplineMPE applied to the realtime benchmark simulations. The data points show the p-value of the KS test comparing the distribution of the 100 -2ΔLLH values of each resimulated event and the χ^2 distribution. Adapted from [136].

The results with the other ice models used in the simulation (which are in all cases more up to date than the ice model used for the reconstruction) are very similar to one another, hinting at the fact that the systematic uncertainties on the ice parameters might not be so relevant for SplineMPE as the location of the track within the detector.

7.3.2 Improved Millipede

The other option is to implement all possible improvements to the Millipede reconstruction method, since it should be more precise as it uses more of the available information [138]. One of the most relevant changes in this updated version of Millipede is to include the improvements in cascade modeling [139] for the track reconstruction, since the muon energy losses in Millipede are reconstructed as a series of cascades. These reflect the elevation change in the ice layers in the (x, y)-plane, called ice tilt, which affects the depth dependency of the scattering and absorption coefficients. Another difference in this version is that it only includes a sparse array of unhit DOMs in the reconstruction, instead of all of the unhit DOMs. This preserves the information of a lack of detection, while accelerating the process. Other optimizations have been applied, such as a better vertex seed calculation and fine-tuning the time binning of the hits.

Figure 7.3 shows the cumulative distribution of the -2ΔLLH values for a subsample of the realtime benchmark simulations reconstructed with this updated version of Millipede in colored curves, compared to the cumulative χ^2 distribution in black. There are still big variations in the -2ΔLLH values from one event to another, but it nevertheless shows an improvement over the Millipede algorithm currently in use in the realtime program, where the 50% and 90% containment values are at 22.4 and 64.2.

[138]: Abbasi et al. (2023), 'Approximating New Ice Models with B-splines for Improved IceCube Event Reconstruction: Application to Cascades and Tracks'

[139]: Yuan (2023), 'Detecting neutrinos in IceCube with Cherenkov light in the South Pole ice'

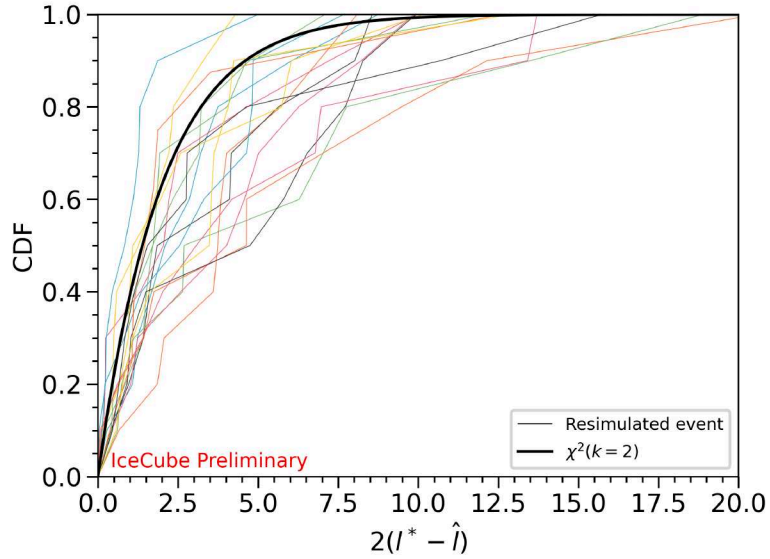

Figure 7.3: Results from the new version of Millipede applied to a subset of the realtime benchmark simulations. The curves are the cumulative distribution of the -2ΔLLH values of the resimulations and the χ^2 distribution, in colors and in black, respectively. From [138].

7.4 Outlook

The work that has been presented in these Chapters was developed throughout the duration of this thesis. Even though the original plan was not completed due to the underperformance of Millipede compared to other reconstruction methods, this decision was only possible thanks to the simulation and reconstruction of events done by the author of this thesis. Before this work, a systematic study of the resolution and coverage of Millipede for high-energy neutrinos has never been done. In both samples of the Golden Muons and the resimulations of alerts, scaling the contours from Wilks' theorem by the fixed factor derived from the IC160427A resimulations leads to error contours with the wrong confidence level uncertainty.

Either option of the two discussed here constitutes an improvement over the current algorithm, although more checks need to be conducted to assure that the coverage is correct. Once the new realtime angular reconstruction method is decided, the alert events in the IceCat-1 catalog will be reconstructed again and an updated version will be released.

Search for correlations of neutrino alert events and candidate sources

Active Galactic Nuclei as neutrino sources

8

An Active Galactic Nucleus (AGN) is the central part of a galaxy that contains a supermassive black hole (SMBH) at its center, whose accretion of material is powerful enough to emit electromagnetic radiation. While all galaxies are believed to contain a SMBH in their center, only 5% to 10% of them are considered active due to accretion [140]. AGNs are promising source candidates of high-energy neutrinos, since they might be capable of accelerating protons and other nuclei up to relativistic speeds, and are surrounded by radiation fields and matter, where those protons can interact in pp and $p\gamma$ interactions [141]. In this Chapter, the structure of AGNs and their classification are introduced, and an overview of the state-of-the-art analyses searching from neutrino emission from different classes of AGNs is given.

8.1 Structure of an AGN 89
8.2 Classification of AGNs . . . 90
8.3 Gamma-bright blazars as neutrino sources 91
8.4 Other radio-loud AGNs as neutrino sources 94
8.5 Radio-quiet AGNs as neutrino sources 96

[140]: Peterson et al. (2003), *Quasars*

[141]: Murase et al. (2022), 'High-Energy Neutrinos from Active Galactic Nuclei'

8.1 Structure of an AGN

The elements of an AGN can be seen in Figure 8.1. The central *black holes* (BHs) which power AGNs are extremely massive, with 10^6 to 10^{10} times the solar mass $M_\odot$, and are called supermassive black holes. These are now believed to reside in the centers of most massive galaxies, which would only qualify as active if there is enough material supply for accretion. The high mass of the BH is needed to reach the high luminosities observed in AGNs without exceeding the *Eddington luminosity* (or Eddington limit). Accretion is the main process that can efficiently convert the potential and kinetic energy of the accreting material into radiation [142]. The bolometric luminosity produced by accretion is given by

$$L_{\rm bol} = \eta \dot{M} c^2, \tag{8.1}$$

where $\dot{M}$ is the mass accretion rate and η is the efficiency of the convertion of accretion into emission, and depends on the accretion model assumed [142]. The canonical value is $\eta = 10\%$, although studies show that for many AGNs it must be even smaller [143]. The mass of the BH increases over time, and after n years of accreting material becomes

$$M_{\rm BH} \simeq M_0 \exp(\delta n), \tag{8.2}$$

where M_0 is the starting mass of the BH, and δ is the fractional accretion rate per year, which depends on the already defined parameters as

$$\delta = 2.28 \times 10^{-9} \frac{L_{\rm bol}/L_{\rm Edd}}{\eta}. \tag{8.3}$$

The material that is closer to the SMBH slowly spirals inwards, gets compacted and forms an *accretion disk*. As the material falls onto the SMBH, it heats up and converts the gravitational potential energy to electromagnetic radiation, typically peaking in the optical-ultraviolet

Eddington luminosity

Eddington luminosity is the maximum luminosity a body can achieve for which the force of radiation is compensated by the force of gravity, acting in opposite directions. It depends on the mass M of the body and is given by
$L_{\rm Edd} \simeq 1.3 \times 10^{38} \frac{M}{M_\odot} \,{\rm erg\ s^{-1}}$

[142]: Beckmann et al. (2012), *Active Galactic Nuclei*

[143]: Ho (2009), 'Radiatively inefficient accretion in nearby galaxies'

region. Accretion disks are geometrically thin, optically thick structures in the subparsec scale. Above and below the accretion disk one finds the *corona*, which is comprised of hot material. In the corona, the photons emitted from the accretion disk can be scattered via Inverse Compton up to X-ray energies.

In some AGNs, about 10% of the total population, the accretion disk also produces two jets of highly collimated, relativistic particles. The jets emerge from close to the disk and go in opposite directions, nearly perpendicular to the plane of the disk. There are various theoretical models that explain jet production in AGNs, see [144] for an overview. Jets are brightest in the radio band due to synchrotron radiation, but they emit across all wavelengths.

[144]: Blandford et al. (2019), 'Relativistic Jets from Active Galactic Nuclei'

The material that surrounds the SMBH can also be a source of obscuration [145, 146]. According to the AGN Unification Model [147] (see Section 8.2), this obscuring material takes the form of a geometrically and optically thick *torus*, with a diameter of up to 10 pc.

[145]: Zhao et al. (2021), 'The properties of the AGN torus as revealed from a set of unbiased NuSTAR observations'
[146]: Hickox et al. (2018), 'Obscured Active Galactic Nuclei'
[147]: Antonucci (1993), 'Unified models for active galactic nuclei and quasars.'

From the observation of AGNs, two more regions are defined. In the spectrum of AGNs, there are time-variable emission lines that are redshifted, with Doppler widths of 10^3 to 10^4 km s^{-1} [142]. These are formed in a region with high-density fast-moving gas clouds called *Broad Line Region* (BLR), located close to the SMBH and surrounded by the torus. Along with those lines, in many cases narrower lines are observed ($\sim 10^3$ km s^{-1}), coming from a larger region that is separated kinematically from the BLR, called *Narrow Line Region* (NLR). The NLR is composed of ionized gas clouds located outside of the torus and extending up to the scale of the AGN host galaxy.

[142]: Beckmann et al. (2012), *Active Galactic Nuclei*

8.2 Classification of AGNs

Historically, many classes of AGNs have been discovered and defined based on their observed properties. An *AGN Unification Model* was developed to try to explain all the different subclasses of AGNs by the same underlying model. In 1993 the most simplified version of this model was suggested [147], which is still valid to this day. It states that there are two basic types of AGNs: *radio-quiet* and *radio-loud*. Each type defines a range in intrinsic luminosity, and most of the other properties of AGNs are due to the orientation of the accretion disk plane with respect to the observer. A summary of the subclasses that are presented in this Section is shown in Figure 8.1.

[147]: Antonucci (1993), 'Unified models for active galactic nuclei and quasars.'

Within this unified model, radio-loud AGNs are characterized by the presence of relativistic jets and are further classified as *blazars*, if the radiation beam is pointing towards the Earth, or as *radio galaxies*, for viewing angles $\gtrsim 15°$ [148]. Blazars exhibit high variability due to the nature of their electromagnetic emission, and emit in all wavelengths, from radio frequencies to gamma rays at very high energies above 1 TeV. They are classified into *BL Lac* and *Flat Spectrum Radio Quasars* (FSRQ) based on the width of the emission lines. A (somewhat arbitrary) threshold of 5 Å is established, blazars with weak emission lines below that value are BL Lacs, and those with stronger, broad emission lines are FSRQs.

[148]: Urry et al. (1995), 'Unified Schemes for Radio-Loud Active Galactic Nuclei'

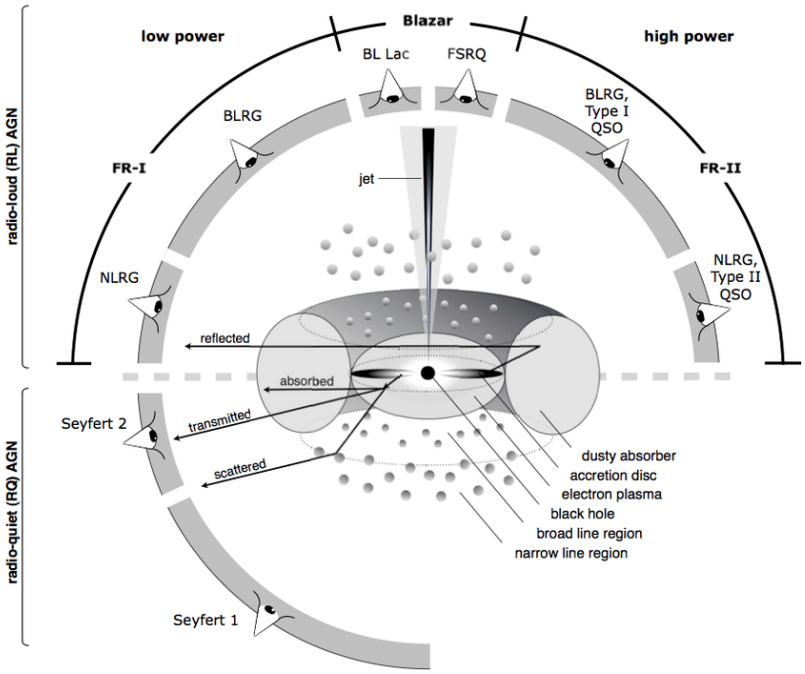

Figure 8.1: Schematic representation of the AGN Unification Model. The different observed properties of each class of AGN depend on the viewing angle and the presence of a jet. The figure also shows the elements of the structure of an AGN. From [142].

Radio galaxies are also classified based on their morphology, which is determined by the appearance of their radio emission [149]. If the majority of the emission is concentrated and located near the core, the galaxy is from the low-luminosity Fanaroff-Riley I (FR-I) class. On the other hand, in high-luminosity FR-II objects, most of the emission comes from the end of the extended emission, and the structure is dominated by the radio lobes. Therefore, FR-II are brighter than FR-I, which serves as a proxy for the trend of the jet luminosity as well.

[149]: Fanaroff et al. (1974), 'The morphology of extragalactic radio sources of high and low luminosity'

Based on the viewing angle, there are further categories for the radio-quiet AGNs. When the AGN is viewed edge-on, the emission lines from the BLR are typically obscured by the torus. In that case, the active galaxy is classified as a *Seyfert 2* galaxy [150] or narrow-line radio galaxy (NLRG) if it also contains a jet. If broad emission lines are present, the active galaxy is classified as a *Seyfert 1* galaxy or a broad-line radio galaxy (BLRG).

[150]: Seyfert (1943), 'Nuclear Emission in Spiral Nebulae.'

8.3 Gamma-bright blazars as neutrino sources

In order to produce a significant flux of high-energy neutrinos in a source, the following conditions must be met: first, there must be acceleration of ions (protons and nuclei) to high energies, at a rate higher than the energy loss rate; second, there must be a target medium of sufficient density. Based on recent multimessenger studies, the particle intensities of neutrinos, high-energy gamma rays and cosmic rays are comparable, suggesting that they are physically connected. However, if neutrinos are produced in hadronic processes as discussed in Chapter 2, the high-energy gamma rays would interact with the necessary photons in the target material and appear at lower energies. This is in agreement

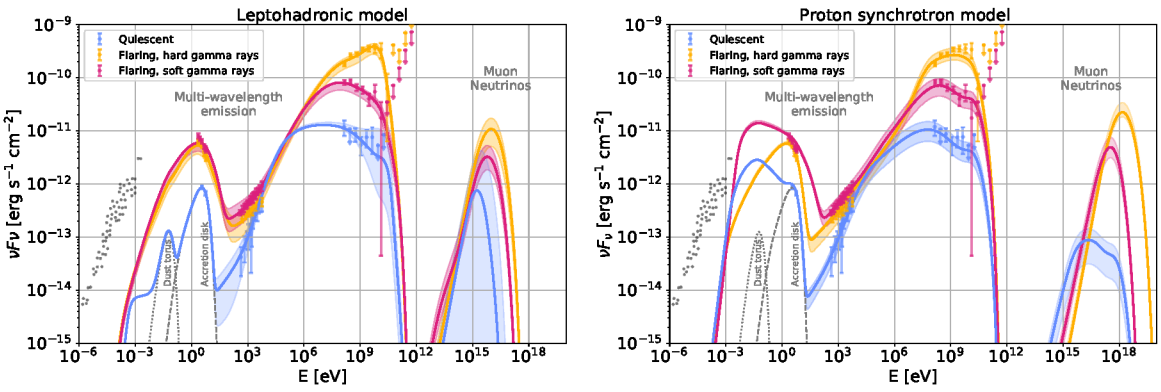

Figure 8.2: Spectral Energy Distribution of the blazar PKS 1502+106, that was contained within the 90% error region of the neutrino alert IC190730A. Two models for the gamma-ray hump are shown. The plot also shows the expected muon neutrino flux, assuming different states of the blazar. From [116].

with the observed fluxes of neutrinos and gamma rays by IceCube and *Fermi*-LAT [151].

Blazars have been one of the first suggested neutrino source candidates, since their highly collimated relativistic jets satisfy the acceleration condition. The Spectral Energy Distribution (SED) of blazars has a two-hump component. The lower-frequency component is due to the acceleration of relativistic electrons in the jet that emit synchrotron radiation. The hump at higher frequencies can be explained in leptonic or hadronic scenarios. In the leptonic case, it is attributed to Compton up-scattering of the same electrons, while in hadronic models the gamma-ray peak is produced in proton synchrotron emission or proton-induced electromagnetic cascades through pion decay. If the SED is explained by the hadronic scenario, or by a leptohadronic scenario that combines leptonic and hadronic elements, neutrino emission is also expected from the same processes that produce gamma rays. An example of the SED of PKS 1502+106, introduced in Chapter 4 as a potential counterpart of a neutrino alert event, is shown in Figure 8.2.

There are various theoretical models that explain the relation between the neutrino flux and the gamma-ray flux. Many assume a linear correlation, where the overall brightness of the blazar dictates the neutrino emission [152, 153]. In other models, the neutrino production and detection probability depend on the instantaneous gamma-ray flux at the neutrino detection time [62]. In the source frame, the energies ε follow the relation $\langle \varepsilon_\nu \rangle \sim \langle \varepsilon_\pi \rangle / 4 \sim \varepsilon_p / 12$, with neutrino energy at Earth being $E_\nu = \varepsilon_\nu / (1+z)$, where z is the redshift of the source [154]. The spectral index of the observed gamma rays may differ from that at the source, as well as from the neutrino spectral index, since the photons can interact further in the source and be reprocessed to lower energies, leading to softer spectra. Despite these differences in spectral indices, the total energy can still be related.

The hypothesis that blazars are the sources of the detected high-energy neutrino flux has been extensively tested using IceCube data. A recent result states that the blazars from the Third Catalog of Hard *Fermi*-LAT Sources (3FHL) [155] can only account for 8.6% to 11.0% of the average astrophysical muon neutrino flux in the neutrino energy range from 40 TeV to 3.5 PeV, when a direct correlation to the integrated gamma-ray

[151]: Murase et al. (2016), 'Hidden Cosmic-Ray Accelerators as an Origin of TeV-PeV Cosmic Neutrinos'

[152]: Murase et al. (2014), 'Diffuse neutrino intensity from the inner jets of active galactic nuclei: Impacts of external photon fields and the blazar sequence'

[153]: Petropoulou et al. (2015), 'Photohadronic origin of γ-ray BL Lac emission: implications for IceCube neutrinos'

[62]: Aartsen et al. (2018), 'Multimessenger observations of a flaring blazar coincident with high-energy neutrino IceCube-170922A'

[154]: Stecker (1979), 'Diffuse fluxes of cosmic high-energy neutrinos.'

[155]: Ajello et al. (2017), '3FHL: The Third Catalog of Hard Fermi-LAT Sources'

flux is assumed [156]. Other analyses, however, have found a significant spatial correlation between blazars from 5BZCat and public neutrino data sets released by IceCube [157, 158], where all the blazars contribute equally to the analyses. This claim has been challenged in other studies, also using public IceCube data [159].

The lower end of the neutrino energy spectrum detected by IceCube is dominated by atmospheric muons and neutrinos, and a possible signal might be indistinguishable from this overwhelming background. Therefore, other studies have focused on samples of high-energy neutrinos. Recently, a 3.23σ evidence that high-energy neutrinos are correlated with the positions of *Fermi*-LAT blazars was found [125]. This indicates that, although blazars cannot account for the total astrophysical neutrino flux, and the gamma-bright blazars do not dominate, they could produce a substantial part of the neutrino flux. This hypothesis is tested in this thesis with a focus on high-energy neutrinos, as will be shown in Chapter 9 and Chapter 10.

[156]: Huber (2020), 'Multi-Messenger Correlation Study of Fermi-LAT Blazars and High-Energy Neutrinos Observed in IceCube'

[157]: Buson et al. (2022), 'Beginning a Journey Across the Universe: The Discovery of Extragalactic Neutrino Factories'

[158]: Buson et al. (2023), 'Extragalactic neutrino factories'

[159]: Bellenghi et al. (2023), 'The correlation between high-energy IceCube neutrinos and 5BZCAT blazars'

[125]: Giommi et al. (2020), 'Dissecting the regions around IceCube high-energy neutrinos: growing evidence for the blazar connection'

8.3.1 TXS 0506+056

As introduced in Chapter 4, the first evidence of an astrophysical neutrino source was the blazar TXS 0506+056, which was spatially coincident with the neutrino alert event IC170922A [62]. The source was located inside of the error region of the neutrino, at a distance of 0.1 deg from its best-fit reconstructed direction.

[62]: Aartsen et al. (2018), 'Multimessenger observations of a flaring blazar coincident with high-energy neutrino IceCube-170922A'

The IC170922A alert was followed-up by telescopes across a wide range of wavelengths. The detection of a factor of 6 increase in the gamma-ray flux of the blazar TXS 0506+056 was reported soon after by the *Fermi*-LAT Collaboration [160]. Not only the gamma-ray activity in the GeV range was enhanced, but also at higher energies, with detected photons of up to 400 GeV coming from the source direction [161].

[160]: Tanaka et al. (2017), 'Fermi-LAT detection of increased gamma-ray activity of TXS 0506+056, located inside the IceCube-170922A error region.'

[161]: Mirzoyan (2017), 'First-time detection of VHE gamma rays by MAGIC from a direction consistent with the recent EHE neutrino event IceCube-170922A'

To assess the probability to obtain a correlation between a neutrino similar to IC170922A with a flaring blazar by chance, the 28-day binned gamma-ray light curves above 1 GeV from 2257 extragalactic *Fermi*-LAT sources were used, along with simulated neutrino alerts. Several models for the correlation of the neutrino and gamma-ray fluxes are tested, all of which consider that the same hadronic interactions that produce high-energy neutrinos in the source also produce at least part of the gamma-ray flux. Three hypotheses were tested: first, a linear correlation to the instantaneous high-energy gamma-ray flux; second, a linear correlation to the very-high-energy gamma-ray flux; and third, a temporal correlation with the variability in the gamma-ray light curve. The chance coincidence in each of these three analyses, with corrections made to account for the multiple tests, is rejected at the 3σ level [62].

After the detection of the IC170922A neutrino, an archival search for neutrino emission from TXS 0506+056 was performed [63]. 9.5 years of data were analyzed, looking for a temporal clustering of events around the source position. An excess of 13 ± 5 neutrinos with respect to the expected background was found between September 2014 and March 2015, with a neutrino flare duration of 158 days. The final significance was 3.5σ, accounting for all the time windows tested. The second most significant time window includes the IC170922A event, but no other event

[63]: Aartsen et al. (2018), 'Neutrino emission from the direction of the blazar TXS 0506+056 prior to the IceCube-170922A alert'

contributes significantly to the result. Based on these measurements, the neutrino energy flux from the source has a calculated index of $\gamma = 2.1 \pm 0.2$.

During this neutrino flare, TXS 0506+056 was in a quiescent state, with no enhanced gamma-ray activity. This seemingly contradicting picture has been studied in detail. The leptohadronic modelling of the source, motivated by the observed X-ray emission, predicts more than 0.14 neutrino events with $E > 120\,\text{TeV}$ in the half-year period of gamma-ray flare activity, which implies a probability < 10% of detecting such a neutrino [162]. This is still consistent with a signal correlation after correcting for the Eddington bias expected for a single astrophysical neutrino detection [163]. However, theoretical modelling of the neutrino flare of 2014-2015 along with the quiescent state of TXS 0506+056 has proven to be more challenging, with no conclusive solution so far [164, 165].

[162]: Gao et al. (2018), 'Modelling the coincident observation of a high-energy neutrino and a bright blazar flare'

[163]: Strotjohann et al. (2019), 'Eddington bias for cosmic neutrino sources'

[164]: Rodrigues et al. (2019), 'Leptohadronic Blazar Models Applied to the 2014–2015 Flare of TXS 0506+056'

[165]: Petropoulou et al. (2020), 'Multi-epoch Modeling of TXS 0506+056 and Implications for Long-term High-energy Neutrino Emission'

[166]: Halzen et al. (2019), 'On the Neutrino Flares from the Direction of TXS 0506+056'

[65]: Aartsen et al. (2021), 'IceCube-Gen2: the window to the extreme Universe'

One hypothesis is that TXS 0506+056 belongs to a subclass of blazars with shared characteristics, that produce neutrino flares once in 10 years. If this subset includes just 5% of the blazars, it can accomodate the neutrino flux measurements without overshooting it [166]. Measuring such a population of sources would require a larger neutrino telescope and more years of data to get the necessary statistics, so this question remains open to this day and could potentially be answered by a future generation of telescopes, such as IceCube-Gen2 [65].

8.4 Other radio-loud AGNs as neutrino sources

8.4.1 Cores of luminous AGNs

Blazar jets are not the only suggested candidate objects for neutrino emission. Neutrinos can also be produced in the accretion disk or the corona region, from the interaction of cosmic rays [167]. The neutrinos would be able to escape this optically thick region, but the GeV and TeV gamma rays would be absorbed and reemitted at lower energies. This motivated a search for neutrino emission from the cores of AGNs, for which all possible blazars in the selected samples were removed to search for neutrino emission from the cores and not the jets [168]. The neutrino flux in the analysis is assumed to be proportional to the accretion disk luminosity, which is in turn proportional to the soft X-ray flux.

[167]: Stecker et al. (1991), 'High-energy neutrinos from active galactic nuclei'

[168]: Abbasi et al. (2022), 'Search for neutrino emission from cores of active galactic nuclei'

The catalogs studied in this analysis were selected based on their radio and infrared luminosities. The radio-selected AGN catalog contains sources with a flux density above 10 mJy at 1.4 GHz. This cut removes most of the non-active star-forming galaxies, since luminous radio sources are usually AGNs, that emit synchrotron radiation in the accretion disk or the radio jets. The infrared wavelength is used to select AGNs that could be hidden from short-wavelength surveys because of reddening and obscuration by dust, which would reprocess the emission from the accretion disk into the infrared. The sources in each catalog were cross-checked with the *Fermi*-LAT 3LAC catalog to remove all gamma-ray blazars.

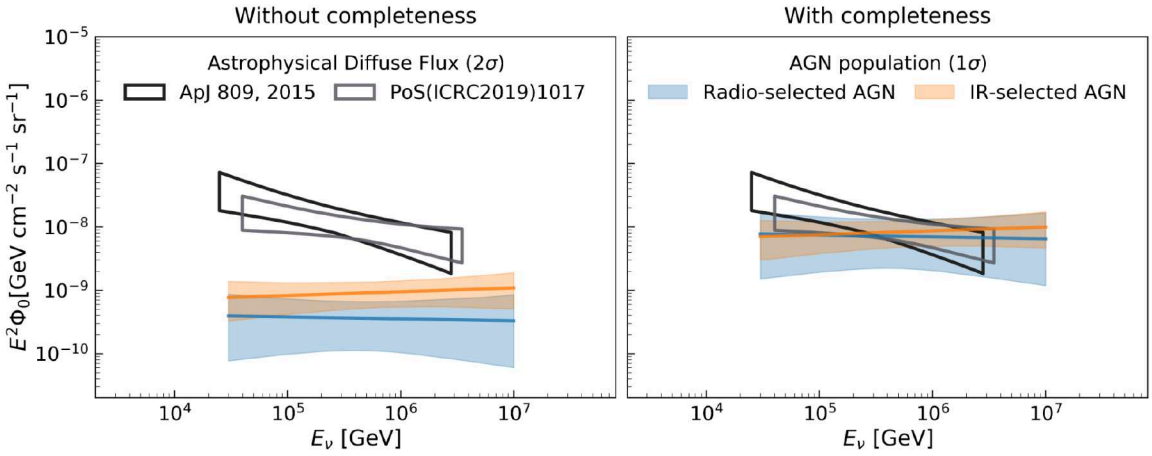

Figure 8.3: Neutrino energy spectrum for the emission in cores of radio-selected and infrared-selected AGNs. From [169].

With the infrared-selected catalog, the excess of neutrino signal events coincident with the position of the sources over the atmospheric background and isotropic neutrino flux is significant at the 2.83σ level [169]. Only the Northern sky was studied (dec ≥ -5 deg). Assuming a single power-law spectrum, the best-fit spectral index is 2.03 ± 0.14. The measured flux from the infrared-selected AGNs cannot account for all the astrophysical diffuse flux detected by IceCube. Assuming that this signal is genuine, and correcting for the unresolved sources that are not included in the catalog, the contribution of AGN cores to the observed neutrinos at 100 TeV can be between 27% and 100%. This is shown in Figure 8.3, with the fluxes calculated directly from the catalogs on the left panel, and the fluxes corrected for the completeness of the catalogs on the right.

[169]: Bradascio (2021), 'Searches for cross-correlations between IceCube neutrinos and Active Galactic Nuclei selected in various bands of the electromagnetic spectrum'

8.4.2 Radio-selected AGNs

Neutrinos produced in the central parsec-scale regions of AGNs are accompanied by gamma rays from the same interactions. However, the resolution of current gamma-ray detectors makes it challenging to directly associate gamma-ray sources with neutrinos. Radio observations provide a means to observe the parsec-scale base of the jet, which might be the origin of neutrino production. Owing to this possibility, one could use the very long baseline interferometry (VLBI) radio observations to resolve the central part of active galaxies and test for neutrino emission from the core. Multiple studies (including part of this thesis) have used the integrated VLBI flux densities from the Radio Fundamental Catalog (RFC)[1], from the Astrogeo[2] database, to search for neutrino production in AGNs.

Very long baseline interferometry

VLBI is a technique that combines the radio signals of an object from various radio telescopes to create a single observation, emulating a telescope with a size equal to the maximum distance between the telescopes.

In Ref. [126], sources selected from the 2019c version of the RFC catalog were correlated to a sample of 56 public high-energy neutrino events, most of them released as neutrino alerts. The selection criteria for the sources involve a minimum flux density integrated over VLBI images at 8 GHz of $S_{8\text{GHz}} \geq 150$ mJy. The sample at 8 GHz is the most complete in the RFC catalogs, that also includes measurements at 2.3, 5, 15 and 22 GHz wavelengths. The chance coincidence that the VLBI flux density of

1: http://astrogeo.org/rfc/

2: http://astrogeo.org/

[126]: Plavin et al. (2020), 'Observational Evidence for the Origin of High-energy Neutrinos in Parsec-scale Nuclei of Radio-bright Active Galaxies'

the sources coincident with the selected neutrinos is as high as observed is found to be 0.2%. A more detailed discussion of this publication can be found in Chapter 10, where their results are also cross-checked with the method developed in this thesis. Another 14 high-energy neutrinos were added in a later study [127], with an updated chance coincidence of 3×10^{-4} after correcting for the multiple tests.

[127]: Plavin et al. (2022), 'Growing evidence for high-energy neutrinos originating in radio blazars'

A follow-up analysis [170] searched for flares of neutrinos at lower energies in coincidence with the neutrinos from Ref. [127] that had a blazar counterpart. The chance probability using IceCube's public data [106] was calculated to be 3.6×10^{-4}.

[170]: Suray et al. (2023), 'Neutrino flares of radio blazars observed from TeV to PeV'

[106]: Abbasi et al. (2023), 'Constraints on Populations of Neutrino Sources from Searches in the Directions of IceCube Neutrino Alerts'

Motivated by the results of Ref. [126], the authors extended the analysis to a wider neutrino energy range using a public data set of IceCube neutrino events [171]. For the candidate sources, a more updated version of the RFC catalog (RFC 2020b) is used, and the sources are selected with a minimum flux density integrated over VLBI images at 8 GHz of $S_{8\mathrm{GHz}} \geq 150\,\mathrm{mJy}$ and a declination of dec > -5 deg. The neutrino sample that is used in this analysis is a skymap of p-values located on a grid. These values represent the probability that a clustering of events in a sky location is rising from background fluctuations. The logarithm of this p-value at the location of each AGN is used to study the significance of the correlation, which is finally calculated to be at 3σ level. The combination of this result with the previous one [126] leads to a final significance of 4.1σ.

[171]: Plavin et al. (2021), 'Directional Association of TeV to PeV Astrophysical Neutrinos with Radio Blazars'

A subsecquent analysis tested the same hypothesis, using a different public neutrino data set released by IceCube [172]. In this data release, instead of a p-value map, the reconstructed direction and energies of the individual events were published. In this study, they analyze the neutrino emission from individual sources and the overall contribution from AGNs from the RFC catalog, using the same version and selection criteria as Ref. [171]. However, none of the sources significantly emit high-energy neutrinos, and the final result combining all contributions is compatible with the background, in disagreement with what was found in Ref. [171].

[172]: Zhou et al. (2021), 'Search for high-energy neutrino emission from radio-bright AGN'

8.5 Radio-quiet AGNs as neutrino sources

Although the search for radio-loud AGNs as neutrino sources is well motivated by the intense luminosities and the extreme particle acceleration that occurs in them, radio-quiet AGNs are also of great interest for neutrino astronomy [173]. Models for neutrino production in Seyfert galaxies assume that the observed X-ray photons are produced via Compton scattering in the corona, which acts as a target for the neutrino production and the gamma-ray absorption [174, 175].

[173]: Kheirandish et al. (2021), 'High-energy Neutrinos from Magnetized Coronae of Active Galactic Nuclei and Prospects for Identification of Seyfert Galaxies and Quasars in Neutrino Telescopes'

[174]: Silberberg et al. (1979), 'Neutrinos as a Probe for the Nature of and Processes in Active Galactic Nuclei'

[175]: Yoast-Hull et al. (2013), 'Active Galactic Nuclei, neutrinos, and interacting cosmic rays in NGC 253 and NGC 1068'

In a recent study, IceCube found evidence of neutrino emission in the nearby Seyfert 2 galaxy NGC 1068, with a global 4.2σ significance [64]. There is an excess of 79^{+22}_{-20} muon neutrinos consistent with the direction of the source, which is 0.11 deg away from the best-fit position of the clustering. This analysis fits the spectral index for the neutrino flux at $\gamma = 3.2 \pm 0.2$, assuming an unbroken power law of the spectrum. The result is much softer than the best-fit diffuse astrophysical flux

[64]: Abbasi et al. (2022), 'Evidence for neutrino emission from the nearby active galaxy NGC 1068'

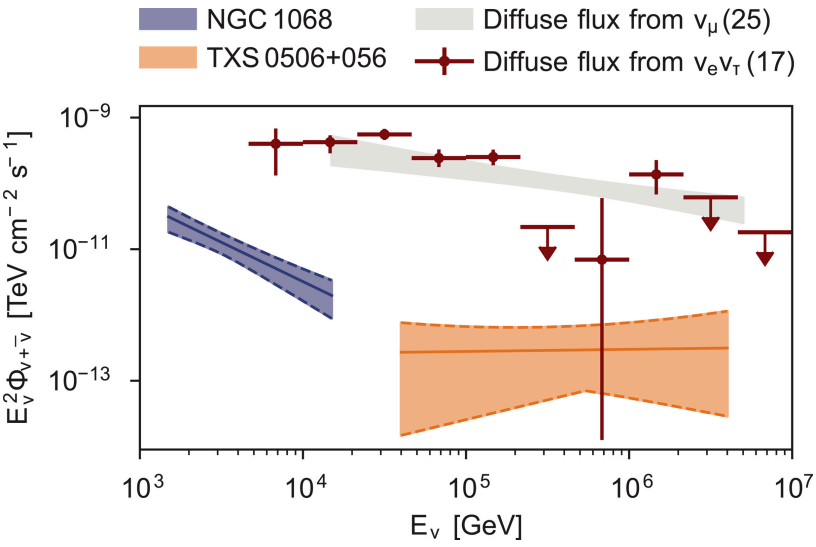

Figure 8.4: Neutrino fluxes multiplied by the energy squared for NGC 1068 (blue line), TXS 0506+056 (orange line) and diffuse neutrino background (brown data points and gray band), given for a single flavor of neutrinos and antineutrinos. Plot from [64], diffuse flux data from [177] and [178].

($\gamma_{\text{diff}} = 2.52 \pm 0.04$) [176] and the flux calculated for the neutrino flare of TXS 0506+056 ($\gamma_{\text{TXS}} = 2.1 \pm 0.2$), and is mainly driven by neutrinos from 1.5 to 15 TeV. NGC 1068 and TXS 0506+056 contribute only $\sim 1\%$ of the total diffuse flux in their respective energy ranges (shown in Figure 8.4). This indicates that there are at least two different populations of neutrino sources, given the variations in spectrum and distances between these two sources. These two populations could have orders of magnitude difference in density and luminosity [64].

[176]: Abbasi et al. (2023), 'Measurement of the astrophysical diffuse neutrino flux in a combined fit of IceCube's high energy neutrino data'

Motivated by this result, other analyses that search for correlations of Seyfert galaxies and neutrino data have been developed in IceCube, selecting sources in the Northern [179] and in the Southern [180] hemispheres. For the Northern hemisphere, the significance is below the 3σ threshold, while for the Sourthern hemisphere only sensitivies have been published so far. However, other analyses that use public IceCube data claim the discovery of Seyfert galaxies as neutrino sources [181]. The baseline assumption is that the expected neutrino flux from a Seyfert galaxy can be estimated using the neutrino signal of NGC 1068 as a template. Two sources (in addition to NGC 1068) are then expected to be detectable in 10 years of IceCube data, and they observe a high-significance excess of neutrinos coming from the direction of both, with a chance coincidence probability of 2.6×10^{-7}.

[179]: Abbasi et al. (2023), 'Searching for High-energy Neutrino Emission from Seyfert Galaxies in the Northern Sky with IceCube'

[180]: Abbasi et al. (2023), 'Search for Neutrino Emissions from Seyfert Galaxies in the Southern Sky using Track Events in IceCube'

[181]: Neronov et al. (2023), 'Neutrino signal from Seyfert galaxies'

9 Statistical analysis

9.1 Hypothesis testing 99
9.2 Stacking analysis 100
9.3 Analysis procedure 101

IceCube's neutrino alert events have been of great interest to the multimessenger community as they allow for prompt follow-up searches. The possibilities of such realtime analyses became obvious with the detection of the IC170922A alert in coincidence with a flare from the blazar TXS 0506+056 (more details in Chapter 4 and Chapter 8), but this has not been the only alert event with potential electromagnetic counterparts. Other, less significant correlations of blazars with neutrino alerts are, for example, IC190730A and PKS 1502+106 (introduced in Chapter 4), IC141209A and GB6 J1040+0617 [182], and IC201021A and PKS 1725+123 [183].

The individual correlations can be combined to calculate the overall probability of different candidate source classes producing high-energy neutrinos. Past studies used only the publicly available information on the alerts, e.g. correlations with radio-selected AGNs in [126, 127], with blazars in [125]. In this thesis, a new method to search for correlations of high-energy neutrino alert events and potential candidate sources was developed. It is more sensitive to the signal than previous analyses, since it uses the likelihood landscapes that are produced by the reconstruction method from the realtime program, which were not made public and only available to IceCube collaborators at the time when the analysis technique was designed.

This analysis method and the results presented in Chapter 10 were partially published in *The Astrophysical Journal* [184].

[182]: Garrappa et al. (2019), 'Investigation of Two Fermi-LAT Gamma-Ray Blazars Coincident with High-energy Neutrinos Detected by IceCube'

[183]: Nanci et al. (2022), 'Observing the inner parsec-scale region of candidate neutrino-emitting blazars'

[126]: Plavin et al. (2020), 'Observational Evidence for the Origin of High-energy Neutrinos in Parsec-scale Nuclei of Radio-bright Active Galaxies'

[127]: Plavin et al. (2022), 'Growing evidence for high-energy neutrinos originating in radio blazars'

[125]: Giommi et al. (2020), 'Dissecting the regions around IceCube high-energy neutrinos: growing evidence for the blazar connection'

[184]: Abbasi et al. (2023), 'Search for correlations of high-energy neutrinos detected in IceCube with radio-bright AGN and gamma-ray emission from blazars'

9.1 Hypothesis testing

In order to know if the result of an analysis is due to correlations that arise from background fluctuations and are simply coincidential, or if they are the product of a physical process, a proper statistical treatment of the data is needed. In IceCube, this is done by *hypothesis testing*, where one tries to determine which hypothesis describes the data better. The *null hypothesis* is the default for a typical hypothesis test and expects no physical correlation between sources and data. The *signal hypothesis* depends on the analysis and describes the underlying physics that is the object of study (here, candidate sources producing high-energy neutrinos).

The procedure for a test starts with the assumption that the null hypothesis describes the data correctly, and a Test Statistic (TS) is defined to quantify the truth of this statement. If the TS value of the data is above a certain pre-defined threshold, the null hypothesis is rejected. However, this does not mean that the signal hypothesis is correct, but simply that the result is unlikely to arise by chance. On the other hand, for a TS value lower than the threshold, the null hypothesis cannot be rejected, which does not mean that the signal hypothesis is incorrect either, only that we cannot confidently say that the null hypothesis is false.

The threshold is defined so that the probabilities of both rejecting the null hypothesis when it is true (Type I error, or false positive) and not rejecting it when it is false (Type II error, or false negative) are as low as possible. There has to be a compromise between both, since it is not possible to make them infinitesimaly small at the same time. However, the Type I error is "riskier", since we could wrongly claim to have discovered signal, thus the threshold is usually chosen to minimize this error. The rate of Type I error that we expect from an analysis is represented by a p-value, which is the probability of obtaining the observed result, assuming the null hypothesis is true. To claim a discovery, the typical threshold in particle physics is a significance of the result of 5σ (p-value $\approx 3 \times 10^{-7}$).

9.2 Stacking analysis

The statistical significance of the overall correlation between neutrino alert events and various candidate source classes is calculated using a *stacking analysis* technique. Each neutrino is treated independently, and then the contributions from all of them are added up together to obtain a final TS. The signal hypothesis is that the neutrino is produced by a coincident source from the candidate source class. The alternative null hypothesis is that the neutrino does not originate in any of the sources from the catalog being tested.

The likelihood function $\mathscr{L}$ represents the probability of observing the data given a hypothesis, and allows us to quantify the truth of said hypothesis. The standard *Point Source Likelihood* is the weighted sum of a signal Probability Density Function (PDF), $\mathcal{S}$, and a background PDF, $\mathcal{B}$,

$$\mathscr{L} = \frac{n_S}{N}\mathcal{S} + \left(1 - \frac{n_S}{N}\right)\mathcal{B}, \tag{9.1}$$

where n_S is the number of signal events and N is the total number of signal and background neutrino events. The most powerful choice for the TS is the ratio between the likelihood of observing the data given the signal hypothesis and given the background hypothesis [185], and for a single neutrino i ($N = 1$) is defined as

[185]: Neyman et al. (1933), 'On the Problem of the Most Efficient Tests of Statistical Hypotheses'

$$\mathrm{TS}_i = 2\log\left(\frac{\mathscr{L}(n_S = 1)}{\mathscr{L}(n_S = 0)}\right) = 2\log\frac{\hat{\mathcal{S}}}{\mathcal{B}}. \tag{9.2}$$

Treating each neutrino independently, the signal hypothesis is tested for each source b in the source catalog, and the TS per neutrino is simply the contribution from the most likely counterpart. If TS < 0, the background hypothesis is chosen, i.e. TS = 0. The signal PDF is calculated as

$$\hat{\mathcal{S}} = \max_b(\mathcal{S}_{\mathrm{signalness},\nu} \cdot \mathcal{S}_{\mathrm{spatial},\nu}(\vec{x_b}) \cdot w_b), \tag{9.3}$$

where the index b runs over all sources in the sample. The first term, $\mathcal{S}_{\mathrm{signalness},\nu}$, is the signalness of the neutrino, as defined in Chapter 4, and acts as a weight for the event. The neutrino point-spread function,

$\mathcal{S}_{\text{spatial},\nu}$, is calculated using the likelihood maps from the reconstruction of the alerts with Millipede (see Section 4.2.3 for more details).

To translate the -2ΔLLH map into a probability map, the 50% and 90% critical values (explained in Section 4.2.4) are matched to the 0.5 and 0.9 percentiles of a χ^2 distribution with 2 degrees of freedom (see Figure 9.1). This defines two regions: from the -2ΔLLH value of 0.0, which is matched to the 0.0 percentile of χ^2, to the 50% critical value; and from the 50% value to the 90% value. In each region, the -2ΔLLH values are scaled by interpolating between the boundaries. Using the matched χ^2 values from the 50%-90% region, we extrapolate up to the 99% contour. Then, the rescaled values are converted to probabilities with an exponential function. Beyond the 99% threshold, the probability is assigned to 0. Then, $\mathcal{S}_{\text{spatial},\nu}(\vec{x}_b)$ returns the value of the neutrino point-spread function at the position of the source $\vec{x}_b$. Finally, w_b is the source weight that depends on the model of the neutrino production mechanism.

Reminder

The -2ΔLLH values that correspond to the 50% and 90% containment of the resimulations of IC160427A are 22.2 and 64.2, respectively. These are used in the realtime program to derive the 50% and 90% error contours.

The most likely counterpart is the source for which Equation 9.3 is maximum, and we denote that in Equation 9.2 as $\hat{\mathcal{S}}$. The signalness is a fixed parameter for each individual neutrino, so it does not affect the selection of the counterpart, which depends only on its position and its value for the proxy of the neutrino emission, represented by w_b.

The probability of finding a correlation by chance can be assumed to be uniform if the distribution of the sources in the sky is compatible with an isotropic distribution with the same selection criteria that are applied to the catalog, and therefore the background PDF is simply defined by

$$\mathcal{B} = \mathcal{B}_{\text{spatial}} = \frac{1}{4\pi}. \tag{9.4}$$

Finally, the TS of the data is calculated by summing over all neutrino alerts, $\text{TS}_{\text{data}} = \sum_i \text{TS}_i$.

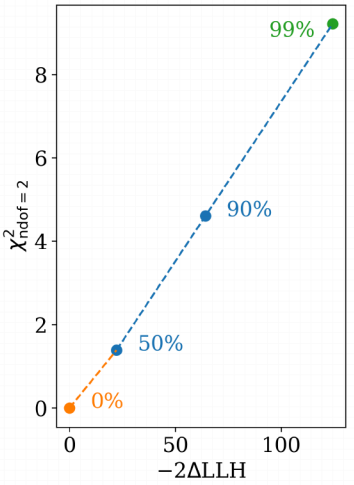

Figure 9.1: The -2ΔLLH map from the Millipede reconstruction is converted to a probability map by matching the 50% and 90% critical values to the 0.5 and 0.9 percentiles of a χ^2 distribution. The values are extrapolated up to the 99% contour.

9.3 Analysis procedure

9.3.1 Background trials and p-values

The significance of the result represents the confidence on the rejection of the null hypothesis. A high significance means that a background-only scenario does not describe the data. The significance is derived by comparing the TS value obtained with the data to the distribution of TS values from a sample of simulated experiments where the possible signal has been erased. These experiments are typically called *background trials*, and can be generated with Monte Carlo simulations of the expected background events, or with randomized data, which has some of its properties (typically, direction) scrambled to remove any signal. The data-based approach assumes that the sample contains mostly background events, and all the potential signal is faint. It has the advantage of not relying on the agreement between data and MC simulations for the interpretation of the result. For the analyses presented in this thesis,

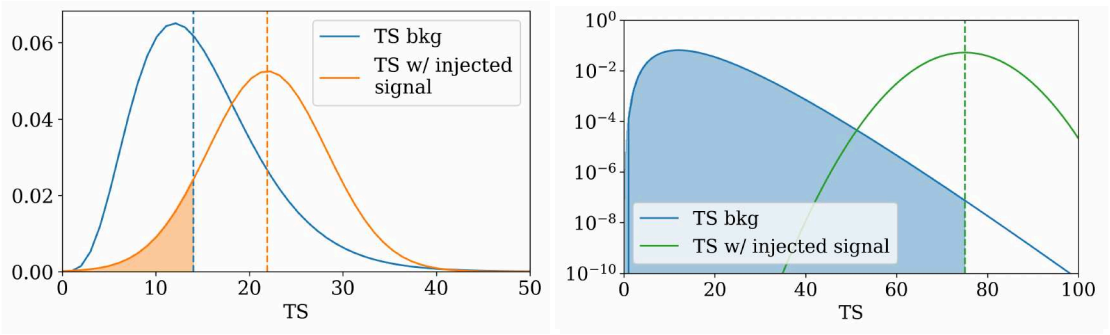

Figure 9.2: Sketch showing the sensitivity and 5σ discovery potential for simulated TS distributions. In both panels, the blue curve shows the same TS distribution of the background, in Panel b) in logarithmic scale. The orange and green curves are the TS distribution of a trial with injected signal, with increased signal injection in the case of the green curve. Panel a) represents the calculation of sensitivity. The injected flux for which the TS distribution is above the median of the background-only case in 90% of the cases is the sensitivity (orange area is 10% of the total area of the curve). In Panel b), the green dashed line represents both the 5σ threshold from the background-only case and the median of the TS distribution with the 5σ discovery potential injected flux (the blue area is equal to $1 - 3 \times 10^{-7}$).

the background trials are produced by scrambling the direction of the potential neutrino sources in right ascension and declination.

The p-value is defined as the probability of obtaining a TS equal or larger than a given TS value, under the assumption that the null hypothesis is true. A large number of background trials are generated, and for each of them the TS is calculated. The distribution of the TS values is then fitted by a χ^2 distribution that Wilks' theorem predicts for a sufficiently large sample with no systematic errors [111]. The p-value of the data is calculated as the area under the curve of the fitted χ^2 distribution from $\mathrm{TS}_{\mathrm{data}}$ to infinity:

$$p\text{-value} = \int_{\mathrm{TS}_{\mathrm{data}}}^{\infty} \chi^2 d\mathrm{TS} \tag{9.5}$$

[111]: Wilks (1938), 'The Large-Sample Distribution of the Likelihood Ratio for Testing Composite Hypotheses'

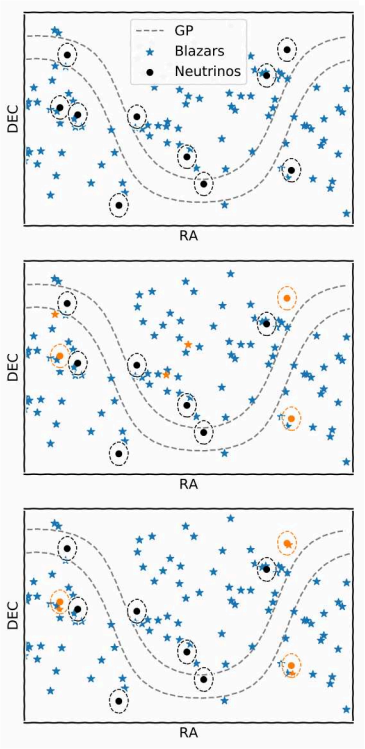

Figure 9.3: Sketch showing the steps for the signal injection. First panel shows a background trial, where the position of the sources in the sky is random. In the second panel, the neutrinos and sources that will be injected as signal are chosen and marked in orange. In the third panel, the direction of the chosen sources is changed so that it lies within the error contours of their correlated neutrinos.

9.3.2 Signal injection, sensitivities and discovery potentials

In order to quantify the efficiency of an analysis method, we can calculate the strength of the signal needed to be able to distinguish it from the background hypothesis. The usual process for this is the *signal injection*, in which a *signal trial* is simulated by combining the expected background with a signal model. Different p-value thresholds from the background distribution can be used to express the performance of the analysis in terms of the signal trials. The *sensitivity* is the signal model that leads to a TS value greater than the background median in 90% of the signal trials (Panel a of Figure 9.2), or $P(\text{type I error}) = 0.5$ and $P(\text{type II error}) = 0.9$. The 3σ and 5σ *discovery potentials* are the models needed to obtain a TS value which yields a p-value corresponding to a significance larger than the 3σ and 5σ thresholds, respectively, in 50% of the signal trials (5σ discovery potential shown in Panel b of Figure 9.2). This corresponds to $P(\text{type I error}) \approx 0.0027$ (3×10^{-7}) and $P(\text{type II error}) = 0.5$ for the 3σ (5σ) discovery potential.

For the analyses presented here, the signal injection consists of forcing correlations between sources and neutrino alert events. For each signal trial, a background trial is generated by scrambling the data, and the

fraction of alert events to be injected is chosen. The number of correlations is calculated assuming a Poisson distribution centered around the number of events corresponding to that fraction. Then, the sources and the neutrinos that will be correlated are randomly selected, weighted by w_b and $\mathcal{S}_{\text{signalness},\nu}$, respectively. For each correlation (each pair neutrino-source), the source direction is changed to a random position inside of the neutrino error contour, according to the $\mathcal{S}_{\text{spatial},\nu}(\vec{x}_b)$ distribution. Therefore, the source gets preferably injected closer to the neutrino best-fit position. These steps are sketched in Figure 9.3. Each neutrino has only one correlated source, and is not used in the other correlations within the trial. Once all the correlations have been injected, the TS_i of each neutrino (Equation 9.2) is calculated using Equation 9.3.

9.3.3 Unblinding process

The analyses in the IceCube collaboration are done in a *blind* manner: they are designed and developed without using the real data to avoid fine tuning the method to find a significant result. The sensitivity and discovery potential are therefore the only metrics used to validate the analysis. Once the method shows that it can perform well with simulated or scrambled data, and after an internal review within the collaboration, the data is ready to be *unblinded*, leading to a measured TS value. The background trials are reutilized to calculate the p-value of the observation after unblinding.

9.3.4 Analysis software

The analysis technique was developed as a `python` package by the author in collaboration with R. Stein. It was designed in a way that allows an easy change of source catalog, so that new analyses would be possible with minimal modifications. The trials were run on the IceCube's computing cluster, and the calculation of sensitivities and discovery potentials take on average less than 10 CPU hours for the analyses presented in Chapter 10.

Results of the stacking analyses 10

The method developed for this thesis and presented in Chapter 9 to search for correlations of high-energy neutrino alerts and candidate sources is used to analyze two catalogs: gamma-ray blazars and radio-loud Active Galactic Nuclei (AGN). With the first catalog, two weighting schemes are considered, which are related to the neutrino production mechanism that is assumed. In total, three stacking analyses are performed. In this Chapter, the catalogs are introduced and motivated, and the results are shown and discussed. Moreover, the findings are compared to a previous study by other scientists based on public IceCube data.

10.1 Samples 105
10.2 Sensitivities and discovery potentials 110
10.3 Results 111
10.4 Discussion 113
10.5 Cross-checks to previous analyses 115

10.1 Samples

10.1.1 IceCube's neutrino alert catalog

The IceCube Event Catalog of Alert Tracks-1 (IceCat-1) [124] (introduced in Chapter 4) includes 275 track-like events that fulfill the selection criteria for realtime alerts and were processed identically. In the accompanying publication [124], a simple directional correlation analysis is also performed, that searches for spatial coincidences between neutrino alerts and sources from some of the most common gamma-ray and X-ray catalogs: the 4FGL-DR2 [186] and 3FHL [155] catalogs, the 3HWC catalog [187], TeVCat [188] and the Swift-BAT catalog [189]. They find that the number of coincidences is consistent with the null hypothesis of chance coincidences. The stacking analysis presented in Chapter 9 is more sensitive to potential signal, since it includes additional information of the alert event and the candidate counterpart, and adds the contributions from each individual neutrino-source pair.

[124]: Abbasi et al. (2023), 'IceCat-1: the IceCube Event Catalog of Alert Tracks'

[186]: Abdollahi et al. (2020), 'Fermi Large Area Telescope Fourth Source Catalog'

[155]: Ajello et al. (2017), '3FHL: The Third Catalog of Hard Fermi-LAT Sources'

[187]: Albert et al. (2020), '3HWC: The Third HAWC Catalog of Very-high-energy Gamma-Ray Sources'

[188]: Wakely et al. (2008), 'TeVCat: An online catalog for Very High Energy Gamma-Ray Astronomy'

[189]: Oh et al. (2018), 'The 105-Month Swift-BAT All-sky Hard X-Ray Survey'

10.1.2 *Fermi*-LAT sources

The *Fermi* Gamma-Ray Space Telescope is a space observatory that detects photons in the 10 keV to 300 GeV energy range. The main instrument on board is the Large Area Telescope (LAT) [39], which detects radiation from 30 MeV to 300 GeV via pair conversion. The photons pass through an anticoincidence shield, which acts as a veto for cosmic rays since it is sensitive to charged particles. Then, the photons traverse thin layers of tungsten material, called conversion foils, where they create electron-positron pairs. The direction and energy of these are measured with silicon-based particle tracking detectors and a calorimeter, respectively. The signal signature requires no charged particle in the anticoincidence shield, two tracks starting from the same position inside of the detector, and an electromagnetic shower. *Fermi*-LAT has a field of view of over 2 steradians and a source location resolution of less than 1 arcminute. An schematic cross-section of *Fermi*-LAT can be seen in Figure 10.1.

[39]: Atwood et al. (2009), 'The Large Area Telescope on the Fermi Gamma-ray Space Telescope mission'

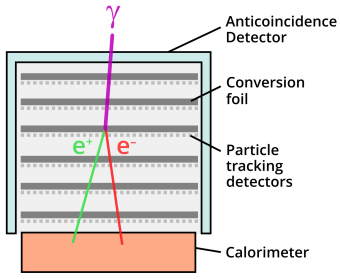

Figure 10.1: Cross-section of *Fermi*-LAT. Credits: NASA's Goddard Space Flight Center.

The secondary instrument on *Fermi*, the Gamma-Ray Burst Monitor (GBM) [40], provides spectral coverage of gamma-ray bursts down to 10 keV. It consists of 12 detectors that detect X-rays and low-energy gamma rays with a field of view that covers the entire sky not occulted by the Earth. The detectors are located on opposite sides of *Fermi* and facing different directions, so that the arrival direction of the burst can be triangulated using the event rate detected by each detector.

[40]: Meegan et al. (2009), 'The Fermi Gamma-Ray Burst Monitor'

One of the two catalogs considered for the analyses presented here is the incremental version of the Fourth Catalog of Active Galactic Nuclei detected by *Fermi*-LAT (4LAC-DR2, for Data Release 2) [190, 191]. It contains all AGNs detected by *Fermi*-LAT between 2008 and 2018 at high galactic latitudes b ($|b| > 10\,\mathrm{deg}$). This catalog is preferred to the 4FGL catalog that covers the whole sky, since the sensitivity of *Fermi*-LAT decreases at low latitudes, and so does its angular resolution. Moreover, the classification of AGNs is very uncertain at low latitudes, because the radio and X-ray surveys are affected by contamination from the Galactic Plane. From 4LAC-DR2, only blazar candidates are selected (BL-Lacs, Flat Spectrum Radio Quasars and blazar candidates of unknown types), which represent 98% of the catalog, as can be seen in Table 10.1.

[190]: Ajello et al. (2020), 'The Fourth Catalog of Active Galactic Nuclei Detected by the *Fermi* Large Area Telescope'
[191]: Lott et al. (2020), 'The Fourth Catalog of Active Galactic Nuclei Detected by the Fermi Large Area Telescope – Data Release 2'

Table 10.1: Number of sources of each AGN type in the 4LAC-DR2 catalog.

AGN Type	Number
BL-Lacs	1236
FSRQs	707
Blazars (unknown)	1120
Non-blazars	68

Isotropy study

One of the conditions that goes into the definition of the Test Statistic (TS) is that the distribution of sources in the sky is isotropic. To fulfill such condition, the catalog was further refined. Several selection criteria were applied to the gamma-ray energy flux $F = (\mathrm{d}N/\mathrm{d}E\mathrm{d}A\mathrm{d}t)E^2$, which is obtained by spectral fitting from 100 MeV to 100 GeV. Cuts on the brightness of the energy flux were studied, from $\log F = -11.6$ to $\log F = -12.0$, in steps of 0.1 in $\log F$. For each cut, the sources are weighted by their energy flux, and the longitude and latitude distributions were compared to those of a uniform distribution with the same number of sources. The cut on latitude of $|b| > 10\,\mathrm{deg}$ that is present in the catalog is also maintained in the isotropy studies. The results are shown in Figure 10.2 and Figure 10.3. The colored histograms show the real data. The black points with error bars are the mean and standard deviation of 200 MC uniform distributions, each of them weighted by a random energy flux distribution with the same cumulative distribution as the real data. Table 10.2 contains the surviving number of blazars after each cut on $\log F$, the cumulative energy flux from the surviving blazars normalized by the total cumulative energy flux, and the p-value of a χ^2 test comparing the MC uniform distribution to the data distribution for each coordinate.

A second isotropy study was performed to check if the distance between blazar pairs correspond to a uniform distribution of sources in the sky.

Table 10.2: Isotropy studies of *Fermi* 4LAC-DR2 catalog.

Cut on $\log F$	Surviving	$\frac{\sum^{\mathrm{surviving}} F}{\sum^{\mathrm{total}} F}$	p-value (l)	p-value ($\sin(b)$)
−12.0	3018	1.00	0.73	0.49
−11.9	2932	1.00	0.73	0.48
−11.8	2754	0.99	0.73	0.45
−11.7	2461	0.97	0.66	0.43
−11.6	2089	0.94	0.60	0.40

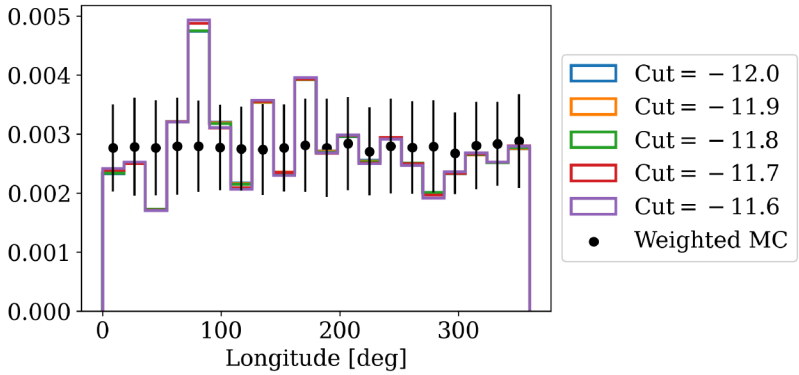

Figure 10.2: Isotropy study of the *Fermi* 4LAC-DR2 catalog for the longitude coordinate. The colored histograms show the distribution of the data weighted by the energy flux, with different cuts on the energy flux applied. In black points, the values of a uniformly distributed simulated sample, with statistical uncertainties.

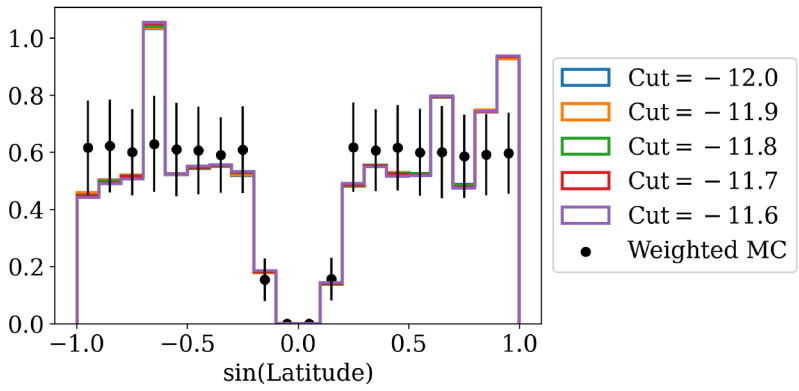

Figure 10.3: Isotropy study of the *Fermi* 4LAC-DR2 catalog for the latitde coordinate. The colored histograms show the distribution of the data weighted by the energy flux, with different cuts on the energy flux applied. In black points, the values of a uniformly distributed simulated sample, with statistical uncertainties.

In a similar manner, increasing limits on the energy flux were compared to a MC sample, and the only cut for which both distributions are compatible is $F \geq 10^{-11.6}\,\mathrm{erg\,cm^{-2}\,s^{-1}}$, with a p-value of 0.6. A cut of $F \geq 10^{-11.6}\,\mathrm{erg\,cm^{-2}\,s^{-1}}$ was chosen based on these results, which still retains over 90% of the cumulative energy flux as can be seen in Table 10.2. From the original 3063 blazars in 4LAC-DR2, 2089 remain in the final selection.

Weighting schemes

For this catalog, two neutrino production mechanisms were considered, which enter the analysis as the source weight w_b in Equation 9.3. The two weighting schemes can be assumed independent, creating two separate analyses. For the first, the weight of each blazar is its normalized 10-year average energy flux in gamma rays above 100 MeV. Theory models predict that blazars with higher flux emit more high-energy neutrinos [152, 153] and, therefore, are more likely to be the source of an alert neutrino. In a previous IceCube publication, this weighting scheme was also applied to a different neutrino catalog [192].

The second weighting scheme includes temporal information, since it utilizes the light curves from the Light Curve Repository[1] detected by *Fermi*-LAT [193]. The weight for the sources is the normalized flux in the 1-month time bin that coincides with the neutrino arrival time, similar to the study performed for the correlation of TXS 0506+056 and IC170922A [62]. The light curve of the TXS 0506+056 blazar can be seen in Figure 10.4, together with the detection of the IC170922A neutrino as the vertical line. Only the blazars that exhibit flux variability are included

[152]: Murase et al. (2014), 'Diffuse neutrino intensity from the inner jets of active galactic nuclei: Impacts of external photon fields and the blazar sequence'

[153]: Petropoulou et al. (2015), 'Photohadronic origin of γ-ray BL Lac emission: implications for IceCube neutrinos'

[192]: Huber (2019), 'Searches for steady neutrino emission from 3FHL blazars using eight years of IceCube data from the Northern hemisphere'

1: https://fermi.gsfc.nasa.gov/ssc/data/access/lat/LightCurveRepository/

[193]: Abdollahi et al. (2023), 'The Fermi-LAT Lightcurve Repository'

[62]: Aartsen et al. (2018), 'Multimessenger observations of a flaring blazar coincident with high-energy neutrino IceCube-170922A'

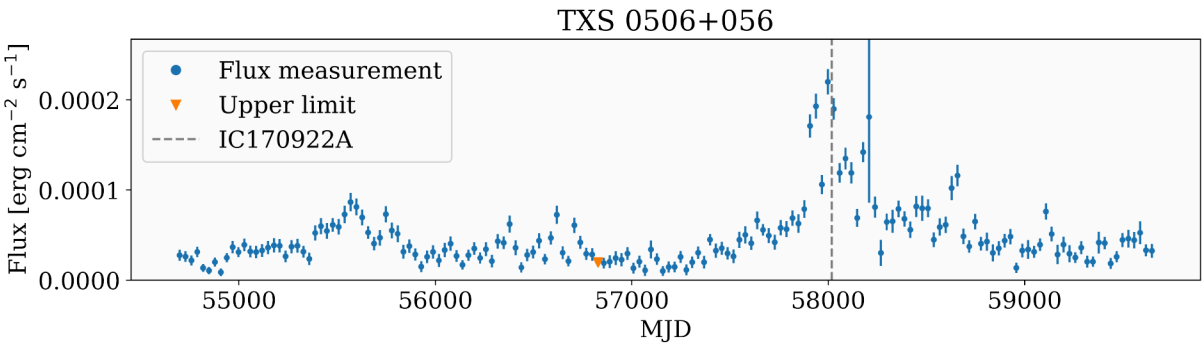

Figure 10.4: Energy flux of TXS 0506+056 as function of time, in monthly time bins. The grey vertical line represents the arrival time of the IC170922A neutrino.

in the light curve repository. The variability is represented by an index which is a proxy for the average fractional variability with $\mathrm{d}F/F$. The threshold is 21.67, so that blazars with a variability index greater than this have an estimated chance of being a steady source of $< 1\%$ [193]. From the 2089 blazars selected for this analysis, 1161 were released in the light curve repository. The weights are calculated as follows:

- The blazars for which the light curve was not provided in the repository are not variable, so the average energy flux is the proxy for the flux at the time of the neutrino's arrival and used as the weight.
- If there is a flux measurement at the neutrino arrival time, it is used as the weight.
- If there is no flux measurement in the time bin of the neutrino arrival or it is an upper limit, we check the monthly time bin before and after the time bin of the neutrino event (neighbouring bins). If both have a flux measurement, the weight is an average of both. If only one of them has a measurement, the weight is equal to that flux. This assumes that the monthly energy flux does not vary greatly from one month to another.
- If there is no flux measurement or only an upper limit is provided in the time bin of the neutrino event and its neighbouring time bins, then a weight of zero is assigned. The weight is set to zero also when there are no measurements available in the neighbouring bins. This is to avoid mixing the hypotheses for the two weighting schemes.

10.1.3 Radio Fundamental Catalog sources

As explained in Section 8.4.2, recent studies suggested that radio-bright AGNs are associated with IceCube neutrino events. Therefore, the second catalog considered for coincidences with IceCat-1 is the Radio Fundamental Catalog (RFC), in its 2022a version[2]. The RFC 2022a catalog contains 20499 objects observed with Very Long Baseline Interferometry (VLBI) observations [194] at 22 GHz, 8.6 GHz, 5 GHz and 2.2 GHz, between 1980-04-11 and 2022-03-24. The best-fit positions are given for all sources with two or more good observations. New versions are released on a quarterly basis, but the 2022a version was the proposed catalog for the

2: http://astrogeo.org/sol/rfc/rfc_2022a/

[194]: Jennison (1958), 'A Phase Sensitive Interferometer Technique for the Measurement of the Fourier Transforms of Spatial Brightness Distributions of Small Angular Extent'

analysis approval request to the IceCube collaboration, which fixes the dataset to be used.

Weighting scheme

For the analysis presented here, the weight is the flux density integrated over VLBI images at 8.6 GHz. AGNs with flux density $S_{8.6\,\mathrm{GHz}} \geq 150\,\mathrm{mJy}$ are selected, which leaves a total of 3413 AGNs. 828 of the sources are present in both catalogs (*Fermi* 4LAC-DR2 and this one), but there is no apparent correlation between the brightness in radio flux density and gamma-ray energy flux, as can be seen in Figure 10.5. Therefore, the analyses are assumed to be independent.

We follow the selection criteria applied in [126] with the purpose of cross-checking the results obtained in their analysis. The procedure followed to compare both methods is explained in Section 10.5 and discussed in Section 10.4.

[126]: Plavin et al. (2020), 'Observational Evidence for the Origin of High-energy Neutrinos in Parsec-scale Nuclei of Radio-bright Active Galaxies'

Isotropy study

The distribution of sources is again studied to check that it is isotropic. The same procedure is performed, but the only selection criterium applied to the catalog is on the flux density and fixed to $S_{8.6\,\mathrm{GHz}} \geq 150\,\mathrm{mJy}$. The data is weighted by the radio flux density and compared to the mean of 200 uniform distributions in both longitude and latitude, shown in Figure 10.6. In both cases, the data is compatible with an isotropic distribution based on a χ^2 test.

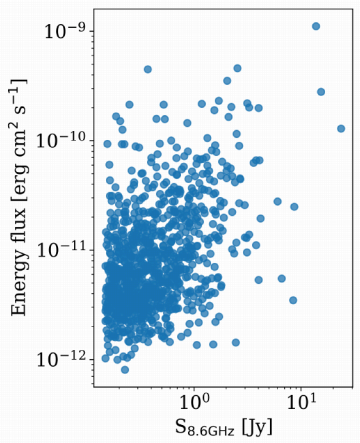

Figure 10.5: Values of the gamma-ray energy flux and the radio flux density $S_{8.6\,\mathrm{GHz}}$ for the sources that appear in both *Fermi* 4LAC-DR2 and RFC 2022a catalogs.

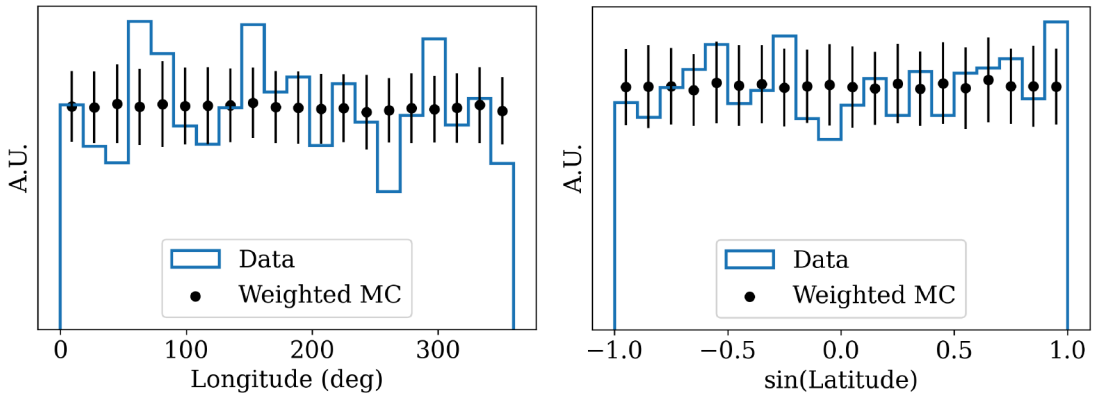

Figure 10.6: Isotropy study of the RFC 2022a catalog. The blue histogram shows the distribution of the data and the black points with error bars are the mean and standard deviation of 200 uniformly distributed simulated samples.

10.2 Sensitivities and discovery potentials

The calculation of the sensitivity and discovery potentials for the three analyses is done using scrambled data as explained in Chapter 9. With the *Fermi*-LAT catalog, the cut on latitude is maintained for the background trials, and the blazars are scrambled always outside of the Galactic Plane with $|b| > 10\,\text{deg}$. To calculate the discovery potentials, signal is injected by forcing correlations between sources and neutrinos. For the *Fermi*-LAT catalog, those blazars that are injected in correlation with a neutrino in the Galactic Plane were assigned a TS value of zero to maintain the latitude cut also during the signal injection.

In practice, due to limited computation, the signal injection is done in steps of 0.05 on the fraction of astrophysical neutrinos with correlations. To get the exact fraction that the analysis is sensible to or that leads to a discovery, one can use interpolation. Figure 10.7 shows the quantile of signal trials with a TS value above the sensitivity, 3σ and 5σ thresholds. One can look for the fraction for which the sensitivity (discovery potential) curve is equal to 0.9 (0.5), which is represented by the dashed lines. This fraction of alerts from IceCat-1 can be translated to astrophysical neutrino flux by dividing it by the average signalness of the catalog, which is 45.1%.

For the analysis using the *Fermi*-LAT 4LAC catalog with average flux weights, the sensitivity flux is at 4.9% of the astrophysical flux, which corresponds to 6.3 signal correlations from the 275 neutrinos in the IceCat-1 catalog, i.e. 6.3 neutrinos correlated with their sources. The 3σ discovery potential is at 11.6% of the astrophysical flux, or 14.4 signal correlations from the IceCat-1 catalog. The 5σ discovery potential is at 20.6% of astrophysical flux, or 25.6 signal correlations.

The sensitivity for the same catalog with the monthly energy flux weighting scheme is at 4.4% of the astrophysical flux, which is equivalent to 5.5 signal correlations. The 3σ (5σ) discovery potential is at 9.1% (16.1%) of astrophysical flux, corresponding to 11.2 (20.0) correlations.

Using the RFC catalog and the average VLBI the sensitivity flux is 6% of the astrophysical flux, or 7.4 signal correlations, and the 3σ (5σ) discovery potential is at 14.1% (24.8%) of flux, equivalent to 17.4 (30.7) correlations.

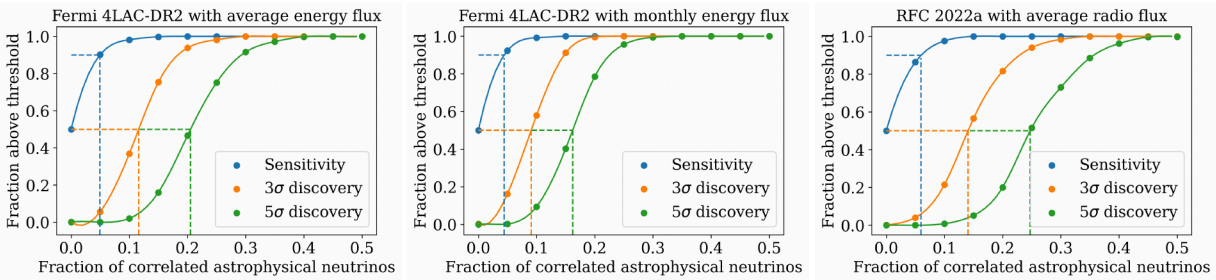

Figure 10.7: Sensitivities and discovery potentials of the three stacking analyses. In every plot, the blue curve represents the sensitivity, and the orange and green curves show the 3σ and 5σ discovery potentials, respectively. The fraction of astrophysical neutrinos with a correlated source needed to reach each threshold is marked by the vertical lines.

10.3 Results

Figure 10.8 shows the results for the three analyses performed. In each Panel, the blue histogram is the TS distribution of 5000 background trials, using the corresponding catalog and weighting scheme, fitted to a gamma distribution (blue line). The orange vertical line represents the TS_{data}, from which the p-value is calculated.

Table 10.3, Table 10.4 and Table 10.5 show the 10 most significant correlations in the data for each of the analyses, i.e. the neutrino-blazar pairs with the highest TS_i. The first column is the neutrino using the nomenclature of the realtime program, the second column is the signalness of each neutrino, the third column is the J2000 name of the most likely counterpart, the fourth column is the angular distance d between the candidate source and the neutrino (calculated as the angle between the two sightlines) and the last column is the contribution TS_i of each correlation to the final TS_{data}.

Finally, the 50% and 90% C.L. uncertainty contours for each of the 10 most significant correlations in each analysis are shown in Appendix D.

10.3.1 *Fermi* 4LAC-DR2 with average energy flux

The result of the analysis with 2089 selected blazars from *Fermi* 4LAC-DR2 weighted by the average 10-year energy flux is compatible with the null hypothesis. The TS_{data}, which is equal to 131.3, can be explained by the background-only scenario, as can be seen in Figure 10.8 Panel (a). This leads to a p-value of 0.248 when compared to the background, whose median is 120.4.

Table 10.3 shows the 10 most significant correlations in the data. The two strongest correlations (TXS 0506+056 with IC170922A and PKS 1502+106 with IC190730A) have been extensively studied, as discussed previously. The third and fourth most significant correlated blazars are 3C 454.3 and Mkn 421, two of the brightest sources in the sky, which explains the high TS_i. In both cases, the area of the error region of the associated neutrino is very large, as can be seen in Figure D.1. The areas of the 90% uncertainty contours are 26.80 deg^2 and 56.07 deg^2 respectively, compared to the median 90% contour area of all alerts which is 5.96 deg^2, or the 90% contour area of IC170922A and IC190730A, of 1.54 deg^2 and 5.61 deg^2, respectively.

Neutrino	Signalness	Blazar	d [deg]	TS_i
IC170922A	63 %	TXS 0506+056	0.11	7.43
IC190730A	67 %	PKS 1502+106	0.27	7.13
IC120523A	49 %	3C 454.3	0.72	7.12
IC111208A	45 %	Mkn 421	0.78	5.63
IC190704A	49 %	NVSS J104516+275136	1.04	5.14
IC190504A	39 %	NVSS J042025-374443	0.50	4.18
IC200109A	77 %	TXS 1100+122	0.36	4.05
IC181014A	39 %	PKS 1454-354	0.99	3.87
IC150104A	45 %	MG2 J180948+2910	0.50	3.41
IC130127A	61 %	PKS B2330-017	0.58	3.17

Table 10.3: The table shows the 10 correlations that contribute most to the TS of the data using the *Fermi* 4LAC-DR2 catalog and average flux weights, with the angular distance d between the candidate source and the neutrino (calculated as the angle between the two sightlines) and the contribution TS_i of each correlation to the final TS_{data}.

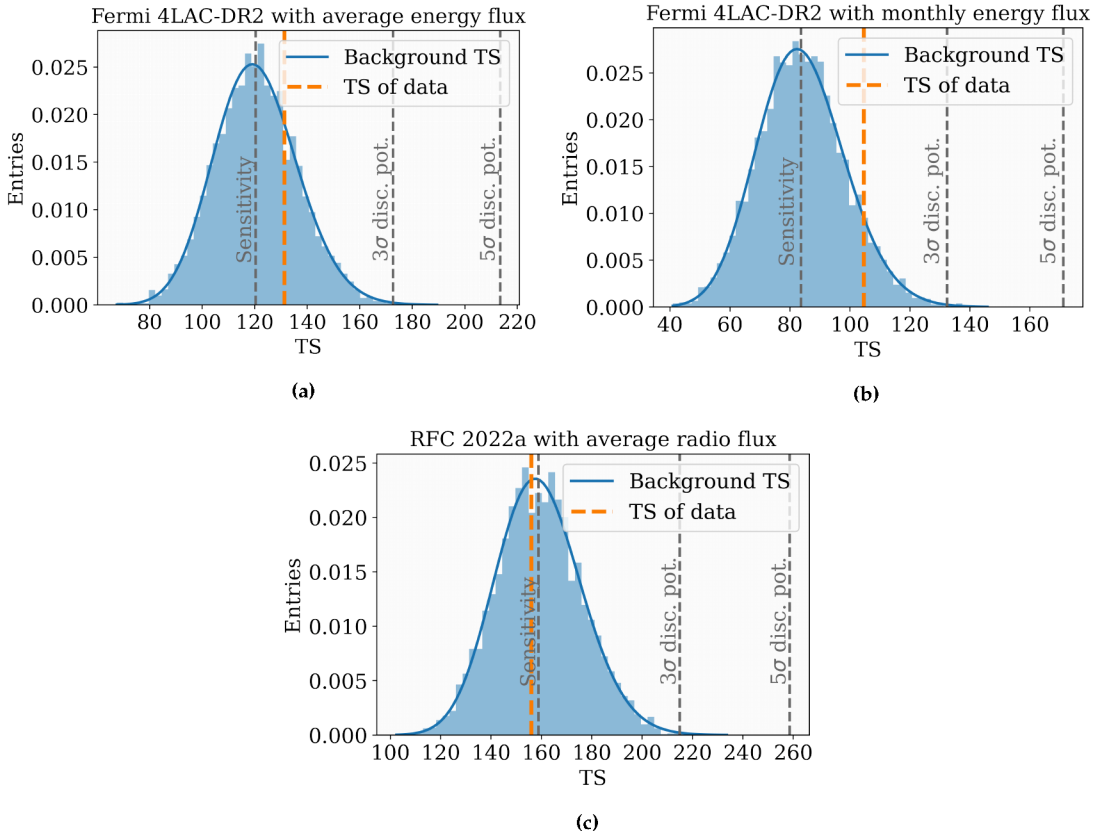

Figure 10.8: The blue histogram shows the distribution of the TS values for $N = 5000$ background maps, fitted to a gamma distribution (blue curve). The orange dotted line represents the observed TS of the data, while the grey lines represent the TS_{data} needed to reject the background hypothesis at the 3σ or 5σ level. Panel a) For the *Fermi* 4LAC-DR2 catalog with the average energy flux weights, $TS_{data} = 131.3$, while TS = 120.4 for the median background maps, leading to a p-value of 0.248. Panel b) For the *Fermi* 4LAC-DR2 catalog with the monthly energy flux weights, $TS_{data} = 104.6$, median background maps has TS = 83.6 and the p-value is 0.08. Panel c) For the RFC 2022a catalog, $TS_{data} = 155.8$, TS = 158.9 for the median background maps and the p-value is 0.57.

10.3.2 *Fermi* 4LAC-DR2 with monthly energy flux

No significant correlation was found when the selected blazars are weighted by the energy flux at the neutrino arrival time, although the p-value is smaller, at 0.08 (see Figure 10.8 Panel b). The median of the TS distribution of the background is 83.6, while $TS_{data} = 104.6$. Table 10.4 shows again the 10 most contributing correlations to the TS. As expected, the main contribution to TS_{data} is given by TXS 0506+056 and IC170922A. The blazar was flaring in gamma rays at the neutrino arrival time, which produces a higher TS_i than the value obtained with the average energy flux weight. On the other hand, one can see that the blazar 3C 454.3 was in a quiescent state at the neutrino arrival time, and therefore, the TS value of that correlation is low and not among the top 10 contributors.

10.3.3 RFC 2022 with average VLBI flux

The result from the analysis using the RFC catalog and the average VLBI flux at 8.6 GHz as weight for the contribution of the AGNs is that the data is compatible with the null hypothesis. This can be seen again in Figure 10.8 Panel (c), where the TS_{data} of 155.8 leads to a p-value of 0.57 when compared to the TS distribution of the background trials, with a

Neutrino	Signalness	Blazar	d [deg]	TS_i
IC170922A	63 %	TXS 0506+056	0.11	9.43
IC190730A	67 %	PKS 1502+106	0.27	5.63
IC111208A	45 %	Mkn 421	0.78	5.36
IC130125A	53 %	S5 0016+73	1.03	4.87
IC190504A	39 %	NVSS J042025-374443	0.50	4.41
IC150104A	49 %	MG2 J180948+2910	0.50	4.28
IC111216A	95 %	TXS 0222+185	0.51	4.13
IC200109A	78 %	TXS 1100+122	0.36	3.96
IC140101A	56 %	PMN J1243-0218	1.33	3.81
IC181014A	39 %	PKS 1454-354	0.99	3.54

Table 10.4: The 10 correlations that contribute most to the TS of the data using the *Fermi* 4LAC-DR2 catalog and monthly flux weights.

Neutrino	Signalness	AGN	d [deg]	TS_i
IC120523A	49 %	J2253+1608	0.72	5.62
IC170922A	63 %	J0509+0541	0.12	5.41
IC190730A	67 %	J1504+1029	0.28	5.21
IC150812B	83 %	J2151+0552	0.47	4.12
IC141110A	29 %	J1652+0618	0.26	3.51
IC150428A	32 %	J0204+1514	0.44	3.48
IC130125A	53 %	J0019+7327	1.02	3.19
IC170422A	39 %	J1550+0527	3.29	3.05
IC140307A	40 %	J2025+3343	1.67	3.02
IC200530A	59 %	J1659+2629	0.48	2.99

Table 10.5: The 10 correlations that contribute most to the TS of the data using the RFC 2022a catalog.

median of 158.9. In Table 10.5 the 10 correlations with the highest TS are shown. It is worth noting that the correlations of TXS 0506+056 with IC170922A and PKS 1502+106 with IC190730A appear on the list (with the nomenclature used in the RFC catalog for the AGNs), since they are both very bright in radio as well.

10.4 Discussion

No significant correlation was found in any of the three analyses performed for this thesis, meaning that the majority of the neutrino alerts are neither produced in bright or flaring gamma-ray blazars nor in radio-bright AGNs.

The analyses, and the method itself, rely heavily on the robustness of the reconstruction. The neutrino spatial PDF depends on the contour calculation, and the findings presented in this thesis indicate that the current method that was applied to the IceCat-1 catalog does not achieve the desired coverage (see Chapter 4, Chapter 5 and Chapter 6). A better handle on the systematic uncertainties is crucial and might give an opportunity to revisit this analysis with improved sensitivity.

The results with the *Fermi* 4LAC-DR2 calatog are, however, compatible with previous hints of signal from individual sources, e.g. [62, 116]. One can calculate the expected number of chance coincidences with a TS_i greater than a certain threshold by using the background trials. This is shown in Figure 10.9 for fixed values of TS_i from 0 to 8 as the blue line, with the 4LAC-DR2 catalog weighted by the average energy flux. The majority of alert events have $TS_i = 0$, which corresponds to either no blazar inside the error region of the neutrino, or a very faint and far away blazar so that the null hypothesis is preferred. The expected number

[62]: Aartsen et al. (2018), 'Multimessenger observations of a flaring blazar coincident with high-energy neutrino IceCube-170922A'
[116]: Rodrigues et al. (2021), 'Multi-wavelength and Neutrino Emission from Blazar PKS 1502 + 106'

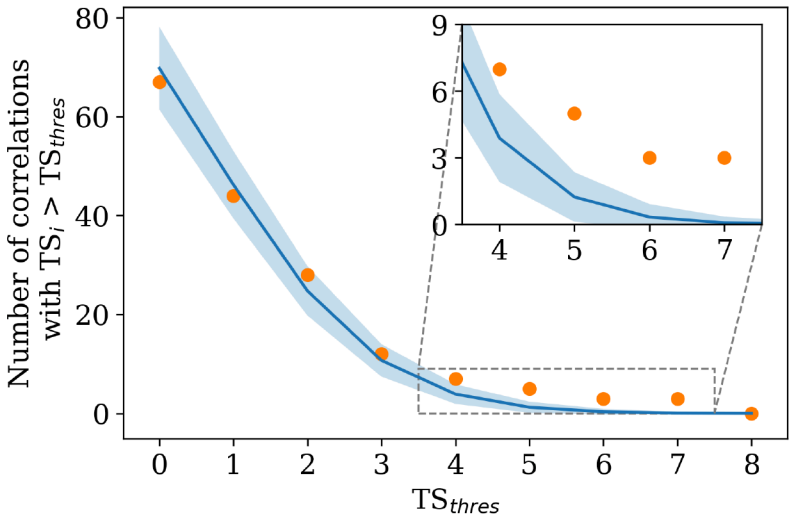

Figure 10.9: Number of correlations with TS_i greater than a certain TS value, using the *Fermi* 4LAC-DR2 catalog. The blue line represents the expected number of correlations under the null hypothesis, with statistical errors, while the orange dots are the correlations present in data.

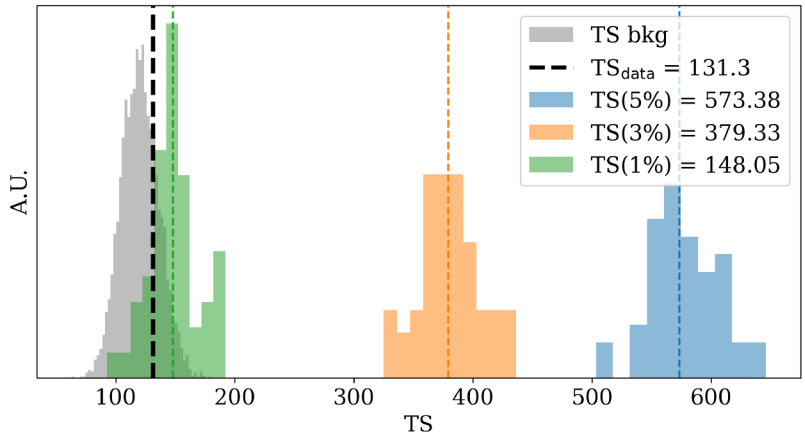

Figure 10.10: TS distributions of x% selected and injected blazars, from the *Fermi* 4LAC-DR2 catalog, weighted by the average energy flux.

of chance correlations that have $TS_i > 7$ is 0.077. In data, shown as the orange points, there are three such correlations, which point to potential signal being present but non discernible from chance coincidences.

The observed TS_{data} is compatible with the TS distribution that one would obtain if only a small percentage of the blazars in the selected *Fermi* 4LAC-DR2 catalog emits neutrinos. As a qualitative study, this is simply calculated by randomly selecting x% of sources and producing multiple signal trials with them, i.e., the location of the blazar is moved into the error region of a neutrino so that a correlation is forced. Figure 10.10 shows the distribution of 50 signal trials selecting and injecting 1%, 3% and 5% of the *Fermi* 4LAC-DR2 catalog (21, 63 or 104 blazars). Note that in this study all blazars are correlated with one neutrino alert event. The TS_{data} is only compatible with the 1% distribution.

The same study was performed with RFC 2022a, with similar results, shown in Figure 10.11. In this case, the TS_{data} is compatible with an even smaller percentage of the total number of sources in the catalog. This indicates the possibility that only a small fraction of the gamma-ray bright and radio-bright AGN population are sources of high-energy neutrinos.

The third correlation analysis was designed to be similar to [126], to allow

[126]: Plavin et al. (2020), 'Observational Evidence for the Origin of High-energy Neutrinos in Parsec-scale Nuclei of Radio-bright Active Galaxies'

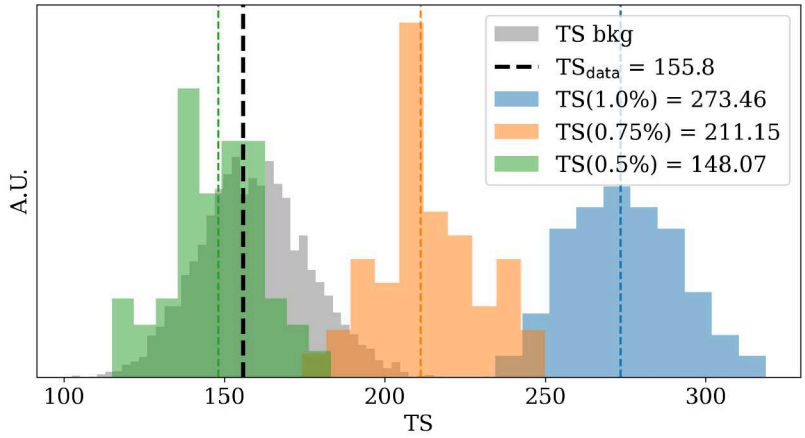

Figure 10.11: TS distributions of x% selected and injected blazars, from the RFC 2022a catalog.

a comparison. The details of these cross-checks can be found in Section 10.5.

The possibility of testing several hypotheses of correlations between neutrino sources and realtime alerts is the main strength of the method that was developed for this thesis. The information from the realtime reconstruction algorithm and the signalness of the alert allow us to be more sensitive to potential signal, and they were used for the first time in the analyses presented here.

10.5 Cross-checks to previous analyses

Neutrino alert events have been used in many analyses, trying to discover the sources of such energetic particles. One of the most recent results is described in Ref. [126], where a 3σ correlation is found between 56 IceCube high-energy neutrinos and a previous version of the Astrogeo catalog[3]. To cross-check this result, the analysis technique presented in Chapter 9 is modified to resemble the method used in Ref. [126], and the same selection criteria is applied to the candidate sources.

[126]: Plavin et al. (2020), 'Observational Evidence for the Origin of High-energy Neutrinos in Parsec-scale Nuclei of Radio-bright Active Galaxies'

3: `http://astrogeo.org/vlbi/solutions/rfc_2019c/`

The neutrino catalog used in the analysis in [126] is not a direct subset of public alerts from IceCat-1, but a selection of alert and alert-like events from different catalogs published by IceCube[4]. It contains 56 events from 2009 to 2019 with energy $E > 200$ TeV, track morphology and good angular resolution ($\Omega_{90} < 10\,\mathrm{deg}^2$). Only 44 overlap with the IceCat-1 catalog, and the remaining 12 events are from the period from 2009 to 2011 that was not included in the IceCat-1 catalog (10) or didn't pass our current alert criteria (2).

4: A table with the full catalog is included with the paper.

There are two main differences between the two analysis techniques, one of them is the definition of the TS. In the method developed for this thesis it is given by Equation 9.2 and includes information about the signalness and the point-spread function of the neutrino. The TS takes into account how well reconstructed the event is, how close the source is to the best-fit position, and how likely the neutrino is to be astrophysical. On the other hand, for the analysis in Ref. [126], the TS is simply the geometric average of the VLBI flux of the sources coincident with each neutrino, summed over the 56 selected events.

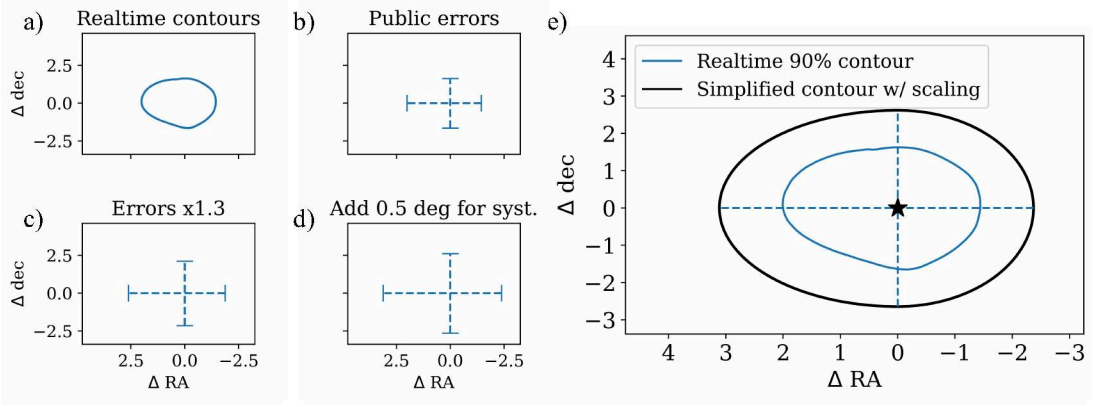

Figure 10.12: Example of the simplification and scaling that is applied to the realtime contours in [126], which is also done in the cross check presented here. From the original contours in Panel a), only the minimum rectangle is published, which is translated to uncertainty in the coordinates (Panel b). Those errors are multiplied by 1.3 (Panel c) and an extra parameter is added to account for systematic uncertainties, leading to a minimum p-value at an added 0.5 degrees (Panel d). The error bars are joined by elliptical segments to obtain the simplified contours corresponding to the best-fit position from the reconstruction, represented by the black star (Panel e).

For the comparison study, the definition of the TS is kept as in Equation 9.2, but the spatial term (and therefore, the definition of coincidence) in the signal PDF is calculated as in Ref. [126]. The only available data when their analysis was published was what IceCube releases in the GCN Circulars when an alert event is detected. As explained in Section 4.1.2, from the error contours calculated with Millipede, only the minimal rectangle that encapsulates the 90% error contour in right ascension and declination is published, along with the reconstructed direction. In Ref. [126] the coordinate-wise errors are multiplied by the ratio of the 90% quantiles of 2D and 1D Gaussian distributions (≈1.3). IceCube already calculates the errors by assuming a 2D distribution, but the extra 1.3 factor is also applied in comparison tests for consistency.

In Ref. [126] the analysis is optimized for a parameter x that is added linearly in all directions to account for possible unknown systematic uncertainties. The minimum pre-trial p-value is found at $x = 0.5\,\text{deg}$ after covering the parameter space from 0 to 1 deg in increments of 0.1 deg. Finally, the error region is assumed to be composed of 4 points joint by elliptical segments. All these steps are shown in Figure 10.12. This scaling of the contours is not well motivated in the light of the technical work done for this thesis, since the systematic uncertainties are already accounted for in the published error contours (Chapter 4). Moreover, the calibration could lead to an overcoverage of the error region for a certain confidence level (see Chapter 5 and Chapter 6). However, other analyses have also found interesting hints of signal following a similar procedure (although with a different neutrino data sample focused on lower energies), e.g., [125, 157], so it is worth investigating.

For the comparison tests the spatial term of the signal PDF is switched to the simpler coincidence-based function described above, instead of being based on the reconstruction's likelihood landscape. The S_{spatial} is then 1 for all AGNs inside the area of the calculated contour and 0 outside. Four tests are performed, two with the datasets described in Section 10.1 (IceCat-1 catalog + RFC 2022a, used for the results in Section 10.3) and two with the original dataset from Ref. [126] (56 alert and alert-like events + RFC 2019c). For each combination, the spatial PDF is calculated with

[125]: Giommi et al. (2020), 'Dissecting the regions around IceCube high-energy neutrinos: growing evidence for the blazar connection'
[157]: Buson et al. (2022), 'Beginning a Journey Across the Universe: The Discovery of Extragalactic Neutrino Factories'

Table 10.6: Results from the cross-checks to Ref. [126].

Check		p-value	Significance
RFC 2022a + IceCat-1	With scaling	0.048	1.67
	Without scaling	0.32	0.47
RFC 2019c + Alert-like events	With scaling	0.0043	2.63
	Without scaling	0.2	0.84

and without the scaling factors, 1.3 from the quantiles + 0.5 degrees for systematic uncertainties. Without scaling, the error bars would be the ones in Figure 10.12 Panel (b), while for the scaled-up contours the error bars would be as in Figure 10.12 Panel (d). As the TS definition is kept the same as in Equation 9.2, the signalness is needed. In the selection of 56 alert and alert-like event catalog not all events have a signalness value. The missing values are assumed to be 45.1%, which is the average of the IceCat-1 catalog.

The results of the four tests can be seen in Table 10.6. The lowest p-value of 0.0043 is achieved with the test that is the most similar to Ref. [126], with the same AGN and neutrino catalogs and using the scaling factors in the spatial PDF. When the angular errors are not scaled up, the p-value increases to 0.2, which indicates that the correlations which are contributing to the TS are from AGNs that are from outside the original 90% contours (note that all the sources inside the error region contribute the same to the spatial PDF), and would not have been considered for follow-up observations of dedicated studies. The significance also drops when more neutrino alert events are added and a newer version of the RFC catalog is used, although one could argue that the stricter selection of events in Ref. [126] helps remove the background events.

From the four correlations that drive the result in Ref. [126] (if removed, the significance drops below 2σ), only the correlation of IC150812B with the AGN J2151+0552 has a TS_i large enough to appear in Table 10.5, when the original analysis technique introduced in this thesis is used. This pair is also included in the list of the most significant correlations in the two tests with the RFC 2019c + alert-like events selection. These are shown in Appendix D, in Table D.4 and Table D.3, with and without the scaling factors, respectively. The high TS_i value is due to the high signalness of the neutrino and the high radio brightness of the AGN, of 0.688 Jy.

All of the four most significant correlations from Ref. [126] are found in the test of RFC 2019c + alert-like events with scaling as expected, since this is the test that is closest to their analysis. However, they do not appear if the original uncertainty values are used. The AGNs are, therefore, outside the initial 90% contours as calculated with Millipede. The comparison of the simplified contours with and without scaling are shown in Figure D.4. With the information available and using a larger sample, the significance of the findings of Ref. [126] gets weaker. The only hint of excess that is seen with the test that more closely resembles their analysis disappears when a more sophisticated description of the spatial PDF for the neutrino events is used.

Conclusion

11 Summary and outlook

This thesis covered two main projects. In the technical part, the angular reconstruction method used for realtime track-like alert events is studied. The work proved that the current procedure to obtain the 90% C.L. contours leads to under-/overcoverage when individual events are considered. Based on this result and using the tools and simulations developed to arrive to that conclusion, new reconstruction methods are being tested as the next generation for the IceCube's Realtime System.

The second half of this thesis was devoted to searches for the sources of the muon-neutrino alert events. A stacking analysis method was developed that utilizes the information contained in the shape of the likelihood contours around the best fit of the maximum-likelihood reconstruction method. This information is included in the neutrino spatial PDF to enhance the sensitivity of correlation studies between high-energy neutrinos and source candidates. The neutrino production mechanism at a candidate source class is considered as well. The observational data of the source is used as a proxy for the neutrino emission and enters the analysis as a weight. The method adds up the contributions from all the alerts to calculate the overall correlation with candidate sources.

Two catalogs of sources were tested, gamma-ray blazars from *Fermi*-LAT 4LAC-DR2 and radio-bright AGNs from RFC 2022a. Two different weighting schemes were considered for the former catalog. In all three cases, the results were compatible with a background-only scenario. The contribution of these sources to the flux of astrophysical neutrino alert events cannot be larger than 1%. Better sensitivity for this analysis method could be achieved by incorporating the results of the systematic studies of this thesis discussed in Chapter 5 and Chapter 6. Even further improvements could be obtained by using the proposed (although still under discussion) algorithms to substitute the current implementation of Millipede for alert events (Chapter 7).

Any signal would become stronger with more detections of candidate sources and neutrinos, optimized selection criteria and better localizations. The future generation of telescopes, such as the Cherenkov Telescope Array (CTA) in gamma rays [195], ULTRASAT in the UV band [196] or SKA in the radio band [197], will perform all-sky surveys that will increase the number of objects in the catalogs and our knowledge of them. They will also be able to follow up the high-energy neutrino alert events and neutrino sources with enhanced performance.

IceCube-Gen2 [65] is planned to be deployed in the next decade and will increase the instrumented volume from 1 km^3 to $\sim$ 8 km^3. The extension will consist of 120 new strings with a total of 9600 improved multi-PMT optical modules that will be able to detect three times as many photons as the IceCube DOMs [198]. The array of strings will be sparser than the current one, with an average horizontal spacing of 240 m, and a sunflower geometry to avoid "corridors" of strings, see Figure 11.1. The in-ice array will also be accompanied by a 500 km^2 radio array deployed near the surface which is optimized for the detection

[195]: (2018), *Science with the Cherenkov Telescope Array*

[196]: Sagiv et al. (2014), 'Science with a wide-field UV Transient Explorer'

[197]: Carilli et al. (2004), 'Motivation, key science projects, standards and assumptions'

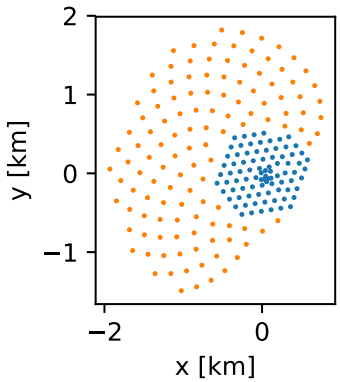

Figure 11.1: Layout of the in-ice strings for IceCube-Gen2. The blue dots represent the current strings in IceCube.

[65]: Aartsen et al. (2021), 'IceCube-Gen2: the window to the extreme Universe'

[198]: Abbasi et al. (2022), 'Design and performance of the multi-PMT optical module for IceCube Upgrade'

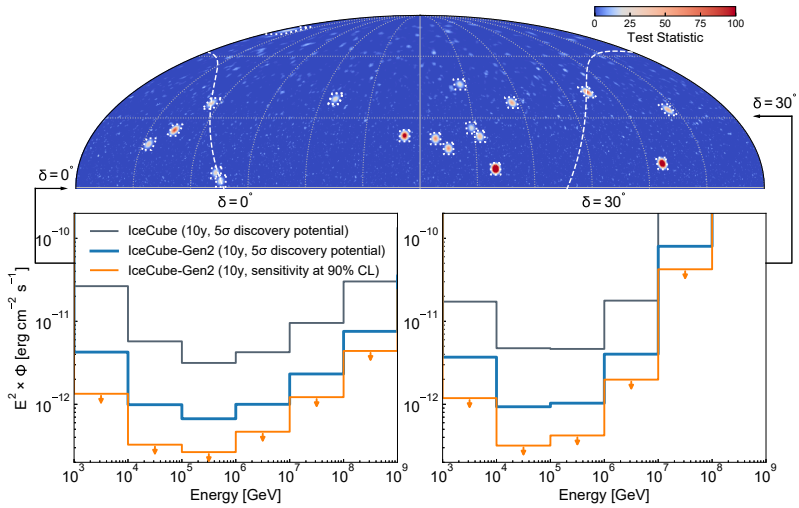

Figure 11.2: Expected sensitivity for neutrino source searches with IceCube-Gen2. From [65].

of >100 PeV neutrinos. This will open the possibility of measuring the cosmogenic neutrinos produced in interactions of UHECRs and photons from the cosmic microwave background [199].

[199]: Meyers et al. (2021), *Radio Detection of EeV Neutrinos in Dielectric Media using the Askaryan Effect* *for Babies*

This upgrade is of special interest to the IceCube Realtime System because it increases the sensitivity at high energies (see Figure 11.2), allowing us to measure more neutrino alert events. IceCube-Gen2 is expected to detect about 5 times more high-energy track-like neutrino events compared to IceCube. The higher energy of the events will help distinguish astrophysical neutrinos from atmospheric backgrounds. A 10 PeV muon will travel on average 17 km before its energy drops below 10 TeV, so a large instrumented volume is needed to detect a significant part of the track. The longer lever arm also results in improved angular resolution, enhancing the significance of a spatial correlation and reducing the fraction of chance coincidences with optical transients.

IceCube-Gen2 will not be the only neutrino telescope completed in the following years. KM3NeT [70] in the Mediterranean Sea and the Gigaton Volume Detector (GVD) [72] in Lake Baikal are under construction. Together with the planned Pacific Ocean Neutrino Experiment (P-ONE) [71] that is under development, the Southern sky will be observed with high sensitivity by these new instruments.

[70]: Margiotta (2014), 'The KM3NeT deep-sea neutrino telescope'

[72]: Shoibonov et al. (2019), 'Baikal-GVD - the Next Generation Neutrino Telescope in Lake Baikal'

[71]: Agostini et al. (2020), 'The Pacific Ocean Neutrino Experiment'

Multimessenger astronomy, including the exciting field of neutrino astronomy, is still in its early stages. However, the future for these areas of research looks extremely promising. In the coming years, neutrino astronomy will hopefully become a well-established discipline, enabling us not only to identify sources of neutrinos, but also to conduct detailed studies by combining the information from all detectable messengers. This will broaden our understanding of the universe and facilitate groundbreaking discoveries.

Appendix

A

GCN Notice and Circular for an example event

Here, examples of a GCN Notice and a GCN Circular for the neutrino alert IC230401A are presented. Figure A.1 shows the likelihood landscape from the Millipede reconstruction, which by the time of the neutrino detection is only available to the members of the IceCube collaboration. In the GCN Notice (Appendix A.1), the angular reconstruction is done with SplineMPE, represented in Figure A.1 as the magenta lines, and published as a direction with a circularized angular error. From the error contours of Millipede, shown as the black lines in Figure A.1, only the coordinate-wise errors in right ascension and declination are published in the GCN Circular (Appendix A.2). These are calculated as the maximum and minimum point in each direction. The links are included here:

- GCN Notice: `https://gcn.gsfc.nasa.gov/notices_amon_g_b/137794_38132005.amon`
- GCN Circular: `https://gcn.nasa.gov/circulars/33552`

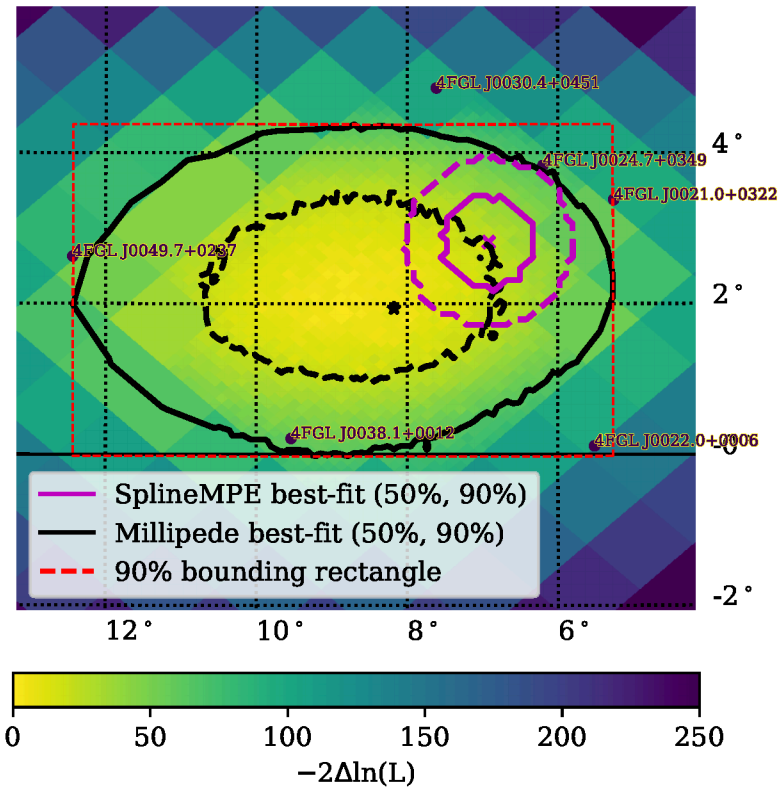

Figure A.1: Millipede reconstruction of the neutrino alert IC230401A. The black star is the best-fit position and the black dashed and solid lines represent the 50% and 90% error contours, respectively. The red rectangle represents the values that are published in the GCN Circulars and is defined as the minimal rectangle that encapsulates the 90% error contour. The magenta cross and the magenta solid and dashed lines represent the best-fit position, and 50% and 90% error contours calculated with SplineMPE and published in the GCN Notice.

A.1 GCN Notice

```
TITLE:            GCN/AMON NOTICE
NOTICE_DATE:      Sat 01 Apr 23 16:15:03 UT
NOTICE_TYPE:      ICECUBE Astrotrack Bronze
STREAM:           25
RUN_NUM:          137794
EVENT_NUM:        38132005
SRC_RA:           6.9169d {+00h 27m 40s} (J2000),
                  7.2156d {+00h 28m 52s} (current),
                  6.2749d {+00h 25m 06s} (1950)
SRC_DEC:          +2.8179d {+02d 49' 04"} (J2000),
                  +2.9463d {+02d 56' 47"} (current),
                  +2.5413d {+02d 32' 29"} (1950)
SRC_ERROR:        93.25 [arcmin radius, stat-only, 90% containment]
SRC_ERROR50:      36.32 [arcmin radius, stat-only, 50% containment]
DISCOVERY_DATE:   20035 TJD;    91 DOY;   23/04/01 (yy/mm/dd)
DISCOVERY_TIME:   58458 SOD {16:14:18.90} UT
REVISION:         0
ENERGY:           1.1079e+02 [TeV]
SIGNALNESS:       2.7409e-01 [dn]
FAR:              4.1124 [yr^-1]
SUN_POSTN:        10.74d {+00h 42m 58s}   +4.62d {+04d 37' 06"}
SUN_DIST:         3.90 [deg]   Sun_angle= 0.2 [hr] (West of Sun)
MOON_POSTN:       144.71d {+09h 38m 51s}  +19.38d {+19d 22' 42"}
MOON_DIST:        132.65 [deg]
GAL_COORDS:       111.17,-59.51 [deg] galactic lon,lat of the event
ECL_COORDS:       7.46, -0.16 [deg] ecliptic lon,lat of the event
COMMENTS:         IceCube Bronze event.
COMMENTS:         The position error is statistical only, there is no systematic
                  added.
```

A.2 GCN Circular

```
TITLE:   GCN CIRCULAR
NUMBER:  33552
SUBJECT: IceCube-230401A: IceCube observation of a high-energy neutrino candidate
DATE:    23/04/01 17:13:32 GMT
FROM:    Cristina Lagunas Gualda at DESY  <cristina.lagunas@desy.de>

The IceCube Collaboration (http://icecube.wisc.edu/) reports:

On 23-04-01 at 16:14:18.91 UT IceCube detected a track-like event with a moderate
probability of being of astrophysical origin. The event was selected by the
ICECUBE_Astrotrack_BRONZE alert stream. The average astrophysical neutrino purity
for Bronze alerts is 30%. This alert has an estimated false alarm rate of 4.11
events per year due to atmospheric backgrounds. The IceCube detector was in a
normal operating state at the time of detection.

After the initial automated alert (https://gcn.gsfc.nasa.gov/notices_amon_g_b/
137794_38132005.amon), more sophisticated reconstruction algorithms have been
applied offline, with the direction refined to:

Date: 23-04-01
Time:  16:14:18.91 UT
RA: 8.17 (+4.26/-2.91 deg  90% PSF containment) J2000
Dec: +1.94 (+2.44/-1.96 deg 90% PSF containment) J2000

We encourage follow-up by ground and space-based instruments to help identify a
possible astrophysical source for the candidate neutrino.

There are several Fermi 4FGL or 3FHL catalog sources in the 90% uncertainty
region. The nearest gamma-ray source is 4FGL J0038.1+0012 at RA: 9.54 deg,
Dec: 0.21 deg (2.20 deg away from the best-fit event position).

The IceCube Neutrino Observatory is a cubic-kilometer neutrino detector operating
at the geographic South Pole, Antarctica. The IceCube realtime alert point of
contact can be reached at roc@icecube.wisc.edu
```

B

Golden Muons

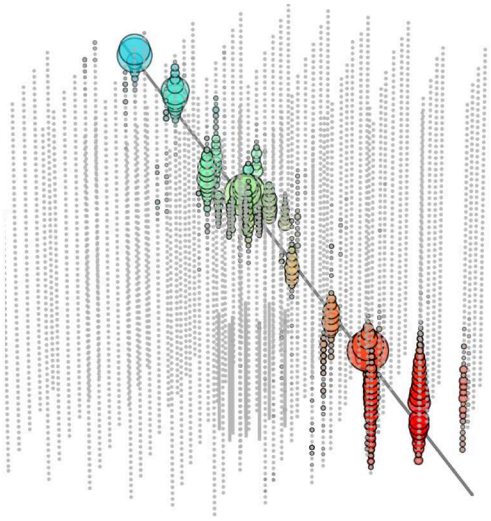

(a) *Upgoing Smooth*

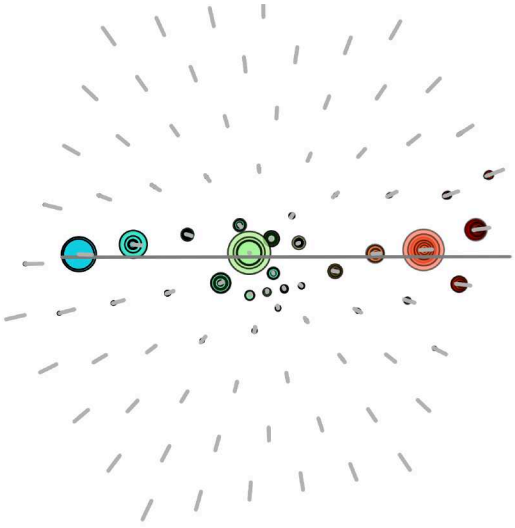

(b) *Upgoing Smooth*, top view.

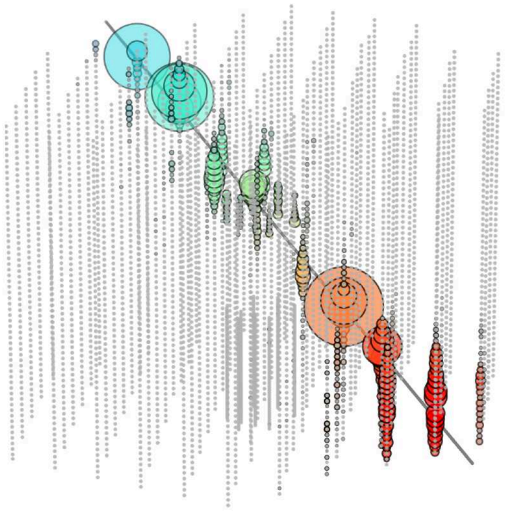

(c) *Upgoing Stochastic*

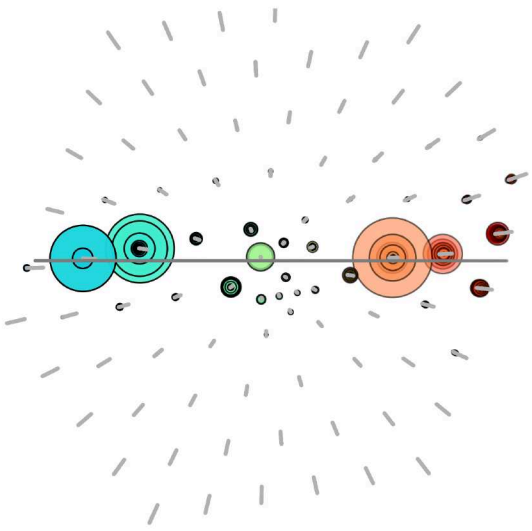

(d) *Upgoing Stochastic*, top view.

Figure B.1: Representative event views of the *Upgoing* categories of Golden Muons. The gray line shows the track of the muon. The color represents the arrival time of the photons, from early (red) to late (blue). The size of the hits is proportional to the deposited charge.

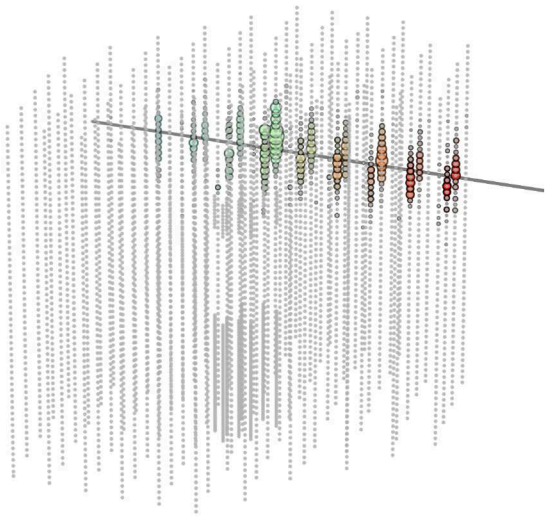

(a) *Horizontal Shallow Smooth Far from DOMs*

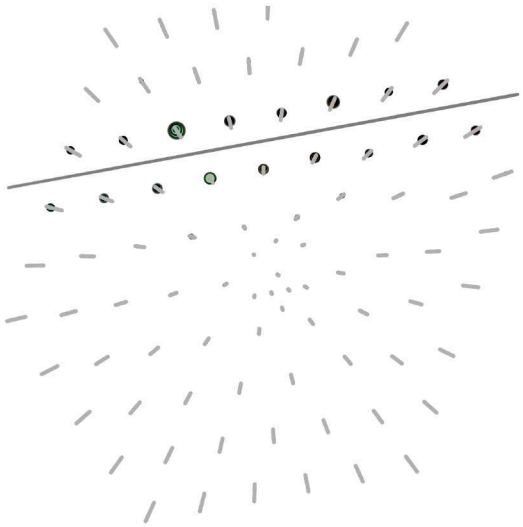

(b) *Horizontal Shallow Smooth Far from DOMs*, top view.

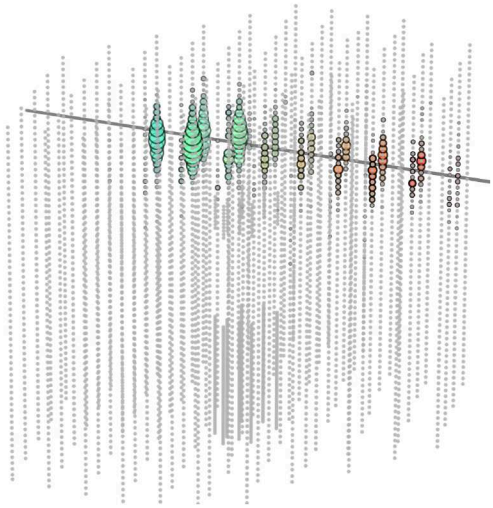

(c) *Horizontal Shallow Stochastic Far from DOMs*

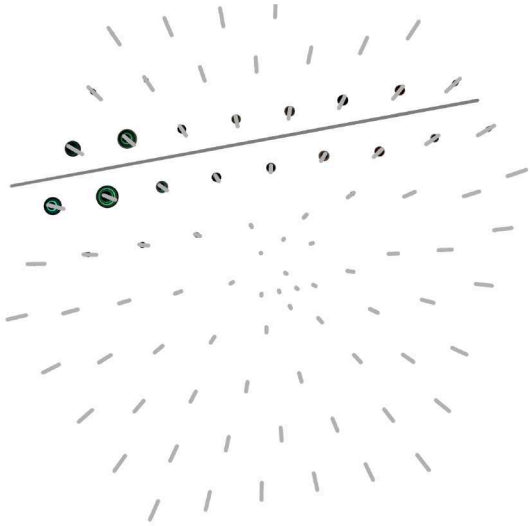

(d) *Horizontal Shallow Stochastic Far from DOMs*, top view.

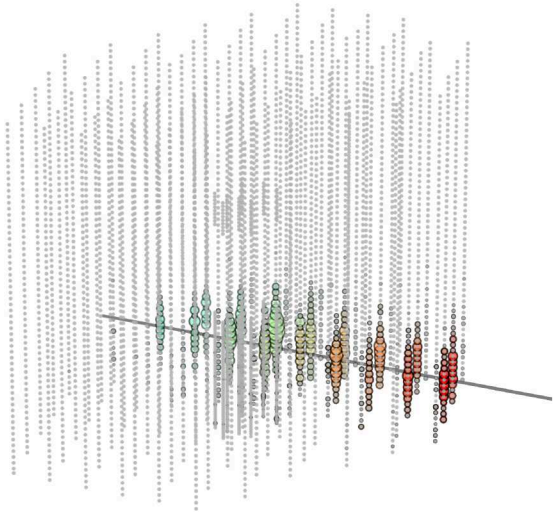

(e) *Horizontal Deep Smooth Far from DOMs*

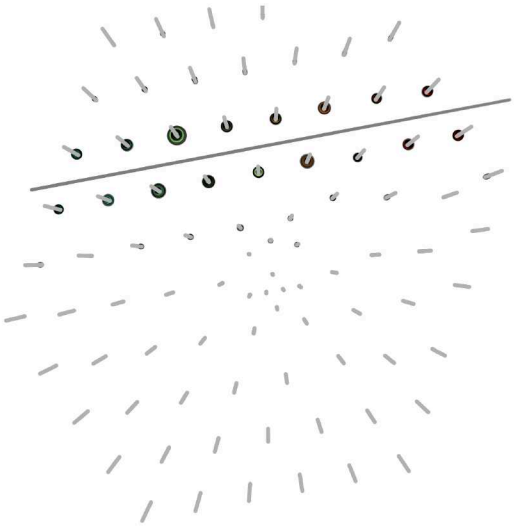

(f) *Horizontal Deep Smooth Far from DOMs*, top view.

Figure B.2: Representative event views of 3 of the *Horizontal* categories of Golden Muons. One can see that events with the same energy produce more light in the lower part of the detector due to the clearer ice.

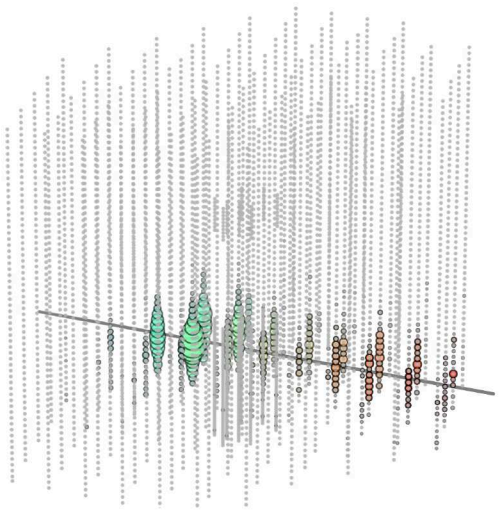

(a) *Horizontal Deep Stochastic Far from DOMs*

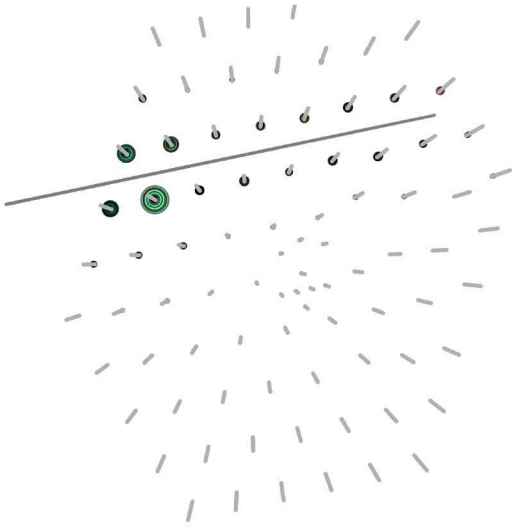

(b) *Horizontal Deep Stochastic Far from DOMs*, top view.

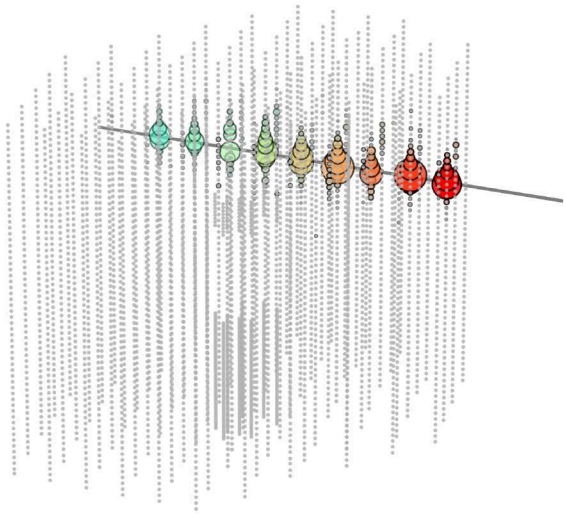

(c) *Horizontal Shallow Smooth Close to DOMs*

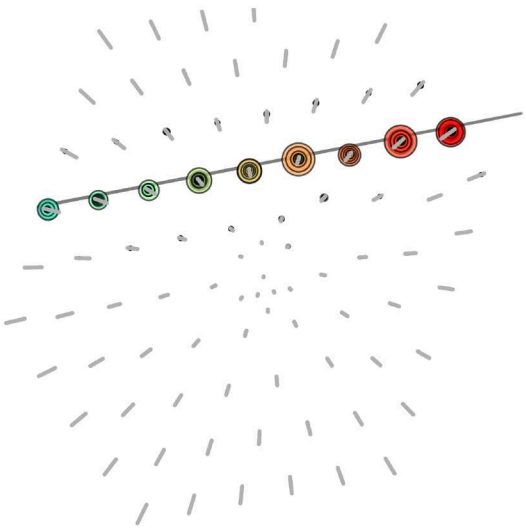

(d) *Horizontal Shallow Smooth Close to DOMs*, top view.

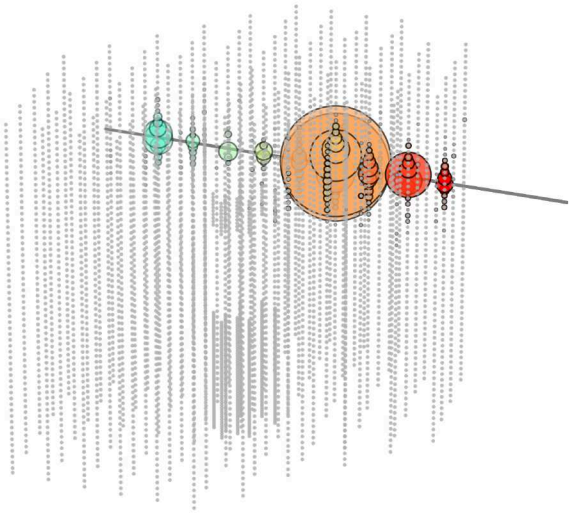

(e) *Horizontal Shallow Stochastic Close to DOMs*

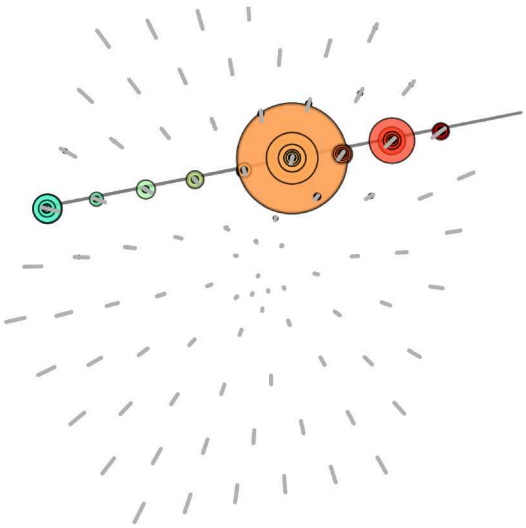

(f) *Horizontal Shallow Stochastic Close to DOMs*, top view.

Figure B.3: Representative event views of 3 of the *Horizontal* categories of Golden Muons.

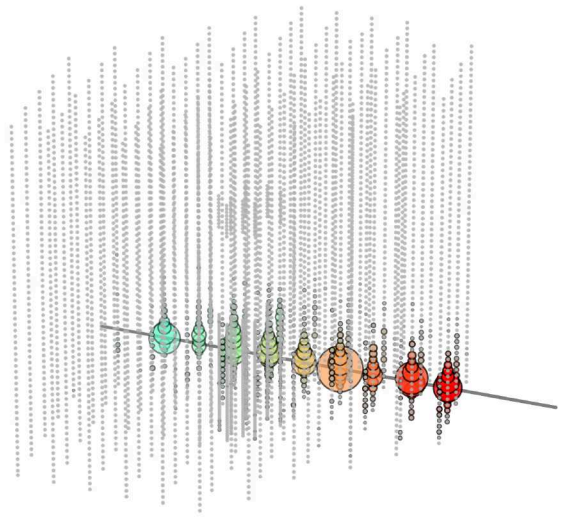

(a) *Horizontal Deep Smooth Close to DOMs*

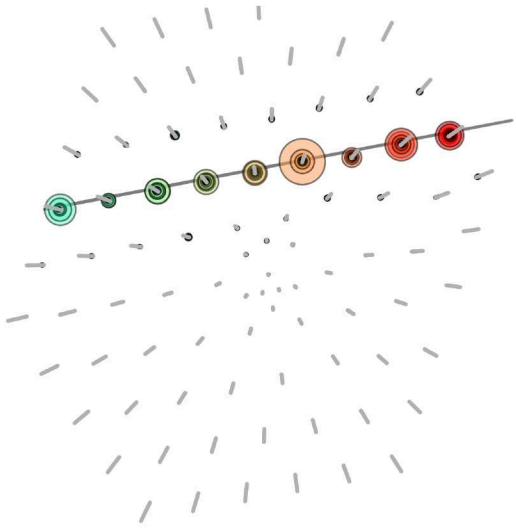

(b) *Horizontal Deep Smooth Close to DOMs*, top view.

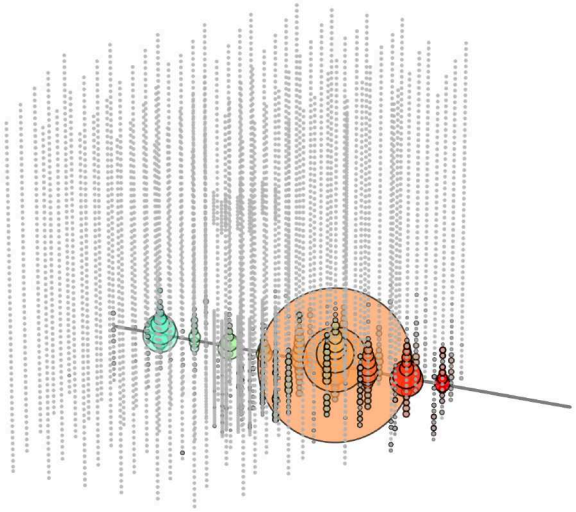

(c) *Horizontal Deep Stochastic Close to DOMs*

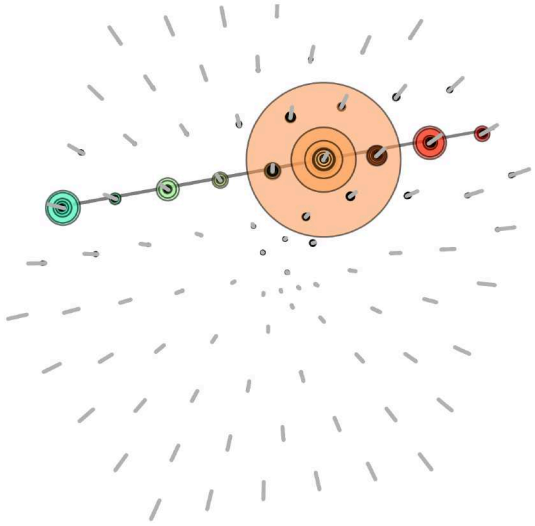

(d) *Horizontal Deep Stochastic Close to DOMs*, top view.

Figure B.4: Representative event views of 2 of the *Horizontal* categories of Golden Muons.

C

Resimulation of realtime alerts

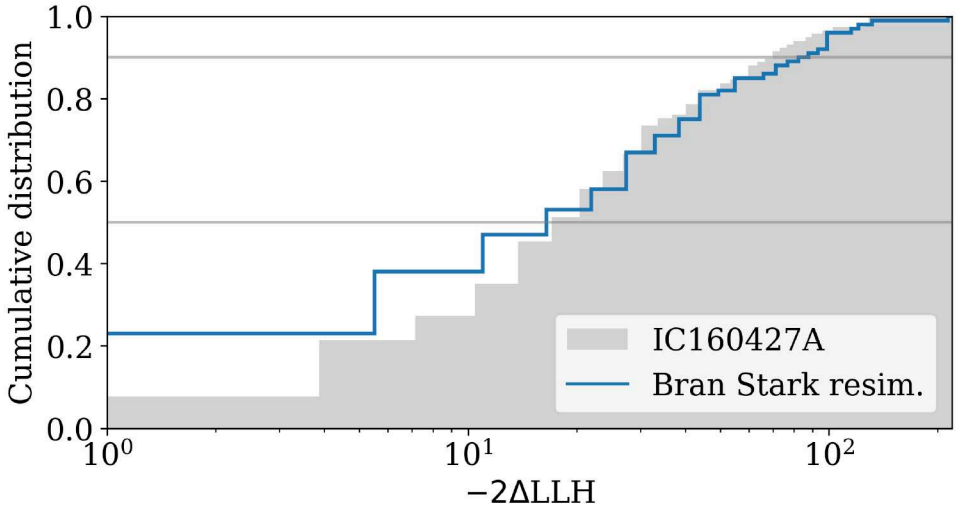

Figure C.1: IC191001A: Cumulative distribution of the −2ΔLLH values for the Bran Stark resimulations

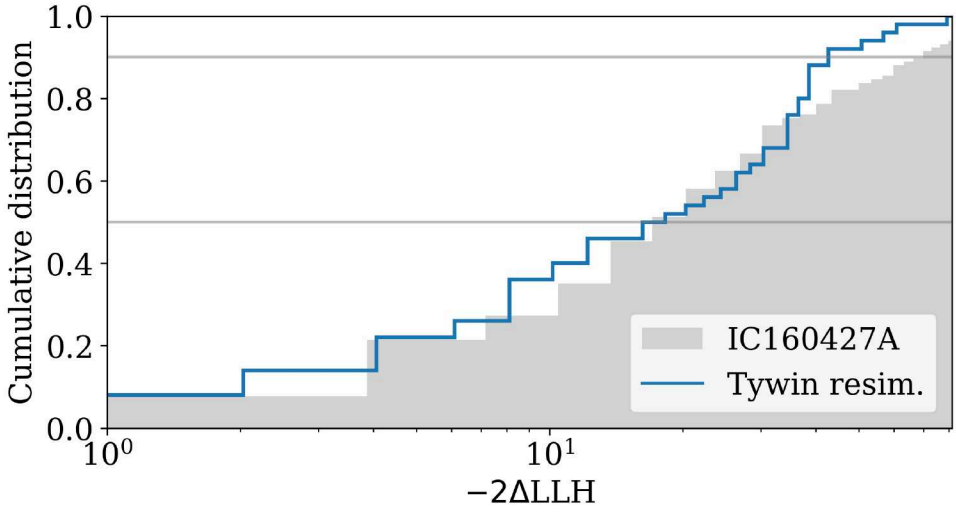

Figure C.2: IC200530A: Cumulative distribution of the −2ΔLLH values for the Tywin resimulations

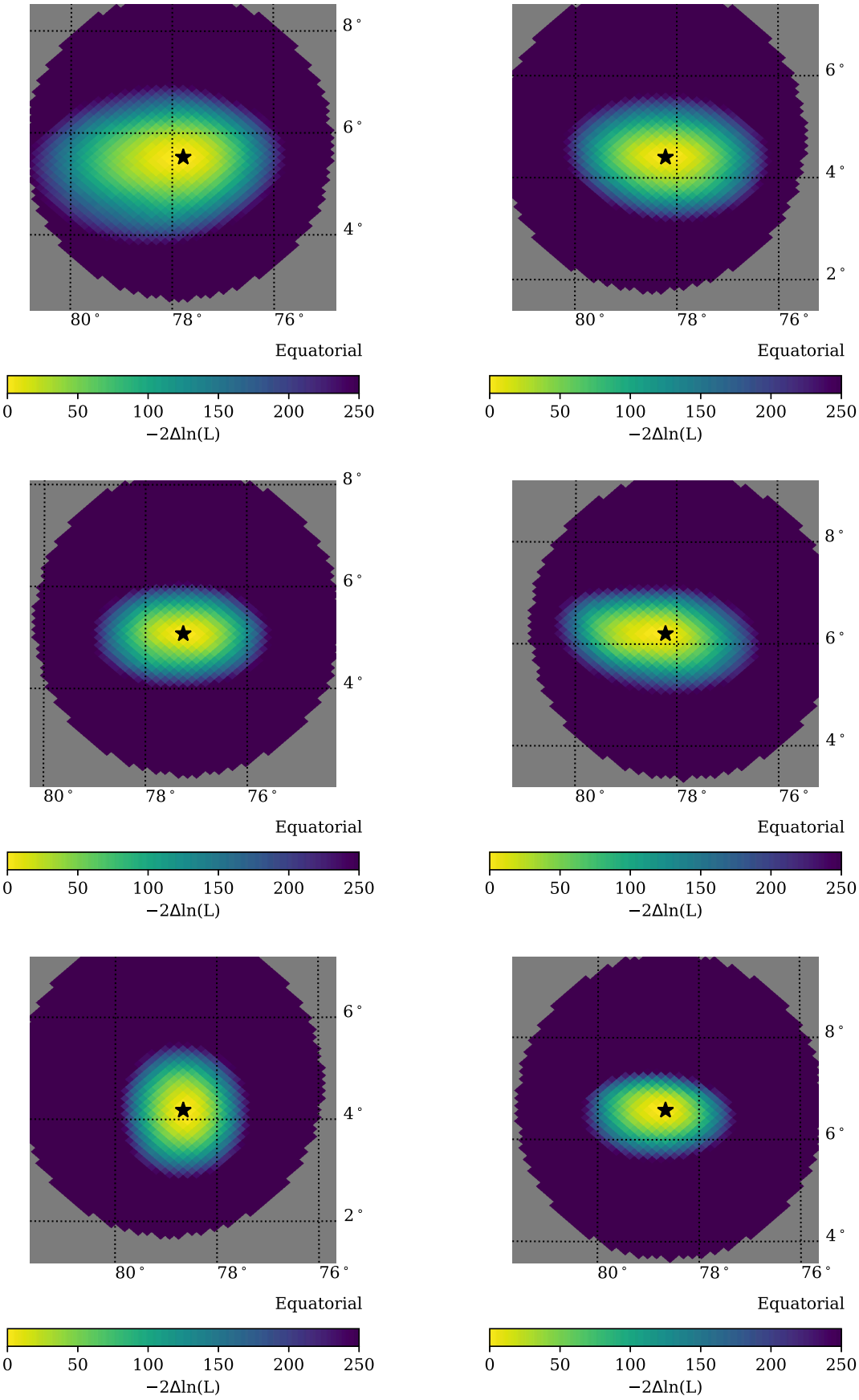

Figure C.3: Zoomed-in likelihood scans of 6 randomly selected resimulated events of the IC170922A (TXS) neutrino, with the *Full Systematics* configuration.

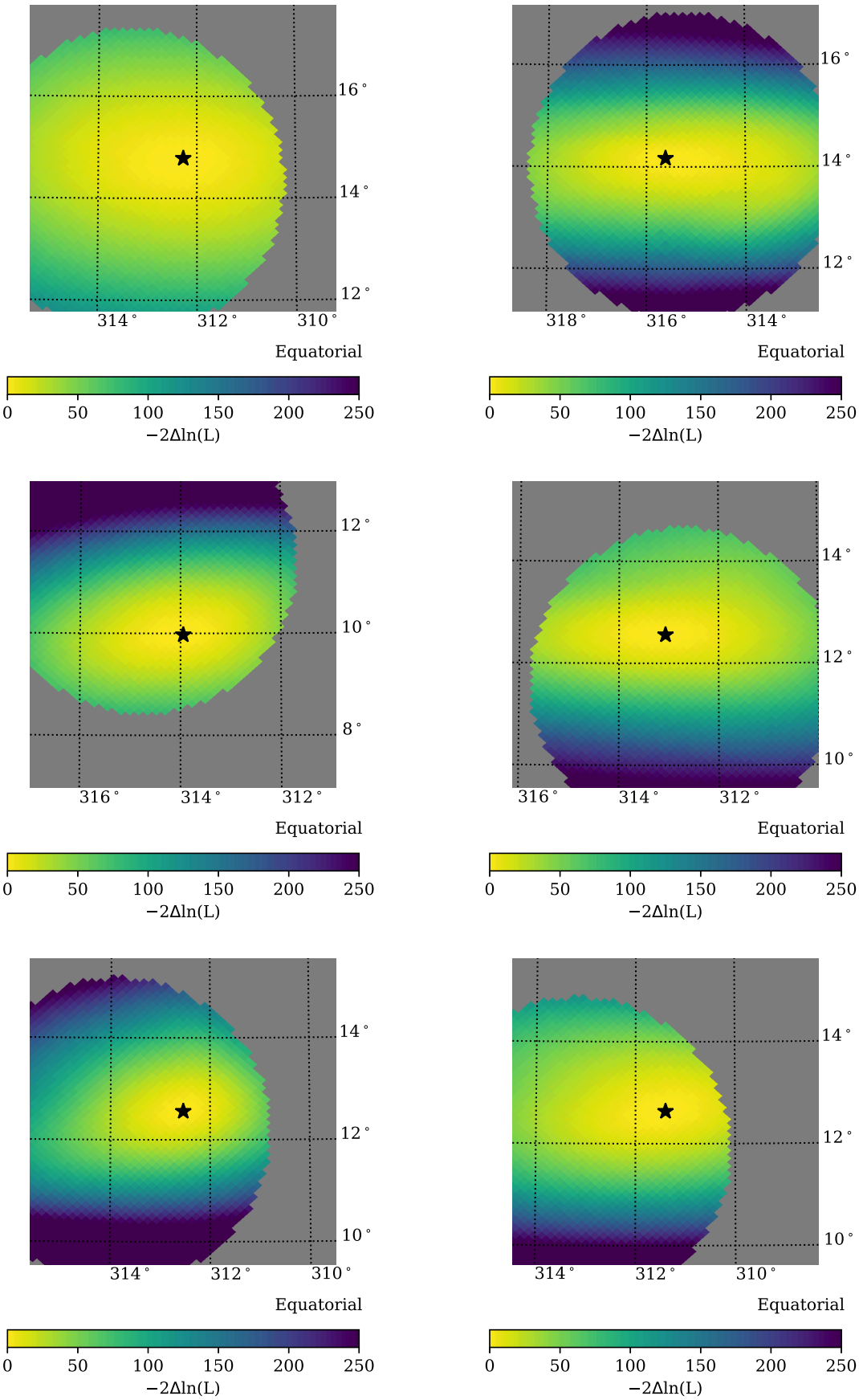

Figure C.4: Zoomed-in likelihood scans of 6 randomly selected resimulated events of the IC191001A (Bran Stark) neutrino.

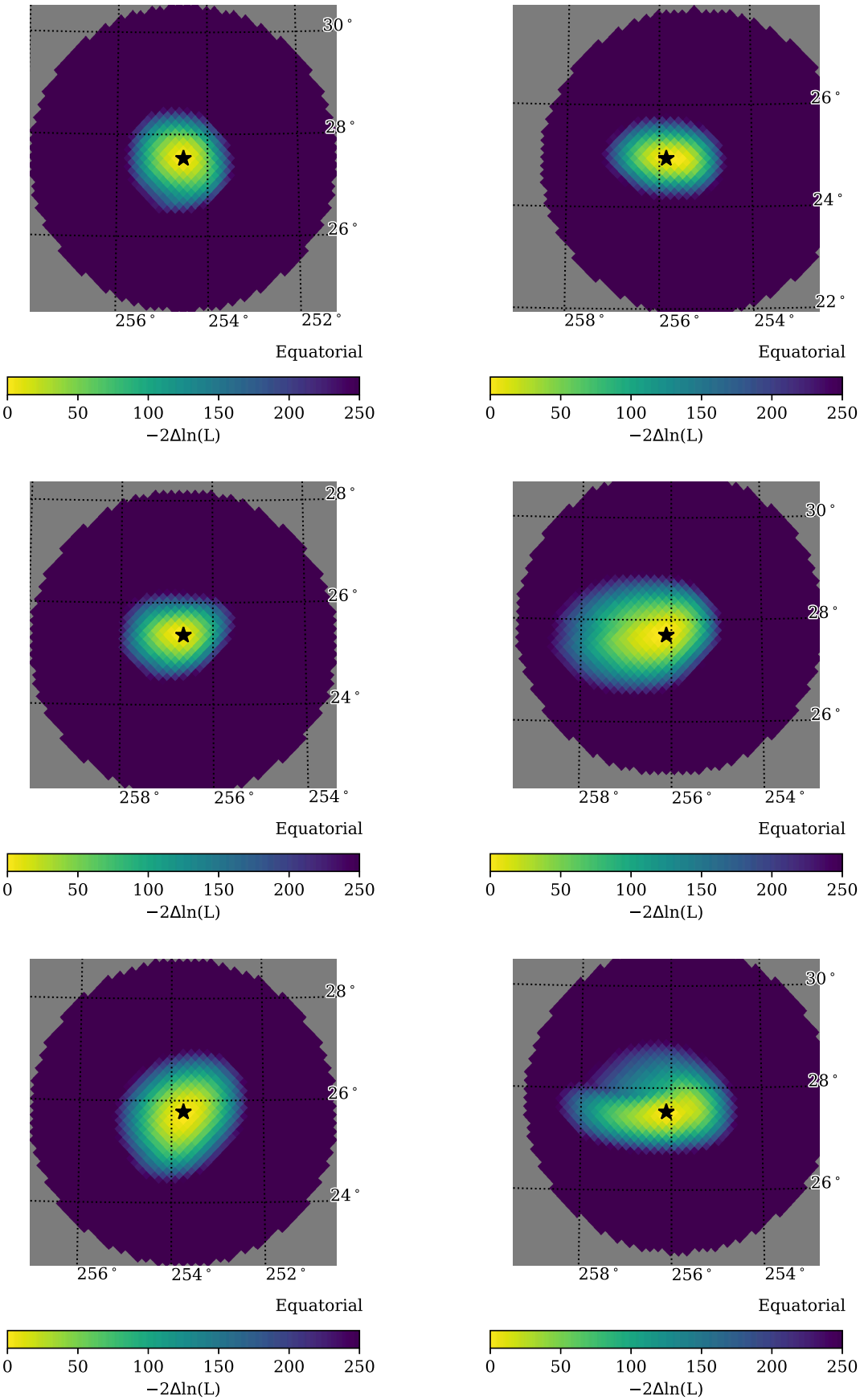

Figure C.5: Zoomed-in likelihood scans of 6 randomly selected resimulated events of the IC200530A (Tywin) neutrino.

D

Additional information to the stacking analyses

In this Appendix, the angular uncertainty regions of the top 10 contributors for each analysis presented in Chapter 10 are shown in Figure D.1, Figure D.2 and Figure D.3. The grey solid and dashed lines are the 50% and 90% uncertainty contours, respectively, corresponding to the best fit (black star). All of the sources from the catalog tested that appear in the area shown in the figures are represented by the colored datapoints. The source that is the most likely counterpart of each neutrino event is mentioned in Table 10.3, Table 10.4 and Table 10.5.

Table D.1, Table D.2, Table D.3 and Table D.4 contain the results of the cross-check on a previously published analysis [126]. In each Table, the 10 most significant correlations of the data are shown. In Table D.3, only 7 correlations appear since there are no more coincidences in the data. The four neutrino events marked in bold in Table D.4 are the top contributors to the result of Ref. [126], and their uncertainty contours are shown in Figure D.4. The dashed grey line is the 90% uncertainty contours from the Millipede reconstruction, while the black solid line is the final contour that is obtained following the scaling procedure, explained in Section 10.5.

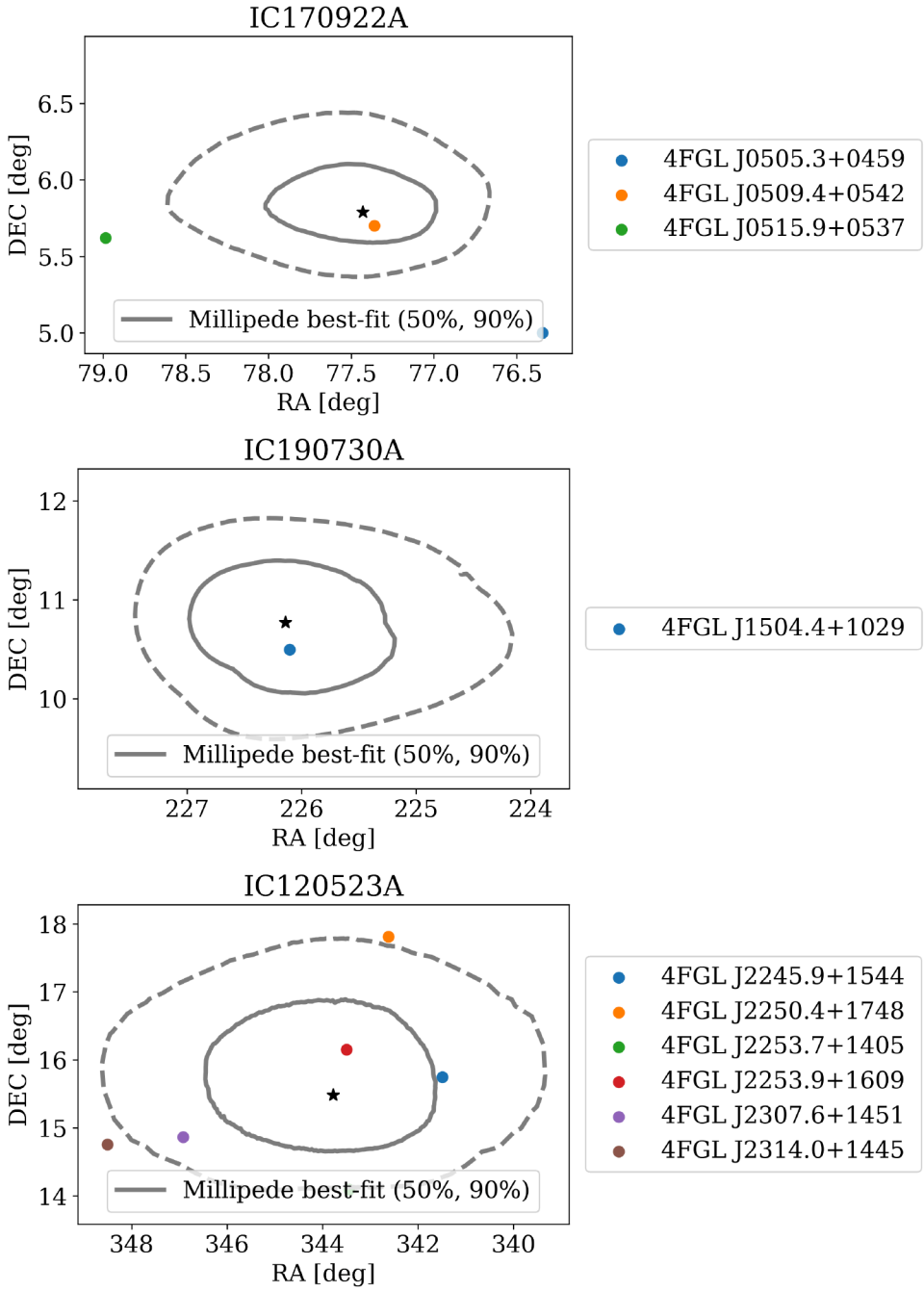

Figure D.1: 50% and 90% error contours for the top 10 contributors to the TS_{data} of the *Fermi*-LAT 4LAC-DR2 catalog with average energy flux weights.The figures are shown in order of the contribution of the neutrino to the TS_{data} value.

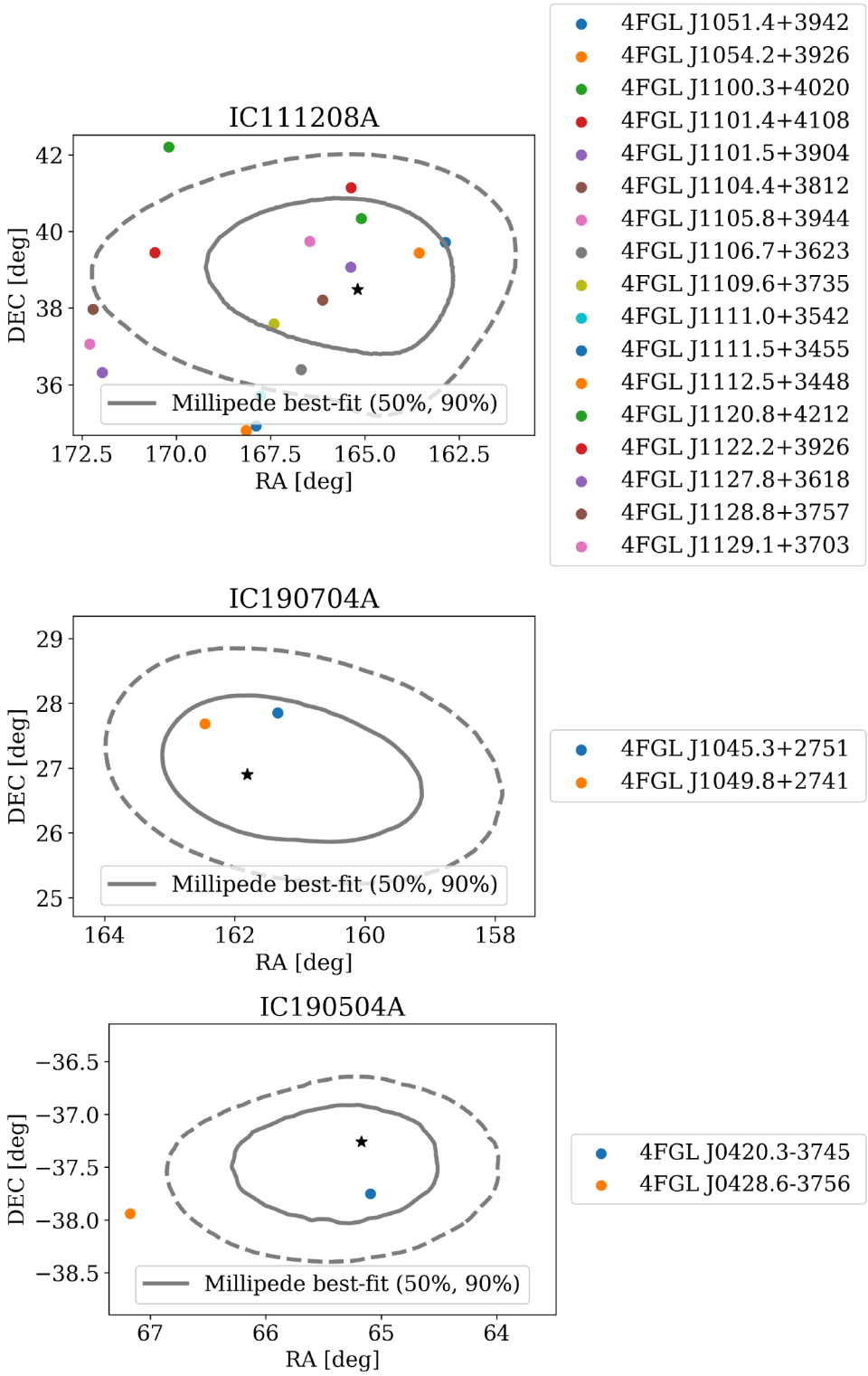

Figure D.1a: Continuation of Figure D.1.

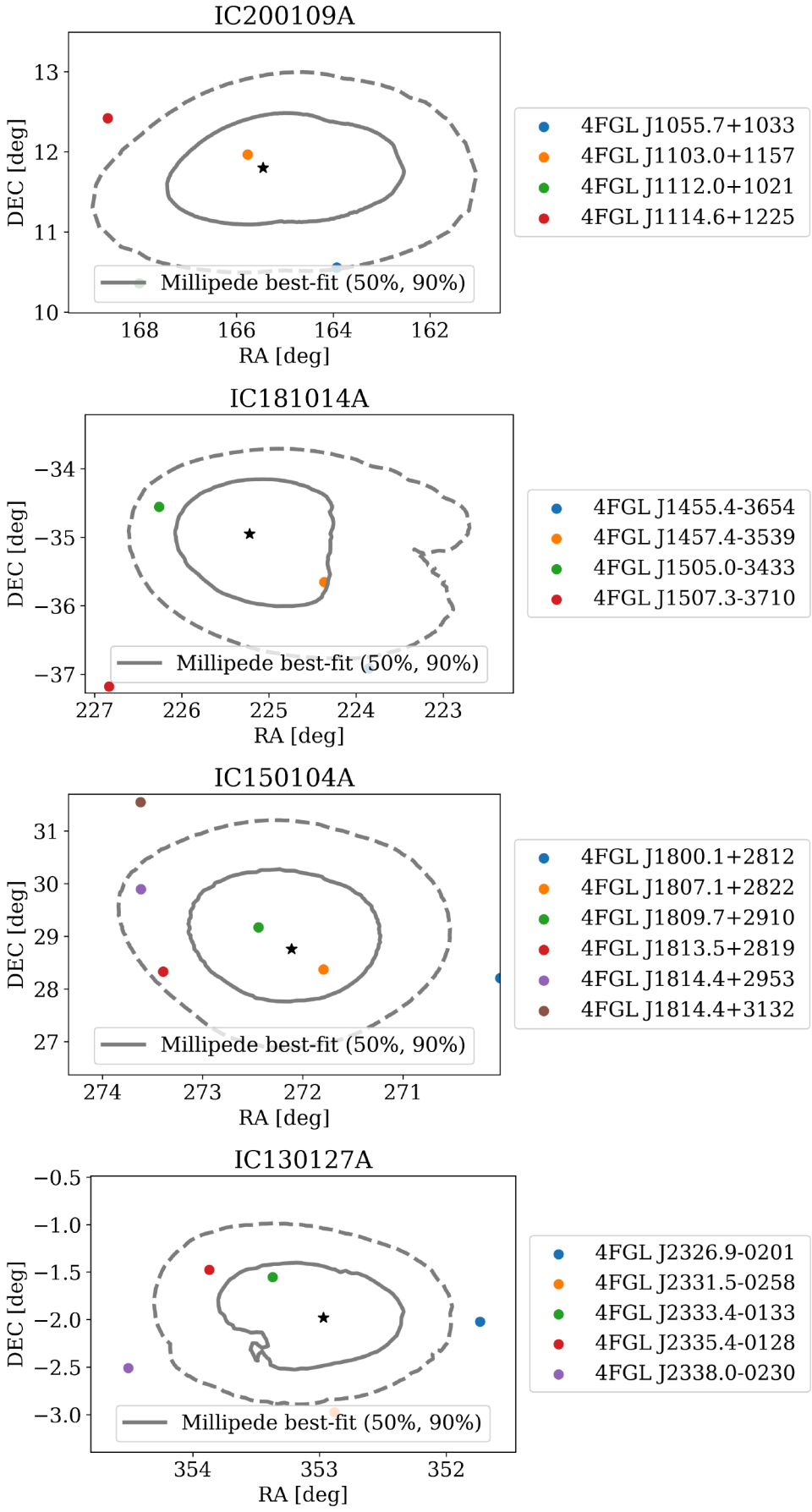

Figure D.1b: Continuation of Figure D.1.

Table D.1: Results from the comparison analysis using RFC 2022a and IceCat-1 catalogs, without scaling of the error contours.

Neutrino	Signalness	AGN	TS_i
IC120523A	49 %	J2253+1608	5.208
IC160812A	53 %	J0555+3948	4.080
IC161127A	45 %	J1927+7358	3.778
IC140103A	42 %	J0217+7349	3.561
IC190730A	67 %	J1504+1029	3.338
IC160924A	51 %	J1549+0237	3.242
IC170422A	39 %	J1550+0527	3.225
IC140223A	43 %	J0741+3112	3.205
IC130125A	53 %	J0019+7327	3.138
IC140307A	40 %	J2025+3343	3.089

Table D.2: Results from the comparison analysis using RFC 2022a and IceCat-1 catalogs, with scaling of the error contours.

Neutrino	Signalness	AGN	TS_i
IC200911A	41 %	J0319+4130	5.495
IC120523A	49 %	J2253+1608	5.208
IC140122A	46 %	J0927+3902	4.840
IC150926A	30 %	J1256-0547	4.814
IC150823A	35 %	J2136+0041	4.383
IC160812A	53 %	J0555+3948	4.080
IC140410A	63 %	J0217+7349	3.964
IC181120A	57 %	J2202+4216	3.923
IC110930A	43 %	J1743-0350	3.843
IC161127A	45 %	J1927+7358	3.778

Table D.3: Results from the comparison analysis using RFC 2019c + Alert-like events, without scaling of the error contours.

Neutrino	Signalness	AGN	TS_i
IC190730A	67 %	J1504+1029	3.277
IC120523A	53 %	J1125+2610	2.530
IC150812B	83 %	J2151+0552	2.416
IC101113A	45 %	J1858+0313	2.114
IC170922A	63 %	J0509+0541	1.976
IC171106A	98 %	J2238+0724	1.785
IC170321A	24 %	J0631-1410	1.278
-	-	-	-
-	-	-	-
-	-	-	-

Table D.4: Results from the comparison analysis using RFC 2019c + Alert-like events, with scaling of the error contours.

Neutrino	Signalness	AGN	TS_i
IC150812B	83 %	J2148+0657	5.004
IC150926A	30 %	J1256-0547	4.818
IC110930A	43 %	J1743-0350	3.853
IC110714A	78 %	J0432+4138	3.383
IC190730A	67 %	J1504+1029	3.277
IC150831A	58 %	J0336+3218	3.237
IC151114A	96 %	J0502+1338	2.806
IC160128A	15 %	J1733-1304	2.759
IC120523A	53 %	J1125+2610	2.530
IC131014A	67 %	J0211+1051	2.472

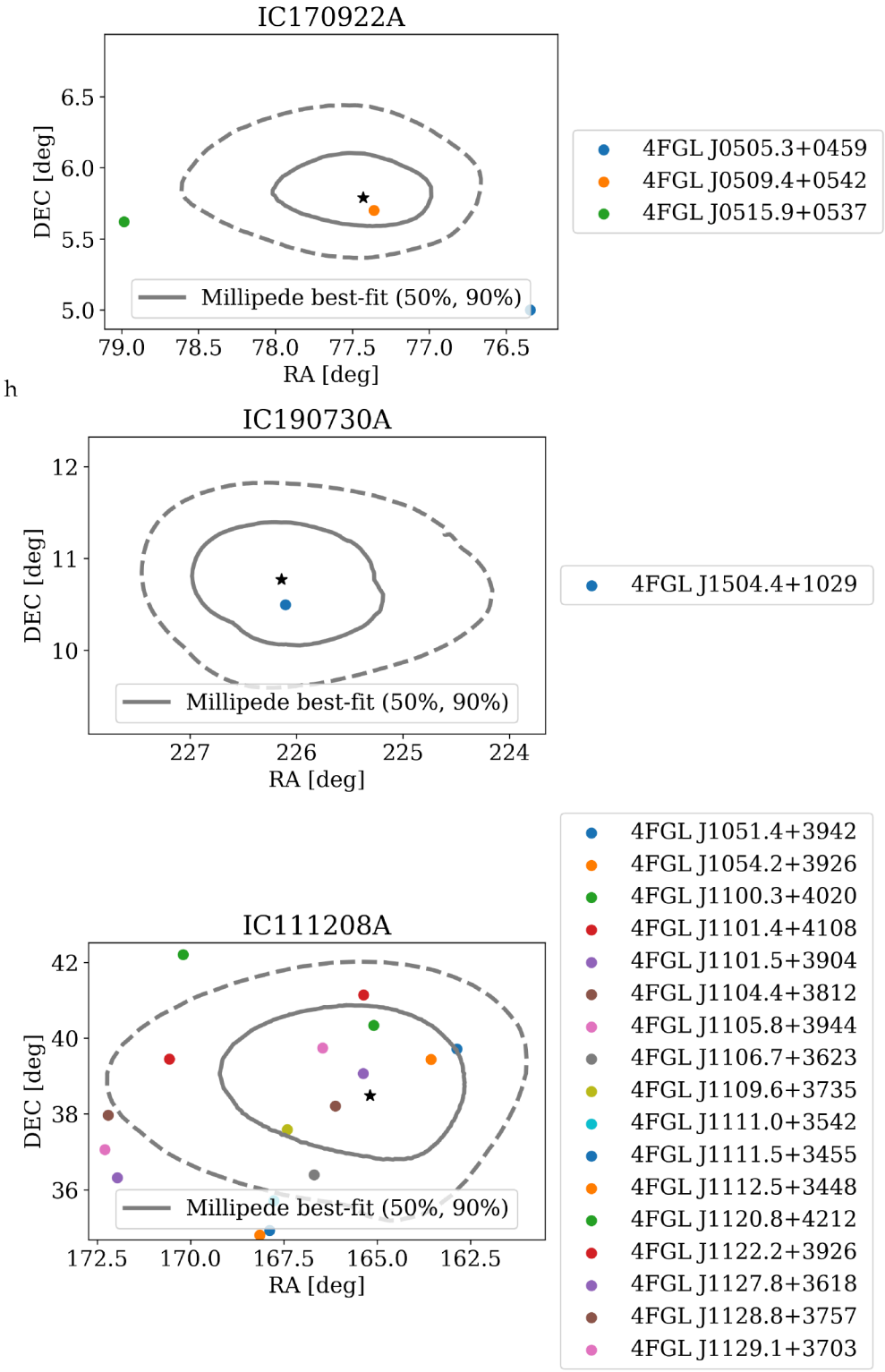

Figure D.2: 50% and 90% error contours for the top 10 contributors to the TS_{data} of the *Fermi*-LAT 4LAC-DR2 catalog with monthly energy flux weights.The figures are shown in order of the contribution of the neutrino to the TS_{data} value.

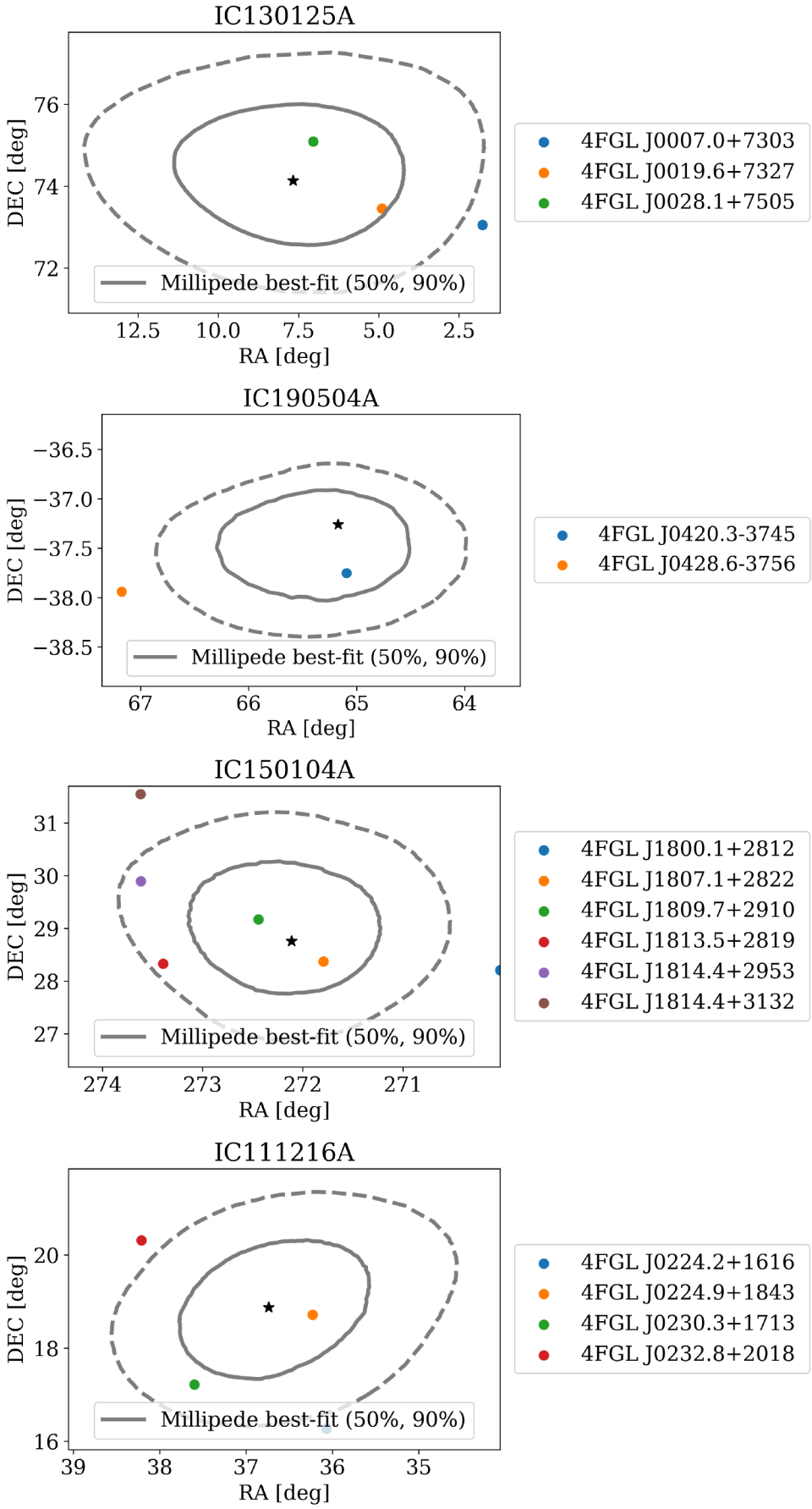

Figure D.2a: Continuation of Figure D.2.

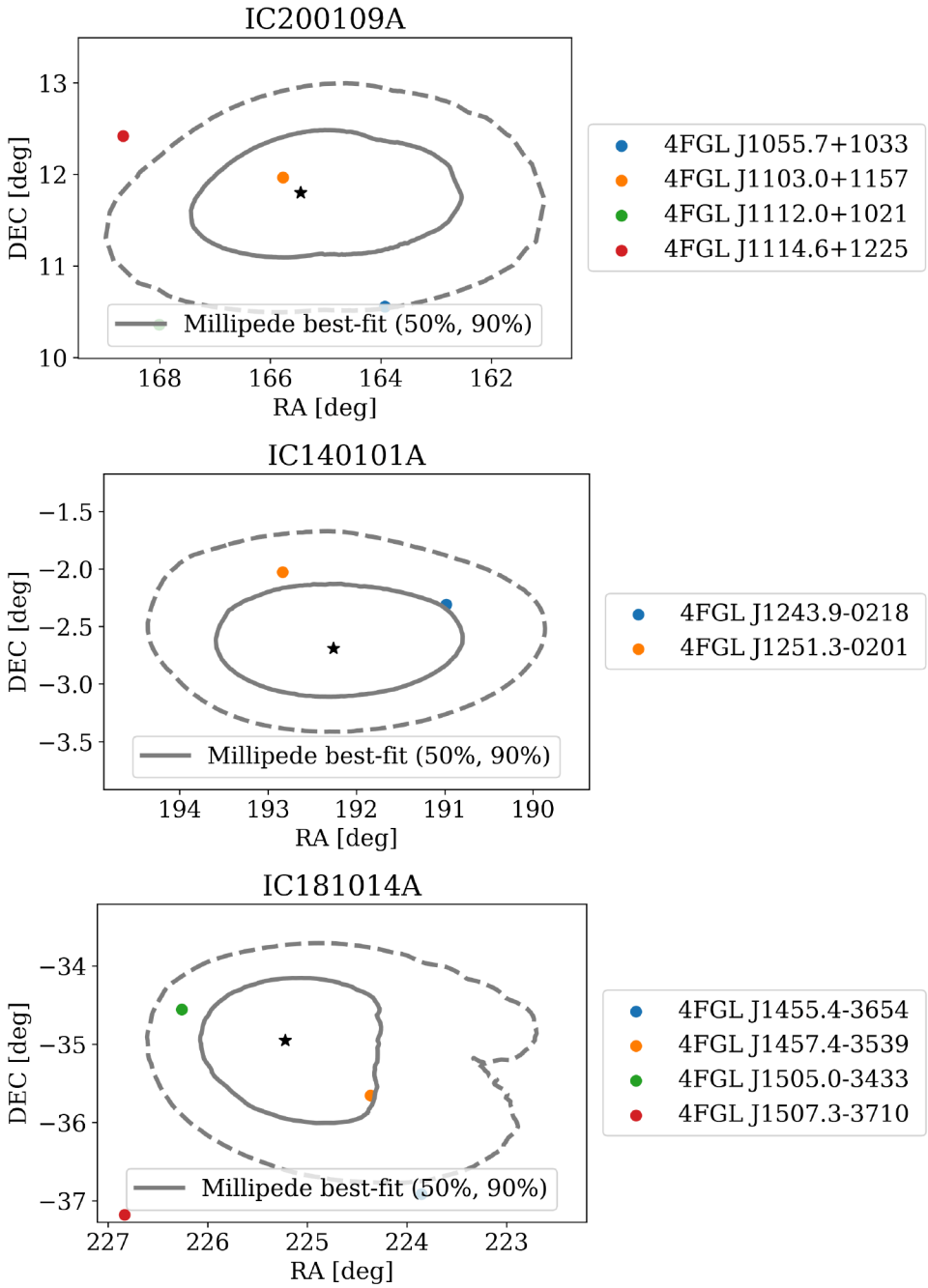

Figure D.2b: Continuation of Figure D.2.

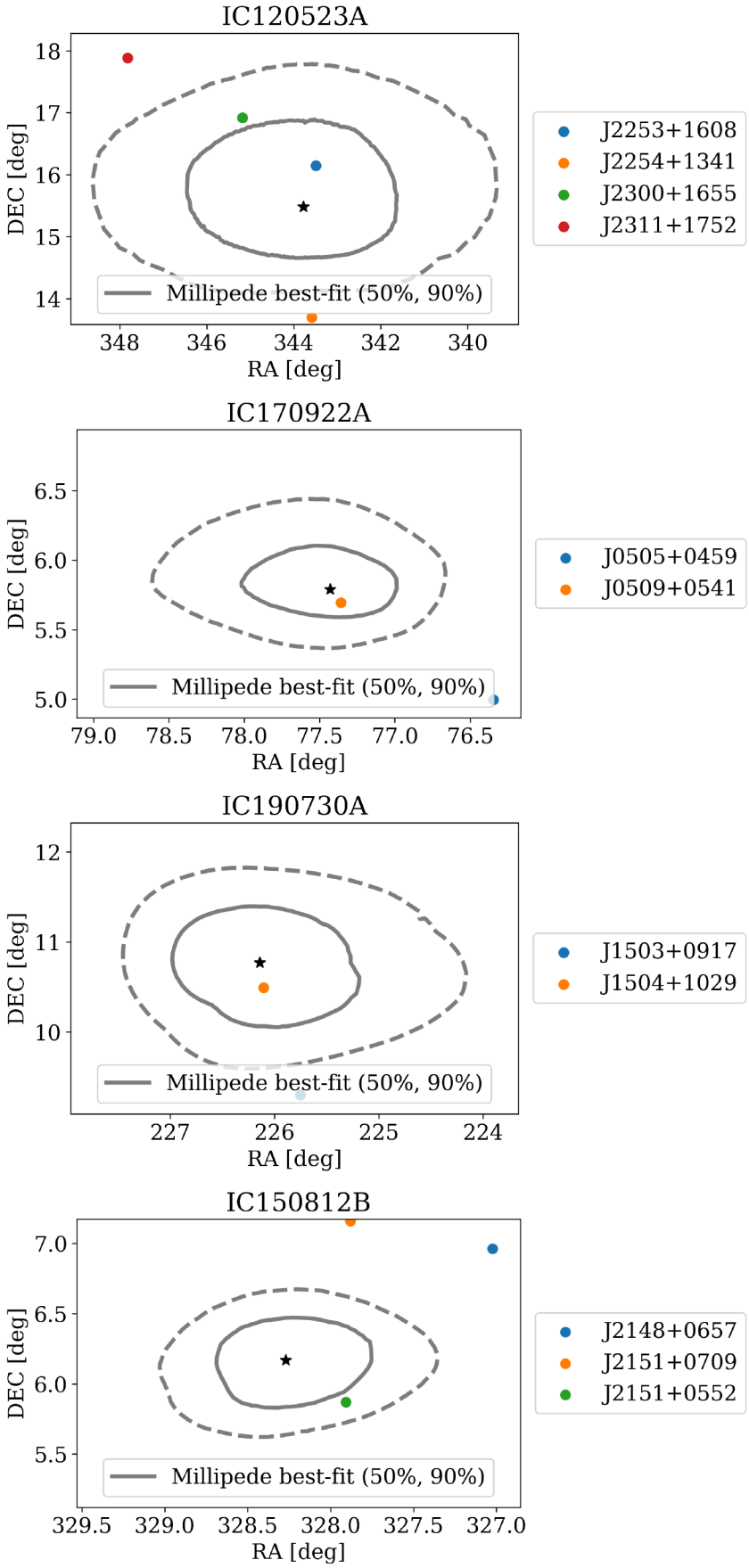

Figure D.3: 50% and 90% error contours for the top 10 contributors to the TS_{data} of the RFC 2022a catalog with average energy flux weights. The figures are shown in order of the contribution of the neutrino to the TS_{data} value.

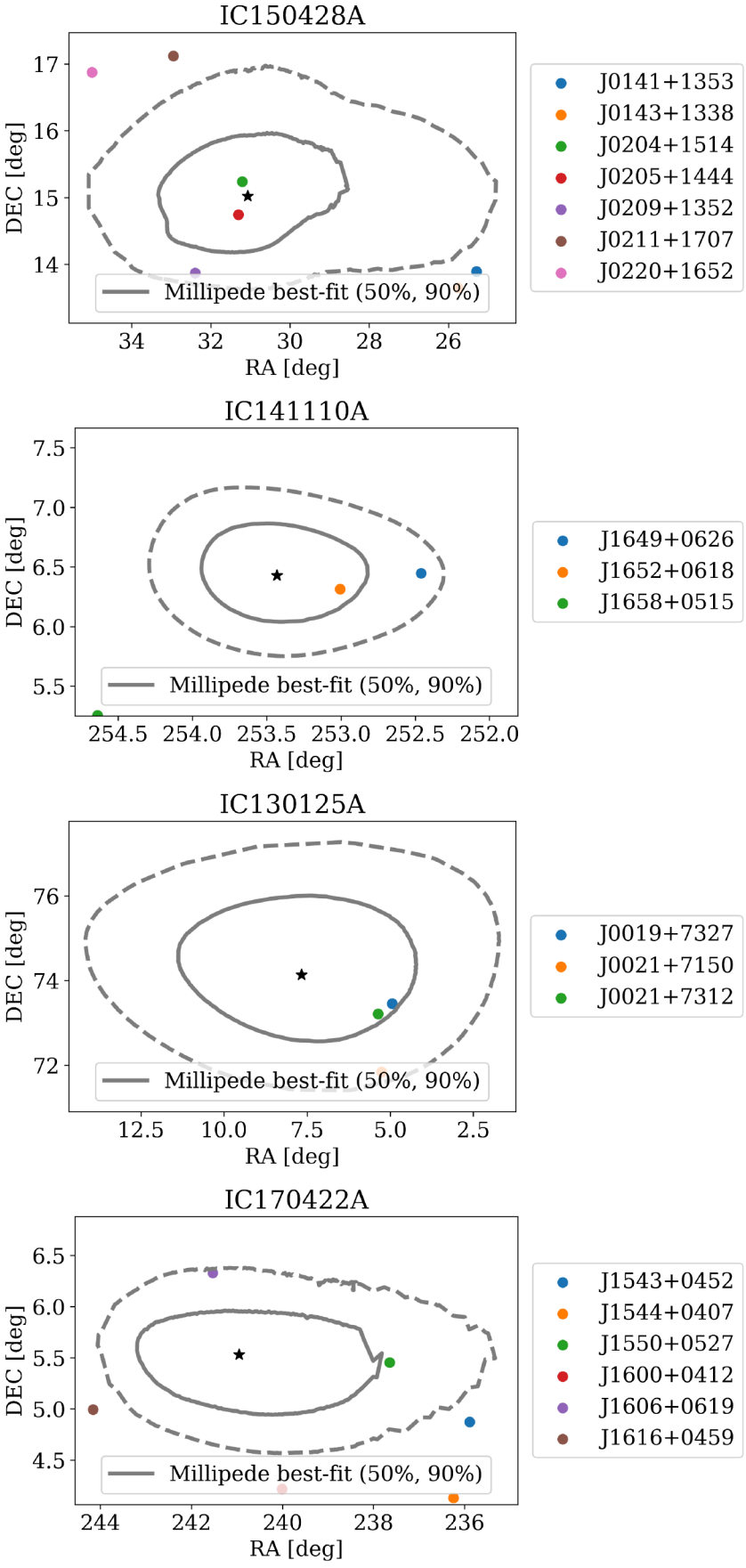

Figure D.3a: Continuation of Figure D.3.

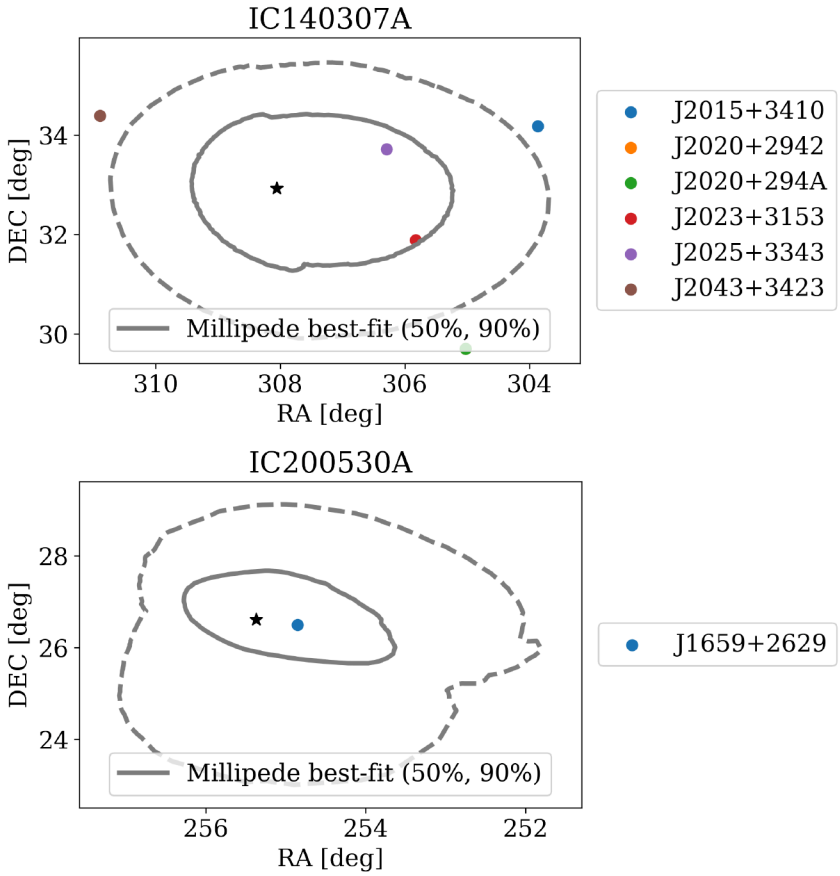

Figure D.3b: Continuation of Figure D.3.

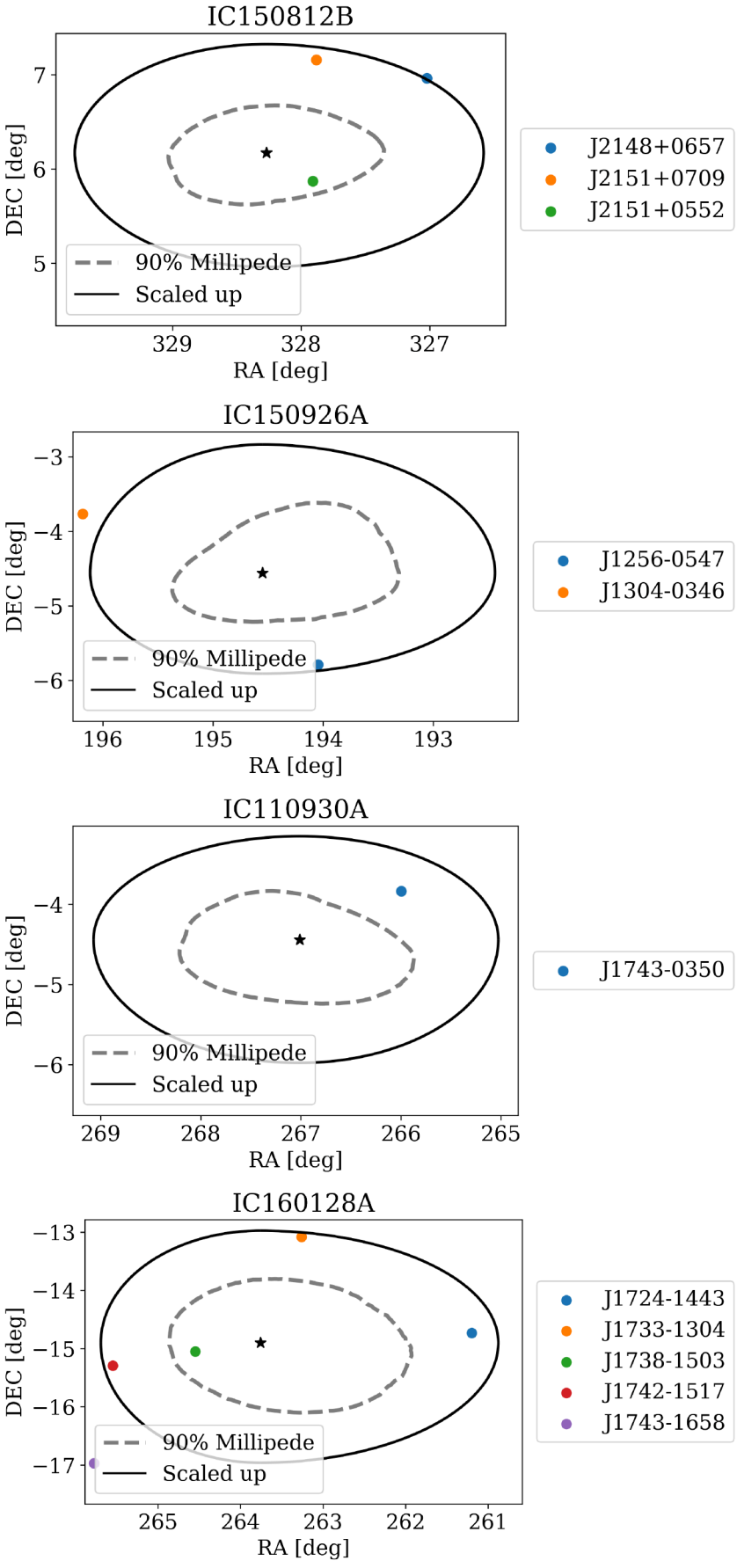

Figure D.4: Neutrino events that contribute the most to the TS_{data} in a previously published study using neutrino alert-like events and the RFC 2019c catalog [126].

Acknowledgements

I would like to thank

Anna Franckowiak, for giving me the opportunity to write this PhD thesis, and for always helping me and guiding me during this time.

Marek Kowalski, Markus Ackermann and Jakob van Santen, for the all the interesting discussions, the support, the crazy and not-so-crazy ideas and for adopting me as their student.

Robert, for being a great friend and introducing me to everything about IceCube, from the basic software to the gossip.

Giacomo and Hans, for pushing through besides me with the technical work that nobody else wanted to do.

Neha, Sofia and Richard, for making 2L04 my second home.

All my friends at DESY, including but not limited to Nora, Leander, Zack, RJ, Jonas, Pavlo, Raffael, Christoph and Alex, for all the fun and for helping me endure the pandemic, the travel-budget and contract-extension crisis and the long list of other problems encountered on the way.

Manu, my family and my friends from Spain, for believing in me and for their constant support throughout the years.

I could not have done it without all of you.

Bibliography

Here are the references in citation order.

[1] M. G. Aartsen et al. 'Evidence for High-Energy Extraterrestrial Neutrinos at the IceCube Detector'. In: *Science* 342.6161 (2013), p. 1242856. DOI: 10.1126/science.1242856 (cited on pages 1, 16).

[2] M. Ackermann et al. 'Astrophysics Uniquely Enabled by Observations of High-Energy Cosmic Neutrinos'. In: *Bull. Am. Astron. Soc.* 51 (2019), p. 185 (cited on page 7).

[3] T. K. Gaisser, R. Engel, and E. Resconi. *Cosmic Rays and Particle Physics*. Cambridge University Press2016, 2016 (cited on page 8).

[4] V. F. Hess. 'Über Beobachtungen der durchdringenden Strahlung bei sieben Freiballonfahrten'. In: *Phys. Z.* 13 (1912), pp. 1084–1091 (cited on page 8).

[5] R. L. Workman et al. 'Review of Particle Physics'. In: *PTEP* 2022 (2022), p. 083C01. DOI: 10.1093/ptep/ptac097 (cited on pages 8, 9, 15, 24, 26).

[6] 'The Pierre Auger Cosmic Ray Observatory'. In: *Nuclear Instruments and Methods in Physics Research Section A: Accelerators, Spectrometers, Detectors and Associated Equipment* 798 (2015), pp. 172–213. DOI: 10.1016/j.nima.2015.06.058 (cited on page 8).

[7] T. Abu-Zayyad et al. 'The surface detector array of the Telescope Array experiment'. In: *Nuclear Instruments and Methods in Physics Research Section A: Accelerators, Spectrometers, Detectors and Associated Equipment* 689 (2012), pp. 87–97. DOI: https://doi.org/10.1016/j.nima.2012.05.079 (cited on page 8).

[8] V. de Souza. 'Testing the agreement between the X_{max} distributions measured by the Pierre Auger and Telescope Array Observatories'. In: *PoS* ICRC2017 (2017), p. 522. DOI: 10.22323/1.301.0522 (cited on pages 8, 9).

[9] J. R. Hörandel. 'Cosmic Rays from the Knee to the Second Knee: 10^{14} to 10^{18} eV'. In: *Modern Physics Letters A* 22.21 (2007), pp. 1533–1551. DOI: 10.1142/s0217732307024139 (cited on page 8).

[10] J. R. Hörandel. 'On the knee in the energy spectrum of cosmic rays'. In: *Astroparticle Physics* 19.2 (2003), pp. 193–220. DOI: 10.1016/s0927-6505(02)00198-6 (cited on page 8).

[11] T. Stanev. *High Energy Cosmic Rays*. Springer Berlin, Heidelberg, 2010 (cited on page 8).

[12] M. Unger, G. R. Farrar, and L. A. Anchordoqui. 'Origin of the ankle in the ultrahigh energy cosmic ray spectrum, and of the extragalactic protons below it'. In: *Physical Review D* 92.12 (2015). DOI: 10.1103/physrevd.92.123001 (cited on page 9).

[13] R. Aloisio, V. Berezinsky, and A. Gazizov. 'Transition from galactic to extragalactic cosmic rays'. In: *Astroparticle Physics* 39-40 (2012), pp. 129–143. DOI: 10.1016/j.astropartphys.2012.09.007 (cited on page 9).

[14] S. Mollerach and E. Roulet. 'Ultrahigh energy cosmic rays from a nearby extragalactic source in the diffusive regime'. In: *Phys. Rev. D* 99 (10 May 2019), p. 103010. DOI: 10.1103/PhysRevD.99.103010 (cited on page 9).

[15] K. Greisen. 'End to the Cosmic-Ray Spectrum?' In: *Phys. Rev. Lett.* 16 (17 Apr. 1966), pp. 748–750. DOI: 10.1103/PhysRevLett.16.748 (cited on page 9).

[16] G. T. Zatsepin and V. A. Kuzmin. 'Upper limit of the spectrum of cosmic rays'. In: *JETP Lett.* 4 (1966), pp. 78–80 (cited on page 9).

[17] A. Aab et al. 'Evidence for a mixed mass composition at the 'ankle' in the cosmic-ray spectrum'. In: *Physics Letters B* 762 (2016), pp. 288–295. DOI: 10.1016/j.physletb.2016.09.039 (cited on page 9).

[18] S. Das, S. Razzaque, and N. Gupta. 'Modeling the spectrum and composition of ultrahigh-energy cosmic rays with two populations of extragalactic sources'. In: *The European Physical Journal C* 81.1 (2021). DOI: 10.1140/epjc/s10052-021-08885-4 (cited on page 9).

[19] A. M. Hillas. 'The Origin of Ultra-High-Energy Cosmic Rays'. In: *Annual Review of Astronomy and Astrophysics* 22.1 (1984), pp. 425–444. DOI: 10.1146/annurev.aa.22.090184.002233 (cited on page 9).

[20] M. G. Aartsen et al. 'Astrophysical Neutrinos and Cosmic Rays Observed by IceCube'. In: *Advances in Space Research* 62 (May 2017). DOI: 10.1016/j.asr.2017.05.030 (cited on page 10).

[21] E. Fermi. 'On the Origin of the Cosmic Radiation'. In: *Phys. Rev.* 75 (8 Apr. 1949), pp. 1169–1174. DOI: 10.1103/PhysRev.75.1169 (cited on page 10).

[22] G. B. Rybicki and A. P. Lightman. *Radiative Processes in Astrophysics*. 1986 (cited on page 11).

[23] P.J. Napier, A.R. Thompson, and R.D. Ekers. 'The very large array: Design and performance of a modern synthesis radio telescope'. In: *Proceedings of the IEEE* 71.11 (1983), pp. 1295–1320. DOI: 10.1109/PROC.1983.12765 (cited on page 13).

[24] M. P. van Haarlem et al. 'LOFAR: The LOw-Frequency ARray'. In: *A&A* 556 (2013), A2. DOI: 10.1051/0004-6361/201220873 (cited on page 13).

[25] A. A. Penzias and R. W. Wilson. 'A Measurement of Excess Antenna Temperature at 4080 Mc/s.' In: *The Astrophysical Journal* 142 (July 1965), pp. 419–421. DOI: 10.1086/148307 (cited on page 13).

[26] A. R. Hewish et al. 'Observation of a Rapidly Pulsating Radio Source'. In: *Nature* 217 (Feb. 1968). DOI: 10.1038/217709a0 (cited on page 13).

[27] L. F. Rodríguez. 'Radio Astronomy: The Achievements and the Challenges'. In: *Solar, Stellar and Galactic Connections Between Particle Physicsand Astrophysics*. Ed. by Alberto Carramiñana, Francisco Siddhartha Guzmán, and Tonatiuh Matos. Dordrecht: Springer Netherlands, 2007, pp. 199–213 (cited on page 13).

[28] H. J. Walker. 'A brief history of infrared astronomy'. In: *Astronomy and Geophysics* 41.5 (Oct. 2000), pp. 5.10–5.13. DOI: 10.1046/j.1468-4004.2000.41510.x (cited on page 13).

[29] J. P. Gardner et al. 'The James Webb Space Telescope'. In: *Space Science Reviews* 123.4 (2006), pp. 485–606. DOI: 10.1007/s11214-006-8315-7 (cited on page 13).

[30] LSST Science Collaboration et al. 'LSST Science Book, Version 2.0'. In: *arXiv e-prints*, arXiv:0912.0201 (Dec. 2009), arXiv:0912.0201. DOI: 10.48550/arXiv.0912.0201 (cited on page 13).

[31] E. C. Bellm et al. 'The Zwicky Transient Facility: System Overview, Performance, and First Results'. In: *Publications of the Astronomical Society of the Pacific* 131.995 (2018), p. 018002. DOI: 10.1088/1538-3873/aaecbe (cited on pages 14, 71).

[32] J. Truemper. 'The ROSAT mission'. In: *Advances in Space Research* 2.4 (Jan. 1982), pp. 241–249. DOI: 10.1016/0273-1177(82)90070-9 (cited on page 14).

[33] N. Gehrels et al. 'The Swift Gamma-Ray Burst Mission'. In: *Astroparticle Physics* 611.2 (Aug. 2004), pp. 1005–1020. DOI: 10.1086/422091 (cited on page 14).

[34] M. C. Weisskopf et al. 'Chandra X-ray Observatory (CXO): overview'. In: *SPIE Proceedings*. Ed. by Joachim E. Truemper and Bernd Aschenbach. SPIE, 2000. DOI: 10.1117/12.391545 (cited on page 14).

[35] F. A. Harrison et al. 'The Nuclear Spectroscopic Telescope Array (NuSTAR) High-Energy X-Ray Mission'. In: *Astrophys. J.* 770 (2013), p. 103. DOI: 10.1088/0004-637X/770/2/103 (cited on page 14).

[36] Z. Cao, F.A. Aharonian, Q. An, et al. 'Ultrahigh-energy photons up to 1.4 petaelectronvolts from 12 γ-ray Galactic sources'. In: *Nature* 594 (2021), pp. 33–36. DOI: 10.1038/s41586-021-03498-z (cited on page 14).

[37] C, Winkler et al. 'The INTEGRAL mission'. In: *A&A* 411.1 (2003), pp. L1–L6. DOI: 10.1051/0004-6361:20031288 (cited on page 14).

[38] M. Tavani et al. 'The AGILE Mission'. In: *A&A* 502.3 (2009), pp. 995–1013. DOI: 10.1051/0004-6361/200810527 (cited on page 14).

[39] W. B. Atwood et al. 'The Large Area Telescope on the Fermi Gamma-ray Space Telescope mission'. In: *The Astrophysical Journal* 697.2 (2009), pp. 1071–1102. DOI: 10.1088/0004-637x/697/2/1071 (cited on pages 14, 105).

[40] C. Meegan et al. 'The Fermi Gamma-Ray Burst Monitor'. In: *The Astrophysical Journal* 702.1 (2009), pp. 791–804. DOI: 10.1088/0004-637x/702/1/791 (cited on pages 14, 106).

[41] A. Balzer et al. 'The H.E.S.S. central data acquisition system'. In: *Astropart. Phys.* 54 (2014), pp. 67–80. DOI: 10.1016/j.astropartphys.2013.11.007 (cited on page 15).

[42] T. C. Weekes et al. 'VERITAS: the Very Energetic Radiation Imaging Telescope Array System'. In: *Astroparticle Physics* 17.2 (2002), pp. 221–243. DOI: 10.1016/s0927-6505(01)00152-9 (cited on page 15).

[43] C. Bigongiari. 'The MAGIC Telescope'. In: *arXiv e-prints* (2005), astro–ph/0512184. DOI: 10.48550/ARXIV.ASTRO-PH/0512184 (cited on page 15).

[44] B. S. Acharya et al. 'Introducing the CTA concept'. In: *Astroparticle Physics* 43 (2013). Seeing the High-Energy Universe with the Cherenkov Telescope Array - The Science Explored with the CTA, pp. 3–18. DOI: https://doi.org/10.1016/j.astropartphys.2013.01.007 (cited on page 15).

[45] W. Springer. 'The High Altitude water Cherenkov (HAWC) Observatory'. In: *Nuclear and Particle Physics Proceedings* 279-281 (Oct. 2016), pp. 87–94. DOI: 10.1016/j.nuclphysbps.2016.10.013 (cited on page 15).

[46] Z. Cao et al. 'The Large High Altitude Air Shower Observatory (LHAASO) Science Book (2021 Edition)'. In: *arXiv e-prints* (2019), arXiv:1905.02773. DOI: 10.48550/ARXIV.1905.02773 (cited on page 15).

[47] C. Spiering. 'Towards high-energy neutrino astronomy'. In: *The European Physical Journal H* 37.3 (2012), pp. 515–565. DOI: 10.1140/epjh/e2012-30014-2 (cited on page 16).

[48] J. Chadwick. 'Intensitätsverteilung im magnetischen Spectrum der β-Strahlen von radium B + C'. In: *Verhandlungen der deutschen Physikalischen Gesellschaft* 16 (1914), p. 383 (cited on page 15).

[49] W. Pauli. 'Dear radioactive ladies and gentlemen'. In: *Phys. Today* 31N9 (1978), p. 27 (cited on page 15).

[50] W. Pauli. 'Structure et propriétés des noyaux atomiques'. In: *Rapport du 7ème Conseil Physique Solvay* (1933), p. 324 (cited on page 15).

[51] F. Reines and C. L. Cowan. 'The neutrino'. In: *Nature* 178 (1956), pp. 446–449. DOI: 10.1038/178446a0 (cited on page 15).

[52] R. Davis, D. S. Harmer, and K. C. Hoffman. 'Search for Neutrinos from the Sun'. In: *Phys. Rev. Lett.* 20 (21 1968), pp. 1205–1209. DOI: 10.1103/PhysRevLett.20.1205 (cited on page 15).

[53] H. A. Bethe. 'Energy Production in Stars'. In: *Phys. Rev.* 55 (5 1939), pp. 434–456. DOI: 10.1103/PhysRev.55.434 (cited on page 15).

[54] Z. Maki, M. Nakagawa, and S. Sakata. 'Remarks on the Unified Model of Elementary Particles'. In: *Progress of Theoretical Physics* 28.5 (Nov. 1962), pp. 870–880. DOI: 10.1143/PTP.28.870 (cited on page 15).

[55] B. Pontecorvo. 'Neutrino Experiments and the Problem of Conservation of Leptonic Charge'. In: *Zh. Eksp. Teor. Fiz.* 53 (1967), pp. 1717–1725 (cited on page 15).

[56] Q. R. Ahmad et al. 'Measurement of the Rate $\nu_e + d \rightarrow p + p + e^-$ Solar Neutrinos at the Sudbury Neutrino Observatory'. In: *Physical Review Letters* 87.7 (2001). DOI: 10.1103/physrevlett.87.071301 (cited on page 15).

[57] Y. Fukuda et al. 'Evidence for Oscillation of Atmospheric Neutrinos'. In: *Phys. Rev. Lett.* 81 (8 1998), pp. 1562–1567. DOI: 10.1103/PhysRevLett.81.1562 (cited on page 15).

[58] M. Aker et al. 'Direct neutrino-mass measurement with sub-electronvolt sensitivity'. In: *Nature Phys.* 18.2 (2022), pp. 160–166. DOI: 10.1038/s41567-021-01463-1 (cited on page 15).

[59] N. Aghanim et al. 'Planck 2018 results'. In: *Astronomy Astrophysics* 641 (2020), A6. DOI: 10.1051/0004-6361/201833910 (cited on page 15).

[60] W. D. Arnett et al. 'Supernova 1987A'. In: *Annual Review of Astronomy and Astrophysics* 27.1 (1989), pp. 629–700. DOI: 10.1146/annurev.aa.27.090189.003213 (cited on page 15).

[61] S. Al Kharusi et al. 'SNEWS 2.0: a next-generation supernova early warning system for multi-messenger astronomy'. In: *New Journal of Physics* 23.3 (2021), p. 031201. DOI: 10.1088/1367-2630/abde33 (cited on page 16).

[62] M. G. Aartsen et al. 'Multimessenger observations of a flaring blazar coincident with high-energy neutrino IceCube-170922A'. In: *Science* 361.6398 (2018). DOI: 10.1126/science.aat1378 (cited on pages 16, 35, 46, 70, 71, 92, 93, 107, 113).

[63] M. G. Aartsen et al. 'Neutrino emission from the direction of the blazar TXS 0506+056 prior to the IceCube-170922A alert'. In: *Science* 361.6398 (2018), pp. 147–151. DOI: 10.1126/science.aat2890 (cited on pages 16, 46, 93).

[64] R. Abbasi et al. 'Evidence for neutrino emission from the nearby active galaxy NGC 1068'. In: *Science* 378.6619 (2022), pp. 538–543. DOI: 10.1126/science.abg3395 (cited on pages 16, 96, 97).

[65] M. G. Aartsen et al. 'IceCube-Gen2: the window to the extreme Universe'. In: *Journal of Physics G: Nuclear and Particle Physics* 48.6 (2021), p. 060501. DOI: 10.1088/1361-6471/abbd48 (cited on pages 17, 25, 94, 121, 122).

[66] B. P. Abbott et al. 'Observation of Gravitational Waves from a Binary Black Hole Merger'. In: *Phys. Rev. Lett.* 116 (6 2016), p. 061102. DOI: 10.1103/PhysRevLett.116.061102 (cited on page 17).

[67] B. P. Abbott et al. 'Multi-messenger Observations of a Binary Neutron Star Merger*'. In: *The Astrophysical Journal Letters* 848.2 (2017), p. L12. DOI: 10.3847/2041-8213/aa91c9 (cited on page 18).

[68] R. Abbasi et al. 'IceCube Search for Neutrinos Coincident with Gravitational Wave Events from LIGO/Virgo Run O3'. In: *The Astrophysical Journal* 944.1 (2023), p. 80. DOI: 10.3847/1538-4357/aca5fc (cited on page 18).

[69] M. Ageron et al. 'ANTARES: The first undersea neutrino telescope'. In: *Nuclear Instruments and Methods in Physics Research Section A: Accelerators, Spectrometers, Detectors and Associated Equipment* 656.1 (2011), pp. 11–38. DOI: 10.1016/j.nima.2011.06.103 (cited on page 19).

[70] A. Margiotta. 'The KM3NeT deep-sea neutrino telescope'. In: *Nuclear Instruments and Methods in Physics Research Section A: Accelerators, Spectrometers, Detectors and Associated Equipment* 766 (2014), pp. 83–87. DOI: 10.1016/j.nima.2014.05.090 (cited on pages 19, 122).

[71] M. Agostini et al. 'The Pacific Ocean Neutrino Experiment'. In: *Nature Astronomy* 4.10 (2020), pp. 913–915. DOI: 10.1038/s41550-020-1182-4 (cited on pages 19, 122).

[72] B. Shoibonov et al. 'Baikal-GVD - the Next Generation Neutrino Telescope in Lake Baikal'. In: *Journal of Physics: Conference Series* 1263.1 (2019), p. 012005. DOI: 10.1088/1742-6596/1263/1/012005 (cited on pages 19, 122).

[73] E. Andres. 'The AMANDA neutrino telescope: principle of operation and first results'. In: *Astroparticle Physics* 13.1 (2000), pp. 1–20. DOI: 10.1016/s0927-6505(99)00092-4 (cited on page 19).

[74] J. A. Aguilar Sánchez et al. 'The Radio Neutrino Observatory Greenland (RNO-G)'. In: vol. ICRC2021. Sept. 2021, p. 001. DOI: 10.22323/1.395.0001 (cited on page 19).

[75] M. G. Aartsen et al. 'The IceCube Neutrino Observatory: instrumentation and online systems'. In: *Journal of Instrumentation* 12.03 (Mar. 2017), P03012–P03012. DOI: 10.1088/1748-0221/12/03/p03012 (cited on pages 19, 20).

[76] R. Abbasi et al. 'Calibration and characterization of the IceCube photomultiplier tube'. In: *Nuclear Instruments and Methods in Physics Research Section A: Accelerators, Spectrometers, Detectors and Associated Equipment* 618.1 (2010), pp. 139–152. DOI: https://doi.org/10.1016/j.nima.2010.03.102 (cited on page 20).

[77] R. Abbasi et al. 'The design and performance of IceCube DeepCore'. In: *Astroparticle Physics* 35.10 (2012), pp. 615–624. DOI: 10.1016/j.astropartphys.2012.01.004 (cited on page 22).

[78] M. G. Aartsen et al. 'Measurement of atmospheric tau neutrino appearance with IceCube DeepCore'. In: *Physical Review D* 99.3 (2019). DOI: 10.1103/physrevd.99.032007 (cited on page 22).

[79] R. Abbasi et al. 'Search for GeV-scale dark matter annihilation in the Sun with IceCube DeepCore'. In: *Physical Review D* 105.6 (2022). DOI: 10.1103/physrevd.105.062004 (cited on page 22).

[80] R. Abbasi et al. 'IceTop: The surface component of IceCube'. In: *Nuclear Instruments and Methods in Physics Research Section A: Accelerators, Spectrometers, Detectors and Associated Equipment* 700 (2013), pp. 188–220. DOI: https://doi.org/10.1016/j.nima.2012.10.067 (cited on page 22).

[81] M. G. Aartsen et al. 'Cosmic ray spectrum and composition from PeV to EeV using 3 years of data from IceTop and IceCube'. In: *Phys. Rev. D* 100 (8 Oct. 2019), p. 082002. DOI: 10.1103/PhysRevD.100.082002 (cited on page 22).

[82] J. A. Formaggio and G. P. Zeller. 'From eV to EeV: Neutrino cross sections across energy scales'. In: *Reviews of Modern Physics* 84.3 (Sept. 2012), pp. 1307–1341. DOI: 10.1103/revmodphys.84.1307 (cited on pages 22, 23).

[83] R. Gandhi et al. 'Neutrino interactions at ultrahigh energies'. In: *Physical Review D* 58.9 (Sept. 1998). DOI: 10.1103/physrevd.58.093009 (cited on page 23).

[84] S. L. Glashow. 'Resonant Scattering of Antineutrinos'. In: *Phys. Rev.* 118 (1 Apr. 1960), pp. 316–317. DOI: 10.1103/PhysRev.118.316 (cited on page 23).

[85] M. G. Aartsen et al. 'Detection of a particle shower at the Glashow resonance with IceCube'. In: *Nature* 591.7849 (Mar. 2021), pp. 220–224. DOI: 10.1038/s41586-021-03256-1 (cited on page 23).

[86] I. Tamm. 'Radiation Emitted by Uniformly Moving Electrons'. In: *Selected Papers*. Ed. by Boris M. Bolotovskii, Victor Ya. Frenkel, and Rudolf Peierls. Berlin, Heidelberg: Springer Berlin Heidelberg, 1991, pp. 37–53. DOI: 10.1007/978-3-642-74626-0_3 (cited on page 24).

[87] L. Rädel and C. Wiebusch. 'Calculation of the Cherenkov light yield from low energetic secondary particles accompanying high-energy muons in ice and water with Geant4 simulations'. In: *Astroparticle Physics* 38 (2012), pp. 53–67. DOI: 10.1016/j.astropartphys.2012.09.008 (cited on page 24).

[88] M. G. Aartsen et al. 'Energy Reconstruction Methods in the IceCube Neutrino Telescope'. In: *JINST* 9 (2014), P03009. DOI: 10.1088/1748-0221/9/03/P03009 (cited on pages 25, 29, 39, 82).

[89] R. Abbasi et al. 'Detection of astrophysical tau neutrino candidates in IceCube'. In: *The European Physical Journal C* 82.11 (2022). DOI: 10.1140/epjc/s10052-022-10795-y (cited on page 25).

[90] Rasha Abbasi et al. 'Summary of IceCube tau neutrino searches and flavor composition measurements of the diffuse astrophysical neutrino flux'. In: *PoS* ICRC2023 (2023), p. 1122. DOI: 10.22323/1.444.1122 (cited on page 25).

[91] J. G. Learned and K. Mannheim. 'High-Energy Neutrino Astrophysics'. In: *Annual Review of Nuclear and Particle Science* 50.1 (2000), pp. 679–749. DOI: 10.1146/annurev.nucl.50.1.679 (cited on page 25).

[92] R. Abbasi et al. 'An improved method for measuring muon energy using the truncated mean of dE/dx'. In: *Nuclear Instruments and Methods in Physics Research Section A: Accelerators, Spectrometers, Detectors and Associated Equipment* 703 (2013), pp. 190–198. DOI: https://doi.org/10.1016/j.nima.2012.11.081 (cited on pages 25, 26, 39).

[93] D. Chirkin and W. Rhode. 'Propagating leptons through matter with Muon Monte Carlo (MMC)'. In: *arXiv e-prints* (July 2004), arXiv:hep–ph/0407075 (cited on page 26).

[94] R. Abbasi et al. 'Improved Characterization of the Astrophysical Muon–neutrino Flux with 9.5 Years of IceCube Data'. In: 928.1 (2022), p. 50. DOI: 10.3847/1538-4357/ac4d29 (cited on pages 27, 36, 50).

[95] R. Abbasi et al. 'The IceCube data acquisition system: Signal capture, digitization, and timestamping'. In: *Nuclear Instruments and Methods in Physics Research Section A: Accelerators, Spectrometers, Detectors and Associated Equipment* 601.3 (2009), pp. 294–316. DOI: 10.1016/j.nima.2009.01.001 (cited on pages 28, 29).

[96] E. Blaufuss et al. 'The Next Generation of IceCube Real-time Neutrino Alerts'. In: *PoS* (ICRC2019) (2019), p. 1021. DOI: 10.22323/1.358.1021 (cited on pages 29, 35).

[97] M. G. Aartsen et al. 'Measurement of South Pole ice transparency with the IceCube LED calibration system'. In: *Nuclear Instruments and Methods in Physics Research Section A: Accelerators, Spectrometers, Detectors and Associated Equipment* 711 (May 2013), pp. 73–89. DOI: 10.1016/j.nima.2013.01.054 (cited on pages 30, 40, 75).

[98] D. Hahn. 'Light Scattering Theory'. In: (Jan. 2004) (cited on page 30).

[99] D. Chirkin and M. Rongen. 'Light diffusion in birefringent polycrystals and the IceCube ice anisotropy'. In: *PoS* ICRC2019 (2019), p. 854 (cited on pages 30, 55).

[100] M. G. Aartsen et al. 'South Pole glacial climate reconstruction from multi-borehole laser particulate stratigraphy'. In: *Journal of Glaciology* 59.218 (2013), pp. 1117–1128. DOI: 10.3189/2013JoG13J068 (cited on page 31).

[101] R. Abbasi et al. 'Follow-up of Astrophysical Transients in Real Time with the IceCube Neutrino Observatory'. In: *The Astrophysical Journal* 910.1 (2021), p. 4. DOI: 10.3847/1538-4357/abe123 (cited on page 35).

[102] M. G. Aartsen et al. 'The IceCube Realtime Alert System'. In: *Astropart. Phys.* 92 (2017), pp. 30–41. DOI: 10.1016/j.astropartphys.2017.05.002 (cited on page 35).

[103] R. Abbasi et al. 'IceCube high-energy starting event sample: Description and flux characterization with 7.5 years of data'. In: *Physical Review D* 104.2 (2021). DOI: 10.1103/physrevd.104.022002 (cited on page 35).

[104] M. G. Aartsen et al. 'Constraints on Ultrahigh-Energy Cosmic-Ray Sources from a Search for Neutrinos above 10 PeV with IceCube'. In: *Physical Review Letters* 117.24, 241101 (Dec. 2016), p. 241101. DOI: 10.1103/PhysRevLett.117.241101 (cited on page 35).

[105] C. Haack and C. Wiebusch. 'A measurement of the diffuse astrophysical muon neutrino flux using eight years of IceCube data.' In: *PoS* ICRC2017 (2017), p. 1005. DOI: 10.22323/1.301.1005 (cited on page 36).

[106] R. Abbasi et al. 'Constraints on Populations of Neutrino Sources from Searches in the Directions of IceCube Neutrino Alerts'. In: *The Astrophysical Journal* 951.1 (2023), p. 45. DOI: 10.3847/1538-4357/acd2ca (cited on pages 37, 96).

[107] R. Abbasi et al. 'A muon-track reconstruction exploiting stochastic losses for large-scale Cherenkov detectors'. In: *Journal of Instrumentation* 16.08 (Aug. 2021), P08034. DOI: 10.1088/1748-0221/16/08/P08034 (cited on pages 40, 76).

[108] A. Kolmogorov. 'Sulla determinazione empirica di una legge di distribuzione.' In: *Giornale dell'Istituto Italiano degli Attuari* 4 (1933), pp. 83–91 (cited on pages 40, 59, 83).

[109] N. Smirnov. 'Table for Estimating the Goodness of Fit of Empirical Distributions'. In: *The Annals of Mathematical Statistics* 19.2 (1948), pp. 279–281. DOI: 10.1214/aoms/1177730256 (cited on page 40).

[110] K. M. Gorski et al. 'HEALPix: A Framework for High-Resolution Discretization and Fast Analysis of Data Distributed on the Sphere'. In: *The Astrophysical Journal* 622.2 (Apr. 2005), pp. 759–771. DOI: 10.1086/427976 (cited on page 41).

[111] S. S. Wilks. 'The Large-Sample Distribution of the Likelihood Ratio for Testing Composite Hypotheses'. In: *The Annals of Mathematical Statistics* 9.1 (1938), pp. 60–62. DOI: 10.1214/aoms/1177732360 (cited on pages 41, 53, 102).

[112] E. Kankare et al. 'Search for transient optical counterparts to high-energy IceCube neutrinos with Pan-STARRS1'. In: *Astron. Astrophys.* 626 (2019), A117. DOI: 10.1051/0004-6361/201935171 (cited on pages 41, 45, 46).

[113] E. Blaufuss. 'ICECUBE-160427A neutrino candidate event: updated direction information.' In: *GRB Coordinates Network* 19363 (Jan. 2016), p. 1 (cited on pages 45, 46).

[114] C. Kopper and E. Blaufuss. 'IceCube-170922A - IceCube observation of a high-energy neutrino candidate event.' In: *GRB Coordinates Network* 21916 (Jan. 2017), p. 1 (cited on page 46).

[115] R. Stein. 'IceCube-190730A - IceCube observation of a high-energy neutrino candidate event'. In: *GCN Circular* 25225 (July 2019) (cited on page 46).

[116] X. Rodrigues et al. 'Multiwavelength and Neutrino Emission from Blazar PKS 1502 + 106'. In: *The Astrophysical Journal* 912.1 (2021), p. 54. DOI: 10.3847/1538-4357/abe87b (cited on pages 47, 92, 113).

[117] S. Kiehlmann et al. 'Neutrino candidate source FSRQ PKS 1502+106 at highest flux density at 15 GHz'. In: *The Astronomer's Telegram* 12996 (Aug. 2019), p. 1 (cited on page 47).

[118] A. Franckowiak et al. 'Patterns in the Multiwavelength Behavior of Candidate Neutrino Blazars'. In: *The Astrophysical Journal* 893.2 (2020), p. 162. DOI: 10.3847/1538-4357/ab8307 (cited on page 47).

[119] E. Kun et al. 'Cosmic Neutrinos from Temporarily Gamma-suppressed Blazars'. In: *The Astrophysical Journal Letters* 911.2 (2021), p. L18. DOI: 10.3847/2041-8213/abf1ec (cited on page 47).

[120] R. Stein et al. 'A tidal disruption event coincident with a high-energy neutrino'. In: *Nature Astronomy* 5.5 (2021), pp. 510–518. DOI: 10.1038/s41550-020-01295-8 (cited on page 47).

[121] K. Hayasaki. 'Neutrinos from tidal disruption events'. In: *Nature Astronomy* 5.5 (Feb. 2021), pp. 436–437. DOI: 10.1038/s41550-021-01309-z (cited on page 47).

[122] S. van Velzen et al. 'Establishing accretion flares from massive black holes as a major source of high-energy neutrinos'. In: *arXiv e-print* (2021), arXiv:2111.09391 (cited on pages 48, 49).

[123] S. Reusch et al. 'Candidate Tidal Disruption Event AT2019fdr Coincident with a High-Energy Neutrino'. In: *Physical Review Letters* 128.22 (2022). DOI: 10.1103/physrevlett.128.221101 (cited on page 48).

[124] R. Abbasi et al. 'IceCat-1: the IceCube Event Catalog of Alert Tracks'. In: *arXiv e-print* (2023), arXiv:2304.01174 (cited on pages 50, 51, 105).

[125] P. Giommi et al. 'Dissecting the regions around IceCube high-energy neutrinos: growing evidence for the blazar connection'. In: *Monthly Notices of the Royal Astronomical Society* 497.1 (2020), pp. 865–878. DOI: 10.1093/mnras/staa2082 (cited on pages 51, 93, 99, 116).

[126] A. V. Plavin et al. 'Observational Evidence for the Origin of High-energy Neutrinos in Parsec-scale Nuclei of Radio-bright Active Galaxies'. In: *The Astrophysical Journal* 894.2 (2020), p. 101. DOI: 10.3847/1538-4357/ab86bd (cited on pages 51, 95, 96, 99, 109, 114–117, 137, 148).

[127] A. V. Plavin et al. 'Growing evidence for high-energy neutrinos originating in radio blazars'. In: *arXiv e-print* (2022), arXiv:2211.09631 (cited on pages 51, 96, 99).

[128] R. Abbasi et al. 'Studies of systematic uncertainty effects on IceCube's real-time angular uncertainty'. In: *PoS* ICRC2021 (2021), p. 1045. DOI: 10.22323/1.395.1045 (cited on page 53).

[129] R. Abbasi et al. 'Testing the Pointing of IceCube Using the Moon Shadow in Cosmic-Ray-Induced Muons'. In: *PoS* ICRC2021 (2021), p. 1087. DOI: 10.22323/1.395.1087 (cited on page 54).

[130] R. Abbasi et al. 'LeptonInjector and LeptonWeighter: A neutrino event generator and weighter for neutrino observatories'. In: *Computer Physics Communications* 266 (Sept. 2021), p. 108018. DOI: 10.1016/j.cpc.2021.108018 (cited on page 54).

[131] J. van Santen. 'Neutrino Interactions in IceCube above 1 TeV: Constraints on Atmospheric Charmed-Meson Production and Investigation of the Astrophysical Neutrino Flux with 2 Years of IceCube Data taken 2010–2012'. PhD thesis. Wisconsin U., Madison, Nov. 2014 (cited on page 54).

[132] D. Heck et al. 'CORSIKA: A Monte Carlo code to simulate extensive air showers'. In: (Feb. 1998) (cited on page 54).

[133] J. H. Koehne et al. 'PROPOSAL: A tool for propagation of charged leptons'. In: *Comput. Phys. Commun.* 184 (2013), pp. 2070–2090. DOI: 10.1016/j.cpc.2013.04.001 (cited on page 54).

[134] M. G. Aartsen et al. 'Efficient propagation of systematic uncertainties from calibration to analysis with the SnowStorm method in IceCube'. In: *JCAP* 10 (2019), p. 048. DOI: 10.1088/1475-7516/2019/10/048 (cited on pages 54, 55).

[135] R. Abbasi et al. 'A calibration study of local ice and optical sensor properties in IceCube'. In: *PoS* ICRC2021 (2021), p. 1023. DOI: 10.22323/1.395.1023 (cited on page 55).

[136] R. Abbasi et al. 'Towards a more Robust Reconstruction Method for IceCube's Realtime Program'. In: *PoS* ICRC2023 (2023), p. 1186 (cited on pages 81, 83, 84).

[137] R. Abbasi et al. 'Search for High-Energy Neutrinos from TDE-like Flares with IceCube'. In: *PoS* ICRC2023 (2023), p. 1478 (cited on pages 81–83).

[138] R. Abbasi et al. 'Approximating New Ice Models with B-splines for Improved IceCube Event Reconstruction: Application to Cascades and Tracks'. In: *PoS* ICRC2023 (2023), p. 1005 (cited on pages 81, 84, 85).

[139] T. Yuan. 'Detecting neutrinos in IceCube with Cherenkov light in the South Pole ice'. In: *Nuclear Instruments and Methods in Physics Research Section A: Accelerators, Spectrometers, Detectors and Associated Equipment* 1054 (2023), p. 168440. DOI: https://doi.org/10.1016/j.nima.2023.168440 (cited on page 84).

[140] B. M. Peterson et al. *Quasars*. Ed. by Robert A. Meyers. Third Edition. New York: Academic Press, 2003, pp. 465–480 (cited on page 89).

[141] K. Murase and F. W. Stecker. 'High-Energy Neutrinos from Active Galactic Nuclei'. In: *arXiv e-print* (2022), arXiv:2202.03381 (cited on page 89).

[142] V. Beckmann and C. Shrader. *Active Galactic Nuclei*. Aug. 2012 (cited on pages 89–91).

[143] L. C. Ho. 'Radiatively inefficient accretion in nearby galaxies'. In: *The Astrophysical Journal* 699.1 (2009), p. 626. DOI: 10.1088/0004-637X/699/1/626 (cited on page 89).

[144] R. Blandford, D. Meier, and A. Readhead. 'Relativistic Jets from Active Galactic Nuclei'. In: *Annual Review of Astronomy and Astrophysics* 57.1 (2019), pp. 467–509. DOI: 10.1146/annurev-astro-081817-051948 (cited on page 90).

[145] X. Zhao et al. 'The properties of the AGN torus as revealed from a set of unbiased NuSTAR observations'. In: *Astronomy and Astrophysics* 650 (2021), A57. DOI: 10.1051/0004-6361/202140297 (cited on page 90).

[146] R. C. Hickox and D. M. Alexander. 'Obscured Active Galactic Nuclei'. In: *Annual Review of Astronomy and Astrophysics* 56 (Sept. 2018), pp. 625–671. DOI: 10.1146/annurev-astro-081817-051803 (cited on page 90).

[147] R. Antonucci. 'Unified models for active galactic nuclei and quasars.' In: *Annual Review of Astronomy and Astrophysics* 31 (Jan. 1993), pp. 473–521. DOI: 10.1146/annurev.aa.31.090193.002353 (cited on page 90).

[148] C. M. Urry and P. Padovani. 'Unified Schemes for Radio-Loud Active Galactic Nuclei'. In: *Publications of the Astronomical Society of the Pacific* 107 (Sept. 1995), p. 803. DOI: 10.1086/133630 (cited on page 90).

[149] B. L. Fanaroff and J. M. Riley. 'The morphology of extragalactic radio sources of high and low luminosity'. In: *Monthly Notices of the Royal Astronomical Society* 167 (May 1974), 31P–36P. DOI: 10.1093/mnras/167.1.31P (cited on page 91).

[150] C. K. Seyfert. 'Nuclear Emission in Spiral Nebulae.' In: *The Astrophysical Journal* 97 (Jan. 1943), p. 28. DOI: 10.1086/144488 (cited on page 91).

[151] K. Murase, D. Guetta, and M. Ahlers. 'Hidden Cosmic-Ray Accelerators as an Origin of TeV-PeV Cosmic Neutrinos'. In: *Physical Review Letters* 116.7 (2016). DOI: 10.1103/physrevlett.116.071101 (cited on page 92).

[152] K. Murase, Y. Inoue, and C. D. Dermer. 'Diffuse neutrino intensity from the inner jets of active galactic nuclei: Impacts of external photon fields and the blazar sequence'. In: *Phys. Rev. D* 90 (2 July 2014), p. 023007. DOI: 10.1103/PhysRevD.90.023007 (cited on pages 92, 107).

[153] M. Petropoulou et al. 'Photohadronic origin of γ-ray BL Lac emission: implications for IceCube neutrinos'. In: *Mon. Not. Roy. Astron. Soc.* 448.3 (2015), pp. 2412–2429. DOI: 10.1093/mnras/stv179 (cited on pages 92, 107).

[154] F. W. Stecker. 'Diffuse fluxes of cosmic high-energy neutrinos.' In: *The Astrophysical Journal* 228 (Mar. 1979), pp. 919–927. DOI: 10.1086/156919 (cited on page 92).

[155] M. Ajello et al. '3FHL: The Third Catalog of Hard Fermi-LAT Sources'. In: *The Astrophysical Journal Supplement Series* 232.2 (2017), p. 18. DOI: 10.3847/1538-4365/aa8221 (cited on pages 92, 105).

[156] M. Huber. 'Multi-Messenger Correlation Study of Fermi-LAT Blazars and High-Energy Neutrinos Observed in IceCube'. PhD thesis. Technische Universität München, 2020 (cited on page 93).

[157] S. Buson et al. 'Beginning a Journey Across the Universe: The Discovery of Extragalactic Neutrino Factories'. In: *The Astrophysical Journal Letters* 933.2 (2022), p. L43. DOI: 10.3847/2041-8213/ac7d5b (cited on pages 93, 116).

[158] S. Buson et al. 'Extragalactic neutrino factories'. In: *arXiv* (2023), arXiv:2305.11263 (cited on page 93).

[159] C. Bellenghi et al. 'The correlation between high-energy IceCube neutrinos and 5BZCAT blazars'. In: *arXiv e-print* (2023) (cited on page 93).

[160] Y. T. Tanaka, S. Buson, and D. Kocevski. 'Fermi-LAT detection of increased gamma-ray activity of TXS 0506+056, located inside the IceCube-170922A error region.' In: *The Astronomer's Telegram* 10791 (Sept. 2017), p. 1 (cited on page 93).

[161] R. Mirzoyan. 'First-time detection of VHE gamma rays by MAGIC from a direction consistent with the recent EHE neutrino event IceCube-170922A'. In: *The Astronomer's Telegram* 10817 (Oct. 2017), p. 1 (cited on page 93).

[162] S. Gao et al. 'Modelling the coincident observation of a high-energy neutrino and a bright blazar flare'. In: *Nature Astronomy* 3.1 (2018), pp. 88–92. DOI: 10.1038/s41550-018-0610-1 (cited on page 94).

[163] N. L. Strotjohann, M. Kowalski, and A. Franckowiak. 'Eddington bias for cosmic neutrino sources'. In: *A&A* 622 (2019), p. L9. DOI: 10.1051/0004-6361/201834750 (cited on page 94).

[164] X. Rodrigues et al. 'Leptohadronic Blazar Models Applied to the 2014–2015 Flare of TXS 0506+056'. In: *The Astrophysical Journal Letters* 874.2 (2019), p. L29. DOI: 10.3847/2041-8213/ab1267 (cited on page 94).

[165] M. Petropoulou et al. 'Multi-epoch Modeling of TXS 0506+056 and Implications for Long-term High-energy Neutrino Emission'. In: *The Astrophysical Journal* 891.2 (2020), p. 115. DOI: 10.3847/1538-4357/ab76d0 (cited on page 94).

[166] F. Halzen et al. 'On the Neutrino Flares from the Direction of TXS 0506+056'. In: *The Astrophysical Journal* 874.1 (2019), p. L9. DOI: 10.3847/2041-8213/ab0d27 (cited on page 94).

[167] F. W. Stecker et al. 'High-energy neutrinos from active galactic nuclei'. In: *Phys. Rev. Lett.* 66 (21 May 1991), pp. 2697–2700. DOI: 10.1103/PhysRevLett.66.2697 (cited on page 94).

[168] R. Abbasi et al. 'Search for neutrino emission from cores of active galactic nuclei'. In: *Phys. Rev. D* 106 (2 July 2022), p. 022005. DOI: 10.1103/PhysRevD.106.022005 (cited on page 94).

[169] F. Bradascio. 'Searches for cross-correlations between IceCube neutrinos and Active Galactic Nuclei selected in various bands of the electromagnetic spectrum'. PhD thesis. Humboldt-Universität zu Berlin, Mathematisch-Naturwissenschaftliche Fakultät, 2021. DOI: http://dx.doi.org/10.18452/22871 (cited on page 95).

[170] A. Suray and S. Troitsky. 'Neutrino flares of radio blazars observed from TeV to PeV'. In: *arXiv e-print* (2023), arXiv:2306.16797 (cited on page 96).

[171] A. V. Plavin et al. 'Directional Association of TeV to PeV Astrophysical Neutrinos with Radio Blazars'. In: *The Astrophysical Journal* 908.2 (2021), p. 157. DOI: 10.3847/1538-4357/abceb8 (cited on page 96).

[172] B. Zhou, M. Kamionkowski, and Y. Liang. 'Search for high-energy neutrino emission from radio-bright AGN'. In: *Physical Review D* 103.12 (2021). DOI: 10.1103/physrevd.103.123018 (cited on page 96).

[173] A. Kheirandish, K. Murase, and S. S. Kimura. 'High-energy Neutrinos from Magnetized Coronae of Active Galactic Nuclei and Prospects for Identification of Seyfert Galaxies and Quasars in Neutrino Telescopes'. In: *The Astrophysical Journal* 922.1 (2021), p. 45. DOI: 10.3847/1538-4357/ac1c77 (cited on page 96).

[174] R. Silberberg and M. M. Shapiro. 'Neutrinos as a Probe for the Nature of and Processes in Active Galactic Nuclei'. In: *International Cosmic Ray Conference*. Vol. 10. 1979, p. 357 (cited on page 96).

[175] T. M. Yoast-Hull et al. 'Active Galactic Nuclei, neutrinos, and interacting cosmic rays in NGC 253 and NGC 1068'. In: *The Astrophysical Journal* 780.2 (2013), p. 137. DOI: 10.1088/0004-637X/780/2/137 (cited on page 96).

[176] R. Abbasi et al. 'Measurement of the astrophysical diffuse neutrino flux in a combined fit of IceCube's high energy neutrino data'. In: *PoS* ICRC2023 (2023), p. 1064 (cited on page 97).

[177] M. G. Aartsen et al. 'Observation and characterization of a cosmic muon neutrino flux from the Northern Hemisphere using six years of IceCube data'. In: *The Astrophysical Journal* 833.1 (2016), p. 3. DOI: 10.3847/0004-637X/833/1/3 (cited on page 97).

[178] M. G. Aartsen et al. 'Characteristics of the Diffuse Astrophysical Electron and Tau Neutrino Flux with Six Years of IceCube High Energy Cascade Data'. In: *Phys. Rev. Lett.* 125 (12 Sept. 2020), p. 121104. DOI: 10.1103/PhysRevLett.125.121104 (cited on page 97).

[179] R. Abbasi et al. 'Searching for High-energy Neutrino Emission from Seyfert Galaxies in the Northern Sky with IceCube'. In: *PoS* ICRC2023 (2023), p. 1052 (cited on page 97).

[180] R. Abbasi et al. 'Search for Neutrino Emissions from Seyfert Galaxies in the Southern Sky using Track Events in IceCube'. In: *PoS* ICRC2023 (2023), p. 1533 (cited on page 97).

[181] A. Neronov, D. Savchenko, and D. V. Semikoz. 'Neutrino signal from Seyfert galaxies'. In: *arXiv e-print* (2023), arXiv:2306.09018 (cited on page 97).

[182] S. Garrappa et al. 'Investigation of Two Fermi-LAT Gamma-Ray Blazars Coincident with High-energy Neutrinos Detected by IceCube'. In: *The Astrophysical Journal* 880.2 (July 2019), p. 103. DOI: 10.3847/1538-4357/ab2ada (cited on page 99).

[183] C. Nanci et al. 'Observing the inner parsec-scale region of candidate neutrino-emitting blazars'. In: *Astronomy and Astrophysics* 663 (July 2022), A129. DOI: 10.1051/0004-6361/202142665 (cited on page 99).

[184] R. Abbasi et al. 'Search for correlations of high-energy neutrinos detected in IceCube with radio-bright AGN and gamma-ray emission from blazars'. In: *ApJ* (2023) (cited on page 99).

[185] Jerzy Neyman and Egon Sharpe Pearson. 'On the Problem of the Most Efficient Tests of Statistical Hypotheses'. In: *Phil. Trans. Roy. Soc. Lond. A* 231.694-706 (1933), pp. 289–337. DOI: 10.1098/rsta.1933.0009 (cited on page 100).

[186] S. Abdollahi et al. 'Fermi Large Area Telescope Fourth Source Catalog'. In: *The Astrophysical Journal Supplement Series* 247.1 (Mar. 2020), p. 33. DOI: 10.3847/1538-4365/ab6bcb (cited on page 105).

[187] A. Albert et al. '3HWC: The Third HAWC Catalog of Very-high-energy Gamma-Ray Sources'. In: *The Astrophysical Journal* 905.1 (2020), p. 76. DOI: 10.3847/1538-4357/abc2d8 (cited on page 105).

[188] S. P. Wakely and D. Horan. 'TeVCat: An online catalog for Very High Energy Gamma-Ray Astronomy'. In: *International Cosmic Ray Conference*. Vol. 3. International Cosmic Ray Conference. Jan. 2008, pp. 1341–1344 (cited on page 105).

[189] K. Oh et al. 'The 105-Month Swift-BAT All-sky Hard X-Ray Survey'. In: *The Astrophysical Journal Supplement Series* 235.1 (2018), p. 4. DOI: 10.3847/1538-4365/aaa7fd (cited on page 105).

[190] M. Ajello et al. 'The Fourth Catalog of Active Galactic Nuclei Detected by the *Fermi* Large Area Telescope'. In: *The Astrophysical Journal* 892.2 (2020), p. 105. DOI: 10.3847/1538-4357/ab791e (cited on page 106).

[191] B. Lott, D. Gasparrini, and S. Ciprini. 'The Fourth Catalog of Active Galactic Nuclei Detected by the Fermi Large Area Telescope – Data Release 2'. In: *arXiv e-print* (Oct. 2020), arXiv:2010.08406 (cited on page 106).

[192] M. Huber. 'Searches for steady neutrino emission from 3FHL blazars using eight years of IceCube data from the Northern hemisphere'. In: *PoS* ICRC2019 (2019), p. 916. DOI: 10.22323/1.358.0916 (cited on page 107).

[193] S. Abdollahi et al. 'The Fermi-LAT Lightcurve Repository'. In: *The Astrophysical Journal Supplement Series* 265.2 (2023), p. 31. DOI: 10.3847/1538-4365/acbb6a (cited on pages 107, 108).

[194] R. C. Jennison. 'A Phase Sensitive Interferometer Technique for the Measurement of the Fourier Transforms of Spatial Brightness Distributions of Small Angular Extent'. In: *Monthly Notices of the Royal Astronomical Society* 118.3 (June 1958), pp. 276–284. DOI: 10.1093/mnras/118.3.276 (cited on page 108).

[195] *Science with the Cherenkov Telescope Array*. WORLD SCIENTIFIC, 2018 (cited on page 121).

[196] I. Sagiv et al. 'Science with a wide-field UV Transient Explorer'. In: 147.4 (2014), p. 79. DOI: 10.1088/0004-6256/147/4/79 (cited on page 121).

[197] C. L. Carilli and S. Rawlings. 'Motivation, key science projects, standards and assumptions'. In: *New Astronomy Reviews* 48.11-12 (2004), pp. 979–984. DOI: 10.1016/j.newar.2004.09.001 (cited on page 121).

[198] R. Abbasi et al. 'Design and performance of the multi-PMT optical module for IceCube Upgrade'. In: *Proceedings of 37th International Cosmic Ray Conference — PoS(ICRC2021), Ed.: A. Kappes*. 37th International Cosmic Ray Conference. ICRC 2021 (Online, July 12–23, 2021). Vol. 395. Pos proceedings of science. Scuola Internazionale Superiore di Studi Avanzati (SISSA), 2022, Art.–Nr.: 1070. DOI: 10.22323/1.395.1070 (cited on page 121).

[199] Z. S. Meyers et al. *Radio Detection of EeV Neutrinos in Dielectric Media using the Askaryan Effect* *for Babies*. DESY, 2021, pp. 1–14 (cited on page 122).

Declaration of independent work

Hiermit erkläre ich, die Dissertation selbstständig und nur unter Verwendung der angegebenen Hilfen und Hilfsmittel angefertigt zu haben. Ich habe mich nicht anderwärts um einen Doktorgrad in dem Promotionsfach beworben und besitze keinen entsprechenden Doktorgrad. Die Promotionsordnung der Mathematisch-Naturwissenschaftlichen Fakultät, veröffentlicht im Amtlichen Mitteilungsblatt der Humboldt-Universität zu Berlin Nr. 42 am 11. Juli 2018, habe ich zur Kenntnis genommen.

I declare that I have completed the thesis independently using only the aids and tools specified. I have not applied for a doctor's degree in the doctoral subject elsewhere and do not hold a corresponding doctor's degree. I have taken due note of the Faculty of Mathematics and Natural Sciences PhD Regulations, published in the Official Gazette of Humboldt-Universität zu Berlin no. 42 on July 11 2018.

Cristina Lagunas Gualda, Berlin 26.07.2023